

**I. Synthesis and Proton Conductivity Studies of
Mesostructured Organosilicates and Bitriazole-Polymer
Composites**

II. Targeted Nanoparticles for siRNA Delivery

Thesis by

Christopher Akinleye Alabi

In Partial Fulfillment of the Requirements

for the Degree of

Doctor of Philosophy



California Institute of Technology

Pasadena, California

2009

(Defended May 15th, 2009)

© 2009

Christopher A. Alabi

All Rights Reserved

Acknowledgements

I feel blessed to have had the opportunity to study here at Caltech among some truly great minds. My experience here has left me intellectually enthused by a wide variety of issues even beyond science for which I am indebted to the whole Caltech and Pasadena community. I would like to start off by thanking my advisor, Mark E. Davis for taking me into his lab and mentoring me for the past five years. When I applied to Caltech, I was fixed on working for Mark not just for his work in certain areas but because he appeared to have such a wide breadth of knowledge across a range of several topics. It felt like I would have several choices all within the same lab. Although this was all idealistic back then, it has turned out to be true. I am thankful to have had the privilege to work and be advised on such a wide range of interesting topics. His constant stream of insightful and creative ideas has left me with a strong desire to pursue research. Last of all, I am grateful for his unwavering guidance and support for my academic advancement.

I would also like to thank my thesis committee members, Dr. Tirrell, Dr. Grubbs, and Dr. Goddard for providing me with research guidance, ideas, and for taking the time to serve on my committee and be a part of my academic growth. In addition, I would like to thank Dr. Stacey Zones and Dr. Yushan Yan for numerous helpful and thought-provoking research discussions. The researchers at City of Hope contributed a great deal to the second part of my thesis project and for that I am truly grateful. Without the rituximab that we obtained from Dr. Raubischek and Dr. David Colcher and their expert advice, I don't think much of the second part of my thesis would have been possible.

Next, I would like to thank all the members of the Davis Lab for working with me and providing me with intangibles. Specifically, I would like to thank Dr. Ryan Zeidan, a

past member whom I overlapped with for a little over two years, for being a good friend, a great researcher, and a constant source of entertainment. Also, I'd like to thank John Mckeen, Brendan Mack, and Jason Gamba for being fun and insightful labmates, roommates, and great friends both in and outside the lab. Next, I owe a big part of my research over the past year or so to Leonard Medrano who took the time to teach me all the biology and biochemistry techniques that I know today. To Nicholas Brunelli and his wife Yoshie Narui, thank you for helping me remember to eat lunch, for bringing me cookies, getting me to play some much needed stress-relief, soccer and great discussions, both scientific and philosophical. You both will always be great and close friends.

My life at Caltech did not only involve the lab, although that is where I spent 95% of my time. In my first year here, I got to know a bunch of good people who became my friends and helped make my experience here balanced. To Joe, Guido, Signe, Winston (and whoever it is I am forgetting because I know I am missing several people), thanks for being there and sharing your time with me.

This thesis would not be possible without my mom and dad who not only brought me into this world, but provided me with early guidance and discipline. I owe my parents everything that I have become and thank them for their trust and for supporting me emotionally and financially throughout my entire academic life. To my sister, Titilayo, thanks for your encouraging words during the first year of my stay here and also for being a great sister and my friend.

I believe I saved the very best for last for I wouldn't be as happy as I am today without the love of my life, Sarah Alabi. She has been here with me through thick and thin, provided me with much of the encouragement that I needed over the past five years. I was

indeed lucky and privileged last year, April 26, 2008, to marry her and make her my wife. The joy of doing good science is nothing compared to the joy of being loved and cared for. I want to thank you Sarah for being with me and enduring my crazy lab hours over the past five years. She should also be getting a doctorate degree for all she has been through. Sarah and I attended Mosaic church here in Pasadena where we made great friends and connected with our Lord and Savior. That brings me to the one who created me, brought me into this world and has kept me whole and safe through out my life, and without whom life would truly be meaningless. I would like to thank God for all the blessings of life and his grace over us all. To him I give all the glory.

Abstract

The underlying theme of the research outlined in both parts of this report is centered on the ability to use synthetic design as a probe to investigate and answer fundamental mechanistic questions in an effort to improve the function of materials employed in energy and biological research. Specifically in the field of energy research, we have designed a new strategy aimed at improving the proton conductivity of organically modified silica-based polymer electrolyte membranes for use in direct methanol fuel cells. Our design involves the incorporation of the desired organic functional group into a siloxane-modified polymerizable surfactant that can be used in mesoporous silicate synthesis. This approach takes advantage of the silicate assembly mechanism, which places surfactants exclusively within the pores of the silicate at high loadings. The desired functional group is revealed upon selective cleavage after hydrothermal silicate synthesis. We have used this approach to synthesize organosilicates with different sized organic groups displaying high organic acid densities and have studied their proton conductivity under fully hydrated conditions. Under these conditions, structural diffusion via a percolated water network is the dominant mechanism of proton transport.

With regards to membranes for use in hydrogen fuel cells that operate best at temperatures above the dew point of water, the need for an alternative to water as the proton conducting medium is desired. Towards this end, we designed a new nitrogen-containing heterocycle (NCH), 4,4-*1H-1H*-bi-1,2,3-triazole (bitriazole) capable of mimicking water in the solid state and have investigated its ability to conduct protons in the presence of polyethylene oxides under anhydrous conditions. With numerous chemical tools at our disposal, we probed the mechanism of proton conduction and confirmed the bitriazole proton

to be the source of anhydrous proton conductivity. Our data suggests structural diffusion as the dominant transport mechanism via synergistic interactions between bitriazole and polyethylene oxides in the polymer-rich region of the composite material that is encapsulated by a crystalline nonconductive bitriazole framework.

In the second part of this report, we shift our focus to the investigation of antibody-mediated targeting, using our well-established cyclodextrin polycation (CDP) nanoparticles containing therapeutic oligonucleotides, to epitopes expressed at the surface of cancer cells as a means of increasing site-specific therapeutic delivery. To do this, we synthesized fragments of anti-CD20 (rituximab) and conjugated them to flexible poly(ethylene glycol) (PEG) linkers with terminal adamantane groups that can interact with the cyclodextrins on the surface of the CDP nanoparticle via the formation of an inclusion complex. With the PEGylated antibody fragments in hand, we investigate, via a B-cell lymphoma model, the binding characteristics of the targeting ligands as well as their effect on the binding, internalization, and efficacy of the targeted CDP-nucleic acid therapeutic nanoparticles.

Table of Contents

Acknowledgements	iii
Abstract	vi
List of Figures	xii
List of Schemes	xix
List of Tables	xx
General Thesis Outline	xxi
Part One: Synthesis and Proton Conductivity Studies of Mesostructured Organosilicates and Bitriazole-Polymer Composites	1
Chapter One: Introduction	2
1.1 Fuel cells and the polymer electrolyte membrane (PEM)	3
1.2 The mechanism of proton transport in water	5
1.3 The nature of proton conductivity in Nafion	6
1.4 Nafion's pitfalls and our new strategy	7
1.5 References	9
Chapter Two: A New Approach for Preparation of Organically Modified Mesostructured Silicates	10
2.1 Abstract	11
2.2 Introduction	12
2.3 Results and discussion	18
2.3.1 Preparation of M41S silicates via siloxane and C ₁₄ -olefin-modified surfactants	18
2.3.1.1 Siloxane-modified surfactants	18
2.3.1.2 MS-5 _{AS} preparation via modified C ₄ -(<i>E</i>)-olefin surfactant..	22
2.3.1.3 MS-5 _{AS} cleavage via ozonolysis	26
2.3.1.4 Porosity – Lack thereof	29
2.3.1.5 Is isomerization responsible for the bent chain configuration?	32
2.3.2 Preparation of M41S silicates via siloxane and C ₁₇ -olefin modified surfactants	36
2.3.2.1 Synthesis of C ₂ -(<i>E</i>)-olefin surfactant and M41S preparation	36
2.3.2.2 Surfactant effect on M41S symmetry	40
2.3.2.3 Attempts at C ₂ -(<i>E</i>)-olefin cleavage in MS-15 _{AS}	41
2.3.3 Preparation of M41S silicates via siloxy-modified acetal and ketal surfactants	45
2.3.3.1 Synthesis of acid labile acetal surfactant	45

2.3.3.2 Preparation and cleavage of MS-25 _{AS}	49
2.3.3.3 Strengthening the silicate pore walls	52
2.3.3.4 Porosity in MS-25 _C silicate	56
2.3.3.5 Organic functionalization of porous MS-25 _C silicate	60
2.4 Further discussion and conclusion	64
2.5 Experimental	68
2.6 References	82
Chapter Three: Proton Conductivity Studies on Organically Modified	
Mesostructured Silicates	85
3.1 Abstract	86
3.2 Introduction	87
3.3 Results and discussion	90
3.3.1 Effect of acid density on proton conductivity	90
3.3.2 Effect of hydrophobicity on proton conductivity	95
3.3.2.1 Synthesis of C ₁₀ -(<i>E</i>) and C ₁₃ -(<i>E</i>)-olefin surfactants	96
3.3.2.2 Preparation of MS-5 _{10AS} and MS-5 _{13AS}	98
3.3.2.3 Preparation of MS-5 _{10C} and MS-8 _{13C}	100
3.3.2.4 Effect of organic chain length on proton conductivity	102
3.3.3 Effect of temperature and water content	103
3.4 Further discussion and conclusion	105
3.5 Experimental	107
3.6 References	113
Chapter Four: Insights into the Nature of Synergistic Effects in Proton	
Conducting 4,4-1<i>H</i>,1<i>H</i>-Bitriazole-Poly(ethylene oxide) Composites	115
4.1 Abstract	116
4.2 Introduction	117
4.3 Results and discussion	122
4.3.1 General properties of bitriazole and its PEO composite	122
4.3.2 Source of anhydrous proton conductivity in bitriazole- PEGDME composites.....	130
4.3.3 Anhydrous proton conductivity as a function of polymer composition	135
4.3.3.1 Effect of polymer concentration	135
4.3.3.2 Effect of PEGDME length	139
4.3.3.3 Effect of PEG-terminated acidic groups	140
4.3.3.4 Effect of bitriazole spacing with ethylene oxides	142
4.3.3.5 Effect of polymer type	145
4.3.4 Probing the synergistic effect between bitriazole and PEGDME via solid and liquid state ¹ H NMR	147
4.4 Further discussion and conclusion	153
4.5 Experimental	160
4.6 References	166

Chapter Five: Future directions and recommendations	169
5.1 Abstract	170
5.2 Increasing the acid strength of densely packed organosilicates	171
5.3 Conductivity enhancement via thin films	172
5.4 Incorporation of bitriazole/PEG composites into pore space of acid modified organosilicates	174
5.5 References	175
Part Two: Targeted Nanoparticles for siRNA Delivery	176
Chapter Six: Introduction	177
6.1 Nanoparticle-based nucleic acid delivery	178
6.2 Targeting nanoparticles: passive and active delivery	178
6.2.1 Passive targeting	178
6.2.2 Active targeting	179
6.3 Targeted delivery to B-cells	180
6.4 References	182
Chapter Seven: Antibody Modification for Nanoparticle Targeting	184
7.1 Abstract	185
7.2 Introduction	186
7.3 Results and discussion	189
7.3.1 Antibody specificity for CD20 on Daudi cells	189
7.3.2 Preparation of Fab and F(ab') ₂ fragments of rituximab	191
7.3.3 Preparation of Fab and F(ab') ₂ PEGylated conjugates	196
7.3.4 Effect of mono-PEGylation on Fab-PEG-Ad affinity	201
7.4 Further discussion and conclusion	202
7.5 Experimental	204
7.6 References	211
Chapter Eight: Characterization of Targeted Nanoparticles for siRNA delivery	213
8.1 Abstract	214
8.2 Introduction	215
8.3 Results and discussion	217
8.3.1 Formulation of targeted nucleic acid particles	217
8.3.2 DLS, zeta potential and salt stability studies	218
8.3.3 In vitro binding and internalization studies	221
8.4 Further discussion and conclusion	226
8.5 Experimental	228
8.6 References	231
Chapter Nine: Future Directions and Recommendations	232
9.1 Abstract	233
9.2 Quantitative binding studies of targeting ligands and particles	234
9.3 Nanoparticle composition: quantification of ligand density	235
9.4 Rate of targeted nanoparticle internalization	236

9.5 Multivalent interactions of Fab and F(ab') ₂ targeted nanoparticles	236
9.6 References	238

List of Figures

Chapter One

Figure 1.1	Left: representative polymer electrolyte fuel cell. Right: reactions at the anode and cathode for a PEMFC and DMFC ...	4
Figure 1.2	Proton transport mechanism in bulk water conceived by Kreuer and Agmon	6
Figure 1.3	Parallel pore structural model of Nafion™	7

Chapter Two

Figure 2.1	X-ray diffraction patterns and possible structures of M41S materials	13
Figure 2.2	Mechanistic pathways for MCM-41 formation	14
Figure 2.3	Traditional surfactant (top) and polymerizable surfactant (bottom)	17
Figure 2.4	X-ray diffraction patterns of as-synthesized mesostructured silicates produced from hydrothermal synthesis with quarternary ammonium surfactants C ₁₄ and C ₁₈ as well as 1a and 1b	19
Figure 2.5	Representative ²⁹ Si CP MAS NMR of as-synthesized MCM-41 with 1a	20
Figure 2.6	X-ray diffraction patterns of MS- 5 _{AS} with varying silicon to surfactant (5) ratio and temperatures	24
Figure 2.7	Liquid ¹³ C NMR of (5) vs. solid-state ¹³ C CP MAS NMR spectra of MS- 5 _{AS} . Inset shows ²⁹ Si CP MAS NMR	25
Figure 2.8	¹³ C CP MAS NMR spectra of MS- 5 _{AS} and MS- 5 _C . Inset shows X-ray diffraction pattern of MS- 5 _{AS} and MS- 5 _C	27
Figure 2.9	Thermogravmetric analysis of MS- 5 _C	29
Figure 2.10	N ₂ adsorption isotherm for MS- 5 _C . Inset – IUPAC classification for adsorption isotherms	30
Figure 2.11	Bent chain (a) and straight chain (b) pore structural models	31

Figure 2.12	X-ray diffraction patterns of M41S materials made with different ratios of (<i>E</i>) to (<i>Z</i>)-olefin surfactants, (10) and (11) ..	34
Figure 2.13	Proposed bent chain configuration of (5) and (11) within the pores of their respective silicates	36
Figure 2.14	As-synthesized MCM-48, MS- 15 _{AS} formation with (15) as a function of ageing time	38
Figure 2.15	¹³ C NMR of (15) and ¹³ C CP MAS NMR of MS- 15 _{AS}	39
Figure 2.16	X-ray diffraction patterns of MS- 14 _{AS} and MS- 15 _{AS}	40
Figure 2.17	¹³ C CP MAS NMR spectra of MS- 15 _{AS} before and after (MS- 15 _C) ozonolysis. Inset shows XRD spectra before and after ozonolysis	42
Figure 2.18	Nitrogen adsorption and desorption isotherms of MS- 15 _C before and after calcination	43
Figure 2.19	¹ H NMR of (18) (and (17) for comparison) and the reaction of (18) with HBr, CH ₃ CN, and H ₂ O at 50°C	46
Figure 2.20	(a) Ease of hydrolysis of cyclic ketals (<i>Adapted from Green's protective groups in organic synthesis.</i>) (b) Dithioacetal formation from a ketone	47
Figure 2.21	¹ H NMR spectra of ketal surfactant before and after cleavage with HBr/CH ₃ CN/H ₂ O. Inset shows reaction scheme for the preparation of ketal surfactant	48
Figure 2.22	¹³ C CP MAS NMR of MS- 25 _{AS} and liquid state (25) . Inset shows X-ray diffraction pattern of MS- 25 _{AS}	50
Figure 2.23	¹³ C CP MAS NMR of MS- 25 _{AS} before and after cleavage with HBr/CH ₃ CN/H ₂ O. Inset shows X-ray diffraction pattern of MS- 25 _{AS} before and after cleavage	51
Figure 2.24	²⁹ Si CP MAS NMR of MS- 25 _{AS} and MS- 25 _C , i.e., before and after acid cleavage	52
Figure 2.25	Powder X-ray diffraction pattern of varying silica (TEOS)-to-surfactant (25) ratio. Sol gel composition of 4:1:1:400 vs. 2:1:1:200. Inset shows effect on via ²⁹ Si CP MAS NMR	54
Figure 2.26	Powder X-ray diffraction pattern of varying base (TMAOH) content. Inset shows effect on via ²⁹ Si CP MAS NMR	55

Figure 2.27	(a) ^{13}C CP MAS NMR spectra of $\text{MS}^*-\mathbf{25}_{\text{AS}}$ before and after cleavage ($\text{MS}^*-\mathbf{25}_{\text{C}}$). Inset shows powder X-ray diffraction spectra of $\text{MS}^*-\mathbf{25}_{\text{AS}}$ and $\text{MS}^*-\mathbf{25}_{\text{C}}$. (b) ^{29}Si CP MAS NMR spectra of $\text{MS}^*-\mathbf{25}_{\text{AS}}$ and $\text{MS}^*-\mathbf{25}_{\text{C}}$	57
Figure 2.28	Nitrogen adsorption-desorption isotherm of $\text{MS}^*-\mathbf{25}_{\text{C}}$	58
Figure 2.29	Transmission electron microscopy of $\text{MS}^*-\mathbf{25}_{\text{C}}$ after calcination at 550°C	59
Figure 2.30	^{13}C CP MAS NMR reaction products of 1, 2- and 1, 3-diols with $\text{MS}^*-\mathbf{25}_{\text{C}}$	61
Figure 2.31	Removal of residual bound pTSA with stoichiometric NaOH wash at room temperature from the reaction of $\text{MS}^*-\mathbf{25}_{\text{C}}$ with methylpropane-1,3-diol	63
Chapter Three		
Figure 3.1	Schematic diagram of the preparation of $\text{MS}-\mathbf{5}_{4\text{C}}$ bearing carboxylic acid groups	89
Figure 3.2	^{13}C CP MAS NMR of MCM-41-CA and $\text{MS}-\mathbf{5}_{4\text{C}}$	91
Figure 3.3	Cole-Cole plot at room temperature for $\text{MS}-\mathbf{5}_{4\text{C}}$. Inset A and B show corresponding magnitude and phase of the impedance vs. frequency plots	92
Figure 3.4	Proton conductivity of $\text{MS}-\mathbf{5}_{4\text{C}}$, MCM-41-CA absolute and normalized values, $\text{MS}-\mathbf{5}_{4\text{AS}}$, and MCM-41	93
Figure 3.5	A representative slice of the distribution of water molecules within the pores of $\text{MS}-\mathbf{5}_{4\text{C}}$	94
Figure 3.6	X-ray powder diffraction pattern of $\text{MS}-\mathbf{5}_{4\text{AS}}$, $\text{MS}-\mathbf{5}_{10\text{AS}}$, and $\text{MS}-\mathbf{8}_{13\text{AS}}$	98
Figure 3.7	^{13}C CP MAS NMR spectra of a. $\text{MS}-\mathbf{5}_{4\text{AS}}$; b. $\text{MS}-\mathbf{5}_{10\text{AS}}$; c. $\text{MS}-\mathbf{8}_{13\text{AS}}$. Inset shows a representative ^{29}Si CP MAS NMR of $\text{MS}-\mathbf{8}_{13\text{AS}}$	99
Figure 3.8	^{13}C CP MAS NMR spectra of $\text{MS}-\mathbf{5}_{4\text{C}}$, $\text{MS}-\mathbf{5}_{10\text{C}}$, and $\text{MS}-\mathbf{8}_{13\text{C}}$	100
Figure 3.9	Proton conductivity of $\text{MS}-\mathbf{5}_{4\text{C}}$, $\text{MS}-\mathbf{5}_{10\text{C}}$, $\text{MS}-\mathbf{8}_{13\text{C}}$, $\text{MS}-\mathbf{5}_{4\text{AS}}$, and MCM-41 at room temperature under fully hydrated conditions	102

Figure 3.10	Arrhenius plot of proton conductivity of MS- 5 _{4C} as a function of temperature for fully hydrated and nonhydrated solids	104
Figure S3.1	Hydrated conductivity setup	112
Chapter Four		
Figure 4.1	Cyclic voltammograms of imidazole (top) and triazole (bottom)	123
Figure 4.2	TGA of bitriazole and bitriazole-poly(ethylene glycol)dimethyl ether (Mn ~ 1000) 20:1	124
Figure 4.3	Proton conductivity of bitriazole at room temperature as a function of time and temperature	125
Figure 4.4	VT-Powder XRD of bitriazole under dry purging argon	126
Figure 4.5	Isothermal dehydration of bitriazole:PEGDME-1K (i.e., Mn ~ 1000) 20:1 at 407 K under flowing argon	127
Figure 4.6	DSC curves of PEGDME-1K and bitriazole-PEGDME-1K (20:1) recorded under N ₂ atmosphere with a heating rate of 10 K/min	127
Figure 4.7	XRD spectra of bitriazole and bitriazole-PEGDME-1K under argon at 25°C and at 150°C	129
Figure 4.8	(a) Representative Cole-Cole plots of bitriazole:PEGDME-1K composite in a 20:1 ratio at various temperatures. (b) Log AC conductivity, σ_{AC} vs. Log frequency at various temperatures	131
Figure 4.9	Conductivity plots for bitriazole-PEGDME-1K and d-bitriazole-PEGDME-1K samples, both at a 20:1 ratio	132
Figure 4.10	FT-IR spectra at room temperature of bitriazole before and after N- <i>H</i> deuterium exchange	133
Figure 4.11	Variation of k_H/k_D in plain and deuterated bitriazole-PEGDME-1K 20:1 as a function of temperature	134
Figure 4.12	Conductivity plots for bitriazole-PEGDME-1K composites with increasing bitriazole content	135

Figure 4.13	Linear fits to VTF equation after applying the vanishing mobility, T_0 to the data points from Figure 4.12	138
Figure 4.14	Conductivity plots of bitriazole with different poly(ethylene glycol) PEG sizes as a function of temperature	139
Figure 4.15	Conductivity plots of bitriazole with different PEG-diacids (20:1 ratio) as a function of temperature. The 20:1 bitriazole:PEG(1K)-Acid corresponds to 9.1 mol% acid groups	141
Figure 4.16	XRD spectra of BtzEO-n (0-4) along with T_m and T_g determined via DSC	143
Figure 4.17	Conductivity of BtzEO-n (0-4):PEGDME-1K composites (20:1) at 353, 373, and 393K	144
Figure 4.18	Conductivity plots of bitriazole with PEG, PEGDME, and PPG polymers. All polymers have a $M_n \sim 1000$	146
Figure 4.19	Room temperature solid state ^1H MAS NMR at spin-speed of 13 kHz of (b) bitriazole and (d) bitriazole:PEGDME-1K (20:1), and liquid ^1H NMR in DMSO- d_6 of (a) bitriazole and (c) bitriazole:PEGDME-1K (20:1)	148
Figure 4.20	(A) ^1H NMR (liquid) in DMSO- d_6 of bitriazole:PEGDME-1K with increasing PEGDME fraction from 20:1 to 1:1., (B) expanded region from (A)	150
Figure 4.21	^1H NMR of bitriazole, bitriazole:PPG (1:1) and bitriazole:PEGDME (1:1) in DMSO- d_6 (expanded region)	151
Figure 4.22	Proposed proton conduction mechanism. One of several possible pathways for proton conduction	158
Chapter Seven		
Figure 7.1	FACS of IgG-AF488 and holo-transferrin-AF488 binding to Daudi cells known to have a high density of CD20 and low density of transferrin receptors	189
Figure 7.2	Dark and bright field fluorescence images of IgG binding to the external surface of Daudi cells that over-express CD20 receptors	190
Figure 7.3	Cleavage of IgG to give Fab or F(ab')_2 via PEPSIN and PAPAINE	192

Figure 7.4	SDS PAGE Gel of PAPAIn digest	193
Figure 7.5	SDS PAGE Gel of PEPSIN digest	194
Figure 7.6	Competitive binding assay of rituximab IgG-AF488 with F(ab') ₂ and Fab	195
Figure 7.7	MALDI of PEGylated Fab reaction mixture	197
Figure 7.8	MALDI trace of purified mono-PEGylated Fab fragment. Inset shows PAGE gel of purified mono-PEGylated Fab fractions ...	198
Figure 7.9	MALDI of PEGylated F(ab') ₂ reaction mixture	199
Figure 7.10	MALDI trace of purified mono-PEGylated F(ab') ₂ fragment. Inset shows PAGE gel of purified mono-PEGylated F(ab') ₂ fraction (circled)	200
Figure 7.11	Competitive binding assay of rituximab Fab-AF488 with unmodified Fab and Fab-PEG-Ad	201
Figure S7.1	HPLC trace from PAPAIn digest	208
Figure S7.2	MALDI of Fab fragment	208
Figure S7.3	HPLC trace from PEPSIN digest	209
Figure S7.4	MALDI of F(ab') ₂ fragment	209
Figure S7.5	HPLC trace of crude Fab-PEG-AD reaction mixture	210
Figure S7.6	HPLC trace of crude F(ab') ₂ -PEG-AD reaction mixture	210
Chapter Eight		
Figure 8.1	Structure of imidazole-terminated β -cyclodextrin-containing polycation	215
Figure 8.2	Schematic of CDP nucleic acid particle assembly	217
Figure 8.3	Effect of targeting ligand on particle size (effective diameter) ..	218
Figure 8.4	Effect of targeting ligand on zeta potential	219

Figure 8.5	Aggregation of siRNA particles in physiological salt (1× PBS). Particles were formulated at a 3+/- charge ratio	220
Figure 8.6	Live cell binding of nanoparticles at 4°C. All polyplexes were PEGylated and formulated at a 3+/- charge ratio	221
Figure 8.7	Luciferase expression 48 hours after transfection of Daudi-Luc cells with siCON, siMOD1, siMOD2, and siMOD3	223
Figure 8.8	Luciferase expression after 48 hours transfection of Daudi-Luc cells with particles containing siMOD-3. Particles were formulated with CDP, PEG, and siMOD-3 at a 3+/- charge ratio	224
Figure 8.9	Representation of Fab targeted nanoparticle and IgG binding to daudi cell surface expressing CD20 receptors (extracellular loops). I – high Fab density, II – low Fab density	226

List of Schemes

Chapter Two

Scheme 2.1	Synthesis of 1a, b	18
Scheme 2.2	Synthesis of (5)	22
Scheme 2.3	Synthesis of MS- 5_{AS} and MS- 5_C	23
Scheme 2.4	Synthesis of (9) and (11)	33
Scheme 2.5	Synthesis of (14) and (15)	37
Scheme 2.6	Synthesis of (19)	45
Scheme 2.7	Synthesis of (22)	47
Scheme 2.8	Synthesis of ketal surfactant (25) via dimethylaminoacetone ...	49
Scheme 2.9	Reaction of MS- 25_C with 1,2- and 1,3 diols	60

Chapter Three

Scheme 3.1	Preparation of MCM-41-CA	90
Scheme 3.2	Synthesis of (5)	96
Scheme 3.3	Synthesis of (8)	97

Chapter Four

Scheme 4.1	Synthesis of bitriazole	122
Scheme 4.2	Synthesis of di-bitriazoles with ethylene oxide spacers (BtzEO-n) where n = 1-4. n = 0 corresponds to plain bitriazole	142

Chapter Five

Scheme 5.1	Retrosynthesis for the preparation of aryl sulfonamide surfactant	172
------------	----------------------------------------------------------------------------	-----

Chapter Seven

Scheme 7.1	Procedure for PEGylation of Fab (and F(ab') ₂) fragment	196
Scheme S7.1	Preparation of Mal-PEG-AD	206

List of Tables**Chapter Four**

Table 4.1	Chemical properties of NCH	119
Table 4.2	Fitting parameters obtained from conductivity data in Figure 4.12 fitted with the VTF equation [4.1]	137

General Thesis Outline

This thesis consists of two separate and unrelated projects and therefore has been broken up into two parts. Part One begins with a new approach for the design of organically modified silicates that can potentially reduce methanol permeation while attaining moderate levels of proton conductivity. These materials are interesting for use as polymer electrolyte membranes (PEMs) in direct methanol fuel cells. The synthetic strategy for this new approach, which involves the incorporation of the desired organic functional group into a siloxane-modified polymerizable surfactant that can be cleaved after mesoporous silicate synthesis, is introduced in Chapter II. Chapter III explores the effect of acid density, hydrophobicity via an increase in the alkyl group chain length, and temperature of several synthesized carboxylic acid bearing organosilicates on proton conductivity under fully humidified conditions. In Chapter IV, we shift gears slightly to systems that can facilitate proton mobility under anhydrous conditions, as these remain an important challenge to the efficient operation of hydrogen fuel cells. Here, we document the possibility of anhydrous proton conductivity via structural diffusion in bitriazole poly(ethylene oxide) composites. We arrive at some key conclusions that provide valuable information for the future development of nitrogen-containing heterocycle-based PEMs.

The second part of this thesis focuses on the preparation of rituximab antibody fragments and their conjugation to PEG adamantane (PEG-AD) linkers towards their use in the assembly of an anti-CD20-targeted CDP delivery vehicle. We launch a preliminary investigation into the effects of PEG-AD rituximab fragment conjugates as targeting ligands on CDP-siRNA nanoparticle formation, binding, and functional siRNA delivery to lymphoma B-cells.

PART I

**Synthesis and Proton Conductivity Studies of
Mesostructured Organosilicates and Bitriazole-Polymer
Composites**

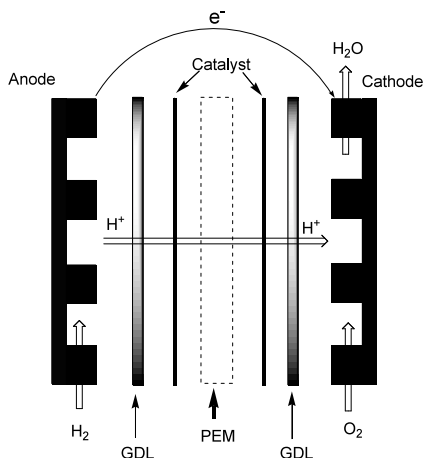
Chapter I

Introduction

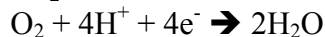
1.1 Fuel cells and the polymer electrolyte membrane (PEM)

Fuel cells are highly efficient electrochemical devices (50-70%) that directly convert chemical energy into electricity with zero or near-zero pollutant emissions, depending on the fuel source used.^{1, 2} The hydrogen fuel cell, also known as the polymer electrolyte membrane fuel cell (PEMFC), is one of several types of fuel cells that has gained attention because of its high power density, solid polymer electrolyte membrane, and renewable fuel supply (i.e. when hydrogen is produced from water or biomass). These attractive features have made PEMFCs promising alternatives as power sources for automotive applications. The operation and full scale commercialization of PEMFCs hinges on the development of low-cost proton conductors that can operate at both low and intermediate temperatures (up to 150 °C) under nonhumidified conditions with high conductivities. The direct methanol fuel cell (DMFC) is a subset of the PEMFC and is typically used for small portable power applications due to its low operating temperature (80–90°C) and easy refueling capabilities. As its name implies, it utilizes methanol directly as its fuel and consequently does not require bulky pressurized hydrogen storage or a reforming subsystem.

The polymer electrolyte membrane (PEM), sandwiched between the anode and cathode, is a pivotal component of both the PEMFC and DMFC. Its main function is to keep the fuels at the anode and cathode separated, as well as facilitate proton transport from the anode where the protons are produced via hydrogen or methanol oxidation to the cathode where oxygen reduction takes place, as shown in Figure 1.1 below.



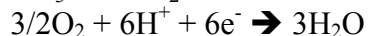
PEMFC



Anode

Cathode

DMFC



Anode

Cathode

Figure 1.1 Left: representative polymer electrolyte fuel cell. Right: reactions at the anode and cathode for a PEMFC and DMFC

The development of a PEM is a balancing act, as several different key requirements have to be juggled for each type of fuel cell. Those common to both PEMFCs and DMFCs include low cost, high chemical stability and mechanical strength, and high proton conductivity. One key requirement that has to be met by PEMs for use in DMFCs is low methanol permeation. Since methanol and water are miscible in all proportions, swelling of the membrane with water results in methanol diffusion through the PEM from the anode to the cathode, which gives rise to fuel and voltage loss. This issue is one of the major problems affecting the practical application of DMFCs. With regards to PEMFCs, a key requirement of the PEM involves the ability to operate at intermediate temperatures (120–180°C) where the vast benefits for operating PEMFCs – such as reduced carbon monoxide poisoning at the anode, better water management at the electrodes, and faster kinetics – can be met. Since the efficiency of the direct conversion of chemical energy into electrical energy hinges on the effectiveness of proton transport across the fuel cell membrane, the development of membranes that meet the aforementioned requirements has been the focus of intense research

over the past few decades. In order to design new PEMs, it is pertinent that we understand the variable mechanisms of proton transport in hydrated systems.

1.2 The mechanism of proton transport in water

In aqueous systems, the proton is well confined within the hydration spheres of two water molecules (H_5O_2^+). In other words, the proton is not a free rotor. Two widely accepted mechanisms are used to describe proton diffusion: first – the vehicular mechanism whereby proton migration occurs via the translational motion of large protonated water clusters such as H_5O_2^+ and H_9O_4^+ . In this case, the proton diffuses together with a water vehicle where it is shielded by the hydrogen-bonded water along the entire path. The second mechanism, known as the Grotthuss mechanism or structural diffusion, involves proton transfer (hopping) within hydrogen bonds from one vehicle to another (H_9O_4^+ to H_5O_2^+). This transfer is mediated by significant local dynamics with respect to formation and cleavage of hydrogen bonds within their bulk water clusters. Reconstruction of the protonic environment by expansion of the static water cluster via the construction of new hydrogen bonds ultimately leads to the formation of a clear path for proton movement.

The reason for the unusually high mobility of protons in water (i.e., acidified water) compared to other ions similar in size to the hydronium ion is explained by structural diffusion, wherein proton transport is determined by the formation and rupture of hydrogen bonds (e.g., from H_9O_4^+ to H_5O_2^+) rather than by the slower diffusion of bulky ionic species (vehicular mechanism).

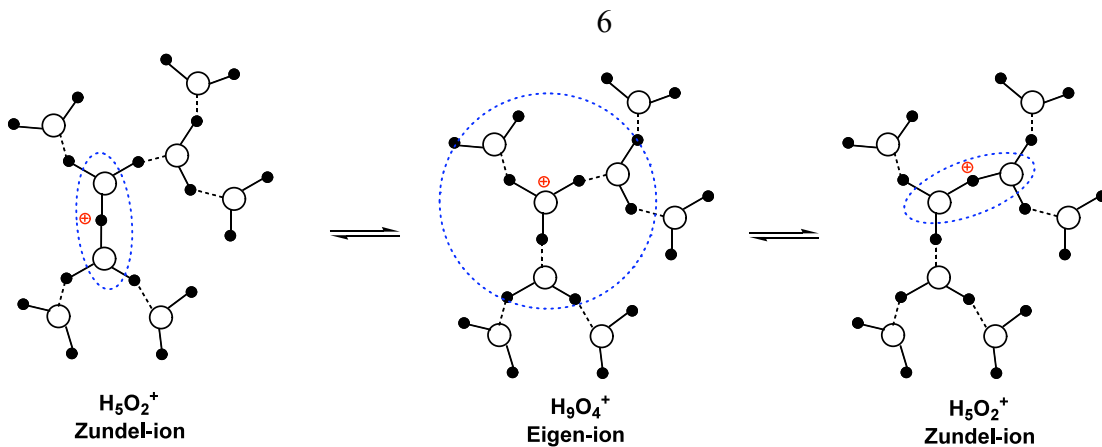


Figure 1.2 Proton transport mechanism in bulk water conceived by Kreuer and Agmon

1.3 The nature of proton conductivity in Nafion

Currently, the most widely used PEMs for both PEMFCs and DMFCs are hydrated perfluorosulfonic acid polymers, such as Nafion, produced by Dupont. Nafion consists of a tetrafluoroethylene backbone with pendant side chains of perfluorinated vinyl ethers which terminate in sulfonic acid groups (Figure 1.3). The sulfonic acid groups form hydrophilic clusters and channels that are surrounded by a hydrophobic fluorocarbon matrix. This hydrophobic Teflon-like backbone gives Nafion an exceptional thermal and chemical stability.^{3, 4} Upon exposure to water, the hydrophilic pores in Nafion expand into large spherical interconnected domains (Figure 1.3) with an estimated diameter of 40-50 Å.⁴ Nafion exhibits excellent proton conductivity when hydrated due to its nonpolar hydrophobic backbone, which facilitates the formation of bulk rather than surface water, and the high dissociation constant of its sulfonic acid groups.⁵⁻⁹ Proton mobility via surface hopping and diffusion have been shown to be slow processes due to strong electrostatic forces between the sulfonate and hydronium ions. However, “bulk water” found in the middle of the pores, has been shown facilitate high proton mobility as a result of structural diffusion or “excess conductivity” of protons through the hydrogen-bonded network formed by bulk water

molecules, as well as traditional mass diffusion of hydronium ion clusters. Under high water uptake, fast proton conduction is observed due to structural diffusion, which has been shown to be the dominant proton transfer mechanism.⁵

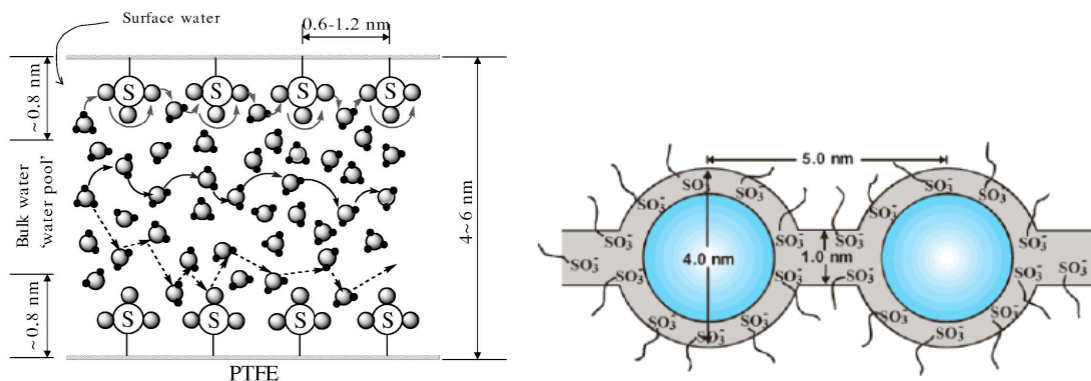


Figure 1.3 Parallel pore structural model of Nafion™

1.4 Nafion's pitfalls and our new strategy

In DMFCs, excessive uptake of water in Nafion leads to polymer swelling and methanol crossover. Thus, the amount of bulk water and the size of hydrophilic channels are key variables in the design of new PEMs for DMFCs. In order to make DMFCs competitive battery substitutes for portable devices, new PEMs that can reduce methanol permeation while attaining high levels of proton conductivity will have to be designed. We address this issue in Chapters II and III through the preparation of ordered densely packed organosilicate structures that have pendant acid groups for proton conductivity and hydrophobic chains that can potentially diminish methanol permeability. In the process of this study, we devised a new strategy for the incorporation of organic groups within the inner pore walls of mesoporous silicates. This strategy led to the preparation of nonporous organosilicates at

high organic densities with moderate proton conductivities. The lack of porosity, potentially low methanol uptake, and high acid density in the organosilicates prepared via this methodology should make them promising alternatives as PEMs in DMFCs.

With regards to PEMFCs, Nafion's capacity for proton conduction is directly proportional to its level of hydration. The dependence on acidic water through which Nafion attains its fast proton mobility via structural diffusion cripples its performance under the preferred PEMFC working conditions of little to no humidity and intermediate temperatures above the dew point of water. As a result, new polymer electrolyte membranes that facilitate high proton mobility under the aforementioned conditions remain an important challenge to the commercialization of PEMFCs. Thus, our second goal in the first part of this thesis involved investigating through careful design the possibility of proton mobility in the solid state by adapting the key principles responsible for ultra-fast proton conductivity in acidic water. This work, presented in Chapter IV, documents the possibility of anhydrous proton conductivity via structural diffusion in bitriazaole poly(ethylene glycol) composites. We arrive at some key conclusions that provide valuable information for the future development of nitrogen-containing heterocycle-based PEMs as alternatives to Nafion for use in PEMFCs.

1.5 References

1. Steele, B. C. H.; Heinzl, A., *Nature* **2001**, 414, (6861), 345-352.
2. Carrette, L.; Friedrich, K. A.; Stimming, U., *Chemphyschem* **2000**, 1, (4), 162-193.
3. Mauritz, K. A.; Moore, R. B., *Chemical Reviews* **2004**, 104, (10), 4535-4585.
4. Sondheimer, S. J.; Bunce, N. J.; Fyfe, C. A., *Journal of Macromolecular Science-Reviews in Macromolecular Chemistry and Physics* **1986**, C26, (3), 353-413.
5. Choi, P.; Jalani, N. H.; Datta, R., *Journal of the Electrochemical Society* **2005**, 152, (3), E123-E130.
6. Commer, P.; Hartnig, C.; Seeliger, D.; Spohr, E., *Molecular Simulation* **2004**, 30, (11-12), 755-763.
7. Kanamura, K.; Mitsui, T.; Munakata, H., *Chemistry of Materials* **2005**, 17, (19), 4845-4851.
8. Paddison, S. J.; Paul, R.; Rasmussen, K. O.; Gronbech-Jensen, N.; Zawodzinski, T. A., *Abstracts of Papers of the American Chemical Society* **1999**, 217, U497-U497.
9. Paddison, S. J.; Paul, R.; Zawodzinski, T. A., *Journal of the Electrochemical Society* **2000**, 147, (2), 617-626.

Chapter II

A New Approach for Preparation of Organically Modified Mesostructured Silicates

2.1 Abstract

We report on a new method for the preparation of densely packed organic groups within mesostructured organosilicates. Our strategy involves the use of modified surfactants bearing two distinct features. The first is a polymerizable siloxane head group that can be permanently incorporated onto the silicate pore wall during preparation of the mesostructured organosilicate. The second is a functional group within the hydrophobic surfactant tail that can be cleaved to generate the desired functionality after assembly. This approach, by virtue of the assembly mechanism, places the organic groups exclusively within the inner pore wall of the mesostructure at high loadings and densities unattainable by either post-synthetic graft or co-condensation methods. In this chapter, we investigate the use of two different but unique cleavage strategies. In the first organosilicate, we employ (*E*)-olefins as our cleavable group. Olefin cleavage via ozonolysis followed by an oxidative workup generates non-porous carboxylic acid modified organosilicates. The lack of porosity is believed to be due to random coiling of surfactant chains within the silicate pores. Isomerization of the (*E*)-olefin surfactant during synthesis was ruled out, as the both (*E*) and (*Z*) isomers of the surfactant form distinctly different structures under similar synthetic conditions. In the second material, we made use of acid cleavable ketals to synthesize disordered but porous architectures, which were able to undergo subsequent ketalizations with selected organic groups, demonstrating the possibility of synthesizing porous networks via this approach.

2.2 Introduction

Among the extensive family of mesoporous silicates known as M41S introduced by the Mobil group back in the late 1980s, MCM-41 is unquestionably the most studied and widely used. MCM-41 has a two-dimensional structure with an X-ray pattern displaying three or more low angle peaks below $10^\circ 2\theta$ that can be indexed to a hexagonal (hk0 lattice, $p6m$) unit cell (Figure 2.1). Other members of the M41S family include other hexagonal structures such as SBA-2 (3-D, $p6_3/mmc$) and SBA-3 (2-D, $p6m$, prepared under acidic synthetic conditions); cubic structures such as MCM-48 ($Ia3d$) and SBA-1 ($Pm3n$); and lamellar structures such as MCM-50. These silicates are traditionally synthesized in basic media using cationic alkyltrimethylammonium surfactants,¹ however, subsequent studies have shown that they can also be prepared under acidic media^{2, 3} with normal amines,⁴ nonionic surfactants,⁵ and dialkyldimethylcationic surfactants.⁶ The M41S silicates share common characteristics such as a uniform pore size distribution with dimensions in the 1.5–20 nm range, amorphous silicate pore walls, and relatively high silanol concentrations, as confirmed by their ^{29}Si NMR spectra.

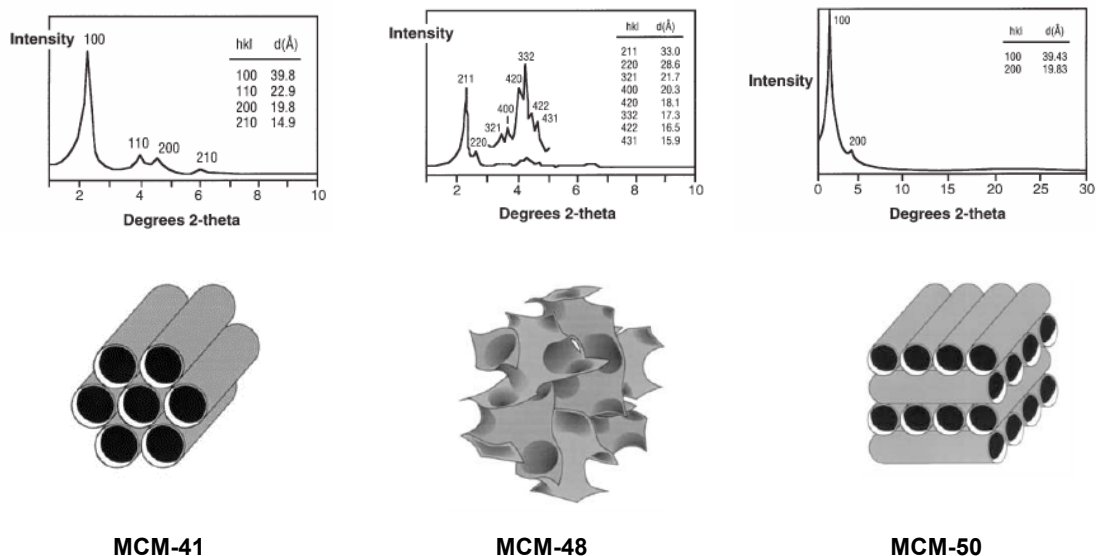


Figure 2.1 X-ray diffraction patterns and possible structures of M41S materials⁷ (Adapted from Reference 7)

While MCM-41 appears to form under a broad range of synthetic conditions and reagents, MCM-48 appears to have a much narrower synthesis regime and is typically prepared using higher surfactant concentrations than those used to form MCM-41.⁸ The diffraction pattern of MCM-48 consists of several peaks that can be assigned to the Ia3d space group and the structure has been proposed to be an infinite periodic minimal surface of the gyroid form $(Q^{230})^3$ (Figure 2.1). Lamellar structures can be prepared using the same surfactant systems under a wide range of conditions and their diffraction patterns exhibit low angle peaks that can be indexed to h00 reflections (Figure 2.1). These structures have been proposed to form stacks of surfactant rods with inorganic silicate sheets. Lamellar silicates have poor thermal stability and typically collapse upon removal of the surfactant templates.

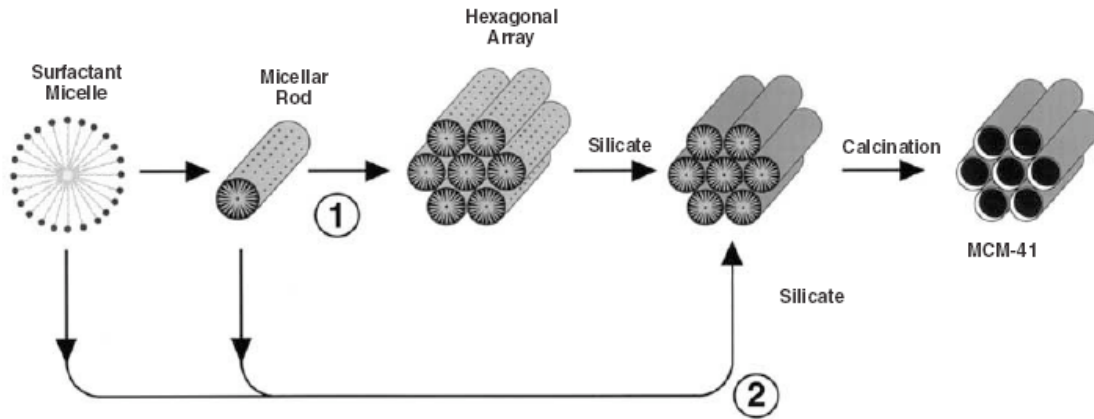


Figure 2.2 Mechanistic pathways for MCM-41 formation: (1) liquid crystal phase initiated⁹ and (2) silicate anion initiated^{3, 10} (Figure adapted from Reference 1)

The mechanism of formation of the M41S silicates is believed to proceed via a liquid crystal templating (LCT) mechanism. Two different pathways exist under this broad definition, as illustrated in Figure 2.2. The first pathway involves the pre-existence of surfactant aggregates, i.e., liquid-crystal like structures in solution, which form the M41S framework due to migration and polymerization of the silicate ions into their aqueous regions. This pathway has been discounted as most M41S syntheses have been accomplished in the surfactant concentration regime below that required for lyotropic liquid crystals (LLC).³ In addition, other results have shown the presence of ordered phases in solution only in the presence of a silica source. The second pathway is now universally accepted in the majority of cases. This pathway has been generally described as involving the multidentate binding of silicate oligomers to the cationic surfactant followed by silicate polymerization in the interfacial region and charge density matching between the surfactant and silicate.² This pathway has been shown to proceed either via stacking of silicated surfactant rods¹⁰ or via the formation of an initial lamellar intermediate.³

Mesoporous silicas are particularly interesting because of their high specific surface area, zero electrical conductivity, open ordered channels of variable dimensions, and high chemical, structural, and mechanical stability. The high specific surface area of these materials allows their surfaces to be modified with acidic organic groups that facilitate increased water uptake and proton conductivity. With regards to the latter, studies have shown that the 2-D pore structure of MCM-41 can promote proton conductivity once functionalized with acidic organic groups, with increasing organic group density leading to increasing conductivities. It has also been shown that methanol permeability can be abated by increasing the density of the hydrophobic organic groups attached to the silicate walls of these materials. Examples where these materials have been used with some success include MCM-41- and MCM-48-containing sulfonic acids, phosphonic acids and carboxylic acids by Mckeen and Davis,¹¹ sulfonic acid functionalized MCM-41 nanoparticles by Wark and Marschall^{12, 13}, CsHSO₄ impregnated mesoporous thin films by Nagomoto and Otomo¹⁴ and several others.¹⁵⁻¹⁷ In all the aforementioned examples, the organically modified mesoporous materials were prepared via co-condensation or post-synthetic graft of organic groups onto the walls of the mesoporous support.

The ability to align the closely packed pores of these mesostructured silicates perpendicularly to the electrode surface (in the case of MCM-41) should maximize conductivity, as a clear path for proton transfer would be created through the pore channels. For example, alignment of the pores of MCM-41 perpendicular to a surface has been successfully carried out in anodic alumina membranes by evaporation-induced self-assembly.¹⁸ Additionally, significant conductivity enhancements were observed in perpendicularly aligned phosphosilicate glass and CsHSO₄-SiO₂ films.^{14, 19}

The above improvement in conductivity due to pore alignment opens the door to the preparation of organically modified aligned mesoporous silicates. As previously mentioned, the ability to increase the acidic organic group density while simultaneously incorporating hydrophobic groups will lead to an increase in proton conductivity accompanied by a decrease in methanol permeability. This should give rise to a highly selective membrane. However, the two known routes to chemically modify the surface of mesoporous silicates, i.e., post-synthetic graft and co-condensation, are incapable of incorporating high densities of long or large hydrophobic acidic groups. Grafting, which involves a post-synthetic modification of the surface silanols with the desired organic groups can lead to pore blockage when large groups are involved and thus result in low loadings. Co-condensation on the other hand attains moderate loading capacities but a fraction of the organic functional groups end up buried within the walls of silicates, thus rendering them inaccessible.

In order to overcome these limitations, we embarked on this study, which involves a new approach towards incorporation of densely packed acidic organic groups onto the inner surface of M41S silicates as a way to enhance proton conductivity in these types of mesostructured materials. Our approach involves the use of functional surfactants that can be permanently attached to the pore walls during synthesis. These modified surfactants have a siloxane head group capable of being incorporated into the pore walls during assembly and a cleavable group embedded within the hydrophobic surfactant tail to generate the desired functional group after M41S formation (Figure 2.3). This approach, by virtue of the assembly mechanism, should place the organic groups on the inner pore walls of mesostructure at high loadings that are unattainable by either grafting or co-condensation.

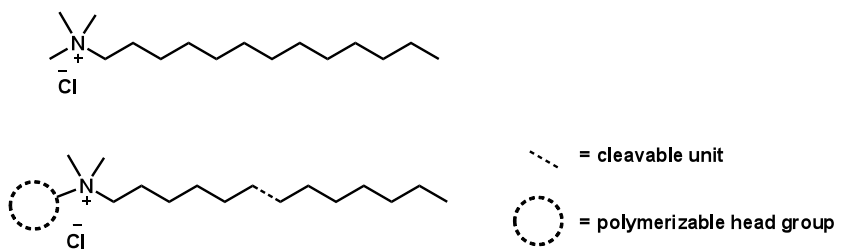


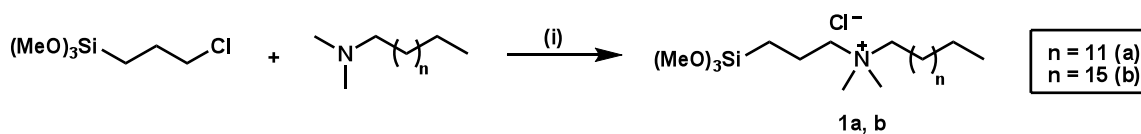
Figure 2.3 Traditional surfactant (top) and polymerizable surfactant (bottom)

2.3 Results

2.3.1 Preparation of M41S silicates via siloxane-modified C₁₄-olefin surfactants

2.3.1.1 Siloxane-modified surfactants

Since the pore walls of mesoporous materials are composed of amorphous silica, we chose to use a hydrolyzable trimethoxysilane functional group for surfactant incorporation to the pore walls. At the time of this research, we came across only one reference²⁰ suggesting the synthesis of MCM-41 and MCM-48 using a trimethoxysilyl modified silica source. To test the feasibility of this idea, we synthesized (**1a**) and (**1b**) by quaternizing N,N-dimethyltetradecane and N,N-dimethyloctadecane with chloropropyl trimethoxy silane (Scheme 2.1).



Scheme 2.1 Synthesis of **1a, b**; (i) MeOH, reflux, 48 h; n = 11 for C₁₄ or n = 15 for C₁₈

The silicates were prepared using tetraethylorthosilicate (TEOS) as the main silica source under alkaline hydrothermal conditions with a sol-gel composition of 1 SiO₂: 0.28 C_n-Si or C_n: 0.29 tetramethylammonium hydroxide (TMAOH): 80 H₂O. After mixing for 1 h, the sol-gel composites were aged for 16 and 24 hours, after which, the samples were washed, dried thoroughly, and analyzed by powder X-ray diffraction (XRD).

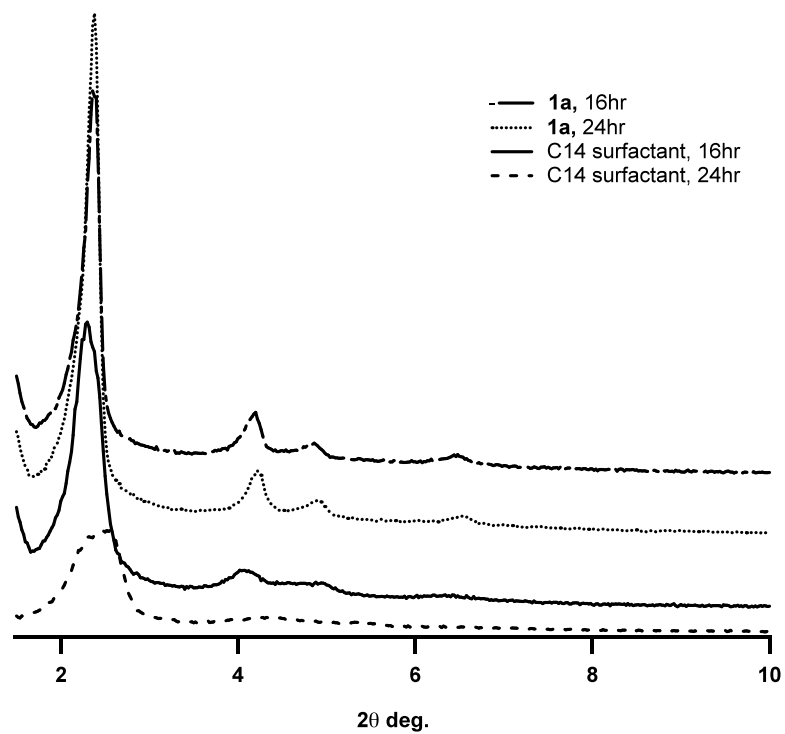
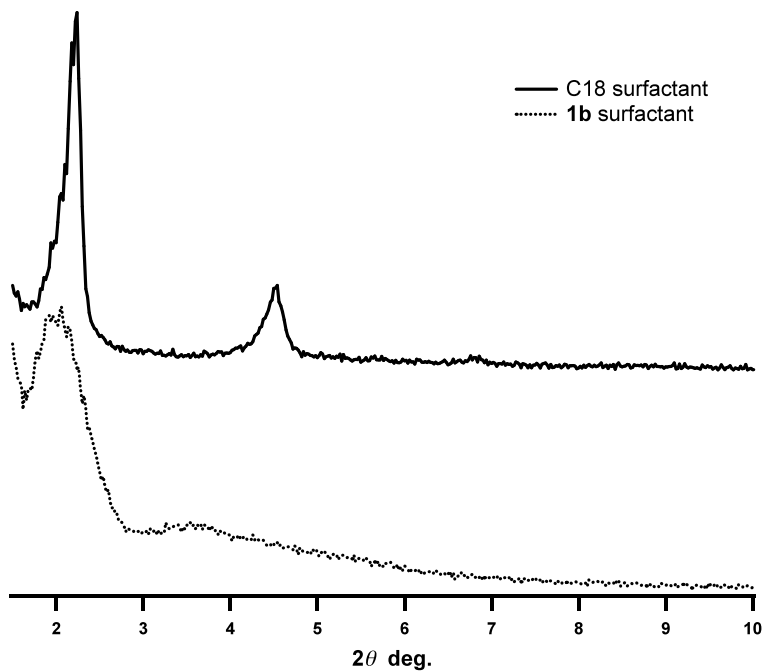


Figure 2.4 X-ray diffraction patterns of as-synthesized mesostructured silicates produced from hydrothermal synthesis with quarternary ammonium surfactants C₁₄ and C₁₈ as well as **1a** and **1b**

The as-synthesized silicates prepared with the C_{18} surfactant gave three low-angle reflections corresponding to the 100, 200, and 300 planes of a lamellae phase (MCM-50). The silica anchored C_{18} surfactant resulted in a single, broad, low-intensity reflection indicating short-range packing but not long-range order.

The C_{14} surfactant, on the other hand, gave three well-defined low-angle reflections after 16 hours that can be indexed on a hexagonal unit cell corresponding to MCM-41, with $a_0 = 2d_{100}/\sqrt{3} = 43.3\text{\AA}$ (Figure 2.4). Assuming a typical pore wall thickness of 10\AA ,⁹ the pore diameter can be estimated to be $(a_0 - 10) = 3.3\text{ nm}$. Prolonging the ageing time to 24 hours gave rise to peak broadening along with a shift towards higher 2θ angles. These changes correspond to a wider pore distribution and pore shrinkage. However, when the C_{14} -Si surfactant was used, MCM-41 with sharper reflections was made corresponding to a narrower pore-size distribution. In addition, the degree of crystallinity, inferred from the peak intensity, appears to worsen with prolonged ageing time.

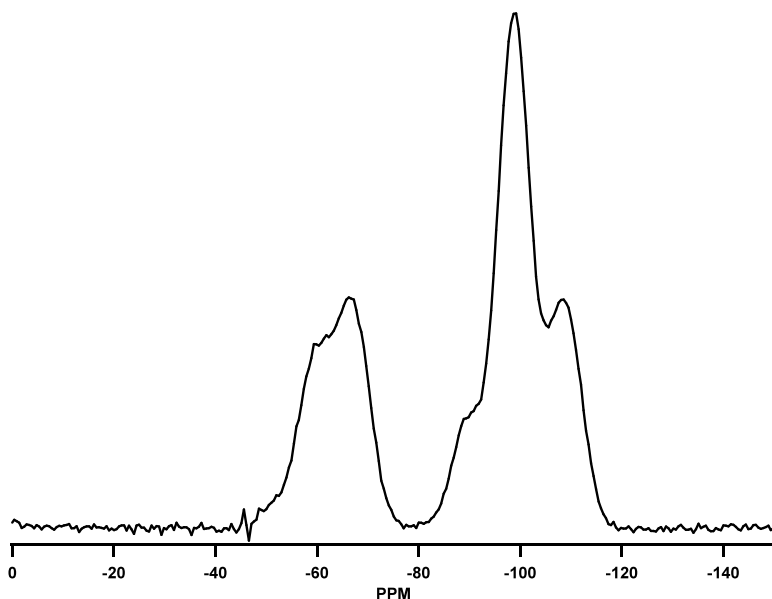


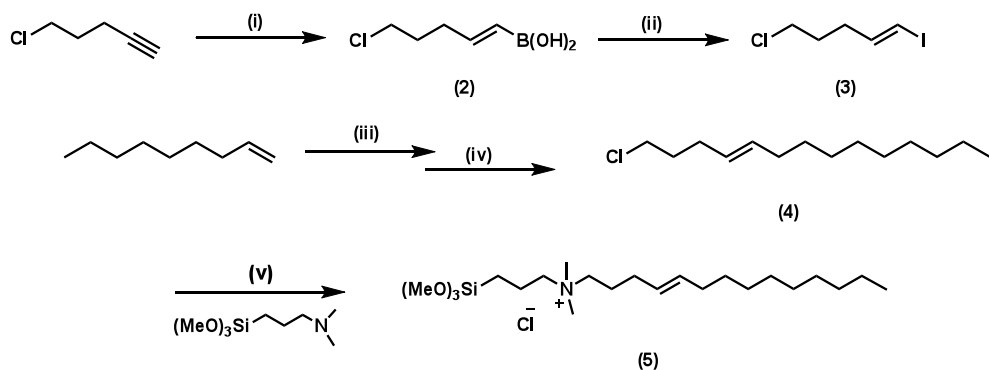
Figure 2.5 Representative ^{29}Si CP MAS NMR of as-synthesized MCM-41 with **1a**

To ensure successful attachment of the surfactant to the pore wall, ^{29}Si CP MAS NMR of the as-synthesized materials was taken and shown (Figure 2.5) to exhibit five distinct signals. The first two signals at -61.5 and -66.8 ppm are assigned to silicon bonded to carbon, i.e., T^1 $[(\text{C})\text{Si}(\text{OH})_2(-\text{OSi})]$ and T^2 $[(\text{C})\text{Si}(\text{OH})(-\text{OSi})_2]$, while the other three at -89.5, -98.7 and -108 ppm are assigned to pure silicon environments Q^2 $[\text{Si}(\text{OH})_2(-\text{OSi})_2]$, Q^3 $[\text{Si}(\text{OH})(-\text{OSi})_3]$ and Q^4 $[\text{Si}(-\text{OSi})_4]$. The presence of the T-peaks confirms the covalent attachment of the polymerized surfactants to the pore walls.

Having demonstrated the feasibility of using (**1a**) as a surfactant for the synthesis of MCM-41, we embarked on the synthesis of polymerizable surfactants with cleavable units within the chain structure of the surfactant tail. We settled on the use of an (*E*)-olefin functional group as the cleavable unit to be installed into the surfactant chain. This functional group was chosen because of its stability under aggressive hydrothermal conditions, its hydrophobicity, and its geometry within the surfactant tail, which when in the (*E*)-olefin conformation is similar to that of the saturated surfactant (**1**). Furthermore, there are numerous reagents available for the effective cleavage of the olefin functional group into carboxylic acids that can serve as the proton conductive group or undergo further derivation if needed.

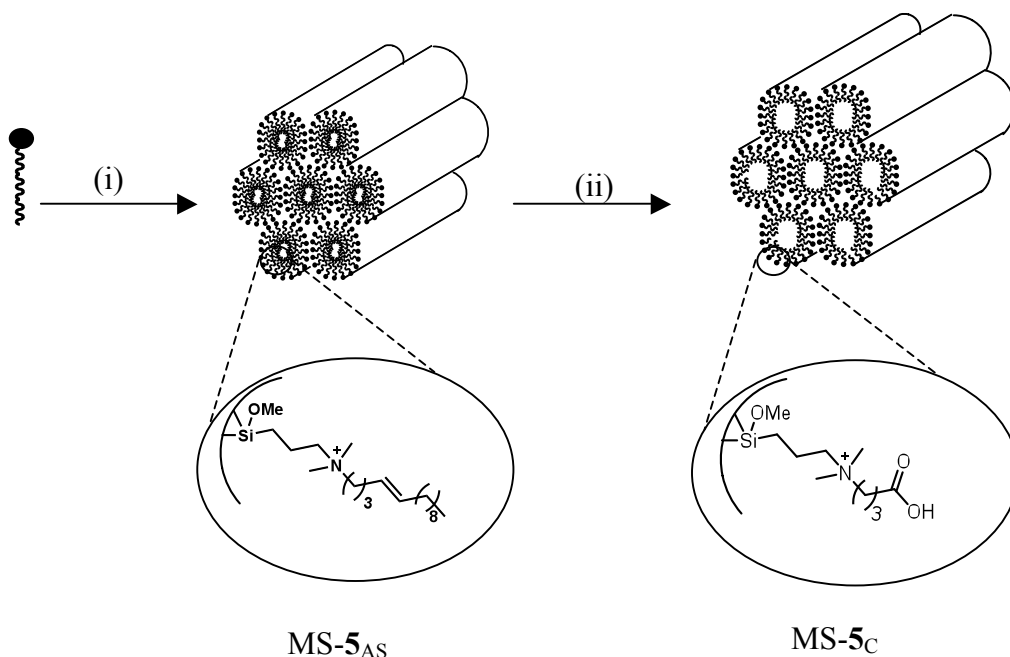
2.3.1.2 MS-5_{AS} preparation via modified C₄-(*E*)-olefin surfactant

Our approach to the desired functional surfactant began with commercially available 5-chloropent-1-yne, as shown in Scheme 2.2.



Scheme 2.2 Synthesis of (5); (i) a. catecholborane, neat, 100°C, 3 h, b. H₂O, 70°C, 2 h; (ii) iodine, NaOH, ether, 0°C, 0.5 h; (iii) 0.5M 9-BBN in THF, 0°C to r.t, 6 h; (iv) PdCl₂(dppf), NaOH, (3), reflux, 16 h; (v) (4), MeOH, reflux, 84 h

(*E*)-5-chloropent-1-enylboronic acid (2) was prepared from the hydrolysis of the catechol boronic ester, which is readily synthesized via hydroboration of 5-chloropent-1-yne with catecholborane. The (*E*)-5-chloropent-1-enylboronic acid (2) was converted to the corresponding (*E*)-5-chloropent-1-enyl iodide (3) by iodine in the presence of a base at 0°C with complete stereochemical purity in near quantitative yield. The organometallic reagent, B-nonyl-9-borabicyclo[3.3.1]nonane (B-nonyl-9-BBN), was readily obtained from the hydroboration of 1-nonene with 9-BBN at room temperature. Cross coupling of (*E*)-5-chloropent-1-enyl iodide, (3) with B-nonyl-9-BBN in the presence of 3 mol% of PdCl₂(dppf) and sodium hydroxide in refluxing THF afforded (4) in good yield. The *J* coupling constant of 15 Hz in the ¹H NMR for the olefin protons verified complete retention of the (*E*)-olefin configuration. Compound (4) was quaternized with *N,N*-dimethylaminopropyltrimethoxysilane in methanol to give the desired surfactant (5) in 40% yield.



Scheme 2.3 Synthesis of MS-5_{AS} and MS-5_C; (i) TMAOH, TEOS, H₂O, 100°C, 24 h; (ii) O₃, -78°C, 6 h, acid/H₂O₂ oxidation, HCl wash. MS-5_{AS} (MS-5_C) stands for: **M**esostructured Silicate – surfactant (**5**) – **a**s synthesized (**c**alcined).

The (*E*)-olefin surfactant (**5**) was subjected to alkaline hydrothermal synthesis with TEOS as the primary silica source. We began with a sol-gel composition similar to that used with **1a**, i.e., 1 SiO₂: 0.28 (**5**): 0.29 TMAOH: 80 H₂O. After ageing at 100°C for 24 hrs, the resulting white precipitate was washed extensively via soxhlet extraction and dried overnight. The powder XRD pattern as shown in Figure 2.6 gave a sharp 100 reflection but a poorly defined broad peak in place of the sharp 110 and 200 reflections.

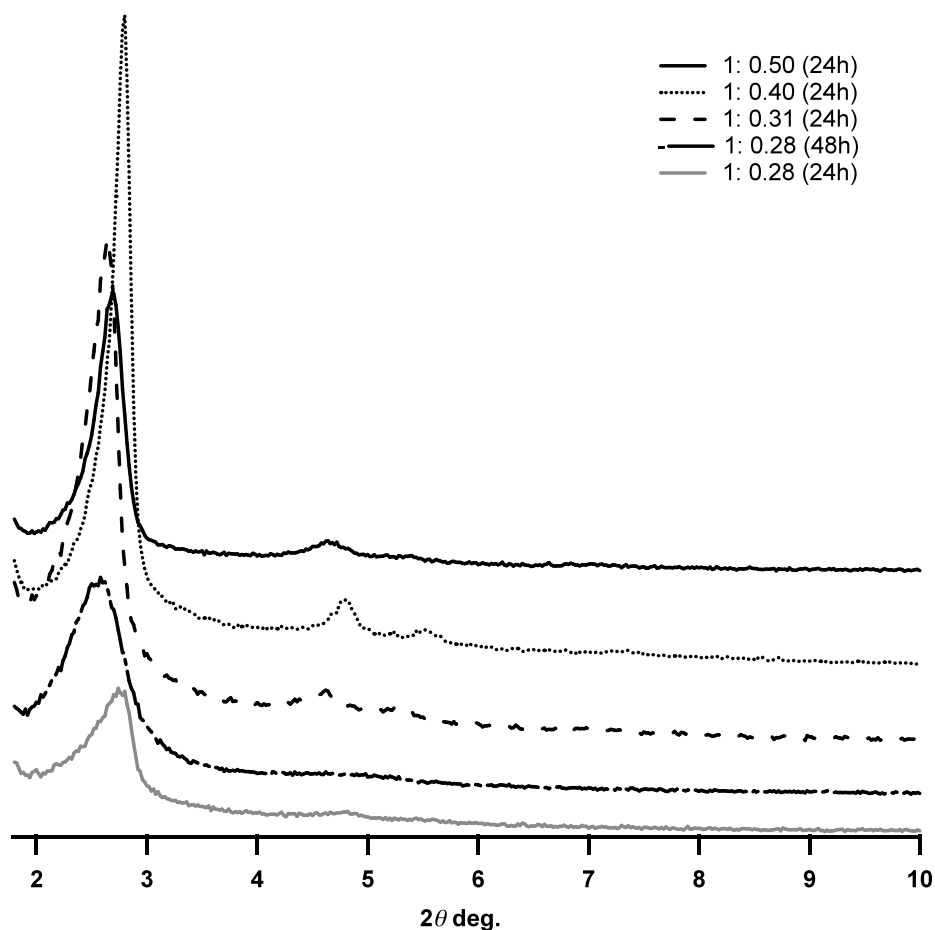


Figure 2.6 X-ray diffraction patterns of MS-5_{AS} with varying silicon to surfactant (**S**) ratio and temperatures

In order to improve the degree of long-range order, the ageing time and silicon-to-surfactant ratio were varied (Figure 2.6). Increasing the ageing time from 24 to 48 hours resulted in better-resolved 110 and 200 peaks. However, increasing the fraction of surfactant from a 1:0.28 to a 1:0.4 (TEOS/ (**S**)) ratio (while keeping the surfactant-to-base ratio constant) led to well-defined MCM-41 reflections. Beyond the 1:0.4 ratio, no further improvement in symmetry was observed.

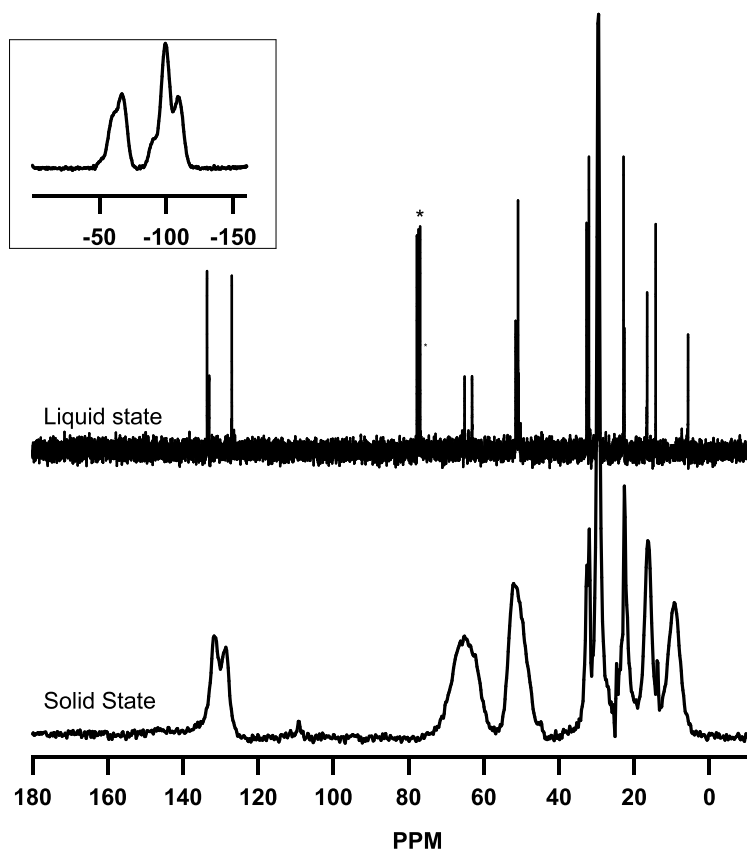


Figure 2.7 Liquid ^{13}C NMR of (**5**) vs. solid-state ^{13}C CP MAS NMR spectra of MS-**5**_{AS}. Inset shows ^{29}Si CP MAS NMR. * chloroform

Structural details of the encapsulated functional surfactant in the as-synthesized materials were examined by solid-state ^{13}C and ^{29}Si CP MAS NMR. The solid-state ^{13}C CP MAS NMR chemical shifts were dominated by a strong resonance at 30 ppm attributed to the methylene carbons on the surfactant tail. The quaternary amine methyl and methylene groups appear at 52.3 and 64.4 ppm, respectively. The three upfield shifts at 22.9, 16.7, and 10 ppm represent the carbons β to the ammonium, the terminal methyl carbon on the surfactant tail, and the β -silicon carbon. The olefin carbons appear at 128.6 and 131.8 ppm. The solid-state ^{13}C CP MAS NMR of the as-synthesized solid matches up with the liquid-state ^{13}C NMR of (**5**) (Figure 2.7) thus verifying the stability of the surfactant to the alkaline

hydrothermal conditions. The ^{29}Si CP MAS NMR spectrum (Figure 2.7 inset) displays the typical T-type organosilica and Q-type pure SiO_2 resonances. Although cross polarization measurements are not quantitative, the relative ratio of the T-peaks to the Q-peaks signifies a large incorporation of the silicon-carbon functionality within the pore walls of the as-synthesized composite. Thus, ^{13}C and ^{29}Si NMR spectra both confirm the presence of the complete functional surfactant occluded within the pores of these highly ordered MCM-41 organosilicates.

2.3.1.3 MS-5_{AS} surfactant (5) cleavage via ozonolysis

Upon verification of intact surfactant within the pores of MS-5_{AS}, we turned our focus to the oxidation of the olefin groups in order to generate porous structures with pendant carboxylic acid groups in the mesopores. Ozone was chosen as a suitable oxidizing reagent because of its strong oxidizing properties at low temperatures, i.e., -78°C , and its relatively mild workup. Other reagents such as $\text{OsO}_4/\text{HIO}_4$ and KMnO_4 , though efficient, would pose serious problems during purification. Ozonolysis of the composite MCM-41 hybrids was carried out by bubbling ozone through a solution of the hybrid material. The required time for complete olefin cleavage via ozonolysis was 7 hours at an ozone concentration of $60\ \mu\text{g}/\text{mL}$ (flowing at 0.0125 liters per minute, LPM). Following ozonolysis, a second oxidative workup was required to convert residual monozide to the carboxylic acid. This was done by treating the sample with formic acid and hydrogen peroxide after ozonolysis. The resulting material was then rinsed with 1N HCl to protonate any residual carboxylate species, and thoroughly washed via soxhlet extraction with dichloromethane to remove any unbound fragments.

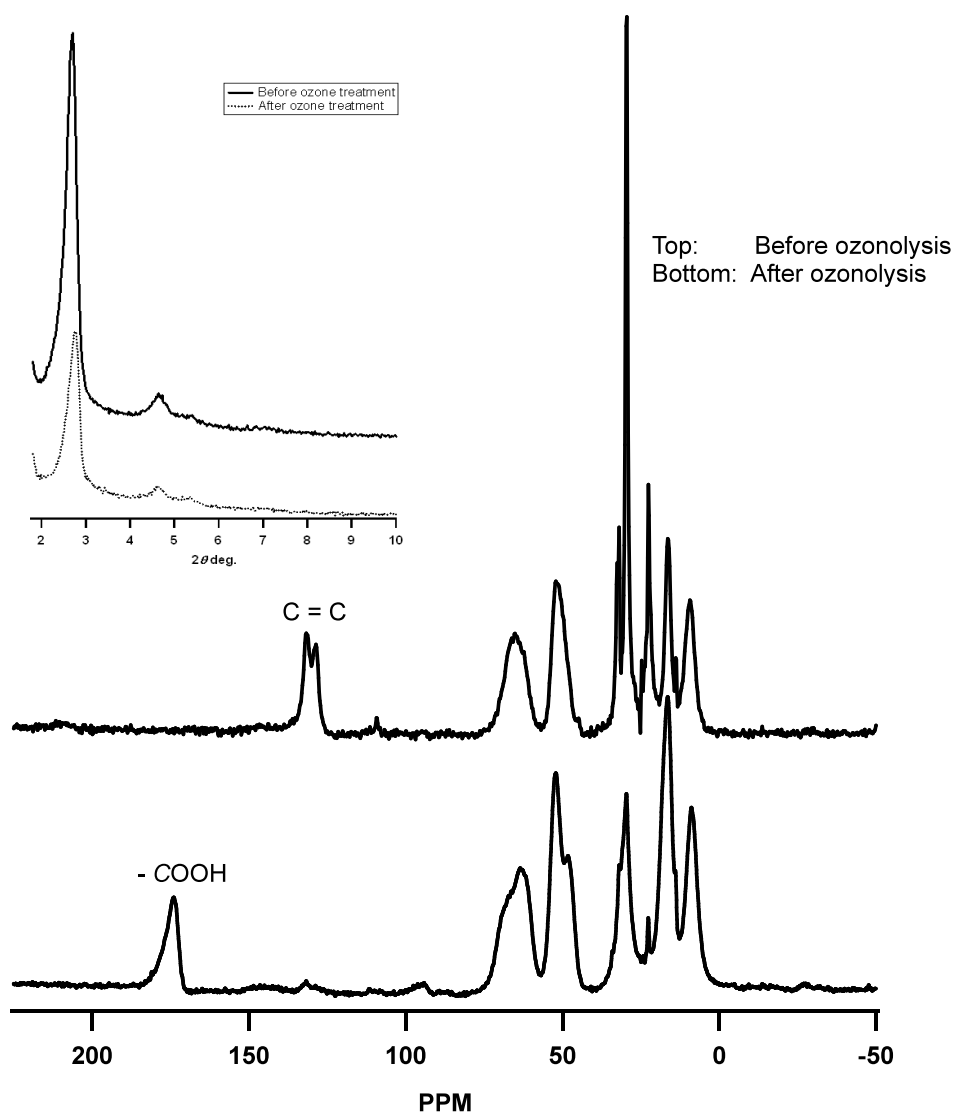


Figure 2.8 ^{13}C CP MAS NMR spectra of MS-5_{AS} and MS-5_C. Inset shows X-ray diffraction pattern of MS-5_{AS} and MS-5_C.

The extent of olefin cleavage by the ozone treatment was verified ^{13}C CP MAS NMR (Figure 2.8). The absence of the olefin carbon peaks at 128.6 and 131.8 ppm and the presence of the downfield carbonyl carbon at 174 ppm confirmed complete cleavage of the surfactant in the pores MCM-41 to give pendant carboxylic acids. Furthermore, the reduction of the 30

ppm peak corresponding to the methylene carbons in the surfactant tail confirms the extraction of unbound organic groups from the composite.

The powder XRD spectra of the solid after ozonolysis and acid treatment (Figure 2.8 inset) shows a similar diffraction profile as that of the as-synthesized material, albeit with lower intensity. This indicates a slight loss in the degree of order upon oxidation. The organic loading determined by thermogravimetric analysis (TGA) after ozonolysis was 2.2 mmol/g (i.e., mmole of organic/gram of composite material). This is one of the highest silica surface loadings reported for a molecule this size. As seen from the TGA plot in Figure 2.9, the organic groups occupy close to a remarkable 50 wt% of the entire mesoporous silicate. The slight mass loss under 200°C represents the removal of physisorbed water from the solid. Decomposition of the organic occurs between 200 and 500°C, as supported by the two large exothermic peaks. Following this decomposition, silanol condensation between vicinal diols takes place between 500 and 700 degrees, as seen by the second smaller exothermic transition. Post-synthetic grafting typically gives loadings of 0.5-1 mmol/g while co-condensation gives higher loadings in the 1-2 mmol/g range. However, the latter sometimes results in groups buried within the silicate walls thus rendering them inaccessible. Both methods place the organic groups both on the inner and outer pore surfaces. Our new approach, by virtue of the silicated liquid crystal templating pathway, places the organic function exclusively on the inner walls of the mesoporous material. Thus, the high loading obtained demonstrates the unique nature of this novel technique for high-density organic incorporation onto the inner walls of mesoporous materials.

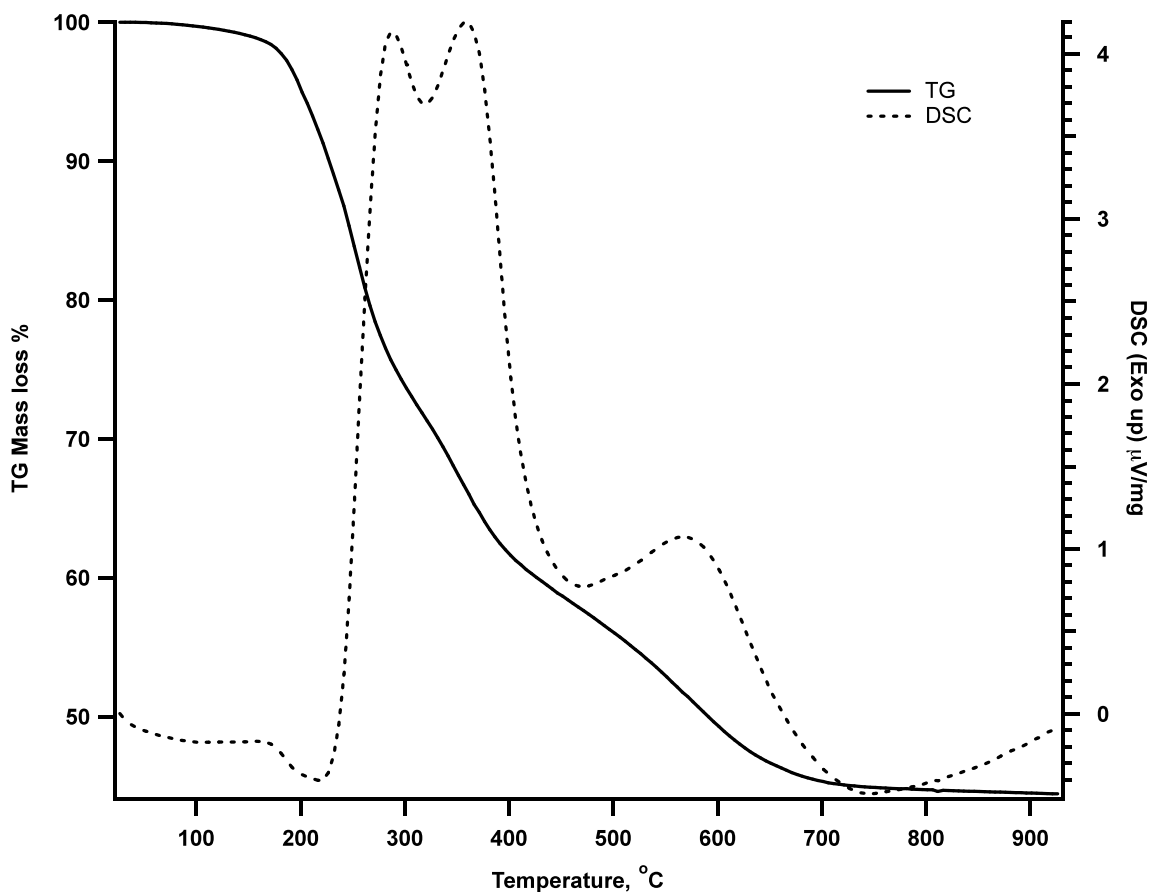


Figure 2.9 Thermogravimetric analysis of MS-5_C

2.3.1.4 Porosity – Lack thereof

After ozonolysis, we probed MS-5_C for porosity by carrying out a nitrogen adsorption/desorption measurement. In this analytical technique, the sample is evacuated and cooled to liquid nitrogen temperature and then dosed with nitrogen gas at a series of pressures. Gas molecules are adsorbed onto the sample surface with each increment in pressure. After initial surface adsorption, the larger pores are filled and this continues until bulk condensation of nitrogen gas molecules. The pressure is then reduced in a step-wise fashion, at which point desorption of the occluded nitrogen gas molecules begins. Analysis of the adsorption and desorption isotherms via the Barret-Joyner-Halenda (BJH) equation gives

the total pore volume. To our surprise, MS-5_C showed a type III isotherm with negligible nitrogen adsorption at all relative pressures.

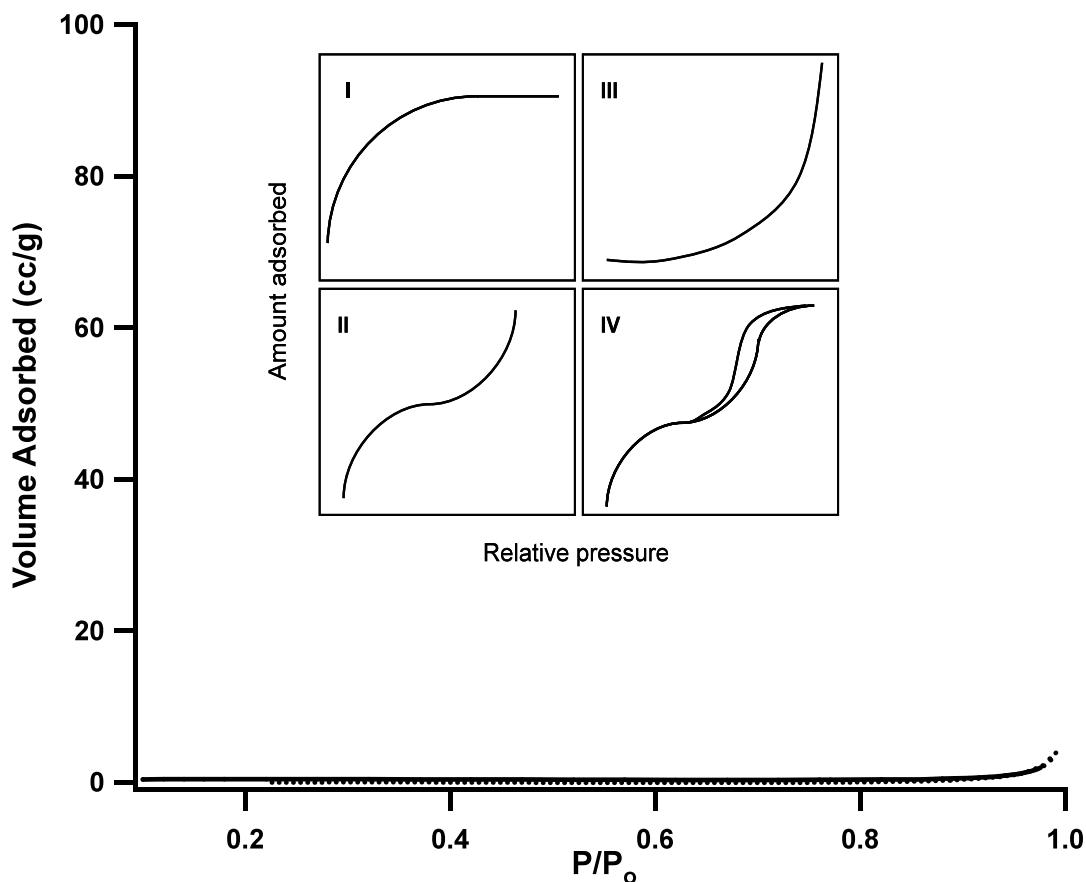


Figure 2.10 N₂ adsorption isotherm for MS-5_C. Inset – IUPAC classification for adsorption isotherms

Mesoporous MCM-41 with large pores typically display a type IV isotherm with capillary condensation giving rise to the hysteresis loop, a common indicator for the presence of mesoporosity. The type III isotherm class that we observe with our composite is characteristic of weak adsorbate-adsorbent interactions and is most commonly associated with nonporous materials. Lack of porosity in these materials can be rationalized by assuming the surfactant takes on a bent rather than a straight chain configuration within the pores of the mesostructured silicates (Figure 2.11).

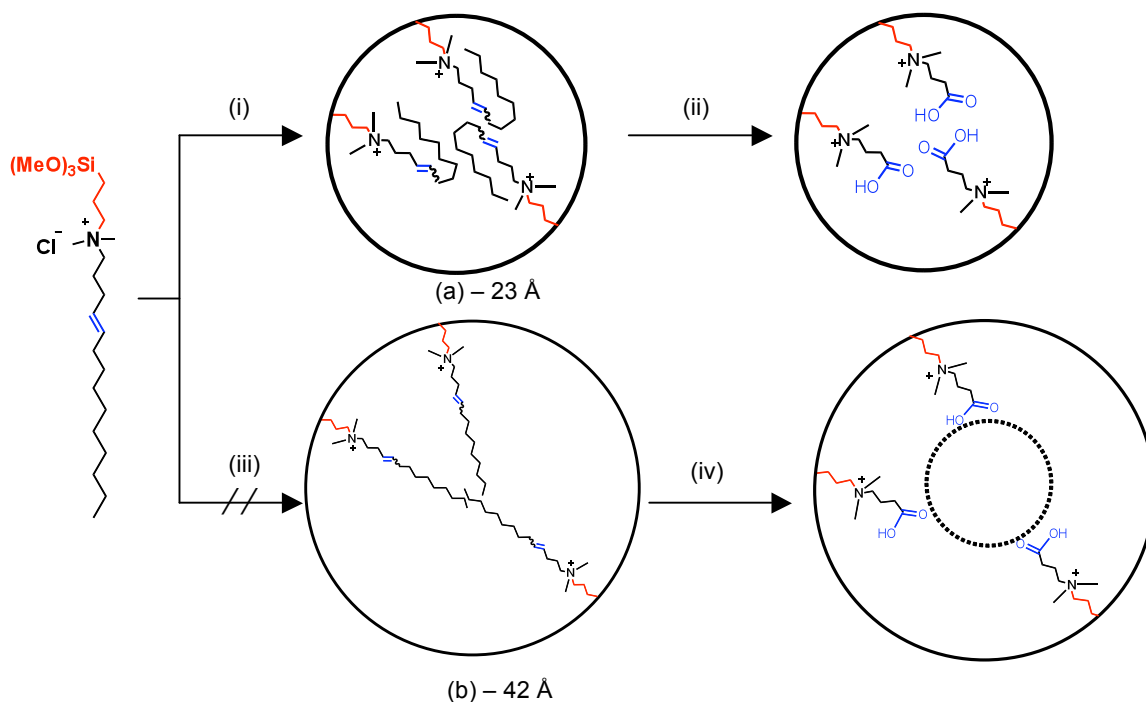
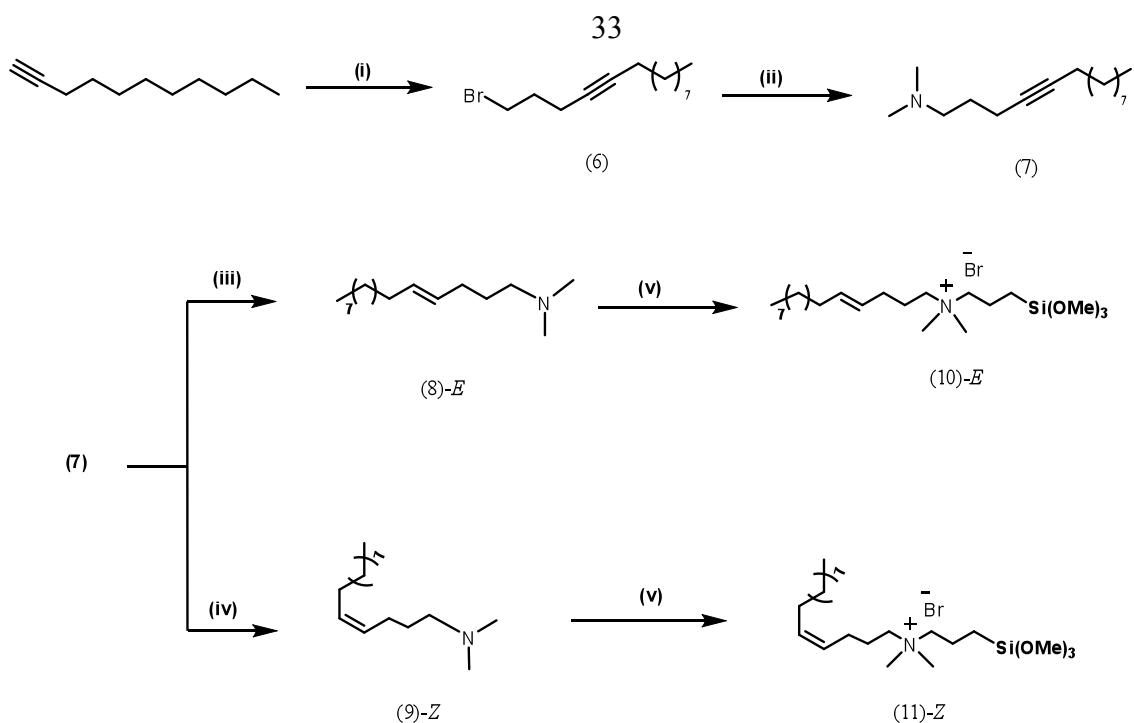


Figure 2.11 Bent chain (a) and straight chain (b) pore structural models

An estimate of 27\AA (using d_{100} from XRD data) obtained for the pore diameter by assuming a typical MCM-41 pore wall thickness of 10\AA ⁹ is consistent with the calculated value of 23\AA predicted by the bent-chain model (Figure 2.11, vs. 42\AA from the straight chain model). As depicted in step (ii) of Figure 2.11, cleavage of the olefin functional group based on the bent chain model should lead to a nonporous silicate.

2.3.1.5 Is Isomerization responsible for the bent chain conformation?

Surfactants within the pores of mesoporous silicates are thought to take on a tail-to-tail arrangement in a linear form (Figure 2.11b), or a tail-to-head coiled format whereby the hydrophobic tail undergoes random coiling (Figure 2.11a). The extent of overlap of the chains within the pores has never been important because both arrangements, in the majority of cases, ultimately (after calcination) lead to silicates with some degree of porosity. However, in MS-5_C, the nature of this configuration determines the porosity or lack thereof. To probe the nature of this configuration, we initiated an investigation into the possibility of olefin isomerization during hydrothermal synthesis. We suspected that the (*Z*)-olefin, if present, can give rise to a coiled tail-to-tail arrangement by virtue of its molecular geometry, which may lead to the configuration in Figure 2.11(a). Since isomerization from the (*E*)-olefin to the (*Z*)-olefin can not be determined directly by solid state ¹H or ¹³C NMR due to the broad nature of the peaks (residual dipolar coupling), we synthesized both (*E*)- and (*Z*)-isomers from the same starting materials and examined their individual and combined effects on organosilicate structure.



Scheme 2.4 Synthesis of **(9)** and **(11)**; (i) BuLi, THF, 1,3-dibromopropane, 0°C, 1 h ; (ii) Dimethylamine, THF, overnight; (iii) Na/NH₃ (liq), 20 mins; (vi) Lindlars catalyst, H₂, 1.5 h; (v) Bromopropyltrimethoxysilane, MeOH, reflux, 72 h

Compound **(6)** was obtained from lithium 1-undecynide and 1,3-dibromo propane. Nucleophilic attack on **(6)** by dimethylamine gave the dimethylaminotetradec-4-yne **(7)**. This alkyne can then undergo a metal-hydride reduction to give the (*E*)-olefin **(8)**, or a Lindlar reduction to give the (*Z*)-olefin **(9)**. Quaternization of the amine with bromopropyltrimethoxysilane gives **(10)** and **(11)** as the desired (*E*)- and (*Z*)-surfactants. The key step in this procedure is the ability to convert the dimethylaminotetradec-4-yne **(7)** to either isomer. This makes the synthesis more efficient than carrying out a Suzuki reaction (Scheme 2.2) twice under different conditions to give either isomer.

Mesoporous silicates were synthesized using the **(10)**, **(11)**, and several mixtures of the two. If the structure of the material derived from the (*E*)- and (*Z*)-olefin surfactants are different, then isomerization from the (*E*)- to the (*Z*)-olefin can be ruled out as the reason for

the bent chain configuration. Hydrothermal synthesis via the **(10)** using a sol-gel composition of 1 SiO₂: 0.4 **(10)**: 0.4 TMAOH: 80 H₂O led to the formation of MCM-41, as determined by the powder diffraction (Figure 2.12), in 61% yield. The yield is calculated as the mass of organic in the composite organosilicates (determined by TGA) per mass of organic added in reactants. Using the same sol-gel composition, surfactant **(11)** gave the cubic MCM-48 in 73% yield.

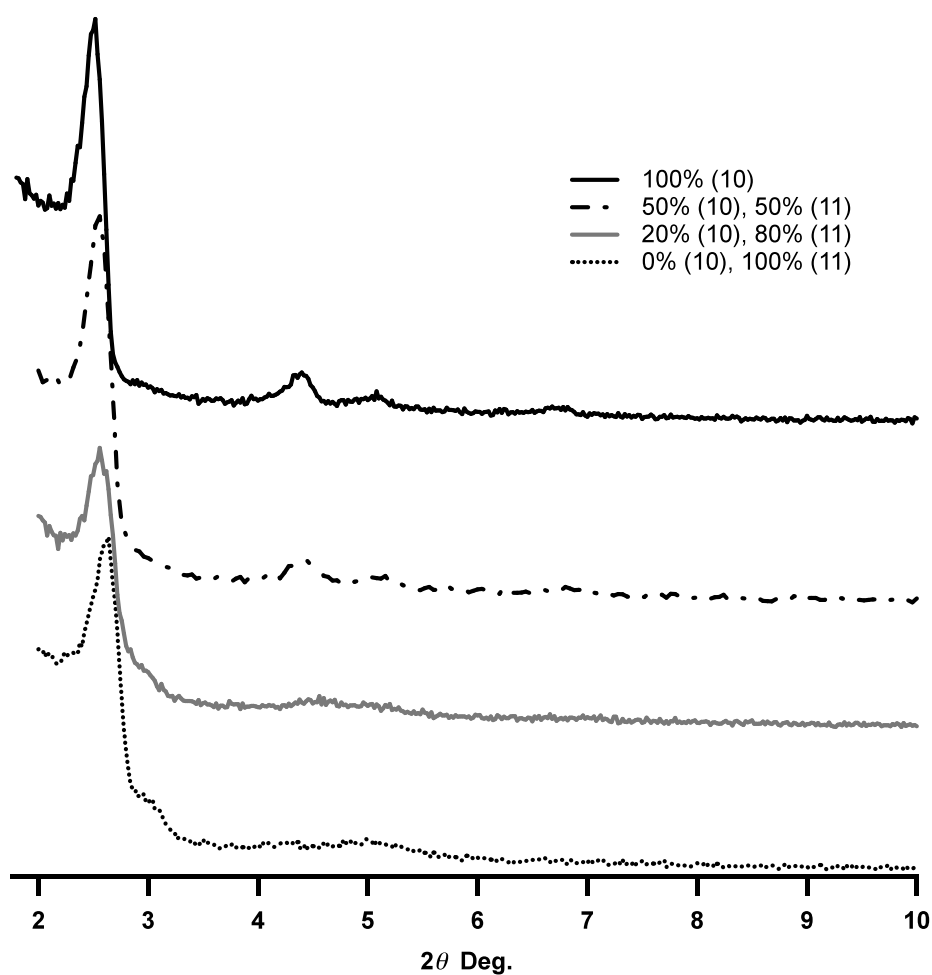


Figure 2.12 X-ray diffraction patterns of M41S materials made with different ratios of (*E*) to (*Z*)-olefin surfactants, **(10)** and **(11)**.

Although this rules out complete isomerization of one isomer to the other, it does not rule out a mixture of the two isomers. Since the yields are lower than expected, we investigated the possibility of isomeric preference in the sol gel mixture by mixing the two surfactants in a 50:50 ratio. The equimolar mixture of the (*E*)/(*Z*) surfactants produced MCM-41 in 87% yield. These results indicate that one isomer isn't favored over the other during hydrothermal synthesis, as this can only result in a maximum yield of 50%. As a test to see if (**10**) serves as a seed for MCM-41 formation in the presence of (**11**), we carried out the hydrothermal synthesis with a 20:80 ratio of (**10**) to (**11**) and obtained MCM-48 in 76% yield. This suggests that the (*E*)-olefin is predisposed to forming MCM-41 while the (*Z*)-olefin is predisposed to forming MCM-48. Given these results, isomerization to a single olefin can be ruled out. As a result, we conclude that the organic chains at the end of the surfactants fold on themselves in a head-to-tail arrangement regardless of the isomeric state of the olefin and that isomerization is not involved in surfactant packing. However, the geometry of the surfactant does play a large role in the final structure of the synthesized silicate.

2.3.2 Preparation of M41S silicates via siloxy modified C₁₇-olefin surfactants

2.3.2.1 Synthesis of C₂-(*E*)-olefin surfactant and M41S preparation

In this section, we considered increasing the length of the organic chain beneath the cleavable olefin group in order to allow for the creation of a greater volume occupied by the coiled surfactant. This concept is illustrated in Figure 2.13 below.

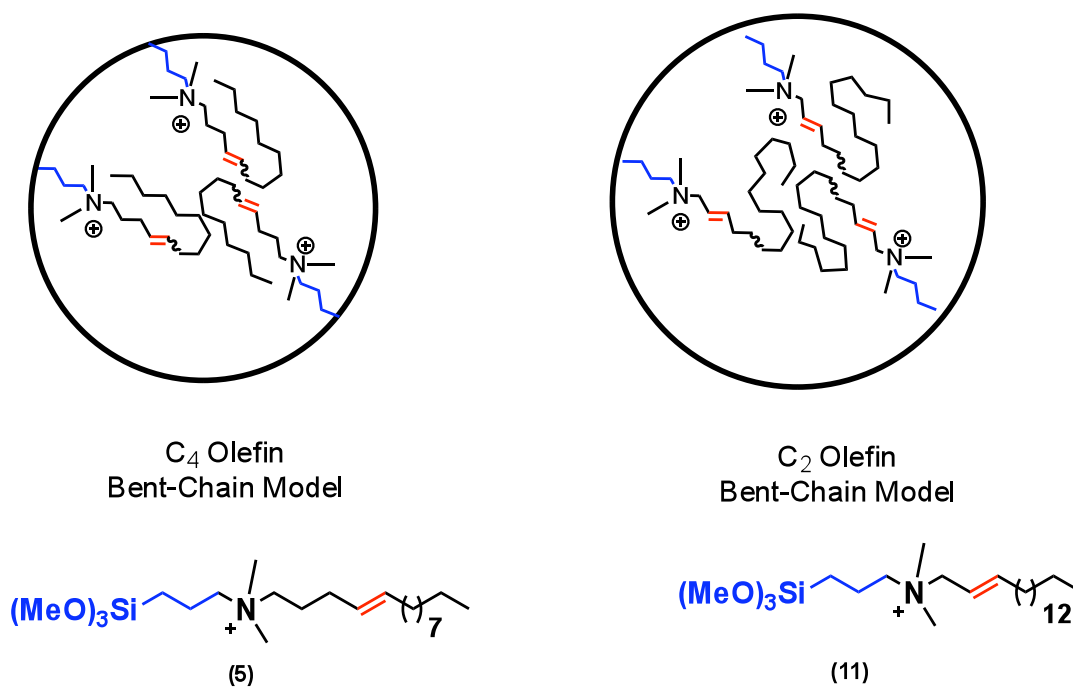
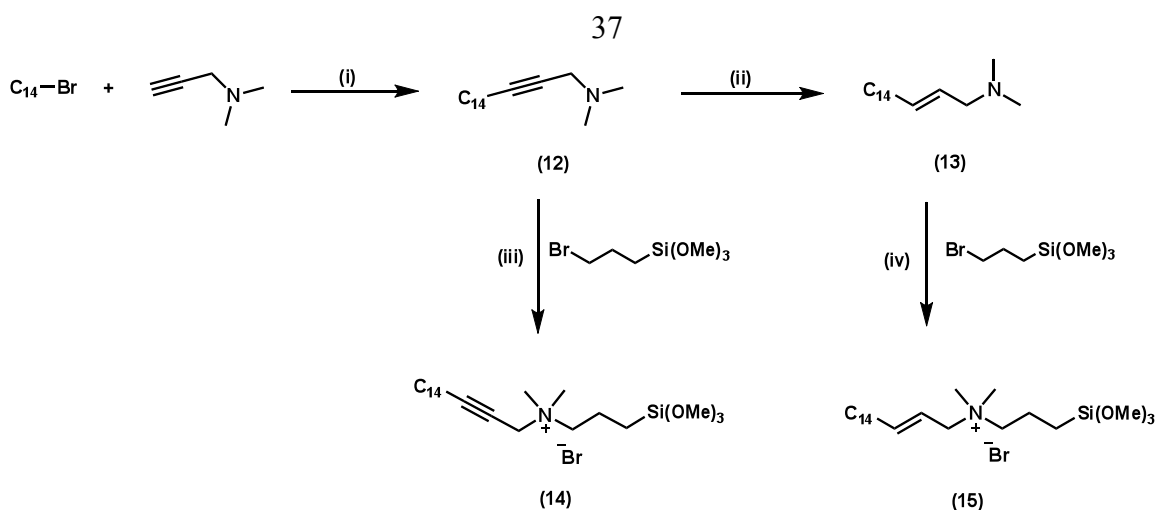


Figure 2.13 Proposed bent chain configuration of (5) and (11) within the pores of their respective silicates

The length of the organic chain beneath the cleavable olefin group was increased by moving the olefin group two carbons closer to the quaternary ammonium head group and increasing the surfactant tail length to C₁₄ from C₉ (previous surfactant). The new surfactant is thus six methylene groups longer in the tail end than (5), although only three methylene groups longer in overall length.



Scheme 2.5 Synthesis of **(14)** and **(15)**; (i) BuLi, THF, HMPA, $-78^\circ\text{C} \rightarrow 60^\circ\text{C}$; (ii) Na/NH₃ (liq), THF, -42°C , 2 h; (iii) and (iv) Methanol, reflux, 3 d

Compound **(12)** was prepared from bromotetradecane and lithium dimethylaminopropynide. The (*E*)-olefin was generated by a metal hydride reduction via Na/NH₃ (liq) to give **(13)**. Surfactants **(14)** and **(15)** were generated from the reaction of their respective amines with bromopropyltrimethoxysilane in methanol under reflux to give the desired quaternized products in 60% yield. Compound **(15)** was subjected to alkaline hydrothermal conditions with a sol-gel composition of 1 SiO₂: 0.4 **(15)**: 0.4 TMAOH: 100 H₂O. After mixing for 1 h, the sol-gel composite was aged for different time periods. The samples were washed, thoroughly dried and analyzed by powder X-ray diffraction (XRD).

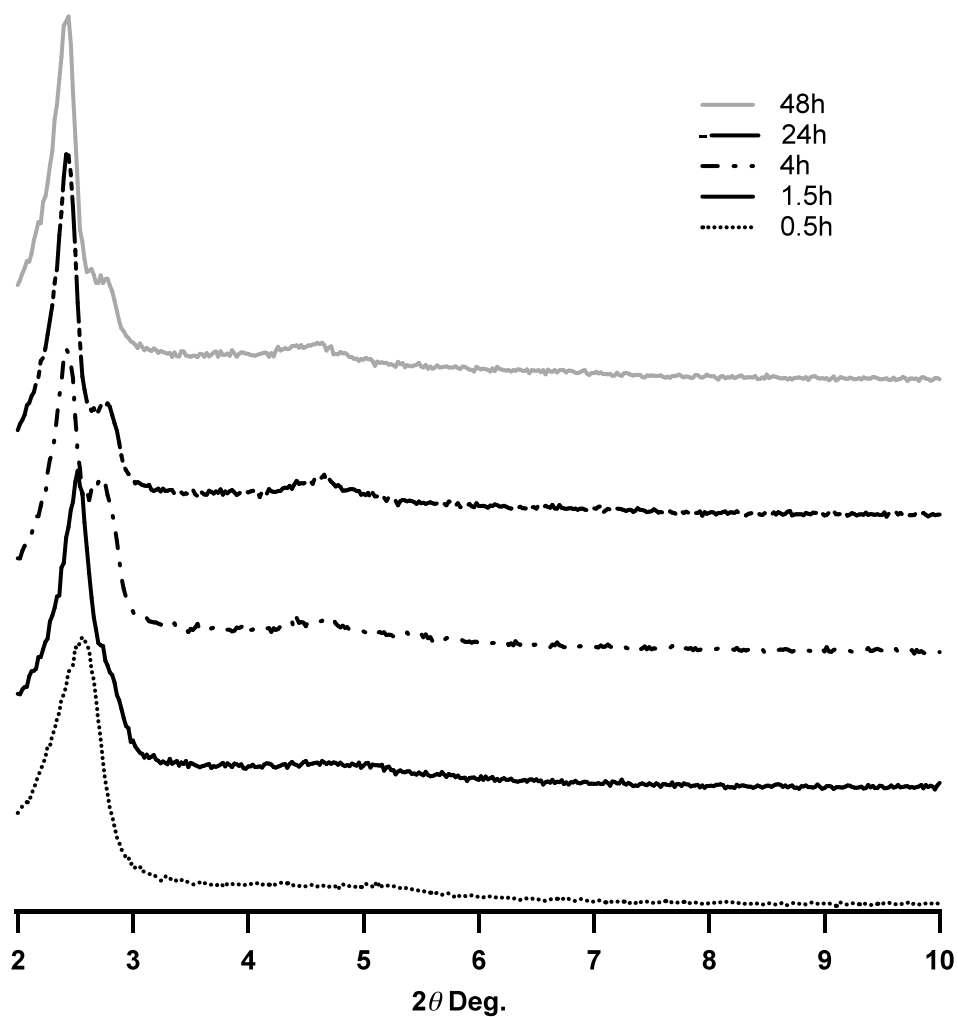


Figure 2.14 As-synthesized MCM-48, MS-15_{AS} formation with (15) as a function of ageing time. Sol gel composition: 1 SiO₂: 0.4 (15): 0.4 TMAOH: 100 H₂O

After 30 minutes, a lamellar phase appeared indicative of MCM-50 formation. However, after 1.5 hours, a gradual formation of a cubic phase indicative of MCM-48 begins. After ageing for 4 hours, a well-defined MCM-48 structure is obtained. Further heating to 48 hours has little effect on the structure formed. This gradual change from a lamellar phase to a cubic phase is reminiscent of the proposed formation pathway to M41S silicates described by Stucky et al.³ via silicate bilayers.

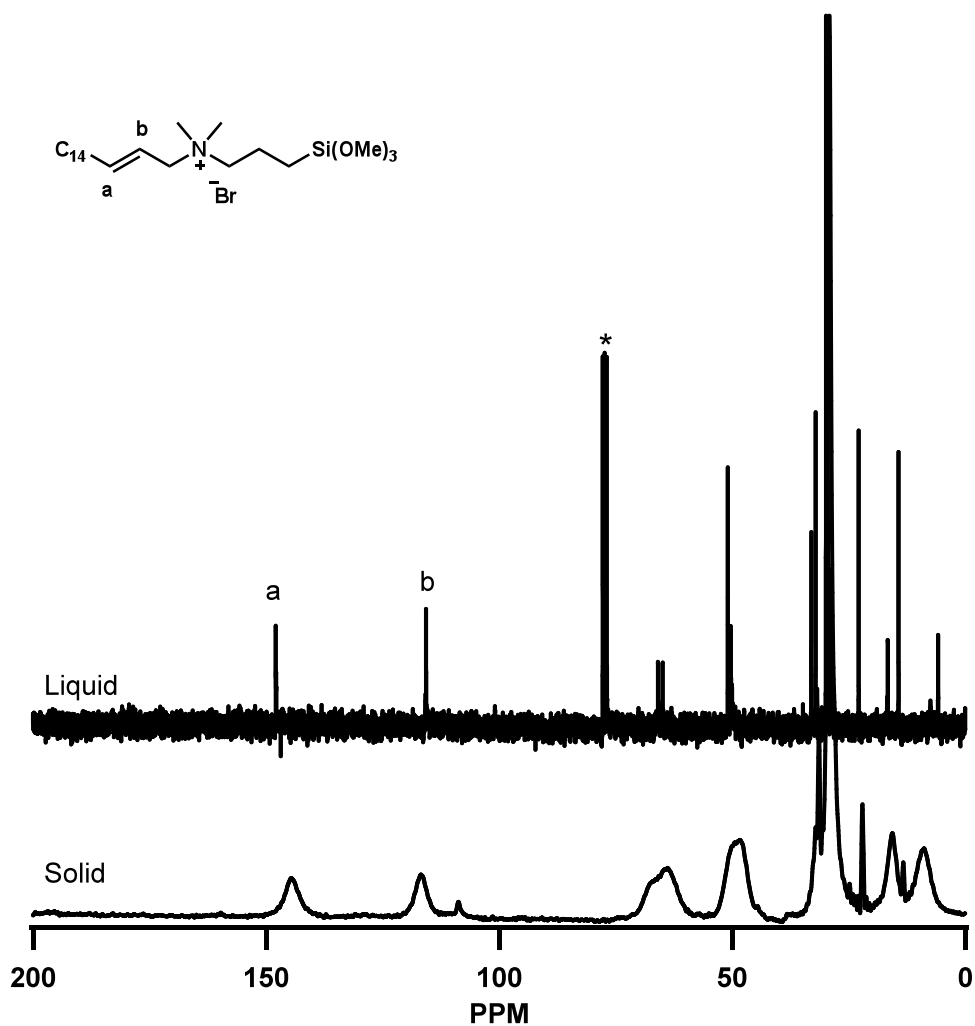


Figure 2.15 ^{13}C NMR of (15) and ^{13}C CP MAS NMR of MS-15_{AS}. * Chloroform

Structural details of the encapsulated surfactant (15) in the as-synthesized materials were examined by solid-state ^{13}C and ^{29}Si CP MAS NMR. The solid-state ^{13}C CP MAS NMR of the as-synthesized material matches up well with the liquid-state ^{13}C NMR of (15) (Figure 2.15) verifying the stability of this surfactant to the alkaline hydrothermal conditions.

2.3.2.2 Effect of surfactant structure on M41S phase

Based on the dramatic effect of isomer type, i.e., (*E*) vs. (*Z*) in Figure 2.12, on the phase of the mesostructured silicate, we were curious to see the effect of an alkyne-based surfactant (**14**) on the phase of the mesostructured silicate. Thus, compound (**14**) was subjected to alkaline hydrothermal conditions with the same sol-gel composition as that used with (**15**), i.e., 1 SiO₂: 0.4 (**14**): 0.4 TMAOH: 100 H₂O. After mixing for 1 h, the sol-gel composite was aged for 24 and 48 hours and the resulting solids were washed, dried, and analyzed by powder X-ray diffraction.

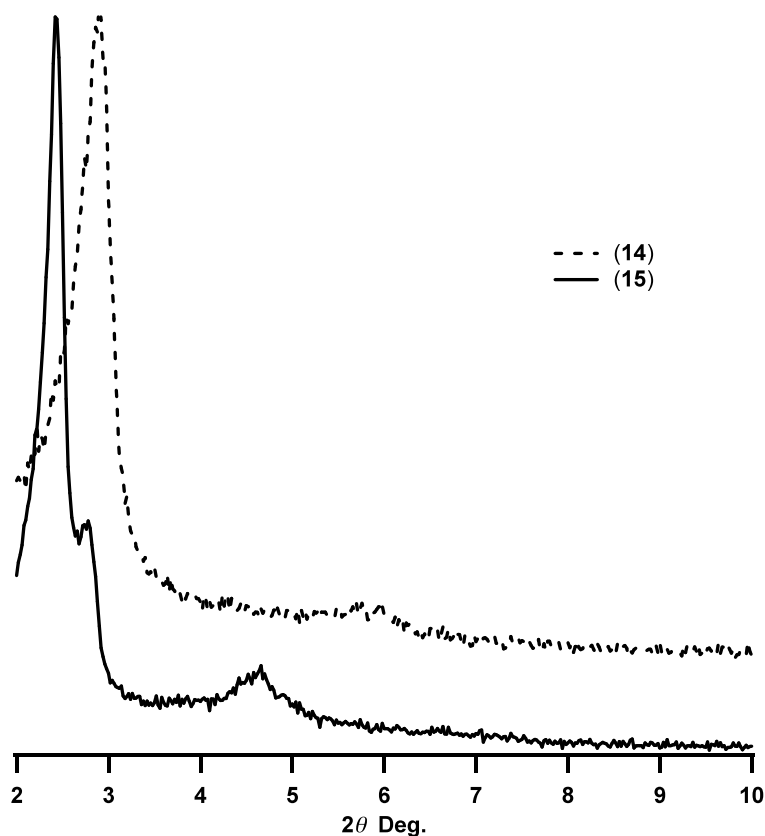


Figure 2.16 X-ray diffraction patterns of MS-**14**_{AS} and MS-**15**_{AS}. Sol gel composition: 1 SiO₂: 0.4 (**14** or **15**): 0.4 TMAOH: 100 H₂O

As shown by the X-ray diffraction analysis in Figure 2.16, the nature of the organic group within the surfactant tail plays a large role in the type of M41S phase formed. The alkyne surfactant (**14**) gave MCM-50, unlike the olefin surfactant (**15**), which formed MCM-48. The formation of the lamellar phase by (**14**) may be due to acetylene-hydrogen (π -H) interactions,²¹ which may serve as a driving force for preferential parallel stacking of the surfactants. This finding along with the data from the (*E*)/(*Z*) isomers in Figure 2.12 suggests that in addition to multidentate binding of silicate oligomers and the charge density matching between surfactant and silicate, surfactant structure and orientation in solution plays a large role in the type of M41S silicates formed.

2.3.2.3 Attempts at C₂-(*E*)-olefin cleavage in MCM-48

Ozonolysis of the composite MCM-48 materials produced from (**15**), i.e., MS-**15**_{AS} was carried out by bubbling ozone through a solution of the hybrid material at different temperatures for different lengths of time.

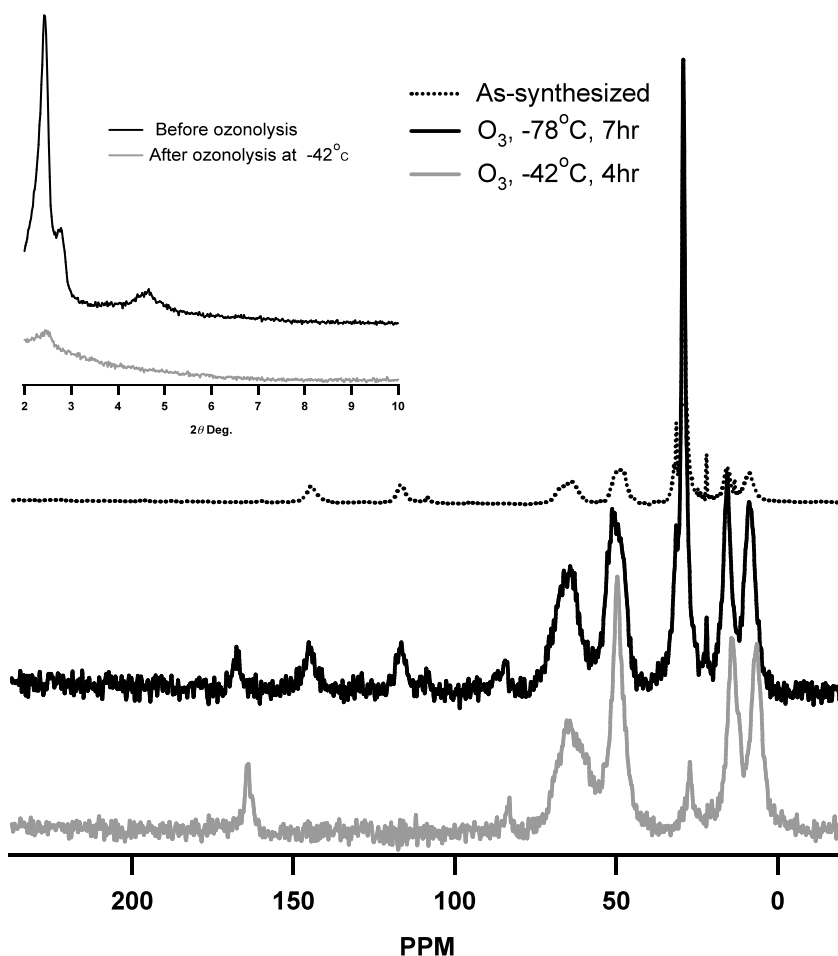


Figure 2.17 ^{13}C CP MAS NMR spectra of MS-15_{AS} before and after (MS-15_C) ozonolysis. Inset shows XRD spectra before and after ozonolysis

Ozonolysis conditions which led to the cleavage of (5) in MCM-41 (i.e., O_3 , -78°C , 7 hours) gave only partial cleavage of (15) in MCM-48. Increasing the time of ozone treatment did not make any appreciable difference in the extent of cleavage (not shown). However, when the temperature was raised to -42°C , complete cleavage was observed and the surfactant could be extracted following an ethanol/HCl wash. Unfortunately, this harsh oxidative treatment gives rise to a large loss of mesostructural order in the composite (Figure 2.17 Inset). To determine if the nonordered material was porous, we carried out a nitrogen

adsorption/desorption experiment. Similar to the materials made with (5), the extracted silicate made with (15) was also nonporous (Figure 2.18). The lack of porosity in this material along with the loss of order indicates a structural collapse upon oxidative treatment, which can be associated with the harsher oxidative conditions employed.

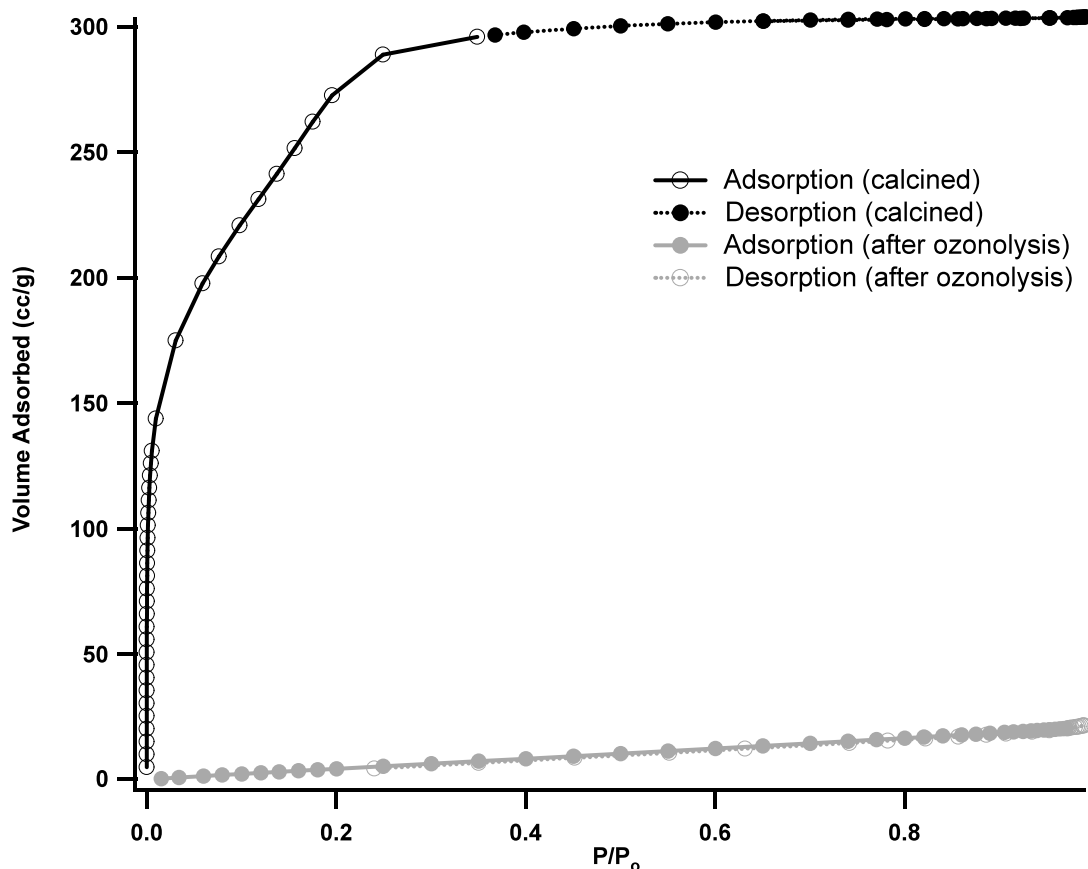


Figure 2.18 Nitrogen adsorption and desorption isotherms of MS-15_C before and after calcination

In addition to MS-15_C being nonporous, the lack of adsorption even at high relative pressures where adsorbent-adsorbent interactions are strong indicates inaccessibility of the high-energy adsorptive silanol sites on the silica surface to nitrogen adsorbate. This could be due to the very large surface coverage and size of the bonded organic groups. When the MS-15_C sample is calcined, these sites are revealed and a type IV isotherm is obtained (Figure

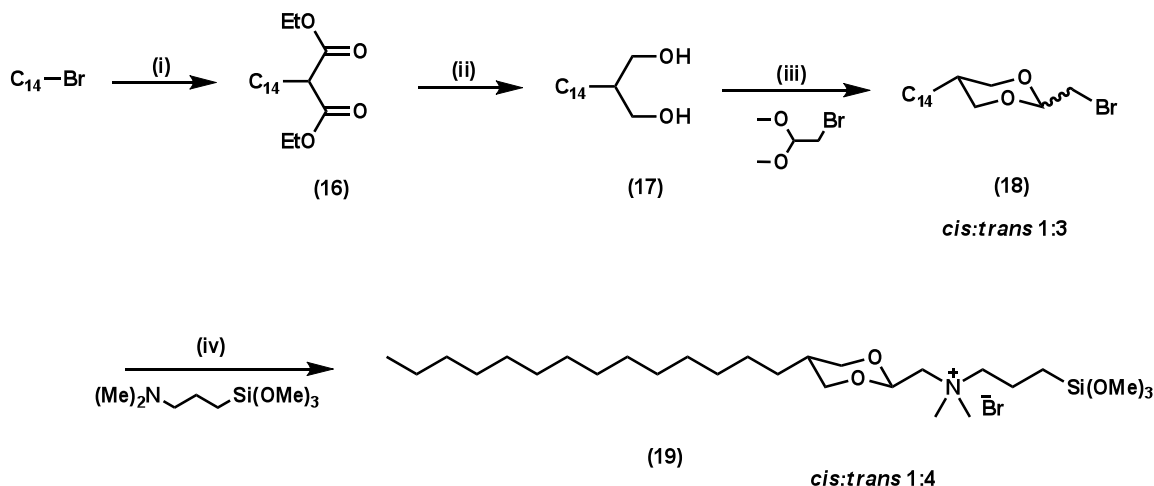
2.18). The adsorption at low relative pressures, P/P_o , is from the monolayer adsorption of nitrogen on the walls of the mesopores. The step in the adsorption isotherm reflects filling of mesopores, with smaller pores being filled at lower P/P_o .

The difficulty in olefin cleavage could be due to the proximity of the olefin group to the electron withdrawing quaternary ammonium center. This electron withdrawing group is β to the olefin and thus can reduce its π -electron cloud thus making the olefin less susceptible to the 1,3-dipolar cycloaddition with ozone. The harsher ozone conditions (i.e., higher temperatures) could lead to silica oxidation, which in turn can lead to structural collapse.

In order to get around this problem, other oxidizing reagents such as OsO_4 /oxone and KMnO_4 were used with limited success. The OsO_4 /oxone system did give complete olefin cleavage without structural collapse, however the surfactant could not be extracted possibly due to the formation of the dihydroxylation side product. Several attempts to retard dihydroxylation via the use of weak bases proved unsuccessful. Oxidative cleavage via KMnO_4 was halted as the permanganate could not be completely removed from the silicate. These unsuccessful attempts prompted us to take a look into the use of other cleavable surfactants that did not involve the use of strong oxidizing agents.

2.3.3 Preparation of M41S silicates via siloxy-modified acetal and ketal surfactants

2.3.3.1 Synthesis of acid labile surfactant



Scheme 2.6 Synthesis of **(19)**; (i) NaOEt, diethylmalonate, THF, reflux, 4 h; (ii) LAH, THF, r.t., 1.5 h; (iii) pTSA (polymer bound), 85°C, 24 h; (iv) CH₃CN, reflux, 72 h

As an alternate to ozone, we selected an acid cleavable cyclic acetal as the new cleavage site in our modified surfactant. Acetal bonds can be cleaved under acidic conditions to give aldehyde groups, which can undergo further chemical modifications. The precursor to the surfactant was synthesized as shown in Scheme 2.6. This precursor can be quaternized with dimethylaminopropyltrimethoxysilane to give the desired surfactant. To test the feasibility of the acid cleavage reaction, we subjected **(18)** to a series of Bronsted and Lewis acidic cleavage conditions (Figure 2.19).

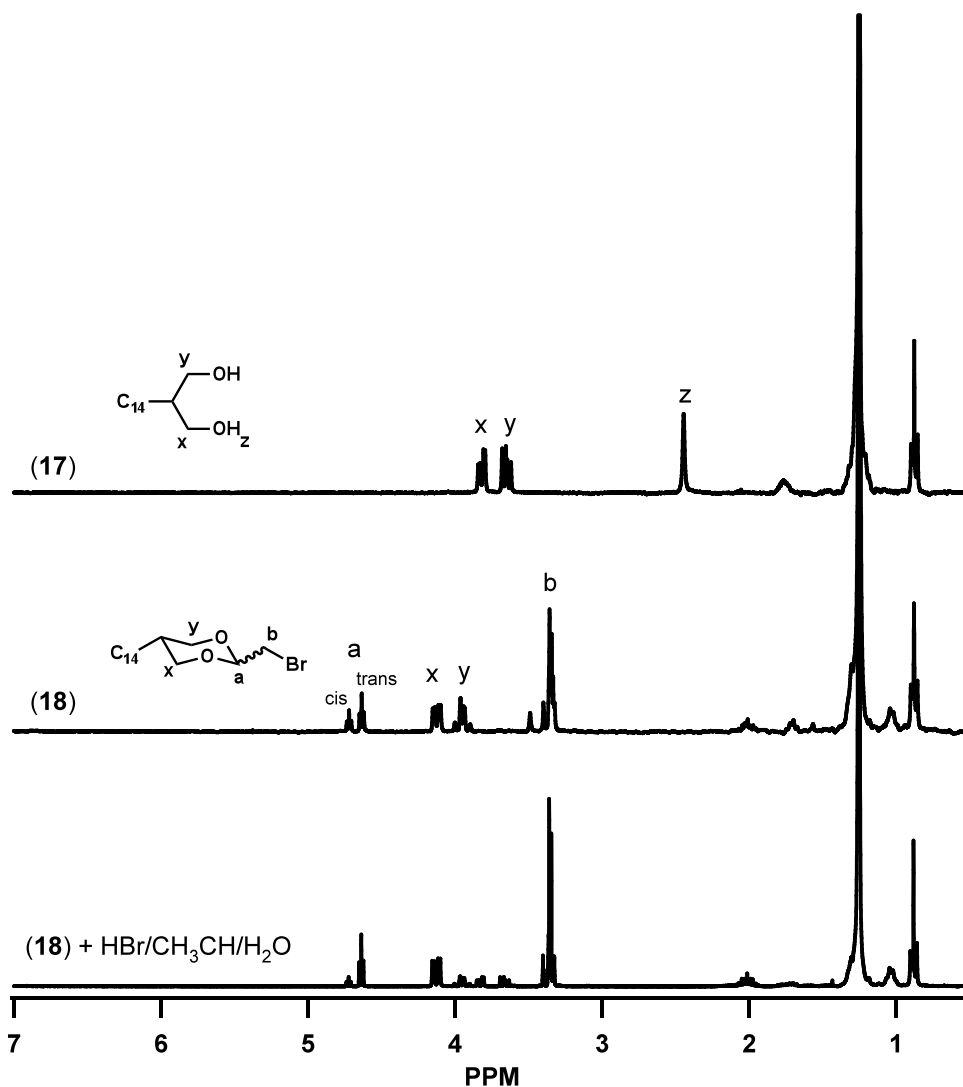
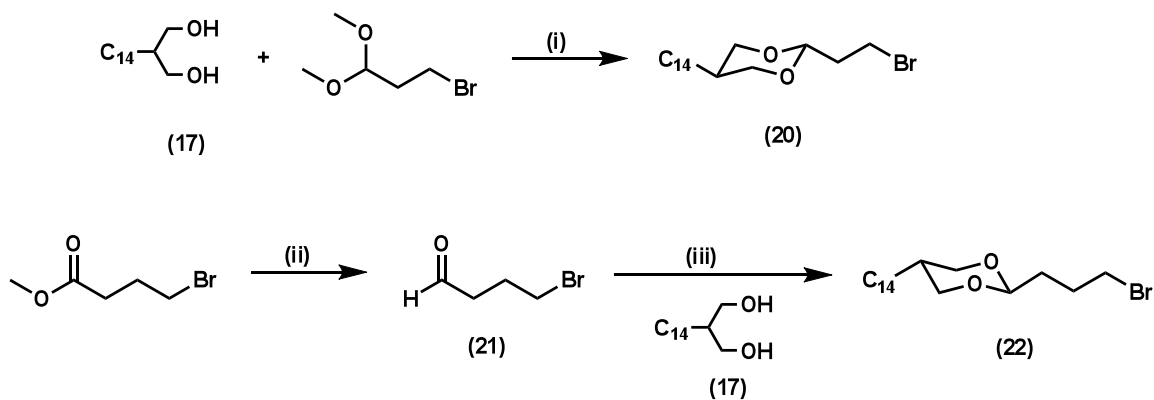


Figure 2.19 ^1H NMR of (18) (and (17) for comparison) and the reaction of (18) with HBr, CH₃CN, and H₂O at 50°C. The following cleavage conditions failed: (a) Er(OTf)₃, CH₃CN, (b) Yt(OTf)₃, THF, (c) BF₃·Et₂O, THF, (d) HCl/THF 80°C, (e) TsOH, acetone, H₂O, r.t. (f) TsOH, acetone, H₂O, 70°C, (g) PPTS, acetone, H₂O, 70°C

The success of cleavage was judged via ^1H NMR by the presence of the protons α to the alcohols at 3.65 and 3.81 ppm in compound (17). To our surprise, all Lewis and Bronsted acid attempts failed completely with the exception of HBr/CH₃CN/H₂O at 50°C, which gave partial cleavage as seen in Figure 2.19. We suspected steric stress due to the proximity of the large bromide group to the cleavage site (i.e., anomeric carbon) as a possible reason for poor

hydrolysis. To investigate this possibility, we incorporated one and two extra methylene units between the bromide and the anomeric carbon (Scheme 2.7).



Scheme 2.7 Synthesis of **(22)**; (i) pTSA, 85°C, 24 h; (ii) DIBAL, CH₂Cl₂, -78°C-r.t.; (iii) pTSA, 85°C, 24 h

The two new surfactant precursors **(20)** and **(22)** were synthesized as shown in Scheme 2.7 and subjected to the acid cleavage with HBr/CH₃CN/H₂O. Increasing the distance between the anomeric carbon and the bromide gave the same degree of cleavage as that of **(18)** in Figure 2.19. Since this acetal appeared to be quite stable and resistant to hydrolysis, we looked to other cyclic acetals and ketals.

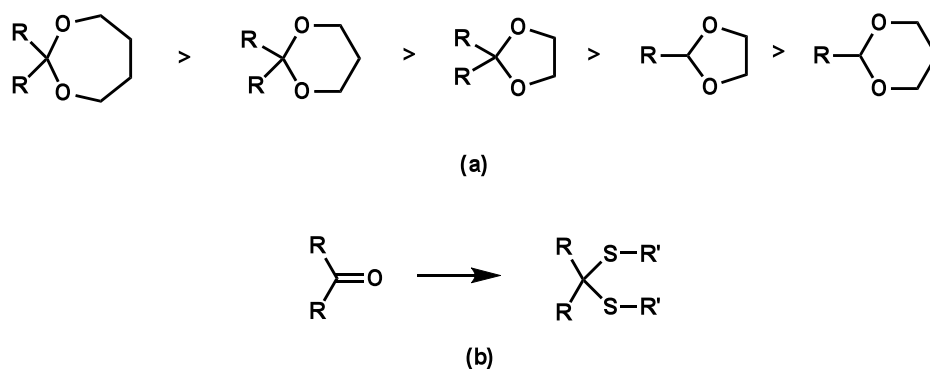


Figure 2.20 (a) Ease of hydrolysis of cyclic ketals (*Adapted from Green's protective groups in organic synthesis.*) (b) Dithioacetal formation from a ketone

After probing the literature, we found that for acid-catalyzed hydrolysis, the generalizations in Figure 2.20 applied. According to Figure 2.20, six-membered ring cyclic acetals (i.e., 1,3-dioxanes) were ranked the hardest to cleave. However, cyclic ketals appear more acid labile and can also be easily prepared (albeit with lower yields) by condensing (17) with the desired ketone. For future use, the ketone functional group can be transformed into a dithioketal with the desired functionality (Figure 2.20b). Dithioketals are known to be robust and stable even to Bronsted acidic conditions.

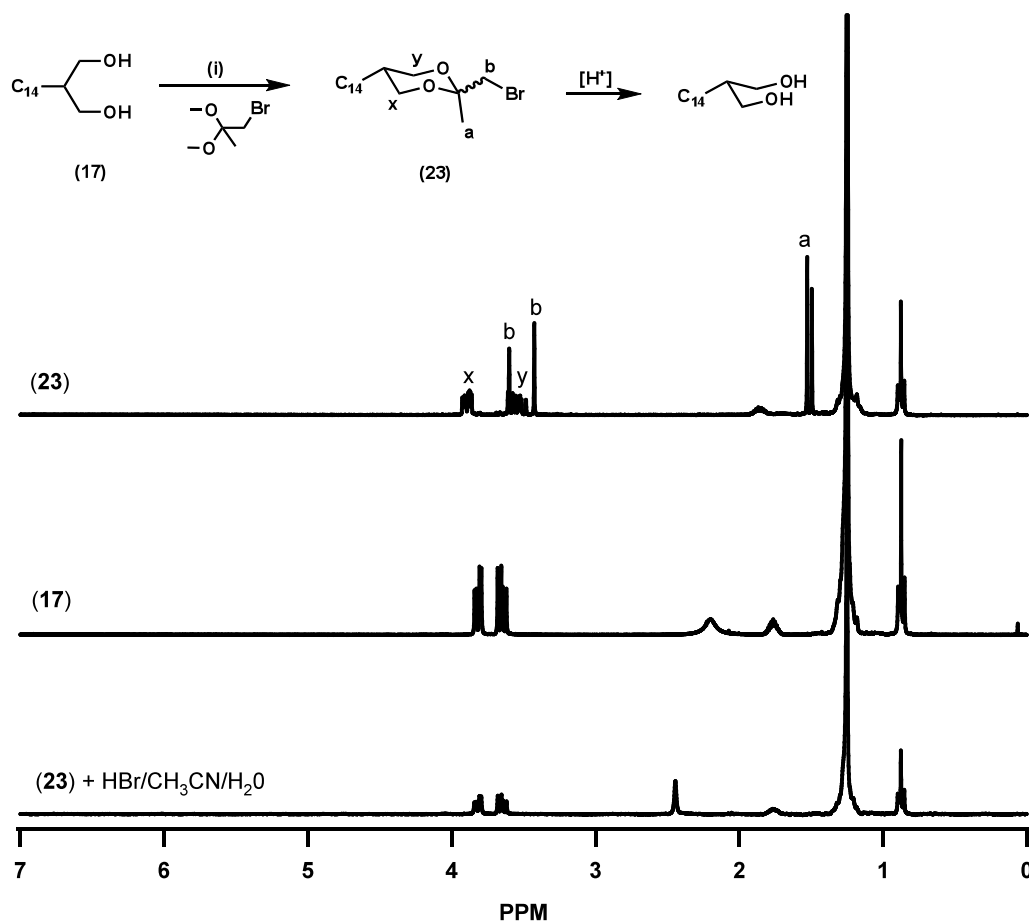
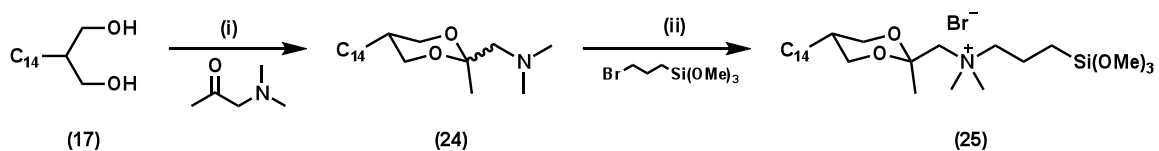


Figure 2.21 ^1H NMR spectra of ketal surfactant before and after cleavage with HBr/CH₃CN/H₂O. Inset shows reaction scheme for the preparation of ketal surfactant (i) pTSA, CHCl₃, 30°C, 4 h

The synthesized ketal (**23**) was subjected to acid hydrolysis via HBr/CH₃CN/H₂O. The ¹H NMR spectrum of the cleavage product confirms complete hydrolysis of the acetal bond after 5 hrs (Figure 2.21). With this in hand, we proceeded to complete the synthesis of the desired ketal surfactant.



Scheme 2.8 Synthesis of ketal surfactant (**25**) via dimethylaminoacetone; (i) pTSA, cyclohexane, reflux, 16 h; (ii) CH₃CN, reflux, 48 h

The desired surfactant could not be obtained from the quaternization of (**23**) with dimethylaminopropyltrimethoxysilane due to steric hindrance from the neopentyl type group β to the bromide. This problem was circumvented by synthesizing the dimethylamino ketal precursor (**24**) and quaternizing it with bromopropyltrimethoxy silane (Scheme 2.8).

2.3.3.2 Preparation of M41S silicates via modified acetal surfactant and acetal cleavage

The cyclic ketal surfactant (**25**) was subjected to alkaline hydrothermal synthesis with an optimized sol-gel composition of 1 SiO₂: 0.5 (**25**): 0.5 TMAOH: 100 H₂O. After ageing at 100°C for 4 hours, the resulting white precipitate, MS-**25**_{AS} was washed extensively via soxhlet extraction and dried overnight. The powder XRD pattern as shown in inset of Figure 2.22 corresponds to the structure of MCM-48.

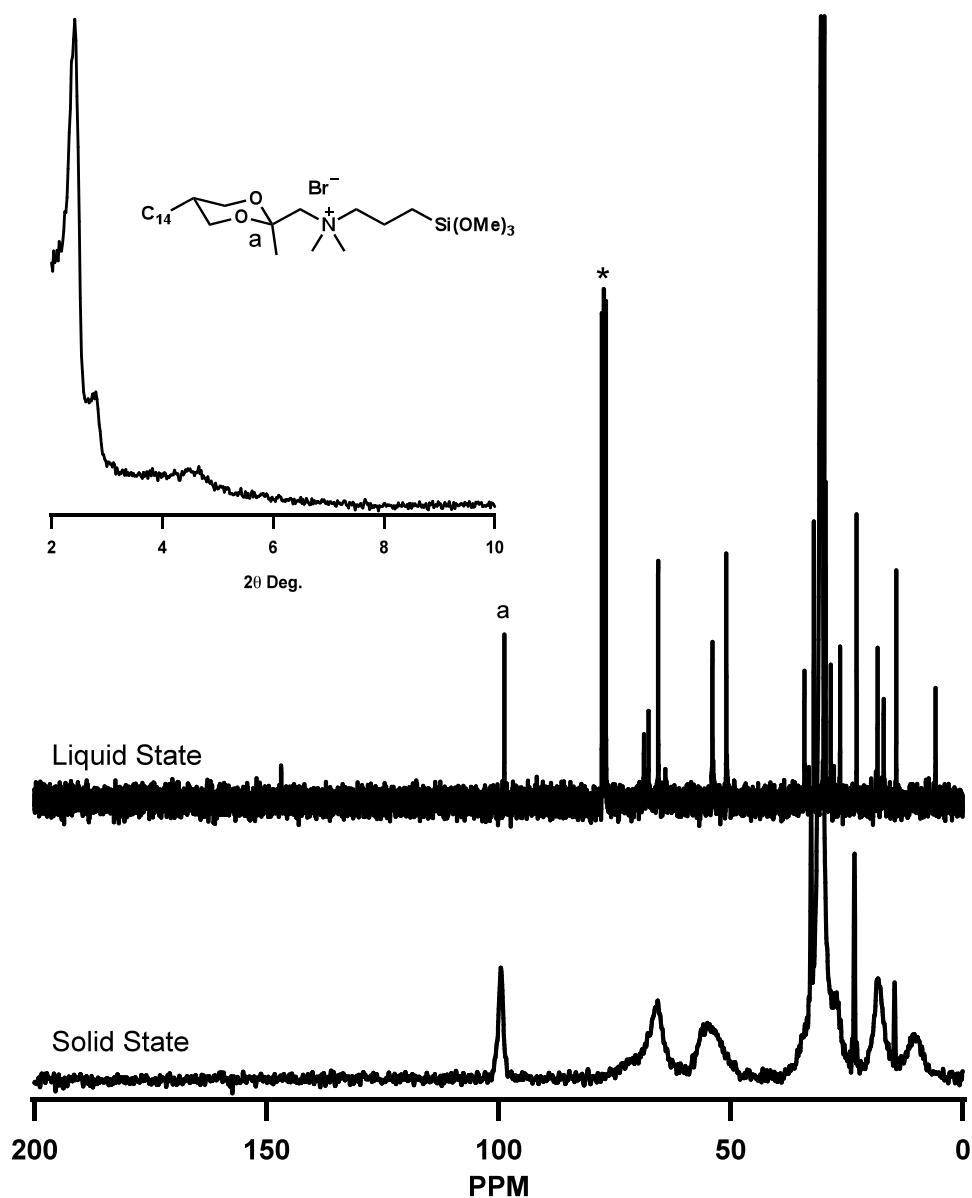


Figure 2.22 ^{13}C CP MAS NMR of MS-25_{AS} and liquid state (**25**). Inset shows X-ray diffraction pattern of MS-25_{AS}. * Chloroform

The structural details of the encapsulated surfactant (**25**) in the as-synthesized materials were examined by solid-state ^{13}C CP MAS NMR and seemed to match up well with the liquid-state ^{13}C NMR of the surfactant (**25**) (Figure 2.22) verifying the stability of this surfactant to the alkaline hydrothermal conditions.

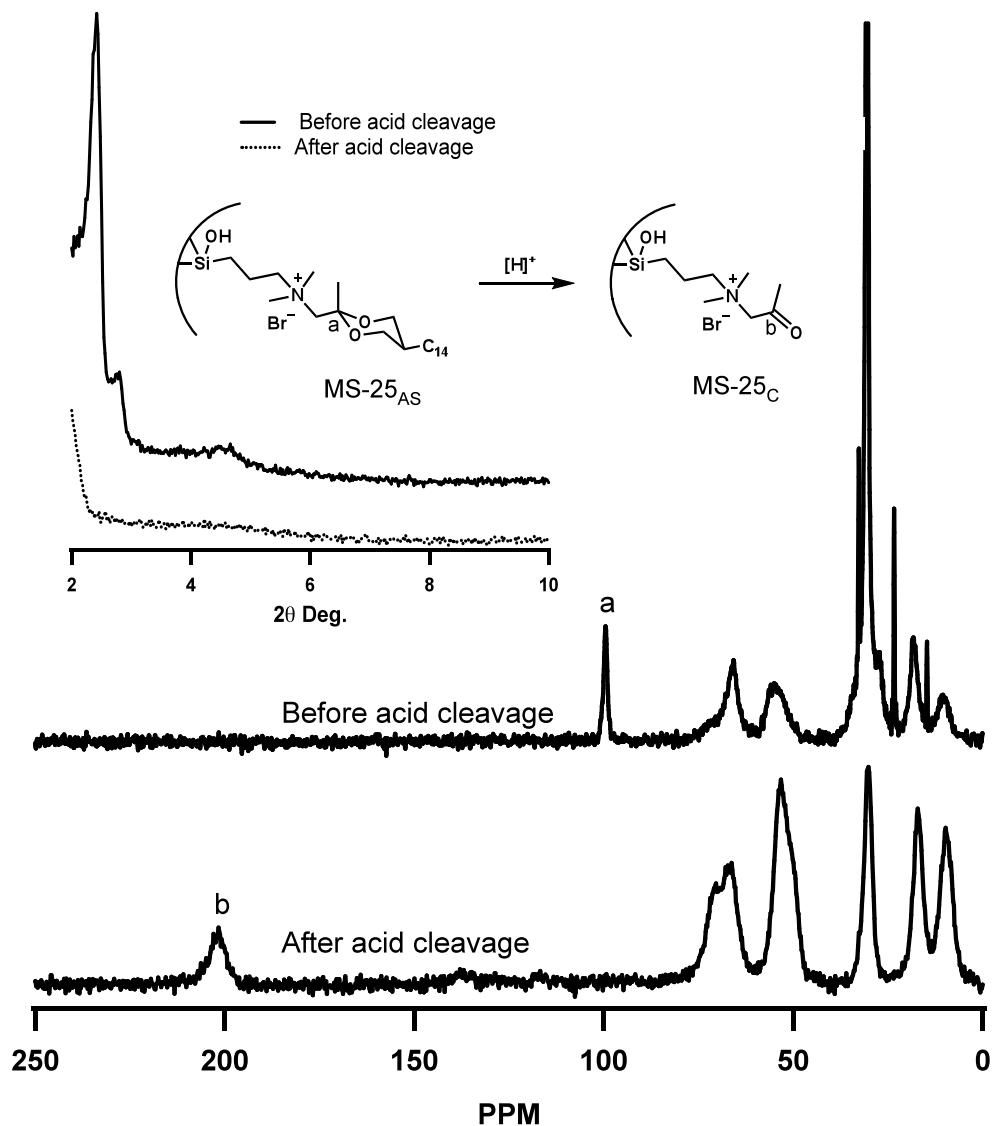


Figure 2.23 ¹³C CP MAS NMR of MS-25_{AS} before and after cleavage with HBr/CH₃CN/H₂O. Inset shows X-ray diffraction pattern of MS-25_{AS} before and after cleavage

The acetal surfactant (**25**) was cleaved from the pores of MS-25_{AS} using the established liquid state protocol (HBr/CH₃CN/H₂O). Treatment of the solid with this mixture for 4 hours at 50°C led to complete cleavage and extraction of the C₁₄-diol tail (**17**) from the pores of MS-25_{AS} (Figure 2.23). The 100 ppm peak corresponding to the anomeric carbon on the surfactant completely disappears and the carbonyl carbon of the ketone appears around

202 ppm (Figure 2.23). Also, the 30 ppm peak is greatly reduced indicating successful extraction of the C₁₄-diol chain from the pores of the silicate. However, after cleavage, the MCM-48 cubic symmetry of MS-25_{AS} as judged by the powder XRD pattern (Figure 2.23 inset) was completely lost. Needless to say, this material lacked any porosity when probed by nitrogen adsorption.

2.3.3.3 Strengthening the silicate pore walls

The reason for the loss in order and lack of porosity was traced back to the ²⁹Si spectra (Figure 2.24).

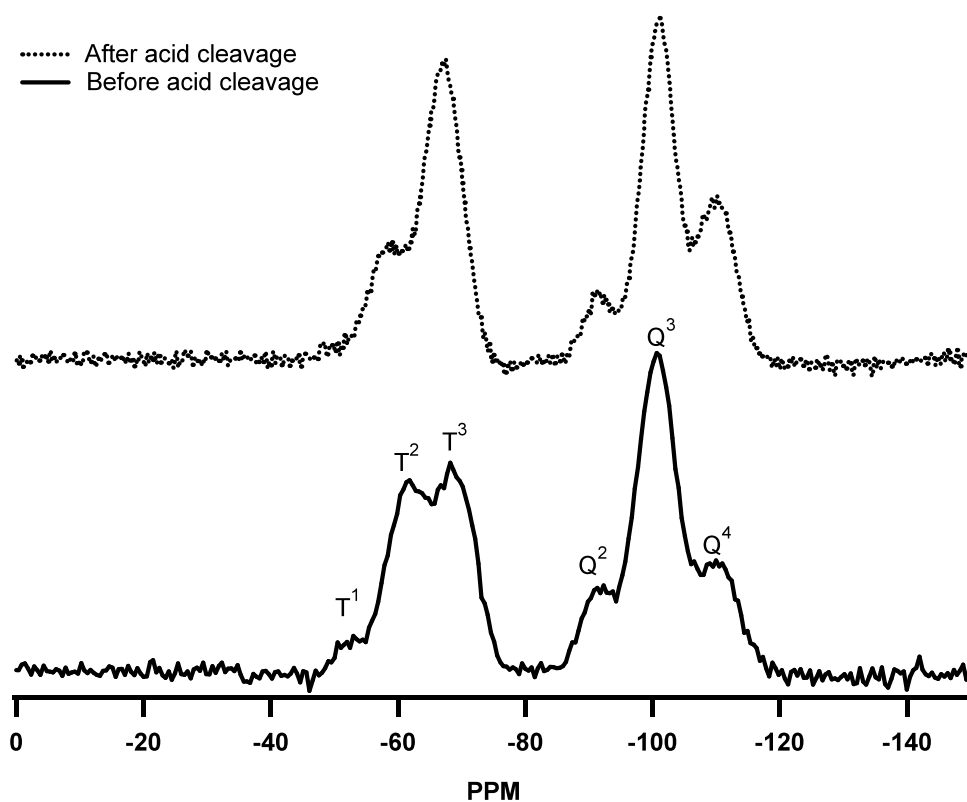


Figure 2.24 ²⁹Si CP MAS NMR of MS-25_{AS} and MS-25_C, i.e., before and after acid cleavage

The ^{29}Si CP MAS NMR in Figure 2.24 shows a dramatic decrease in the ratio of T^2 to T^3 peaks upon acid cleavage. This implies that silanol groups associated with the surfactants are undergoing further condensation after the introduction of the acid. This is not unexpected since acid-catalyzed condensation of silanols is well known and has been seen in acid treated MCM-41 samples.¹⁰ However, the complete loss of order, sample collapse, and decrease in the T^2 to T^3 ratio indicates that the surfactants were not fully condensed into the walls of the MS-25_{AS}. Thus, the structural collapse witnessed in the XRD pattern in the inset of Figure 2.23 may be due to the reorganization of the surfactants during acid cleavage as a result of incomplete condensation and silanol defect sites. To address this issue, we launched an investigation into the synthetic conditions that give rise to a stronger pore wall structure by tracking the T^2 -to- T^3 ratio in the ^{29}Si CP MAS NMR. A lower T^2 -to- T^3 ratio will indicate improved surfactant condensation and incorporation into the silicate walls.

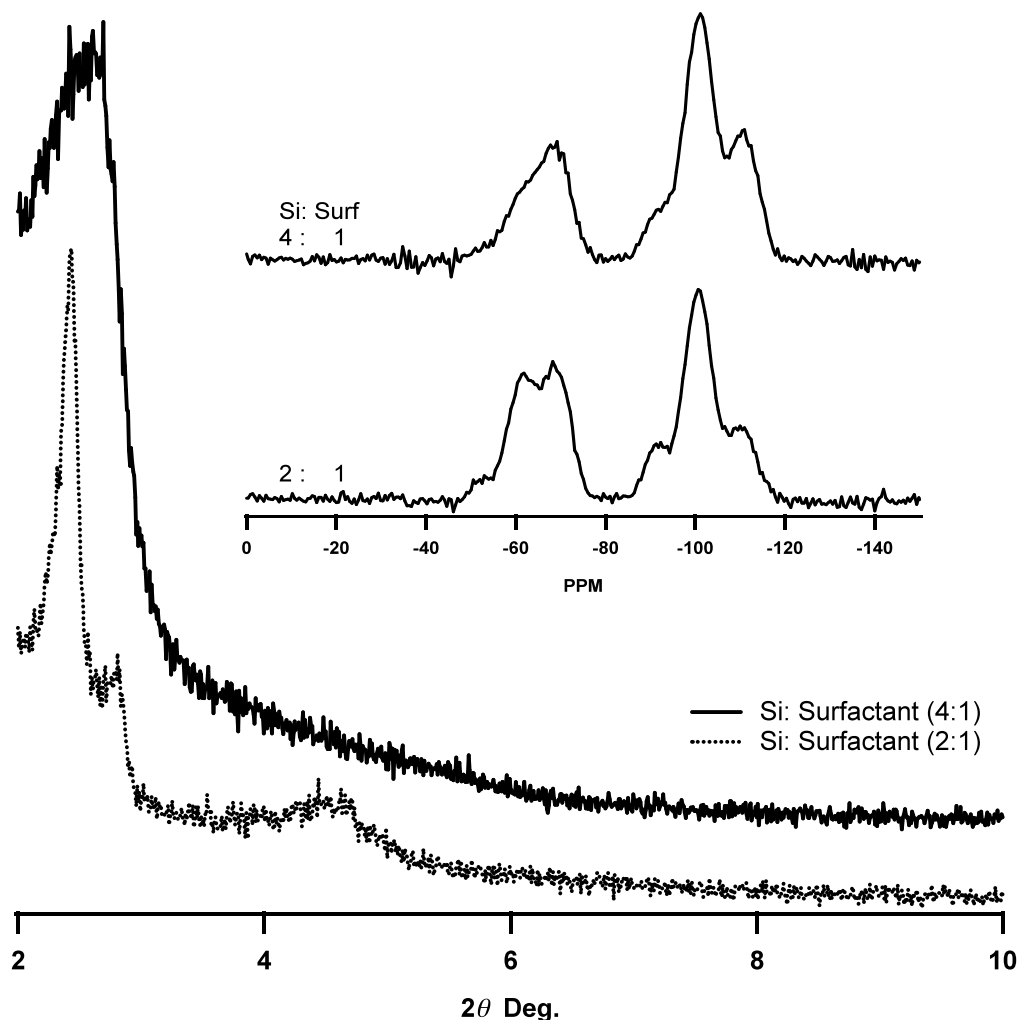


Figure 2.25 Powder X-ray diffraction pattern of varying Silica (TEOS)-to-surfactant (25) ratio. Sol gel composition of 4:1:1:400 vs. 2:1:1:200. Inset shows effect on via ^{29}Si CP MAS NMR

Several factors were examined but those that made a noticeable difference in the ^{29}Si CP MAS NMR were the silica-to-surfactant ratio and the amount of base. Increasing the silica-to-surfactant ratio from a 2:1 to a 4:1, while keeping the silica-to-water ratio as well as the surfactant-to-water ratio constant, resulted in a decrease in the T^2 -to- T^3 ratio (Figure 2.25). In addition, the ratio of Q^2 to Q^4 peaks decreased, indicating greater silicate condensation. Increasing silica-to-surfactant ratio further beyond this point did not give an

appreciable decrease (not shown). The single large broad peak in the powder X-ray diffraction indicates a distortion of the long-range ordering of the mesoporous structure and/or badly constructed cubic arrays. In addition to varying the silica-to-surfactant ratio, we also tried increasing the amount of water and ageing time, but neither provided any further decrease in the T^2 -to- T^3 ratio. However, varying the amount of base gave some interesting results.

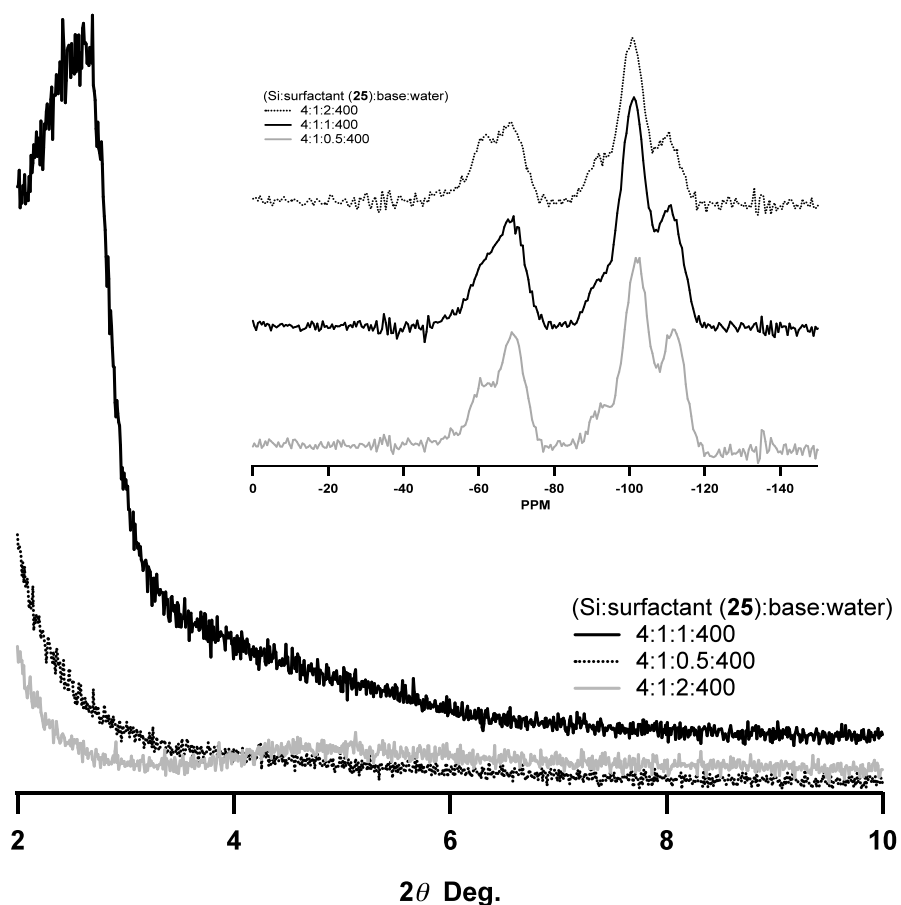


Figure 2.26 Powder X-ray diffraction pattern of varying base (TMAOH) content. Inset shows effect on via ^{29}Si CP MAS NMR

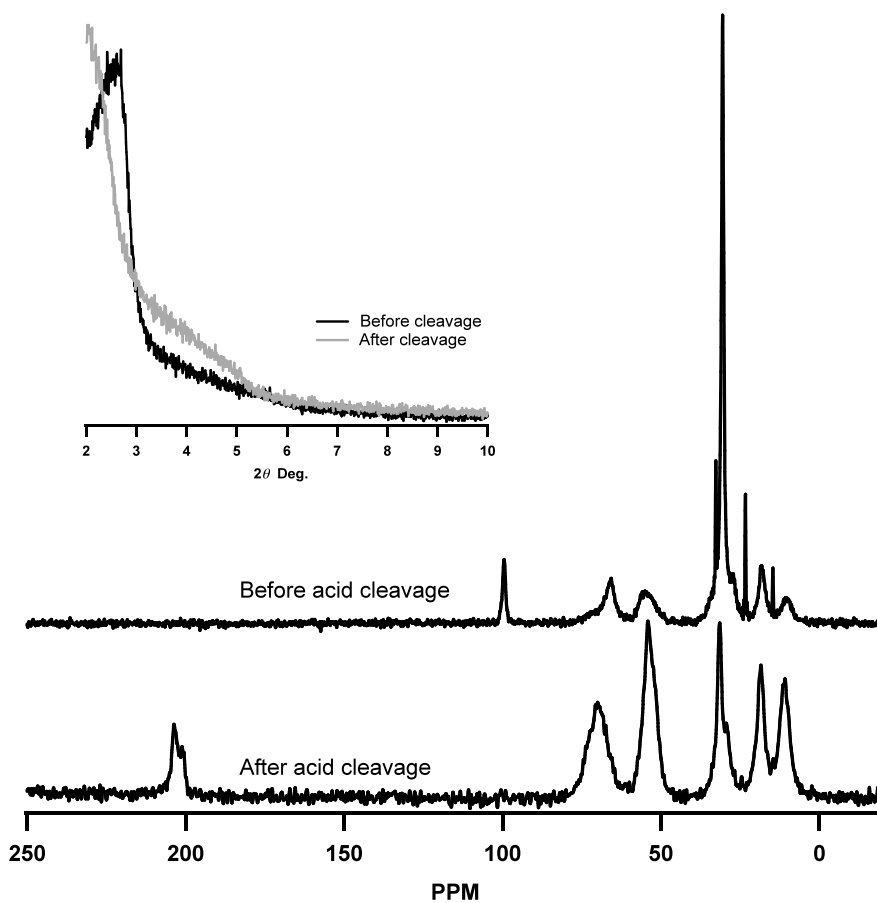
Increasing the fraction of base led to an increase in the T^2 to T^3 ratio. Decreasing the base content to half the typical amount used did not lead to an appreciable change. However,

all reflections in the powder XRD pattern were lost when the base content was either increased or decreased (Figure 2.26).

2.3.3.4 Porosity in MS-25_C silicate

MS-25_{AS} synthesized with a higher silica-to-surfactant ratio (4:1:1:400 sol-gel composition), MS*-25_{AS}, was cleaved and probed for stability by subjecting it to the HBr/CH₃CN/H₂O cleavage conditions.

(a)



(b)

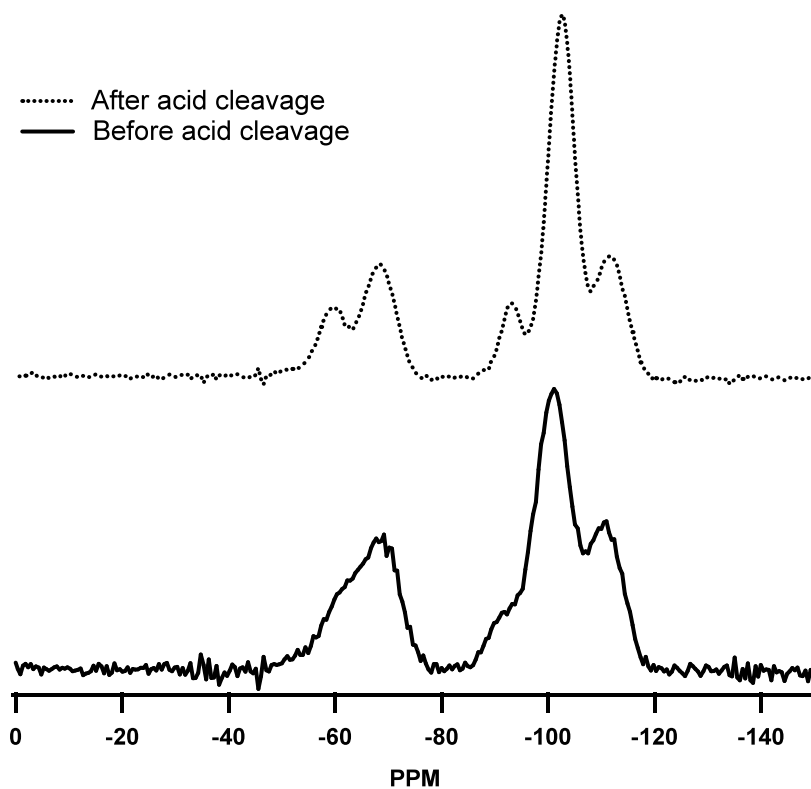


Figure 2.27 (a) ^{13}C CP MAS NMR spectra of $\text{MS}^* -25_{\text{AS}}$ before and after cleavage ($\text{MS}^* -25_{\text{C}}$). Inset shows powder X-ray diffraction spectra of $\text{MS}^* -25_{\text{AS}}$ and $\text{MS}^* -25_{\text{C}}$ (b) ^{29}Si CP MAS NMR spectra of $\text{MS}^* -25_{\text{AS}}$ and $\text{MS}^* -25_{\text{C}}$

These new silicates still undergo facile cleavage under acidic conditions to give the ketone as judged by the ^{13}C CP MAS NMR spectra in Figure 2.27. The ^{29}Si CP MAS NMR before and after cleavage remain relatively similar, indicating improved stability of the silicate structure under cleavage conditions. The powder XRD pattern still gives a single broad peak, but right shifted from its previous position. The right shift could be due to a slight re-organization of the silicate structure as a result of acid hydrolysis. The occurrence of silicate re-organization with modest changes to the ^{29}Si CP MAS NMR implies that

hydrolysis of the silicate wall still occurs, but with less influence on the composite stability as a result of increasing the fraction of silica incorporated.

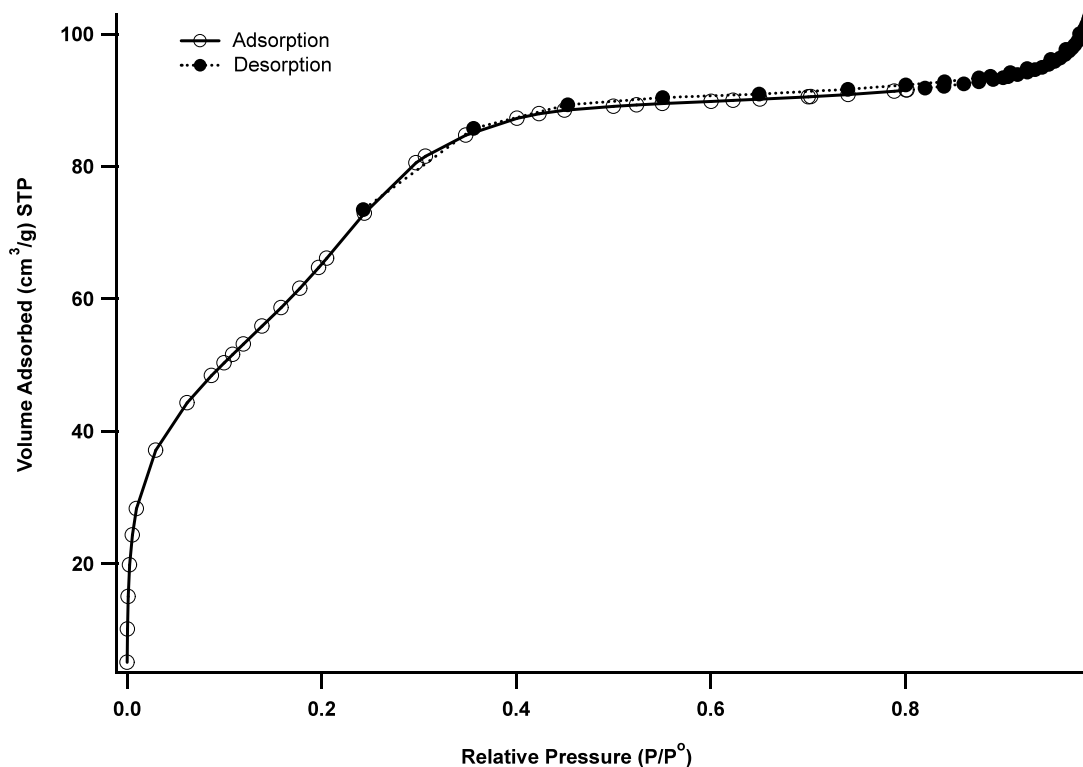


Figure 2.28 Nitrogen adsorption-desorption isotherm of MS^{*}-25_c

The porosity of the silicate probed by nitrogen adsorption revealed a type IV isotherm showing a characteristic pore-filling step, which is completed by P/P_o of ca. 0.3. The stepped increase of nitrogen adsorbed at P/P_o above ca. 0.9 can be attributed to inter-particle capillary condensation. The adsorption isotherm rises slowly over a wide relative pressure range indicating a broad pore distribution, also noted by the broad peak in the X-ray diffraction pattern. However, this rise in the volume adsorbed occurs over a low relative pressure value ($P/P_o \sim 0.3$) indicative of small pores. As seen from Figure 2.28, the adsorption isotherm is completely superimposed with the desorption isotherm, i.e., there is no adsorption hysteresis

for the sample. Adsorption hysteresis loops are only observed below the critical temperature and, as the pore size decreases, the critical temperature also decreases.^{22, 23} Consequently, at sufficiently small diameters of the channels, the adsorption hysteresis loop disappears. According to experimental data from literature,²⁴ this diameter corresponds to 4 nm. The estimated pore size from the BJH desorption isotherm is ~ 3 nm. This small pore size explains the lack of hysteresis in our type IV isotherm. The BJH pore volume is estimated at $0.2 \text{ cm}^3/\text{g}$ and the Brunauer, Emmett, and Teller (BET) surface area is $210 \text{ m}^2/\text{g}$. These low values are most likely the result of the high organic content occluded within the pore structure. Upon calcination, the BET surface area and pore volume increase to $437 \text{ m}^2/\text{g}$ and $0.23 \text{ cm}^3/\text{g}$, respectively.

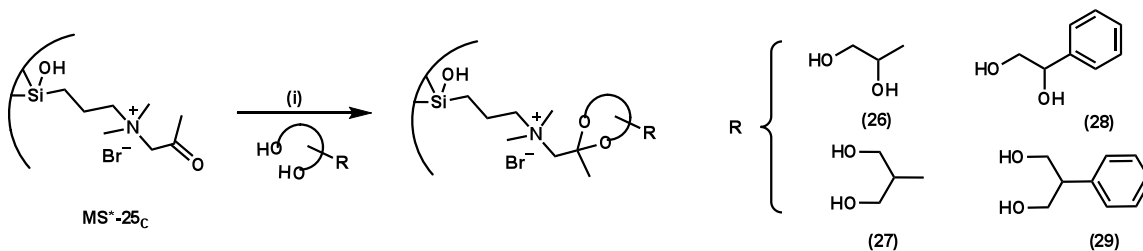


Figure 2.29 Transmission electron microscopy of MS*_{-25C} after calcination at 550°C

The acid-cleaved material was calcined at 550°C prior to analysis via transmission electron microscopy (TEM) so as to gain image contrast. The TEM image shown in Figure 2.29 confirms the presence of mesopores with local ordering. However, long-range order appears absent as the locally ordered regions take on different arrangements over a large scale. This observation is confirmed by the lack of higher-order reflections in the powder XRD pattern (Figure 2.27a, inset). The TGA of the material gave an organic content of 1.24 mmol/g of composite. A better judge of organic density within the pores can be obtained by calculating the amount of organic per square nanometer, since a large percentage of the total surface area arises from the internal surface of the pores. Using the BET surface area obtained from the nitrogen adsorption experiment, the experimental organic density is 2.8 $\mu\text{mol}/\text{m}^2$, which corresponds to 1.7 molecules/ nm^2 . This is a high organic density, considering the surface silanol density is typically estimated at 4.9 OH/nm^2 .²⁵

2.3.3.4 Organic functionalization of porous M41S silicate

In order to demonstrate accessibility of the occluded ketones within the pores of the silicate, we carried out test reactions with 1,2- and 1,3-diols bearing different-sized organic groups.



Scheme 2.9 Reaction of MS-25_C with 1,2- and 1,3 diols; (i) pTSA (0.4 eq.), cyclohexane, 1, 2- or 1, 3-diol (2 eq), reflux, 22 hrs

After numerous trials with different conditions, ketalization was optimized with cyclohexane as the solvent under reflux in the presence of pTSA. The resulting modified silicate was washed via soxhlet extraction to remove residual organics.

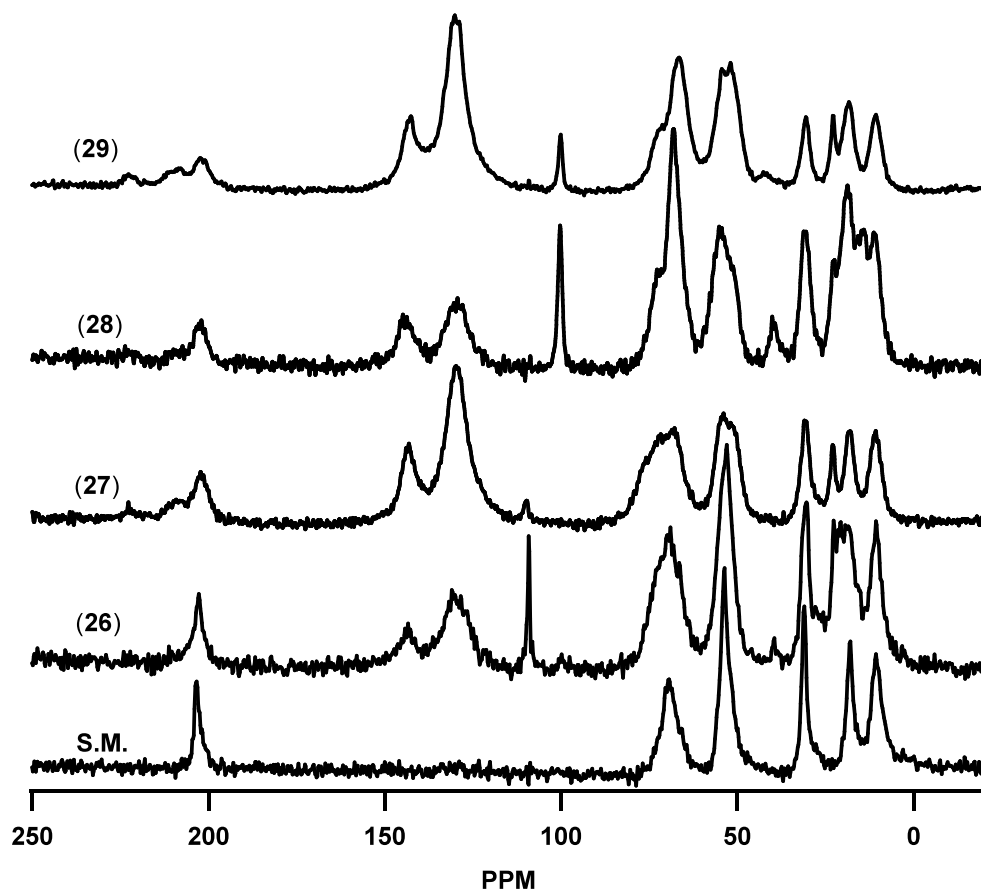


Figure 2.30 ^{13}C CP MAS NMR reaction products of 1, 2- and 1, 3-diols with $\text{MS}^* -25\text{C}$

Ketalization was confirmed by the presence of the 100 and 110 ppm peak for the 1, 3- and 1, 2-diol, respectively, in the ^{13}C CP MAS spectra and the reduction or disappearance of the carbonyl at 202 ppm. In all the samples tested, quantitative conversion of the ketone could not be achieved. This could be due to the high density of functional groups on the pore surface ($1.7 \text{ molecules/nm}^2$) which may lead to steric crowding as the reaction proceeds. The results in Figure 2.30 indicate that the 1,3-dioxane, i.e., the six-membered ring ketal, is more

stable than the 1,3-dioxolane, i.e., the five-membered ring ketal, as expected (same trend seen in solution). The use of phenyl-1, 2- and 1,3-diols (**28**, **29**) led to a much lower ketal yield (as seen in Figure 2.30) compared to the methyl-substituted diols (**26**, **27**). However, the presence of the phenyl groups leads to the broadening of the carbonyl resonance at 202 ppm and the appearance of extra broad carbonyl resonances at 209 and 222 ppm. The broadening is due to the decrease in mobility of the neighbouring carbonyl groups due to the presence of the bulky phenyl group within the tight confines of the pores. The extra carbonyl resonances appear as a result of the heterogeneous distribution phenyl groups within the silicate pores, which will lead to varying degrees of dipolar interaction with the carbonyl carbon. The peaks at 129 and 144 ppm correspond to residual paratoluenesulfonic acid. The presence of these groups even after soxhlet extraction indicates that the sulfonate ions may have exchanged with the bromide ions on the quaternary ammonium during the reaction. These groups can be removed by a simple wash with a stoichiometric amount of sodium hydroxide at room temperature, as shown in Figure 2.31.

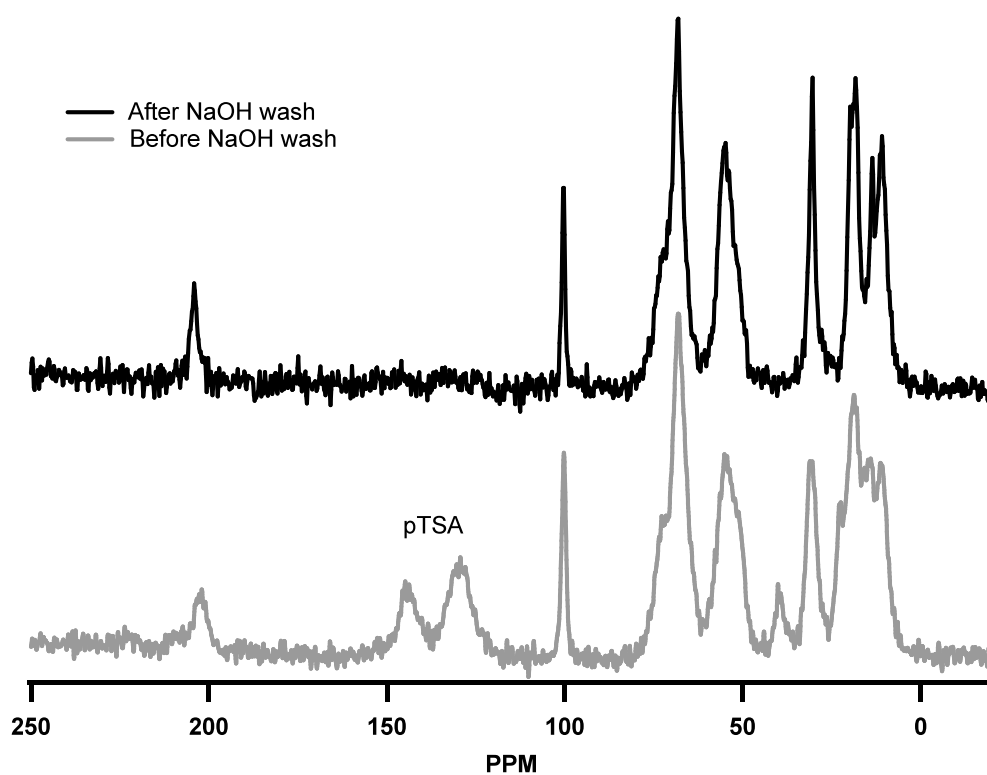


Figure 2.31 Removal of residual bound pTSA with stoichiometric NaOH wash at room temperature from the reaction of MS^{*}-25_C with methylpropane-1,3-diol

We have successfully synthesized a porous, locally ordered structure with densely packed organic groups that are accessible for further modification. Although the silicates in this subsection cannot be directly used as proton-conducting solids, this lays the ground work for future high organic acid density materials that can be synthesized with larger pores, possibly via organic additives, towards their use as acidic organosilicates for proton conductivity and possibly other catalytic applications.

2.4 Discussion

Our goal in this chapter was to uniformly incorporate a high density of organic acid functional groups of various sizes within the pores of mesoporous silicates towards their potential use as PEMs for DMFCs. In order to meet the high internal organic functionalization and uniformity requirements, we designed a new approach that employs the incorporation of a masked version of the desired functional group into a siloxane polymerizable surfactant used for silicate mediated self assembly of the ensuing mesoporous solid. We demonstrated the feasibility of this idea with the successful preparation of MCM-41 via (**1a**). With this validation in hand, we proceeded with the synthesis of an (*E*)-olefin surfactant (**5**) that can be cleaved post silicate assembly to give a carboxylic acid modified mesoporous silicate. After optimizing the sol-gel composition, well ordered MCM-41, i.e., MS-**5**_{AS}, was prepared using compound (**5**). Both ¹³C and ²⁹Si CP MAS NMR confirmed the presence of the complete functional (*E*)-olefin surfactant occluded within the pores of MS-**5**_{AS}. Ozonolysis followed by extraction of the resulting silicate gave the carboxylic acid silicate, MS-**5**_C, with a high organic loading (2.2 mmol/g). This value is double the amount typically obtained for the post-synthetic grafting of similar sized organic groups. This new approach by virtue of the silicate-mediated liquid-crystal templating pathway places the organic surfactant (and thus the functional group) exclusively within the inner walls of the mesoporous silicate.

The nitrogen adsorption on MS-**5**_C showed a type III isotherm indicative of weak adsorbate-adsorbent interactions and lack of porosity. The inaccessibility and lack of exposed silanols or siloxane sites, known to have strong interactions with the nitrogen probe gas, due to steric crowding by the organic groups might explain the lack of adsorption at low relative

pressures. The lack of pore filling at higher relative pressures is simply due to the lack of mesopores or macropores, indicative of a dense type material. The lack of mesoporosity can be rationalized if the surfactant takes on a bent chain conformation within the pores of MS-**5**_C. This conformation, which involves surfactant tail folding and overlap, as seen in Figure 2.11, will result in a nearly nonporous solid.

The calculated pore size of 23 Å using the assumed bent chain configuration of the surfactants within the pore space of MS-**5**_C is consistent with the estimated pore size of 27 Å from the XRD d_{100} spacing data. This supports the validity of such a surfactant arrangement within the pore space of MS-**5**_C. To probe whether olefin isomerization during isothermal synthesis is responsible for this conformation, we prepared both (*E*)- (**10**) and (*Z*)- (**11**) surfactants and examined their individual and combined effects on organosilicate structure. The (*E*)-isomer formed MCM-41 while the (*Z*)-isomer formed MCM-48 under similar sol-gel compositions. The possibility of isomeric preference in the sol-gel mixture was ruled out, since an equimolar mixture of the two isomers produced MCM-41 in 78% yield. These results suggest that either the (*Z*)-isomer is incorporated into MCM-41 or the formation of MCM-48 by the (*Z*)-isomer at a 50:50 mixture is less prominent. However, varying the amount of (*Z*)-olefin to (*E*)-olefin from 0 to 100% simply showed a shift from MCM-41 to MCM-48, indicating the latter. Based on these results, isomerization of the (*E*)-olefin surfactant during synthesis can be ruled out as the reason for the bent chain configuration.

In order to create a porous version of MS-**5**_C, we increased the surfactant chain tail length and moved the olefin group further up the chain (**15**). After optimizing the sol-gel conditions, MS-**15**_{AS} was prepared with cubic symmetry (MCM-48). Formation of this phase, along with the data from the (*E*) vs. (*Z*) isomers and MS-**15**_{AS} vs. MS-**14**_{AS}, suggests that in

addition to multidentate binding of silicate oligomers and charge density matching between the surfactant head group and anionic silicate, the surfactant structure and orientation in solution play a large role during M41S silicate formation. Due to the proximity of the olefin to the bulky quaternary ammonium head group, cleavage of MS-**15**_{AS} with ozone proved difficult at -78°C and had to be carried out at -42°C. This was accompanied by a large loss of symmetry. In addition, MS-**15**_C also lacked porosity when probed by nitrogen adsorption. Earlier in this discussion, we mentioned that the lack of adsorption at low relative pressures in MS-**5**_C was due to the steric crowding by the organic groups and thus lack of silanol or siloxane group accessibility. This was verified in MS-**15**_C by the increase in adsorption at lower relative pressures ($p/p_0 < 0.1$) after calcination. Uptake between $0.1 < p/p_0 < 0.25$ indicates the presence of mesoporosity although no hysteresis is observed. Collapse of the MS-**15**_{AS} symmetry due to harsh ozone conditions prompted us to take a look at the use of alternative cleavable surfactants that do not involve the use of strong oxidizing agents.

As an alternative to olefin-based surfactants, we turned to acid-cleavable cyclic ketal-based surfactants, which turned out to be easier to cleave than their cyclic acetal counterparts. The cyclic ketal surfactant (**25**) was able to generate MS-**25**_{AS} with cubic symmetry (MCM-48). Cleavage under aqueous acidic conditions to give MS-**25**_C resulted in loss of symmetry and lack of porosity. The latter was attributed to surfactant reorganization during cleavage due to siloxane hydrolysis; a result of incomplete silicate condensation. We discovered that increasing the silica fraction during sol-gel condensation enhanced silicate condensation, which led to more stable structures after ketal hydrolysis. Although long-range order was lost, we were able to generate stable porous ketone-modified silicates with short range order (TEM in Figure 2.29). The organic density obtained was 1.24 mmol/g or 1.7 molecules/nm².

This corresponds to 35% of the total silanol coverage on the surface of the silicate. Porosity was further confirmed via ketalization in cyclohexane with various 1,2 and 1,3 diols bearing methyl and phenyl groups. The small pores of MS-**25**_C seem to show size selectivity as well as a preference for 1,3-dioxanes over 1,3-dioxolanes. With further optimization, ordered silicate materials with larger pores can be realized for use not just as PEMs but also for use in catalysis.

2.5 Experimental

Materials

All silane reagents were purchased from Gelest and used as received. All other reagents were purchased from Sigma-Aldrich or TCI organics and used as received. All reactions were run under an inert argon atmosphere. All solvents were purified by fractional distillation from the appropriate drying agents or dried by filtration through the appropriate drying agents prior to use.

Instrumentation

^1H and ^{13}C liquid NMR (300 MHz) spectra were obtained on a Varian Mercury-300 NMR Spectrometer with samples dissolved in either d-chloroform or d-dimethylsulfoxide (DMOS- d_6). ^{29}Si and ^{13}C solid-state CP MAS NMR spectra were recorded at 4 kHz using a Bruker Avance 200MHz spectrometer with a 7 mm rotor. Thermogravimetric analyses (TGA) were performed on a Netzsch STA 449 C with Pt/Rh crucibles. The samples were heated under argon or air at a heating rate of $10^\circ\text{C}/\text{min}$ for all data collections. Powder X-ray diffraction patterns were collected using a Scintag XDS 2000 diffractometer using Cu k- α radiation. Mid-infrared spectra were recorded on a Nicolet 800 FTIR spectrometer. Nitrogen adsorption/desorption isotherms were collected at -196°C on an Omnisorp 100CX analyzer.

(E)-5-chloropent-1-enylboronic acid (2)

Catecholborane (5.85 mmol, 0.7 g) was carefully added to neat chloropent-1-yne (4.9 mmol, 0.5 g) under argon. The mixture was then heated to 100°C under vigorous stirring for 3 hours. The mixture was cooled to 70°C and quenched with (10 mL) water. After 2 hours of stirring, the mixture was further cooled to 0°C, and the resulting white precipitate was filtered over a buchner funnel, washed with cold water and recrystallized from hot water to give the desired product (**2**) in 60% yield.

(E)-5-chloro-1-iodopent-1-ene (3)

To a mixture of (**2**) (4.9 mmol, 0.73g) in ether (5 mL) at 0°C was added aqueous sodium hydroxide (15 mmol, 5 mL, 3N) followed by elemental iodine (5.85 mmol, 1.49 g in 15 mL ether). The mixture was stirred at 0°C for 30 minutes after which the excess iodine was removed by adding a saturated solution of sodium thiosulfate until the dark color of iodine is visibly removed. The ether layer was separated and washed with water and collected. The resulting ether solution was dried over sodium sulfate, concentrated, and distilled (95°C at 0.5 mmHg) to give (**3**) in 85% yield.

(E)-1-chlorotetradec-4-ene (4)

To a flame-dried flask under argon was added non-1-ene (0.48 mmol, 60.2 mg) and dry THF (0.3 mL). 9-borabicyclo[3.3.1] nonane (9-BBN) (0.5 M in THF, 0.477 mmol, 0.95 mL) was slowly added to this mixture at 0°C and slowly warmed up to room temperature. After stirring for 6 hours, (*E*)-5-chloro-1-iodopent-1-ene (0.43 mmol, 100 mg), [1,1'-bis(diphenylphosphino)-ferrocene]dichloropalladium (II) complex with dichloromethane

(1:1) (3 mol%, 0.013, 10.6 mg), sodium hydroxide (1.3 mmol, 3M, 0.43 mL) and additional THF (1 mL) were added. The mixture was refluxed for 16 hours under vigorous stirring. The resulting dark mixture was diluted with hexanes (3 mL), washed with brine, and dried over magnesium sulfate. The crude mixture was purified over a column with hexanes to give desired product (4) in 75% yield.

1-bromotetradec-4-yne (6)

10 g (65.7 mmol) of 1-undecyne and 90 mL THF was cooled to -40 °C using an acetonitrile and dry ice bath. 2.5 M butyl lithium (59.1 mmol, 23.6 mL) was added dropwise before warming to 0 °C with an ice bath. After stirring the mixture for an hour, 1,3-dibromopropane (131.3 mmol, 26.5 g) was added to 90 mL of THF, cooled to 0 °C, and then added to the reaction flask containing undecyne and butyl lithium. The reaction was warmed to room temperature and stirred for 24 hours. Approximately 9 g of the desired product was obtained via distillation (160-180 °C).

***N,N*-dimethylaminotetradec-4-yne (7)**

6 g of 1-bromotetradec-4-yne (6) (22 mmol) was added to dimethylamine (43.9 mmol, 7.8 mL) in 200 mL of THF. The reaction was allowed to stir overnight. The THF was rotovaped off and the remaining solution was diluted with ether and taken up in 6M NaOH. The ether extracts were concentrated under vacuo and dried to give the desired product (7) in 57% yield.

(E)-N,N-dimethylaminotetradec-4-ene (8)

Liquid ammonia was condensed into a pre-vacuumed round bottom at -42 °C. Sodium (22.4 mmol, 0.514g) was added to the liquid ammonia and the resulting blue mixture was stirred for 20 minutes. Compound (7) (2.14 mmol, 0.5 g) in 10 mL of THF was added to the mixture and allowed to stir for 2 hours. Ammonium chloride was added slowly to the solution until all blue color had disappeared. The reaction was stirred at room temperature for another 2 hours while open to the atmosphere. The remaining solution was diluted with 40 mL of ether and washed with 60 mL of water and brine to give the desired product in 64% yield.

(Z)-N,N-dimethylaminotetradec-4-ene (9)

0.56 g of Lindlars catalyst (2.5 mol%) was added to a dry round-bottom flask. The flask was placed under vacuo and subsequently filled with hydrogen gas. Compound (7) in methanol (10 mL/g (7)) was added to catalyst under hydrogen and the reaction was allowed to stir for no more than 90 minutes. The reaction mixture was filtered through a celite pad to remove the spent catalyst and solvent was removed under vacuo. The desired product (9) was obtained in near quantitative yield.

N,N-dimethylaminoheptadec-2-yne (12)

Butyl lithium (120.3 mmol, 48.1 mL) was added to a cooled solution (-78°C) of N,N-dimethylaminopropyne (120.3 mmol, 10 g) in 100 mL THF and 40 mL HMPA under argon. After stirring for one hour, bromotetradecane (109.4 mmol, 30.3 g) was added and the mixture was warmed to room temperature and then heated at 60°C for 2 hours. After cooling to room temperature, 60 mL of brine was added and the mixture was poured into 300 mL of

ether. The organic layer was washed twice with 300 mL of water, dried over MgSO₄ and concentrated under vacuo to give the desired product in 90% yield.

(E)-N,N-dimethylaminoheptadec-2-ene (13)

Liquid ammonia was condensed into a pre-vacuumed round bottom at -42 °C. Sodium (179 mmol, 4.1 g) was added to the liquid ammonia and the resulting blue mixture was stirred for 20 minutes. Compound (12) (17.9 mmol, 5 g) in 80 mL of THF was added to the mixture and allowed to stir for 2 hours. Ammonium chloride was added slowly to the solution until all blue color had disappeared. The reaction was stirred at room temperature for another 2 hours while open to the atmosphere. The remaining solution was diluted with ether and the organic layer was washed with water and brine and purified via flash chromatography (CHCl₃:MeOH 16:1) to give the desired product in 80% yield.

Diethyl 2-tetradecylmalonate (16)

To a cooled (0°C) suspension of Sodium hydride (65 mmol, 2.6 g) in 20mL of THF was added diethylmalonate (88.4 mmol, 14.2 g) dissolved in 25 mL of THF. The mixture was stirred for 20 minutes, after which bromotetradecane in 65 mL of THF was added. The mixture was stirred at room temperature for 2 hours and then heated to 70°C for 15 hours. After cooling, the mixture was taken up in 250 mL of ethyl acetate and washed three times with 150 mL of water, a saturated sodium thiosulfate solution and brine. The organic layer was dried over MgSO₄, concentrated and distilled (product distills at 175°C) to give the desired product in 72% yield.

2-tetradecylpropane-1,3-diol (17)

71.2 mL of lithium aluminum hydride (LAH) solution (71.2 mmol, 1.0 M in THF) was added to a dry empty flask and cooled to 0°C. Compound (16) (28.5 mmol, 10.2 g) in 35 mL of THF was added slowly to the flask. After the addition, the mixture was warmed to room temperature and stirred for 90 minutes. The reaction was quenched by carefully (VERY SLOWLY) adding wet THF to the chilled reaction mixture. The quenched reaction was then diluted in 150 mL of ether, washed with a sulfuric acid solution, and extracted with 200 mL ethyl acetate. The desired product was recrystallized from hexanes and obtained in 77% yield.

4-Bromobutanal (21)

To a cooled solution (-78°C) of ethyl 4-bromobutyrate (18.2 mmol, 3.55 g) in 20 mL of dichloromethane was added DIBAL dropwise over 15 minutes. The reaction was stirred for another 30 minutes at -78°C after which it was poured onto cold 10% HCl and stirred for an additional hour. The organic layer was separated, washed with brine, dried over MgSO₄, and concentrated. The resulting product was used without further purification.

General procedure for acetal and ketal formation

All acetal reactions were carried out in a 1:1 ratio of (**17**) to the corresponding protected aldehydes or 1:2 ratio of (**17**) to the corresponding protected ketone. Acetal formation was carried out with polymer bound para-toluenesulfonic acid (0.1 mol%) at 85°C. Ketal formation was carried out with polymer bound para-toluenesulfonic acid (0.5 mol%) in CHCl₃ at 30°C for 4 hours with one exception. Ketalization of (**17**) with dimethylamino acetone was carried out with 220 mol% para-toluenesulfonic acid in cyclohexane at 120°C for 16 hours.

(2r,5r)-2-(bromomethyl)-5-tetradecyl-1,3-dioxane (18)

Compound (**17**) and 2-bromo-1,1-dimethoxyethane (1 eq) with pTSA (0.1 mol%, polymer bound) were heated neat at 85°C for 24 hours. The desired product was taken up in hexanes to remove the polymer beads then recrystallized from methanol and obtained in 80% yield.

(2r,5r)-2-(2-bromoethyl)-5-tetradecyl-1,3-dioxane (20)

Compound (**17**) and 3-bromo-1,1-dimethoxypropane (1 eq) with pTSA (0.1 mol%, polymer bound) were heated neat at 85°C for 24 hours. The desired product was taken up in hexanes to remove the polymer beads then recrystallized from methanol and obtained in 80% yield.

(2r,5r)-2-(3-bromopropyl)-5-tetradecyl-1,3-dioxane (22)

Compound (17) and 4-bromobutanal (1 eq) with pTSA (0.1 mol%, polymer bound) were heated in neat at 85°C for 24 hours. The desired product was taken up in hexanes to remove the polymer beads then recrystallized from methanol and obtained in 78% yield.

(2r,5r)-2-(bromomethyl)-2-methyl-5-tetradecyl-1,3-dioxane (23)

Compound (17) and 1-bromo-2,2-dimethoxypropane (2 eq) with pTSA (5 mol%, polymer bound) were heated in CHCl₃ at 30°C for 4 hours. The mixture was purified by washing with 1N NaOH or saturated sodium carbonate and brine followed by drying the organic layer over MgSO₄ and concentrating under vacuo. The desired product was recrystallized from methanol.

N,N-dimethyl-1-((2r,5r)-2-methyl-5-tetradecyl-1,3-dioxan-2-yl)methanamine (24)

Compound (17) and dimethylamino pentane (2 eq.) and pTSA (2.2 eq, polymer bound) were refluxed with a dean stark trap in cyclohexane for 16 hours. The mixture was purified by washing with 1 N NaOH or saturated sodium carbonate and brine followed by drying the organic layer over MgSO₄ and concentrating under vacuo. The desired product was recrystallized from pentane and obtained in 80 % yield.

Surfactants via quarternization

Compound (1a) and (1b)

Chloropropyltrimethoxysilane (50 mmol, 9.94g), *N,N*-dimethylaminotetradecane (50 mmol, 12.07g) or *N,N*-dimethylaminooctadecane (50 mmol, 14.88 g) and methanol (10mL) were placed under argon in a round bottom flask and refluxed at 90°C for 2 days. After 2 days, the reaction was cooled to room temperature and the methanol removed under reduced pressure. The resulting product was washed with cold hexanes and dried overnight to give the desired product in 30% yield. ¹H NMR (300 MHz, CDCl₃) δ 3.66 – 3.19 (m, 19H), 1.89 – 1.70 (m, 2H), 1.65 (s, 2H), 1.40 – 1.10 (m, 22H), 0.90 – 0.75 (m, 3H), 0.63 (t, *J* = 7.8, 2H).

Compound (5)

N,N-dimethylaminoltrimethoxysilane (14.5 mmol, 3g), compound (4) (16 mmol, 3.7 g) and methanol (6 mL) were placed under argon in a round bottom flask and refluxed at 90°C for 48-72 hours. The reaction was cooled to room temperature and the methanol removed under reduced pressure. The resulting product was washed with cold hexanes and dried overnight to give the desired product in 40 % yield. ¹H NMR (300 MHz, CDCl₃) δ 5.47 – 5.32 (m, 1H), 5.31 – 5.15 (m, 1H), 3.63 – 3.13 (m, 19H), 2.01 (d, *J* = 7.0, 2H), 1.88 (d, *J* = 6.6, 2H), 1.80 – 1.57 (m, 4H), 1.34 – 0.99 (m, 14H), 0.78 (t, *J* = 6.7, 3H), 0.58 (t, *J* = 7.8, 2H); ¹³C NMR (75 MHz, CDCl₃) δ 133.63, 127.00, 65.10, 63.13, 51.52, 50.89, 32.66, 32.04, 29.75, 29.65, 29.56, 29.49, 29.39, 22.83, 16.57, 14.28, 5.68.

Compound (10)

Bromopropyltrimethoxysilane (12.6 mmol, 3.1g), compound (8) (12.6 mmol, 3 g) and methanol (5 mL) were placed under argon in a round bottom flask and refluxed at 95°C for 48-72 hours. The reaction was cooled to room temperature and the methanol removed under reduced pressure. The resulting product was washed with cold hexanes and dried overnight to give the desired product in 34 % yield. ¹H NMR (300 MHz, CDCl₃) δ 5.47 – 5.32 (m, 1H), 5.31 – 5.15 (m, 1H), 3.63 – 3.13 (m, 19H), 2.01 (d, *J* = 7.0, 2H), 1.88 (d, *J* = 6.6, 2H), 1.80 – 1.57 (m, 4H), 1.34 – 0.99 (m, 14H), 0.78 (t, *J* = 6.7, 3H), 0.58 (t, *J* = 7.8, 2H); ¹³C NMR (75 MHz, CDCl₃) δ 133.63, 127.00, 65.10, 63.13, 51.52, 50.89, 32.66, 32.04, 29.75, 29.65, 29.56, 29.49, 29.39, 22.83, 16.57, 14.28, 5.68.

Compound (11)

Bromopropyltrimethoxysilane (9.2 mmol, 2.3 g), compound (9) (9.2 mmol, 2.2 g) and methanol (5 mL) were placed under argon in a round bottom flask and refluxed at 95°C for 48-72 hours. The reaction was cooled to room temperature and the methanol removed under reduced pressure. The resulting product was washed with cold hexanes and dried overnight to give the desired product in 34 % yield. ¹H NMR (300 MHz, CDCl₃) δ 5.42 (dt, *J* = 10.8, 7.2, 1H), 5.23 (dt, *J* = 8.6, 7.0, 1H), 3.72 – 3.18 (m, 19H), 2.10 (q, *J* = 7.0, 2H), 1.94 (dd, *J* = 13.5, 6.7, 2H), 1.74 (dd, *J* = 8.1, 3.8, 4H), 1.38 – 1.11 (m, 14H), 0.90 – 0.75 (m, 3H), 0.63 (t, *J* = 7.8, 2H). ¹³C NMR (75 MHz, CDCl₃) δ 133.08, 126.43, 65.41, 63.36, 51.65, 50.96, 50.81, 50.54, 32.07, 29.76, 29.52, 27.59, 23.83, 22.86, 22.81, 16.63, 14.32, 5.65.

Compound (14)

Bromopropyltrimethoxysilane (7.16 mmol, 1.68 g), compound (**12**) (7.16 mmol, 2 g) and methanol (6 mL) were placed under argon in a round bottom flask and refluxed at 95°C for 72 hours. The reaction was cooled to room temperature and the methanol removed under reduced pressure. The resulting product was washed with cold hexanes and dried overnight to give the desired product in 81 % yield. ¹H NMR (300 MHz, CDCl₃) δ 4.59 (s, 2H), 3.63 – 3.49 (m, 9H), 3.39 (d, *J* = 9.1, 8H), 2.22 (s, 2H), 1.95 – 1.69 (m, 2H), 1.58 – 1.42 (m, 2H), 1.23 (s, 22H), 0.91 – 0.78 (m, 3H), 0.65 (dd, *J* = 14.7, 6.7, 2H). ¹³C NMR (75 MHz, CDCl₃) δ 94.10, 68.20, 57.42, 52.85, 32.11, 29.88, 29.85, 29.70, 29.56, 29.27, 29.21, 28.34, 22.89, 18.95, 14.33.

Compound (15)

Bromopropyltrimethoxysilane (17.24 mmol, 4.85 g), compound (**13**) (17.24 mmol, 4.2 g) and methanol (8 mL) were placed under argon in a round bottom flask and refluxed at 95°C for 72 hours. The reaction was cooled to room temperature and the methanol removed under reduced pressure. The resulting product was washed with cold hexanes and dried overnight to give the desired product in 75 % yield. ¹H NMR (300 MHz, CDCl₃) δ 6.34 – 6.10 (m, 1H), 5.50 (dt, *J* = 15.1, 7.6, 1H), 4.22 (d, *J* = 7.5, 1H), 4.14 (m, 1H), 3.64 – 3.50 (m, 9H), 3.45 (s, 3H), 3.29 (s, 3H), 3.23 (m, 2H), 2.26 – 2.03 (m, 2H), 1.90 – 1.71 (m, 2H), 1.26 (m, 24H), 0.86 (t, *J* = 7.3, 6.2, 3H), 0.64 (t, *J* = 7.9, 2H). ¹³C NMR (75 MHz, CDCl₃) δ 147.93, 115.68, 65.91, 64.92, 50.94, 50.53, 50.30, 33.02, 32.09, 29.85, 29.76, 29.59, 29.54, 29.47, 28.67, 22.87, 16.61, 14.31, 5.82.

Compound (19)

N,N-dimethylaminoltrimethoxysilane (17.9 mmol, 3.7 g), compound (**18**) (17.9 mmol, 6.75 g) and acetonitrile (20 mL) were placed under argon in a round bottom flask and refluxed at 95°C for 72 hours. The reaction was cooled to room temperature and the acetonitrile removed under reduced pressure. The resulting product was washed with cold hexanes and dried overnight to give the desired product in 45 % yield. ¹H NMR (300 MHz, CDCl₃) δ 5.17 (t, *J* = 4.0, 1H), 4.06 (dd, *J* = 11.6, 4.6, 2H), 3.79 – 3.64 (m, 2H), 3.56 (s, 11H), 3.48 (m, 8H), 2.11 – 1.88 (m, 1H), 1.81 (s, 2H), 1.23 (s, 24H), 1.04 (m, 2H), 0.86 (t, *J* = 6.6, 3H), 0.72 – 0.59 (t, 2H).

Compound (25)

Bromopropyltrimethoxysilane (2.38 mmol, 0.58 g), compound (**24**) (2.38 mmol, 0.85 g) and acetonitrile/methanol (4 mL, 3:1) were placed under argon in a round bottom flask and refluxed at 95°C for 48 hours. The reaction was cooled to room temperature and the acetonitrile and methanol removed under reduced pressure. The resulting product was washed with cold hexanes and dried overnight to give the desired product in 78 % yield. ¹H NMR (300 MHz, CDCl₃) δ 3.86 (d, *J* = 5.0, 2H), 3.82 (d, *J* = 4.8, 2H), 3.76 – 3.31 (m, 19H), 1.89 (m, 1H), 1.82 (m, 2H), 1.48 (s, 3H), 1.20 (s, 24H), 0.99 (m, 2H), 0.83 (t, *J* = 6.5, 3H), 0.60 (t, 2H). ¹³C NMR (75 MHz, CDCl₃) δ 98.76, 68.69, 67.70, 65.63, 53.94, 50.95, 34.12, 32.10, 29.95, 29.84, 29.75, 29.60, 29.55, 28.45, 26.43, 22.88, 18.35, 17.04, 14.33, 5.86.

Preparation of mesostructured silicates

The surfactant was mixed with water until a clear gel was formed. TMAOH and TEOS were added and stirred vigorously for 1 hour. The stir bar was removed and the material was aged for the desired time in an oven at the desired temperature, typically 100°C. The material was washed with water and acetone. Further extraction was carried out with a soxhlet apparatus with the desired solvent. The resulting solid was dried under vacuum at 40°C.

General procedure for ozonolysis of M41S materials

Ozonolysis was carried out by bubbling ozone (60-84 µg/mL) through a suspension of the M41S silicate in dichloromethane at -78°C or -42°C. After the desired time, the solution was purged with argon while warming to room temperature, filtered and washed with acetone and water. Oxidation of the ozone treated solid was carried out with formic acid (5 mL) and hydrogen peroxide (2.5 mL) in water (2.5 mL) at 50°C for 1 hour followed by a 1N hydrochloric acid (10 mL) post treatment for another hour to give the corresponding carboxylic acid groups. The solids were then washed with acidic ethanol at 50°C to remove any adsorbed species.

General procedure for acetal cleavage in M41S materials

The M41S solid (~ 300- 400 mg) was suspended in a solution containing 4.2 mL 48wt% HBr, 4.2 mL water and 50 mL CH₃CN. The mixture was heated to 50°C for 4 hours. After cooling, the mixture was filtered, washed with acidic ethanol to extract residual organics and dried under vacuum.

General procedure for ketalization in M41S materials

The MS*-25_C silicate (~200-300 mg) was suspended in cyclohexane (32 mL). To this mixture, 0.4 eq of pTSA (crystalline solid) and 2 eq. of the 1,2- or 1,3-diol was added. The mixture was refluxed at 120°C for 22 hours. After cooling, the solid was filtered and washed with ethanol. To remove residual pTSA, a stoichiometric amount of NaOH is added to the solid in 10 mL of water and the mixture is stirred at room temperature for 24 hours. The solid is filtered, washed with water and dried under vacuoo overnight.

2.6 References:

1. Kresge, C. T.; Leonowicz, M. E.; Roth, W. J.; Vartuli, J. C.; Beck, J. S., *Nature* **1992**, 359, (6397), 710-712.
2. Huo, Q. S.; Margolese, D. I.; Ciesla, U.; Feng, P. Y.; Gier, T. E.; Sieger, P.; Leon, R.; Petroff, P. M.; Schuth, F.; Stucky, G. D., *Nature* **1994**, 368, (6469), 317-321.
3. Monnier, A.; Schuth, F.; Huo, Q.; Kumar, D.; Margolese, D.; Maxwell, R. S.; Stucky, G. D.; Krishnamurty, M.; Petroff, P.; Firouzi, A.; Janicke, M.; Chmelka, B. F., *Science* **1993**, 261, (5126), 1299-1303.
4. Tanev, P. T.; Pinnavaia, T. J., *Science* **1995**, 267, (5199), 865-867.
5. Bagshaw, S. A.; Prouzet, E.; Pinnavaia, T. J., *Science* **1995**, 269, (5228), 1242-1244.
6. Sayari, A.; Karra, V. R.; Reddy, J. S.; Moudrakovski, I. L., *Chemical Communications* **1996**, (3), 411-412.
7. J.C. Vartuli, W. J. R., J.S. Beck, S.B. McCullen, C.T. Kresge, *Molecular Sieves* **1998**, 1, 98-119.
8. Vartuli, J. C.; Schmitt, K. D.; Kresge, C. T.; Roth, W. J.; Leonowicz, M. E.; McCullen, S. B.; Hellring, S. D.; Beck, J. S.; Schlenker, J. L.; Olson, D. H.; Sheppard, E. W., *Chemistry of Materials* **1994**, 6, (12), 2317-2326.
9. Beck, J. S.; Vartuli, J. C.; Roth, W. J.; Leonowicz, M. E.; Kresge, C. T.; Schmitt, K. D.; Chu, C. T. W.; Olson, D. H.; Sheppard, E. W.; McCullen, S. B.; Higgins, J. B.; Schlenker, J. L., *Journal of the American Chemical Society* **1992**, 114, (27), 10834-10843.
10. Chen CY, B. S., Li HX, Davis ME, *Microporous and Mesoporous Materials* **1993**, 2, (1), 17-26.

11. McKeen, J. C.; Yan, Y. S.; Davis, M. E., *Chemistry of Materials* **2008**, 20, (16), 5122-5124.
12. Marschall, R.; Bannat, I.; Caro, J.; Wark, M., *Microporous and Mesoporous Materials* **2007**, 99, (1-2), 190-196.
13. Marschall, R.; Rathousky, J.; Wark, M., *Chemistry of Materials* **2007**, 19, (26), 6401-6407.
14. Otomo, J.; Wang, S. Q.; Takahashi, H.; Nagamoto, H., *Journal of Membrane Science* **2006**, 279, (1-2), 256-265.
15. Hamoudi, S.; Kaliaguine, S., *Microporous and Mesoporous Materials* **2003**, 59, (2-3), 195-204.
16. Munakata, H.; Chiba, H.; Kanamura, K., *Solid State Ionics* **2005**, 176, (31-34), 2445-2450.
17. Yang, Q. H.; Liu, J.; Yang, J.; Kapoor, M. P.; Inagaki, S.; Li, C., *Journal of Catalysis* **2004**, 228, (2), 265-272.
18. Platschek, B.; Petkov, N.; Bein, T., *Angewandte Chemie-International Edition* **2006**, 45, (7), 1134-1138.
19. Nogami, M.; Mitsuoka, T.; Hattori, K.; Daiko, Y., *Microporous and Mesoporous Materials* **2005**, 86, (1-3), 349-353.
20. Huo, Q. S.; Margolese, D. I.; Stucky, G. D., *Chemistry of Materials* **1996**, 8, (5), 1147-1160.
21. Scheiner, S.; Grabowski, S. J., *Journal of Molecular Structure* **2002**, 615, (1-3), 209-218.
22. Nakanishi, H.; Fisher, M. E., *Journal of Chemical Physics* **1983**, 78, (6), 3279-3293.

23. Tovbin, Y. K.; Votyakov, E. V., *Langmuir* **1993**, 9, (10), 2652-2660.
24. L. D. Gelb, K. E. G., R. Radhakrishnan, M. Sliwinska-Bartowiak, *Rep. Prog. Phys.* **1999**, 62, 1573.
25. Zhuravlev, L. T., *Langmuir* **1987**, 3, (3), 316-318.

Chapter III

Proton Conductivity Studies on Organically Modified Mesostructured Silicates

3.1 Abstract

We report on the use of our new strategy, which involves the synthesis of densely packed carboxylic acid groups within the pores of MCM-41, towards the enhancement of proton conductivity by increasing the organic acid content. The carboxylic acid silicates prepared via our new route gave conductivities that were fivefold greater than post synthetically grafted organosilicates at room temperature under fully hydrated conditions. This enhancement was attributed to a combination of higher acid content and lower acid dissociation constants in the densely packed organosilicates. The effect of hydrophobicity was probed by synthesizing organosilicates via our new approach with varying organic acid chain lengths by changing the position of the olefin group within the surfactant. Proton conductivity results on these silicates suggest that the negative effect of hydrophobicity on conductivity sets in when the alkyl ammonium organic chain length is longer than ten methylene groups. Temperature-dependent conductivity experiments under fully hydrated and dry conditions pointed to structural diffusion as the dominant mechanism of proton transport via a percolated water network. The potential for low methanol uptake via long hydrophobic alkyl groups and high acid density should make organosilicates prepared via this methodology promising alternatives as electrolyte membranes in direct methanol fuel cells operated below the dew point of water.

3.2 Introduction

Despite high conductivities below the dew point of water, the current state of art membrane, Nafion™, poses several disadvantages such as high cost, environmental inadaptability, and high methanol permeability.¹ The latter is one of the major problems affecting the practical application of direct methanol fuel cells (DMFCs). The liquid methanol fuel in a DMFC is completely miscible with water and thus crosses through the membrane as a result of protonic drag, similar to the electro-osmotic drag of water from anode to cathode.^{2, 3} This unwanted methanol diffusion across the polymer electrolyte membrane, referred to as “methanol crossover”, wastes fuel by undergoing chemical oxidation at the anode, thus causing a voltage drop and an overall reduction in cell efficiency.

In the past decade, several solid proton conductive materials have been proposed as alternatives to Nafion. Some of these include sulfonated polymers such as sulfonated polysulfone,⁴ poly-(ether ether ketone),⁵ polyimides,⁶ and poly(benzeneimidazole).⁷ Although each material has its advantages, they all fail to curb methanol diffusion due to the swelling of their soft polymeric backbone upon hydration. In an attempt to curb methanol diffusion through these polymers, inorganic additives such as hard silica nanocomposites have been incorporated into the membranes to introduce a winding pathway for methanol diffusion.^{8, 9} Given that these particles are embedded within the hydrophilic pores of the polymers, they also act as obstacles to structural (Grotthuss) diffusion in bulk water and thus, slow down proton mobility.

To circumvent this problem, a new class of polymer electrolyte membranes (PEMs) based on the use of proton conductive hybrid organic-inorganic particles as the primary membrane structure has been investigated.¹⁰⁻¹³ Some of these inorganic membranes include

silica-based microporous or mesoporous structures prepared by the sol-gel processing route. Mesoporous silicas are particularly interesting, as discussed in the previous chapter, because of their high specific surface area, zero electrical conductivity, open ordered channels of variable dimensions, and high chemical, structural, and mechanical stability. Their large surface area allows these materials to accommodate a high amount of organic groups bearing strong acids that can promote conductivity through vehicular or structural diffusion under fully hydrated conditions. In addition, their rigid condensed silica wall prohibits swelling when hydrated, thus limiting methanol diffusion due to electro-osmotic drag.¹⁴

In the previous chapter, we described the synthesis of densely packed carboxylic acid groups within a mesoporous material, MS-5_C, as a way to enhance proton conductivity in M41S silicates under fully humidified conditions by increasing the organic group density within the pores of the silicate.¹⁰ Our strategy involved the use of polymerizable functional surfactants that were permanently attached to the pore walls during hydrothermal synthesis, and olefin functional groups embedded within the hydrophobic surfactant tail that generates the desired acid group upon cleavage after silicate assembly (Figure 3.1).

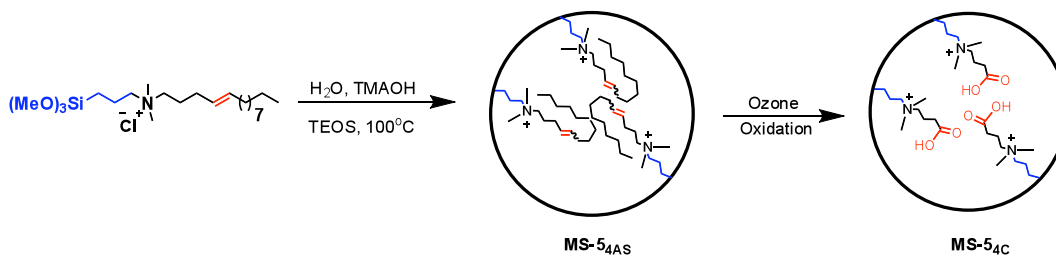


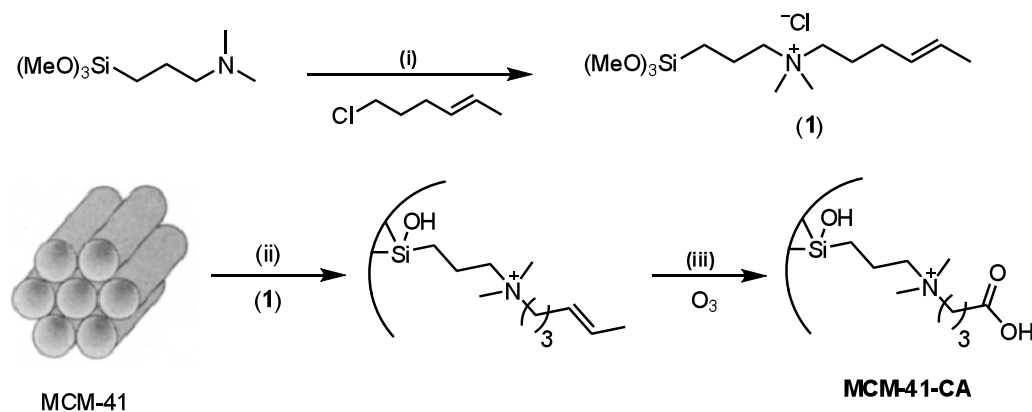
Figure 3.1 Schematic diagram of the preparation of $\text{MS-5}_{4\text{C}}$ bearing carboxylic acid groups. $\text{MS-5}_{4\text{C}}$ denotes the mesostructured silicate with the olefin group at the 4-position in the surfactant tail, C - denotes cleaved and AS – as-synthesized

The mesostructured silicate obtained after cleavage, i.e., $\text{MS-5}_{4\text{C}}$, was nonporous as determined by a nitrogen adsorption-desorption experiment. However, this should not be taken to mean that these materials are completely impervious fluids. Data from TGA experiments show that these materials still adsorb water due to their hydrophilic interior (9 mg $\text{H}_2\text{O}/\text{g}$ composite after drying). In this chapter, we take a look at this class of high density nonporous silicates and examine how their ability to conduct protons is influenced by the organic acid group density, the length of the carbon chain in the surfactant tail (i.e., hydrophobicity), temperature, and water content.

3.3 Results and Discussion

3.3.1 Effect of organic acid density

To study the effect of organic acid density, we synthesized an analogous carboxylic acid-modified MCM-41 composite via the post-synthetic graft method from commercially available MCM-41 (Sigma-Aldrich). In order to closely mimic the MS-5_{4C} system (Chapter II, page 14), we grafted an olefin bearing quarternary ammonium silane onto MCM-41 and subjected it to the same ozonolysis conditions as MS-5_{4C}. This silicate was prepared as outlined in Scheme 3.1 below.



Scheme 3.1 Preparation of MCM-41-CA. (i) MeOH, reflux, 72 h; (ii) Reflux, toluene, 24 h; (iii) ozone, CH₂Cl₂, 7 h, formic acid, H₂O₂, 1 h

The carboxylic acid bearing MCM-41 was obtained after ozonolysis of the grafted precursor. The ¹³C CP MAS NMR spectrum of MCM-41-CA is almost identical to that of MS-5_{4C} (Figure 3.2) indicating that both materials are chemically identical. The organic content determined by TGA after ozonolysis was 0.85 mmol/g. This is 2.7-fold lower than

the amount obtained for MS-5_{4C} and further highlights the uniqueness of the in situ cleavage approach for high organic incorporation onto the inner wall of the mesoporous silicate.

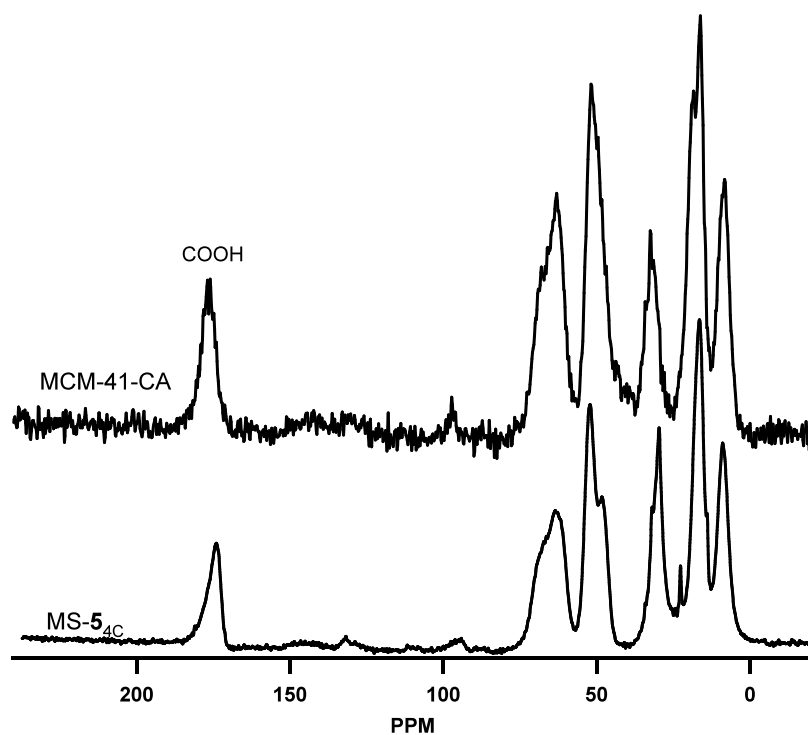


Figure 3.2 ^{13}C CP MAS NMR of MCM-41-CA and MS-5_{4C}

In order to check if all the organic groups were accessible, MS-5_{4C} was titrated to determine the number of accessible carboxylic acid groups. Back titration gave a carboxylic acid loading of 2.1 mmol/g that is within 95% of the 2.2 mmol/g obtained from TGA analysis. This confirms that a high percentage of the surfactants end up in the pores and most of the surfactant tail is removed from the pores after oxidation and extraction.

Proton conductivity measurements were performed on thoroughly washed samples. The solids were washed and centrifuged until a constant pH was obtained. The samples were compressed in a clear polyetherimide cylindrical cell between two Pt/Ir rod electrodes at 100% relative humidity (R.H.), i.e., fully hydrated. Proton conductivity was obtained via

two-electrode impedance spectroscopy. Details of the experimental setup are provided in the experimental section.

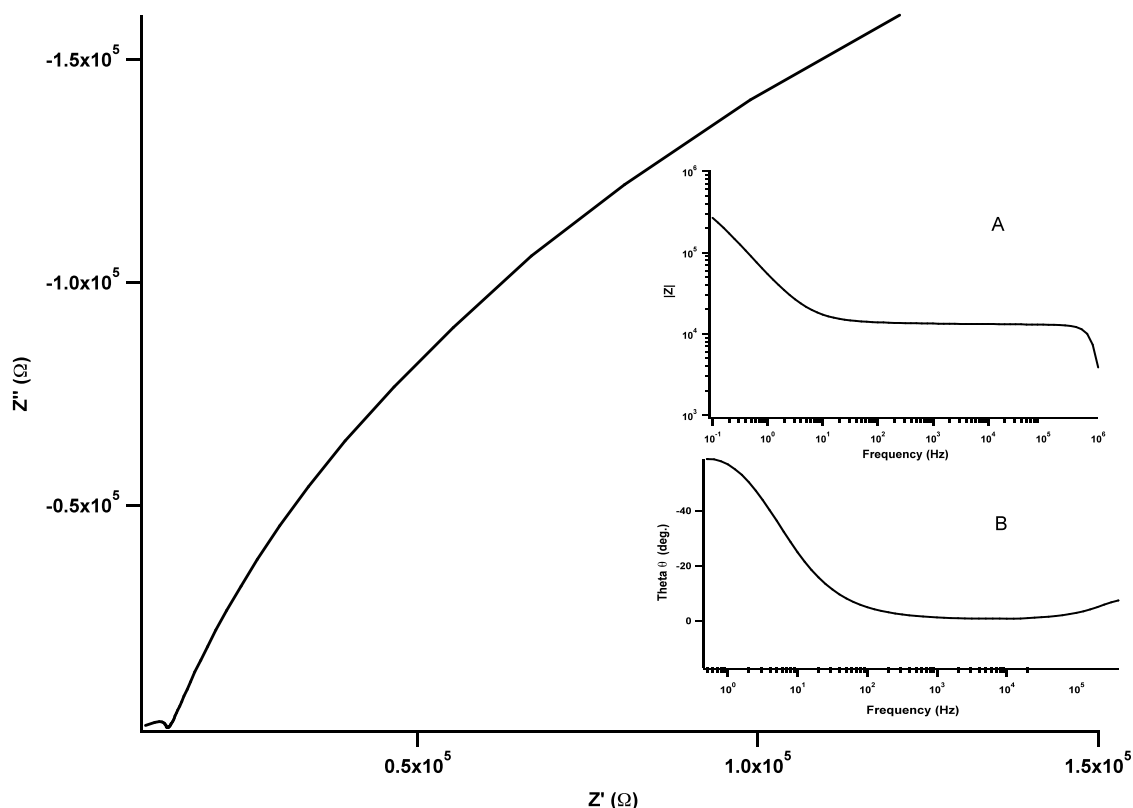


Figure 3.3 Cole-Cole plot at room temperature for MS-5_{4C}. Inset A and B show corresponding magnitude and phase of the impedance vs. frequency plots.

DC conductivities, σ_{DC} were calculated from resistance values by applying $\sigma_{DC} = l / RS$ where l represents the thickness of the pellet, S is the cross-sectional area of the pellet (i.e. the electrode area), and R is the resistance of the composite membrane. The insets in Figure 3.3 (A and B) show the magnitude and phase of the impedance as a function of frequency. The minimum in the phase curve corresponds to the intercept of the semicircular arc in the Cole-Cole plot (Figure 3.3) with the real axis. The resistance was obtained by extrapolating the Cole-Cole plots to the real axis. This point represents the frequency-independent plateau in the absolute impedance vs. frequency plot (Figure 3.3A), which

corresponds to DC conductivity, σ_{DC} in the sample. Frequency independence occurs when the rate of change of electric field is in resonance with ion (proton) motion through the sample. The low-frequency tail is generally attributed to the accumulation of charge at the contacts.

The values obtained from the proton conductivity measurements represent a bulk value, which includes proton conductivity through the cylindrical pores, as well as the conductivity between each particle (i.e. grain boundary effects). Since the samples were fully hydrated and compressed into pellets prior to the measurements, proton motion between the grains must occur via bulk water.

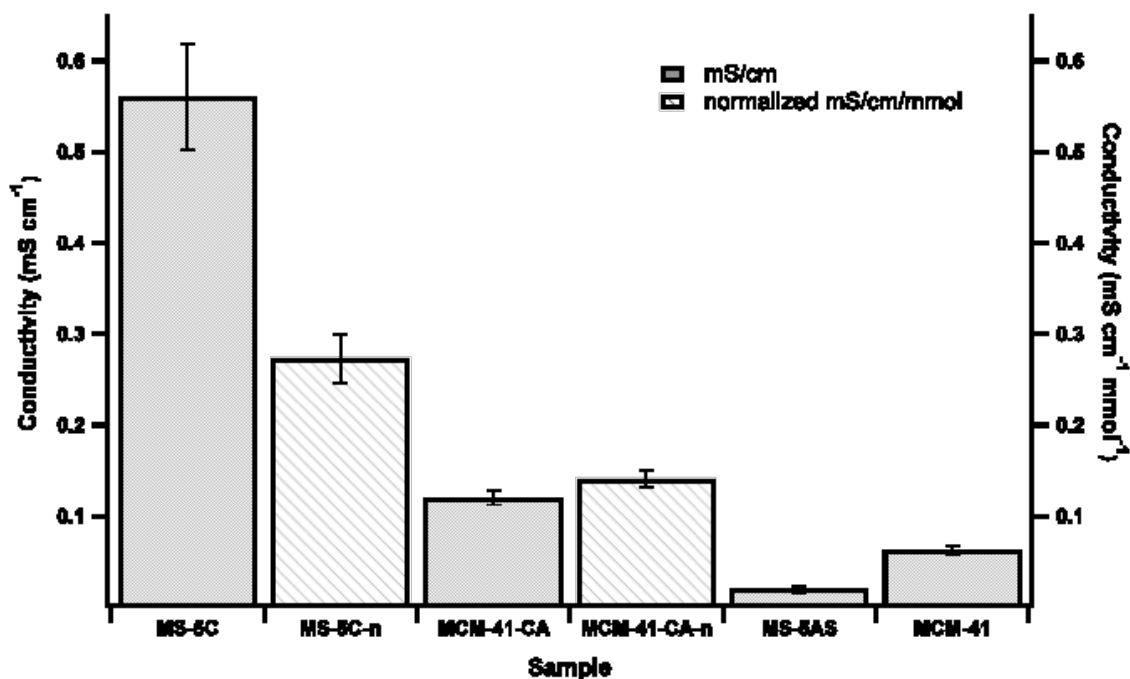


Figure 3.4 Proton conductivity of MS-5_{4C}, MCM-41-CA absolute and normalized values, MS-5_{4AS}, and MCM-41.

MS-5_{4C} gave a room temperature conductivity of $\sim 0.6 \text{ mS cm}^{-1}$, which is an order of magnitude higher than unmodified mesoporous MCM-41 and the nonporous as-synthesized silicate, MS-5_{4AS}. This result illustrates the importance of the acid groups in promoting

proton conductivity. Mesoporous MCM-41 without any organic modification conducts protons via residual surface silanol groups, which are known to be weakly acidic. The threefold difference between the MCM-41 and MS-5_{4AS} implies that the silanols on the interior pore surface play a large role towards facilitating proton conductivity. This is expected because the bulk surface area of mesoporous silicates is located within their pores.

MCM-41-CA gave a fivefold decrease in conductivity when compared to MS-5_{4C}, which is mainly due to its lower acid capacity. However, when the conductivities are normalized with respect to acid content, the conductivity of MCM-41-CA is still almost twofold lower than that of MS-5_{4C}. This shows that conductivity is not simply a linear function of organic acid content.

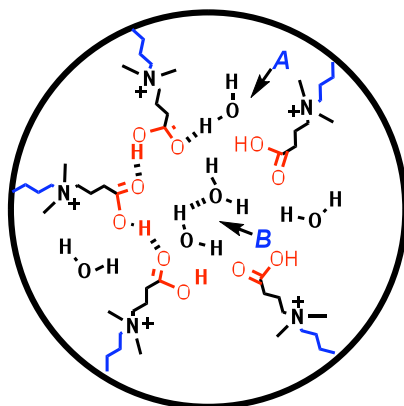


Figure 3.5 A representative slice of the distribution of water molecules within the pores of MS-5_{4C}

In MS-5_{4C} depicted in Figure 3.5, three distinct aqueous environments can be distinguished. The water near the carboxylic acid groups will be termed “surface water” (region A), while water between bulk particles, i.e., grains (not shown), or within the pores (one or two monolayers away from the acid surface layer) will be known as “bulk water” (region B). Proton mobility near the surface in region A is dependent on structural diffusion mediated by water across the carboxylic acid groups. This surface structural diffusion is

known to be slow¹⁵ due to the strong electrostatic attraction between the carboxylate group and the hydronium ion. In addition, reorientation of tethered carboxylic acid groups after proton transfer will be very slow. Since acidified bulk water undergoes fast proton transport via structural (Grotthuss) diffusion through a percolated water network, the factors that affect the conductivity of these silicates are the hydronium ion concentration and the extent of water percolation through the sample. The latter is dependent on the particle size of the silicates, which we can assume to be similar in all the materials (micron-sized amorphous particles via SEM). As a result, proton mobility in the bulk water region, i.e., between the grains and in the narrow pore structure if any, should be dependent on concentration of hydronium ions in solution.

Thus, the observed nonlinearity between MS-5_{4C} and MCM-41-CA could be due to a decrease in the acid dissociation constant (pKa) of the carboxylic acids in MS-5_{4C} brought about by hydrogen bonding between neighboring acid groups as a result of the high organic density in MS-5_{4C}. Lowering the pKa of these acid groups by proximity-induced hydrogen bonding can increase the hydronium ion concentration and lead to the higher observed conductivities in MS-5_{4C} even after normalizing the conductivities with organic acid content.

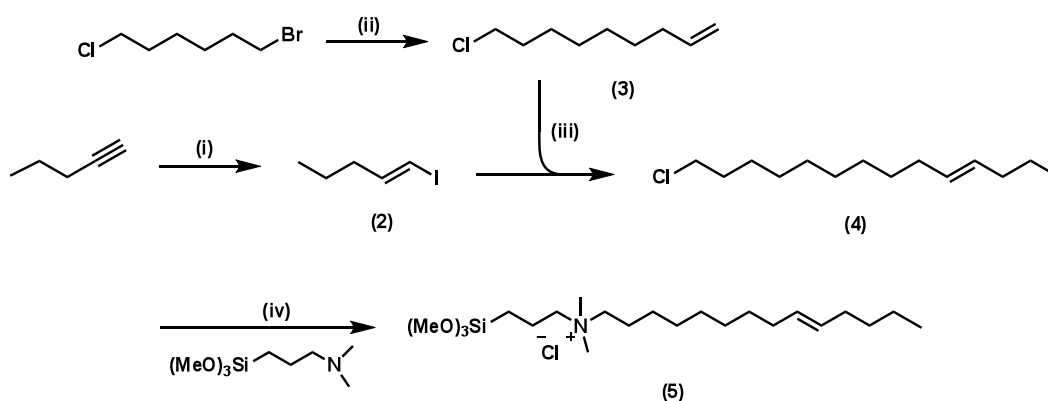
3.3.2 Effect of hydrophobicity on proton conductivity

It has been reported that the membrane selectivity (proton conductivity-to-methanol permeability ratio) can be increased by increasing the amount of acid groups while simultaneously increasing hydrophobicity.¹⁶ Thus, in this study, we varied the hydrophobicity of our organosilicates and investigated the effect on proton conductivity. We

changed the hydrophobicity in the pore structure by systematically increasing the length of the organic acid occluded within the pores of the silicate. This was achieved by moving the cleavable olefin unit within the hydrophobic surfactant tail from the C-4 position to the C-10 and C-13 positions, while keeping the overall surfactant chain length constant. Cleavage of the resulting olefins after silicate assembly led to the desired carboxylic acid-modified silicates.

3.3.2.1 Synthesis of C₁₀-(*E*) and C₁₃-olefin surfactants

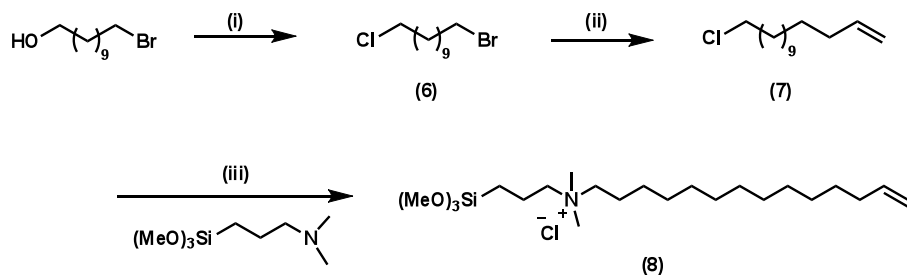
Following the success of the Suzuki coupling reaction (Chapter II, Scheme 2.2), we adopted a similar approach for the synthesis of the C₁₀ surfactant bearing an olefin group between the C₁₀ and C₁₁ carbons. Synthesis of C₁₀ surfactant is outlined below in Scheme 3.2.



Scheme 3.2 Synthesis of (5); (i) a. catecholborane, neat, 70 °C, 2 h, b. H₂O, 1 hr, r.t, c. iodine, NaOH, ether, 0°C, 0.5 h; (ii) allylmagnesium chloride, THF, r.t, 2.5 h; (iii) a. (3), 0.5 M 9-BBN in THF, 0°C to r.t, 6 h, b. PdCl₂(dppf), NaOH, reflux, 16 h; (iv) (4), MeOH, reflux, 72 h

Hydroboration of 1-pentyne followed by hydrolysis of the resulting catchol ester gave the pent-1-enylboronic acid, which was converted to the *trans*-pent-1-enyl iodide (**2**) in high stereochemical purity in the presence of iodine and aqueous sodium hydroxide at 0°C. Substitution of the bromide group on 1-Bromo-6-chlorohexane with allylmagnesium gave (**3**) in moderate yields. Subsequent hydroboration of (**3**) with 9-BBN followed by cross coupling with (**2**) in the presence of PdCl₂(dppf) and sodium hydroxide afforded (**4**) in good yield. The ¹H NMR of the product obtained confirmed the structure of (**4**) but the double bond splitting pattern was too broad to give any information about the geometry of the olefin. Quaternization of (**4**) with *N,N*-dimethylaminopropyl trimethoxysilane gave the desired product (**5**) in 50% yield.

The C₁₃ surfactant was designed as the limiting case where the full surfactant is occluded within the pores of the silicate while bearing the proton conductive acid group.



Scheme 3.3 Synthesis of (**8**); (i) thionyl chloride, pyridine, benzene, 80°C, 6 h; (ii) allylmagnesium chloride, THF, r.t., 2.5 h; (iii) (**7**), MeOH, reflux, 84 h

Synthesis of the terminal olefin surfactant began with the chlorination of 1-bromo-undecanol with thionyl chloride to give (**6**) followed by a reaction with allylmagnesium chloride to give the terminal olefin precursor (**7**) in good yield. Subsequent quaternization of (**7**) with *N,N*-dimethylaminopropyl trimethoxysilane gave the desired surfactant (**8**) in 55% yield.

3.3.2.2 Preparation of MS-5_{10AS} and MS-5_{13AS}

Both surfactants (**5**) and (**8**) were subjected to alkaline hydrothermal synthesis with TEOS as the primary silica source at a sol-gel composition similar to that used for MS-5_{4AS} i.e., 1 SiO₂: 0.4 (**5**): 0.4 TMAOH: 80 H₂O. After ageing at 100°C for 24 hrs, the resulting white precipitates were washed, dried, and analyzed via X-ray diffraction.

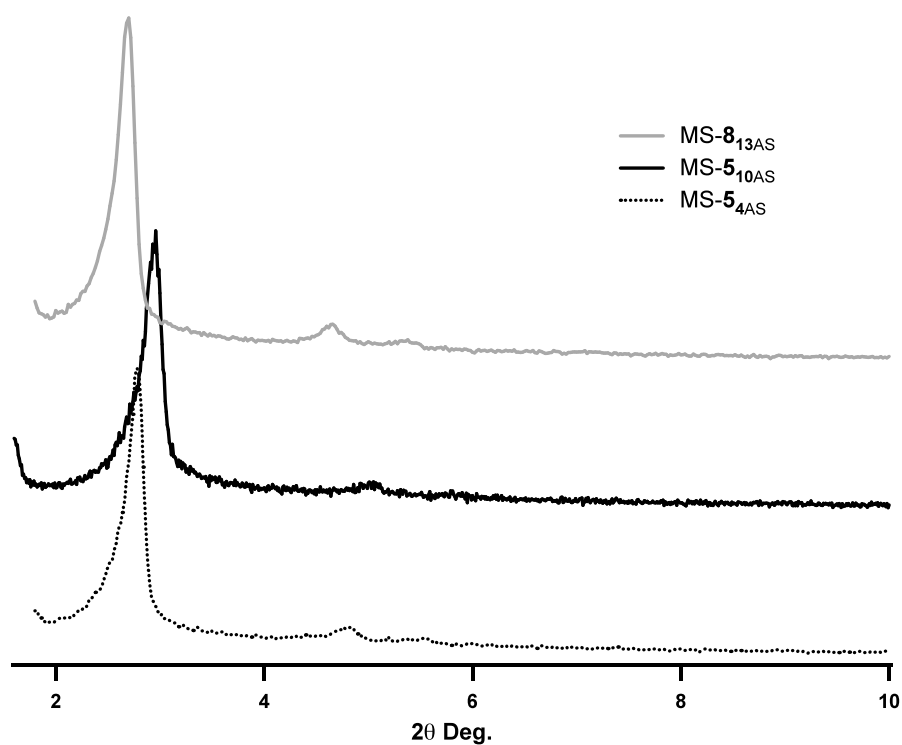


Figure 3.6 X-ray powder diffraction pattern of MS-5_{4AS}, MS-5_{10AS}, and MS-8_{13AS}.

The X-ray powder diffraction pattern in Figure 3.6 confirms the formation of MCM-41 by both C₁₀ and C₁₃ surfactants, i.e., (**5**) and (**8**), similar to the C₄ surfactant in Chapter II (also shown in Figure 3.6 for comparison). The diffraction patterns of the MS-5_{4AS} and MS-8_{13AS} silicates gave a similar d_{100} spacing at 32 and 33 Å, respectively. The MS-5_{10AS} silicate showed a slight shift in all its reflections towards higher angles with a d_{100} spacing of 30 Å,

indicative of pore shrinkage. However, the diffraction patterns of all three silicates revealed three peaks in the low angle diffraction regime corresponding to the well-ordered two-dimensional hexagonal structure of MCM-41. Structural details of the encapsulated functional surfactants in the as-synthesized silicates were examined by solid-state ^{13}C and ^{29}Si CP MAS NMR (Figure 3.7).

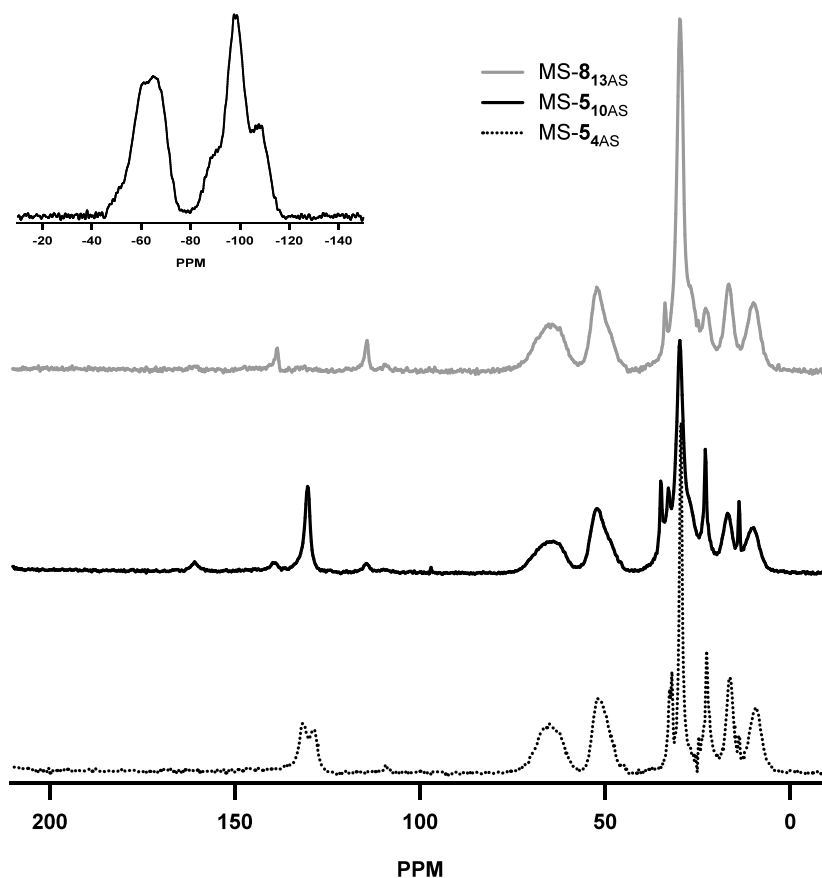


Figure 3.7 ^{13}C CP MAS NMR spectra of MS-**5**_{4AS}, MS-**5**_{10AS}, and MS-**8**_{13AS}. Inset shows a representative ^{29}Si CP MAS NMR of MS-**8**_{13AS}.

The chemical shifts for all the surfactants are dominated by a strong resonance at 30 ppm attributed to the methylene carbons on the surfactant tail. The solid-state ^{13}C CP MAS NMR of all the as-synthesized silicates were identical to their respective liquid-state ^{13}C NMRs (not shown, signals in experimental section) thus verifying the stability of all the

surfactants to the alkaline hydrothermal conditions. A representative ^{29}Si CP MAS NMR spectrum (Figure 3.7 insert) displays the typical T-type organosilica resonance confirming organic attachment to the silicate walls.

3.3.2.3 Preparation of MS-5_{10C} and MS-8_{13C}

Ozonolysis of the composite MCM-41 hybrids was carried out by bubbling ozone through a solution of the hybrid material for 7 hours. Subsequent oxidation with formic acid and hydrogen peroxide followed by a 1 N HCl post treatment gave the corresponding carboxylic acids (Figure 3.8).

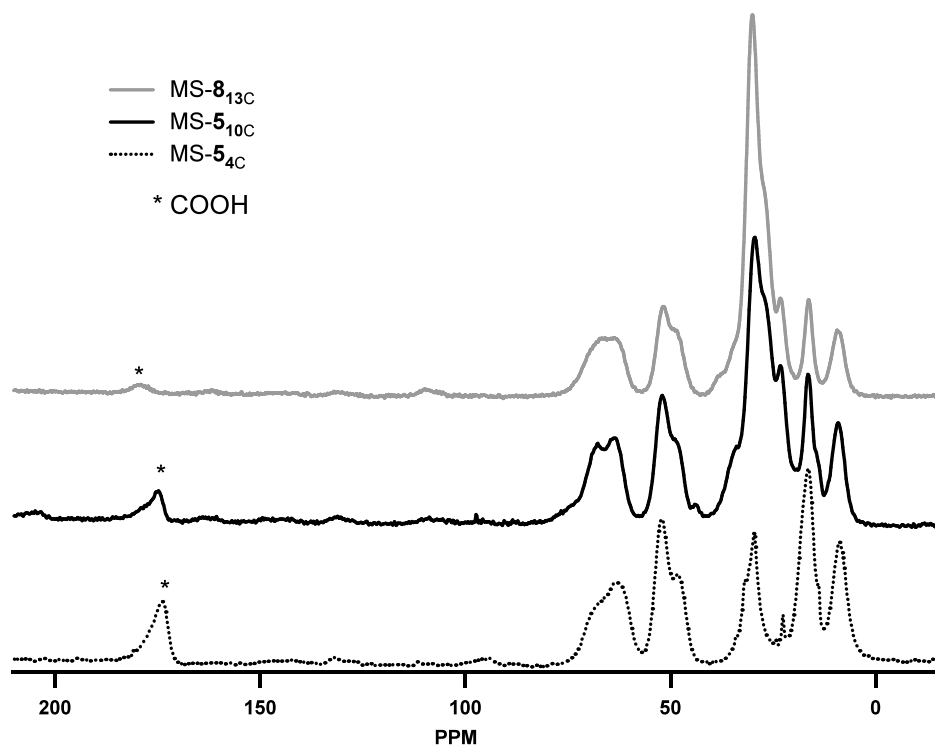


Figure 3.8 ^{13}C CP MAS NMR spectra of MS-5_{4C}, MS-5_{10C}, and MS-8_{13C}

The intensity of the 30 ppm peak corresponding to the surfactant tail increases as we move from MS-**5**_{4C} to MS-**8**_{13C} as expected, due to the elimination of shorter segments from the tail end. The absence of the double bond peaks of the starting materials confirmed complete cleavage of the olefin bonds via ozonolysis. The carboxylic acid carbon peaks appear at 174, 175, and 180 ppm for the MS-**5**_{4C}, MS-**5**_{10C}, and MS-**8**_{13C}, respectively. The broadening of the carboxylic acid carbon with increasing organic chain length is due to two factors. First, an increase in the organic chain length leads to a decrease in molecular motion causing an increase in the chemical shift distribution due to a variety of local conformations. The second factor is due to broadening arising from the ¹³C-¹H dipolar interaction which is typically removed by high-power decoupling. However, when reorientation rate of the nuclei is comparable to the frequency of the proton decoupling field, the decoupling efficiency is reduced and the linewidth broadens. Both these factors are more pronounced with the carboxylic acid carbon due to its slower rate of relaxation.

The organic loading of MS-**5**_{10C} and MS-**8**_{13C} determined by TGA was 1.7, and 1.5 mmol/g (i.e., mmol of organic per gram of composite material), respectively. The organic loading previously reported for MS-**5**_{4C} was 2.2 mmol/g. The differences in organic loading reflect the differences in the molecular weight of the organic groups and differences in the amount of silica incorporated. However, the acid loading as determined by back titration was 2.1 meqH⁺/g for all three silicates.

3.3.2.4 Effect of organic chain length on proton conductivity

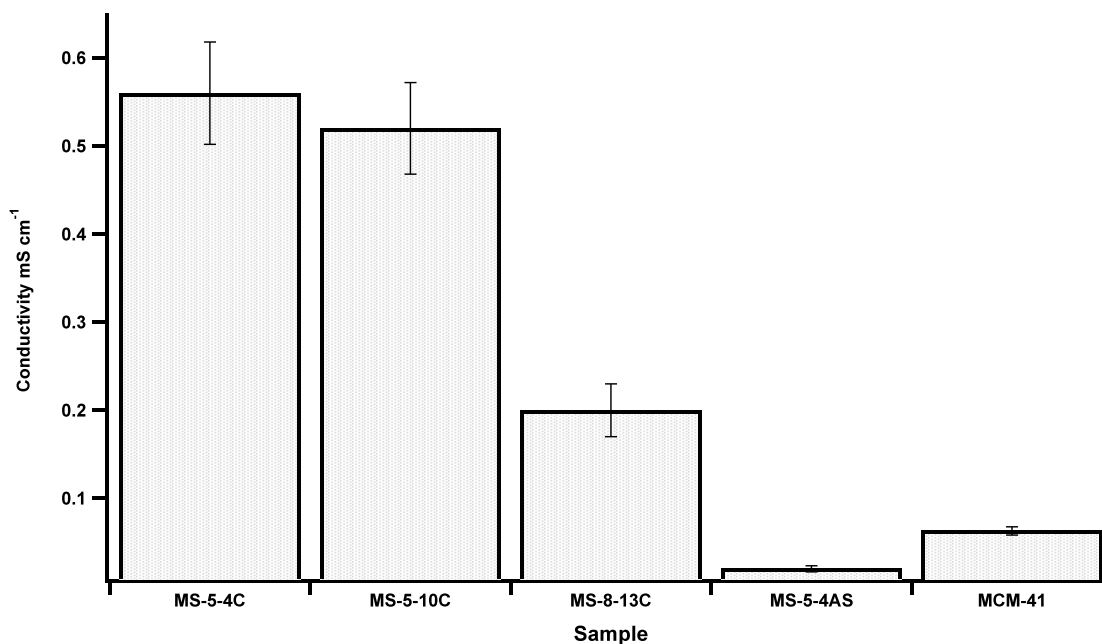


Figure 3.9 Proton conductivity of MS-5_{4C}, MS-5_{10C}, MS-8_{13C}, MS-5_{4AS}, and MCM-41 at room temperature under fully hydrated conditions

Under fully hydrated conditions, the conductivities appear to decrease as we increase the surfactant tail length in the pores from MS-5_{4C} to MS-8_{13C} (Figure 3.9). Since all three carboxylic acid-bearing silicates have similar acid contents (2.1 meqH⁺/g via back titration) and particle sizes, the decrease in conductivity is likely due to the exclusion of water within the pore structure. Lack of a continuous water network within the pore structure can cause a deviation in the pathway for proton transport. The exclusion of water within the pores should increase with hydrophobicity and lead to lower conductivities, as observed with MS-5_{4C}, MS-5_{10C}, and MS-8_{13C} in Figure 3.9. Another possible explanation for the decrease in conductivity with organic chain length could be the inability of the carboxylic acids to form well-defined hydrogen bonds (and thus lower pK_as are not achieved) due to surfactant crowding. The ability to maintain proton conductivity while increasing hydrophobicity will be important to

maintaining good selectivity in membranes for DMFC applications. From Figure 3.9, we see that the addition of an extra six methylene groups, i.e., MS-**5**_{10C} vs. MS-**5**_{4C}, does not significantly alter the proton conductive pathway in these solids. Thus, the detrimental effect of hydrophobicity on proton conductivity does not fully materialize for chain lengths below C-10. This is similar to the silicate surfactant assembly process whereby supramolecular assembly of mesoporous silica typically does not take place with surfactant chain lengths below C-10. When the as-synthesized material MS-**5**_{4AS} is compared to MS-**8**_{13C}, the conductivity increases by an order of magnitude, while unmodified MCM-41 gives only a meager 1.5-fold increase in conductivity relative to MS-**5**_{4AS}. The larger difference in the former relative to the later highlights the importance of the carboxylic acid group modification over silanols-to-proton conductivity.

3.3.3 Effect of temperature and water content

To further probe the proton transfer mechanism, we carried out temperature-dependent conductivity experiments. These measurements were carried out both under fully hydrated and dry conditions.

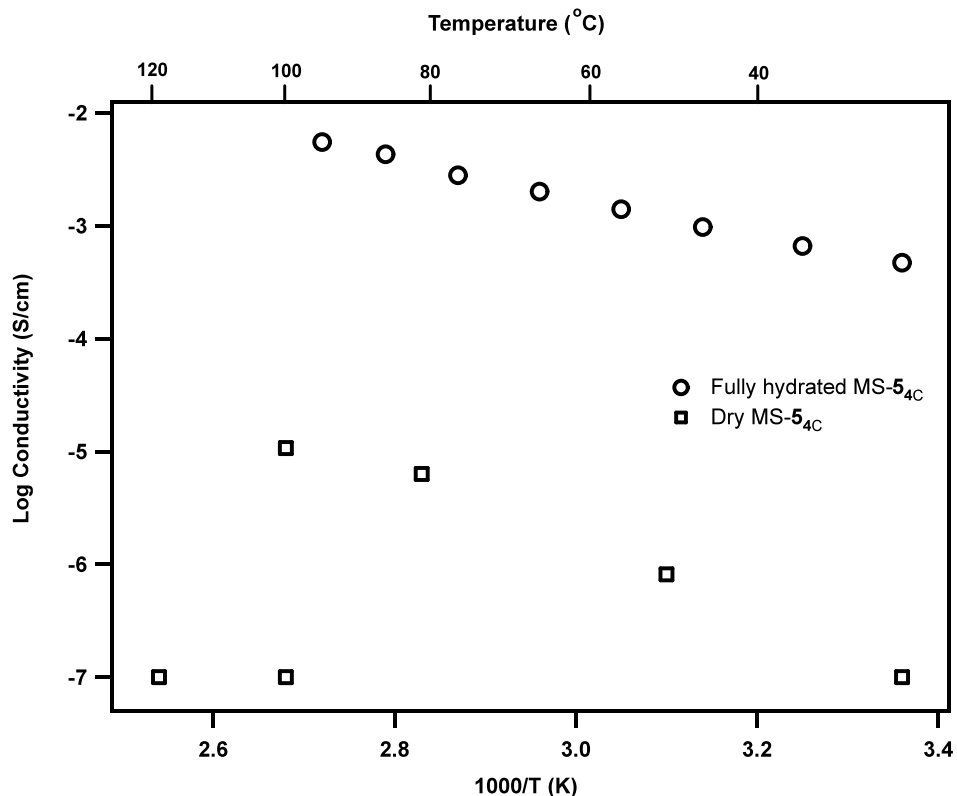


Figure 3.10 Arrhenius plot of proton conductivity of MS-5_{4C} as a function of temperature for fully hydrated and nonhydrated solids

The proton conductivity of MS-5_{4C} increased with increasing temperature under fully hydrated conditions and showed an Arrhenius-type temperature dependence (Figure 3.10). The activation energy (E_a) determined from the Arrhenius plot was 14.2 kJ/mol (0.15 eV). According to this value, proton migration is dominated by structural diffusion as expected, seeing that the activation energy for conduction via this mechanism has been found to be between 0.14-0.4 eV.¹⁷

However, under nonhydrated conditions, the conductivity decreases by more than three orders of magnitude. This supports the proposed pathway of proton motion via a percolated water network. In the absence of this network, proton conductivity is drastically reduced. The residual conductivity observed could be due to proton hopping along carboxylic

acid groups mediated by surface silanols and some residual bound water to the silica surface. Upon further heating and complete dehydration, the conductivity plummets below the measurement range of the potentiostat. Thus, although these types of materials may be advantageous for use in fully hydrated DMFCs, they still suffer from a dependence on water, which makes them inactive at intermediate temperatures similar to Nafion.

3.4 Further discussion and conclusion

In this chapter, we have examined how the certain properties of our organically modified mesostructured silicates, such as organic acid density and hydrophobicity, affect proton transport under fully hydrated conditions. With our new approach to organosilicate synthesis via polymerizable surfactant assembly and cleavage, we have been successful in the preparation of materials that display unusually high surface loadings of organic groups within the interior pore space of the organosilicate. When compared to the traditional post-synthetically grafted silicates with lower organic loadings (0.85 mmol/g), we observe a conductivity enhancement due to a higher acid capacity. We also observe an additional two-fold increase after normalization with organic acid content. The latter is believed to be the result of an increase in the acid dissociation constant of the carboxylic acid groups due to hydrogen bonding of proximal carboxylic acid groups. This proximity is the result of tight surfactant packing during assembly of the as-synthesized organosilicates.

With regards to our investigation into the effects of hydrophobicity, we synthesized three carboxylic acid-modified silicates differing by the length of their organic segment via systematically varying the olefin position within their surfactant tail. From their room-temperature conductivities, we observed that the negative effects of hydrophobicity, judged

by the length of the residual organic chain occluded in the silicate, only sets in beyond the C-10 silicate, i.e., MS-5_{10C}. This knowledge can be used to potentially improve selectivities in membranes for DMFC applications employing organosilicates with similar-length ammonium organic acids. Although the conductivities of these carboxylic acid modified organosilicates do not match up to those of Nafion-bearing strong sulfonic acid groups, the introduction of this new concept of modification should be amenable to any acid group that can be masked within a surfactant backbone. The combination of this technique, which yields high organic density silicates with strong acid groups, should lead to highly proton-conductive membranes under fully humidified conditions.

To elucidate the mechanism of proton transport, we followed proton conductivity as a function of temperature under fully hydrated conditions. The results were plotted with an Arrhenius equation and an activation energy of 0.15 eV was obtained, indicating structural diffusion as the dominant conduction mechanism. When dehydrated, the conductivity decreased drastically below the measurement range of the instrument, thus confirming the occurrence of structural diffusion via the percolated water network. Thus, although these types of materials maybe advantageous for use in fully hydrated DMFCs, they still suffer from a dependence on water, which makes them inactive at intermediate temperatures similar to Nafion. This observation prompted our investigation into the nature and types of solid state protogenic groups that can facilitate proton transport in the absence of water.

3.5 Experimental:

Materials

All silane reagents were purchased from Gelest and used as received. All other reagents were purchased from Sigma-Aldrich or TCI organics and used as received, except for pent-1-yne which was distilled prior to use. All reactions were run under an inert argon atmosphere. All solvents were purified by fractional distillation from the appropriate drying agents or dried by filtration through the appropriate drying agents prior to use.

Compound (1)

N,N-dimethylaminopropyltrimethoxysilane (38.4 mmol, 7.97 g) was added to a solution of 6-chlorohex-2-ene (40 mmol, 4.78 g) stirring in methanol (8 mL) in a round-bottom flask purged with argon. The mixture was heated to reflux at 95°C for 3 days. The mixture was then concentrated under vacuum, washed twice with hexanes and then further dried under vacuum to give (1) in 60% yield.

(*E*)-1-iodopent-1-ene (2)

1-Pentyne (228 mmol, 15.6 g) and catecholborane (228 mmol, 27.4 g) were added to a 2-neck flask, purged with argon and heated to 70°C. After 2 hours of heating, the reaction was cooled, quenched with water, and stirred vigorously for an additional hour. The resulting white precipitate was filtered over a fritted funnel and dried to give the (*E*)-pent-1-enylboronic acid, which was used without further purification. (83.3 mmol, 9.5 g) of the (*E*)-pent-1-enylboronic acid was added to 120 mL of ether and cooled to 0°C. To this solution was added 120 mL of a 3 N NaOH solution and iodine (100 mmol, 25.4 g) in 340 mL ether.

The mixture was stirred at 0°C for 30 minutes, after which a thiosulfate solution was added until the iodine layer was visibly removed (i.e., dark layer solution became clear). The ether layer was removed and washed with water concentrated to give the desired product in 18 % overall yield.

9-Chloronon-1-ene (3)

To a solution of allylmagnesium chloride (200 mmols, 100 mL, 2M in THF) was added 1-bromo-6-chlorohexane (66.7 mmol, 13.3 g) in 125 mL of THF. The mixture was stirred at room temperature for 2 hours and 45 minutes, after which it was quenched with 100 mL of 1 N HCl. The entire solution was diluted with 120 mL of ether and subsequently washed with sodium bicarbonate and brine. The organic layer was dried over MgSO₄, concentrated, and distilled at 80°C/0.2 torr to give the desired product in 38% yield.

(E)-14-chlorotetradec-4-ene (4)

To a flame-dried flask under argon was added 9-chloronon-1-ene (**3**) (25 mmol, 4 g) and dry THF (50 mL). 9-borabicyclo[3.3.1] nonane (9-BBN) (0.5 M in THF, 25 mmol, 25 mL) was slowly added to this mixture at 0°C and slowly warmed up to room temperature. After stirring for 7 hours, (*E*)-1-iodopent-1-ene (**2**) (25 mmol, 4.9 mg), [1,1'-bis(diphenylphosphino)-ferrocene]dichloropalladium (II) complex with dichloromethane (1:1) (3 mol%, 612 mg), sodium hydroxide (50 mmol, 16.7 mL), and additional THF (50 mL) were added. The mixture was refluxed for 16 hours under vigorous stirring. The resulting dark mixture was diluted with hexanes (130 mL), washed with brine, and dried over

magnesium sulfate. The crude mixture was purified over a column with hexanes to give desired product (**4**) in 25% yield.

Compound (5)

N,N-dimethylaminotrimethoxysilane (5.24 mmol, 1.09 g), (*E*)-14-chlorotetradec-4-ene (**4**) (5.5 mmol, 1.27 g) and methanol (4 mL) were placed under argon in a round-bottom flask and refluxed at 90°C for 84 hours. The reaction was cooled to room temperature and the methanol removed under reduced pressure. The resulting product was washed with cold hexanes and dried overnight to give the desired product in 50 % yield. ¹H NMR (300 MHz, CDCl₃) δ 5.33 (dt, *J* = 13.5, 6.0, 2H), 3.59 – 3.50 (m, 9H), 3.44 – 3.40 (m, 2H), 3.36 (s, 6H), 3.30 (m, 2H), 1.90 (m, *J* = 11.1, 4H), 1.83 – 1.56 (m, 4H), 1.43 – 1.15 (m, 14H), 0.92 – 0.78 (t, 3H), 0.64 (t, *J* = 7.8, 2H). ¹³C NMR (75 MHz, CDCl₃) δ 130.64, 130.35, 65.36, 63.97, 51.48, 50.95, 50.49, 45.41, 34.89, 32.77, 29.78, 29.60, 29.51, 29.41, 29.31, 29.24, 29.06, 27.06, 26.55, 26.45, 22.92, 22.84, 16.64, 13.85.

1-bromo-11-chloroundecane (6)

11-bromoundecan-1-ol (2.4 mmol, 0.6 g) was added to 10 mL of benzene and pyridine (3.82 mmol, 0.31 mL) and heated to 60°C under argon. After 30 minutes, thionyl chloride (3.82 mmol, 0.28 mL) was added dropwise and the entire mixture was heated at 80°C for six hours. The mixture was cooled to room temperature, slowly quenched with cold water, and extracted with ethyl acetate. The organic layer was washed with brine and sodium bicarbonate, dried over sodium sulfate, and concentrated. The desired product was isolated after flash chromatography (hexanes/CHCl₃, 5:1) in 70% yield.

14-chlorotetradec-1-ene (7)

To a solution of allylmagnesium chloride (3 mmol, 1.5 mL, 2.0 M in THF) was added 1-bromo-11-chloroundecane (**6**) (1 mmol, 269.6 mg) in 2 mL of THF. The resulting solution was stirred at room temperature for 2 hours and 30 minutes, after which the reaction was quenched slowly with 1N HCl. The quenched reaction was diluted with ether, washed with sodium bicarbonate and brine, and dried over sodium sulfate. The desired product was isolated via flash chromatography (Hexanes) in 60 % yield.

Compound (8)

N,N-dimethylaminoltrimethoxysilane (20.6 mmol, 4.27 g), 14-chlorotetradec-1-ene (**7**) (21.7 mmol, 5 g) and methanol (10 mL) were placed under argon in a round-bottom flask and refluxed at 90°C for 72 hours. The reaction was cooled to room temperature and the methanol removed under reduced pressure. The resulting product was washed with cold hexanes and dried overnight to give the desired product in 43 % yield. ¹H NMR (300 MHz, CDCl₃) δ 5.76 (ddt, *J* = 16.9, 10.1, 6.7, 1H), 5.03 – 4.80 (m, 2H), 3.61 – 3.48 (m, 9H), 3.47 – 3.43 (m, 4H), 3.43 – 3.31 (m, 6H), 1.99 (q, 2H), 1.77 (dt, 2H), 1.67 (d, 2H), 1.25 (m, 18H), 0.64 (t, 2H). ¹³C NMR (75 MHz, CDCl₃) δ 139.42, 114.28, 65.16, 63.74, 51.44, 50.95, 50.78, 34.00, 29.74, 29.66, 29.56, 29.44, 29.32, 29.11, 26.48, 22.88, 16.65, 5.75.

Post synthetic Graft of (1) on MCM-41 and ozonolysis

Compound (1) (1.84 mmol, 0.6 g) was dissolved in toluene (90 mL) and added to calcined mesoporous MCM-41. The mixture was heated to reflux for 24 hours under vigorous stirring. After cooling down to room temperature, the mixture was filtered, washed with acetone, and extracted using a soxhlet apparatus in dichloromethane overnight. The resulting powder was then dried overnight.

Ozonolysis was carried out by bubbling ozone (84 $\mu\text{g/mL}$) through a suspension of the grafted MCM-41 (1 g) material in dichloromethane (60 mL) at -78°C . After 7 hours, the solution was purged with argon while warming to room temperature, filtered, and washed with acetone and water. Oxidation of the ozone-treated solid was carried out with formic acid (5 mL) and hydrogen peroxide (2.5 mL) in water (2.5 mL) at 50°C for 1 hour, followed by a 1N hydrochloric acid (10 mL) post treatment for another hour to give the corresponding carboxylic acid groups. The solids were then washed with acidic ethanol at 50°C to remove any adsorbed species.

Electrochemical Impedance Spectroscopy

Electrochemical impedance was measured in the frequency range from 1 Hz to 1 MHz at an A.C. measuring voltage of 100 mV with a potentiostat/galvanostat and frequency response analyzer (Solatron 1287/1260). The setup used for the proton conductivity measurements is shown in Figure S3.1. The measurements were performed by sandwiching the sample in the sample holder (made of Torlon plastic) between two Pt/Ir (80:20) electrodes. Measurements were made initially under 100% R.H. at room temperature and then also at variable

temperature. The temperature range between 25°C and 95°C was explored by using a digital temperature controller (Watlow) hooked up to Kapton heaters sandwiched between brass coolers and the main brass block as shown in Figure S-1. The temperature was measured with an accuracy greater than $\pm 0.1^\circ\text{C}$. The membrane conductivity was calculated using [3.1]

$$\sigma = l/RS \quad [3.1]$$

where σ is the ionic conductivity, l the distance between the two electrodes (i.e. the thickness of the pellet) measured with a digital micrometer at a constant torque of 46 inch-ounce, R is the resistance of the membrane, and S the cross-sectional area of the pellet (i.e., the electrode area).

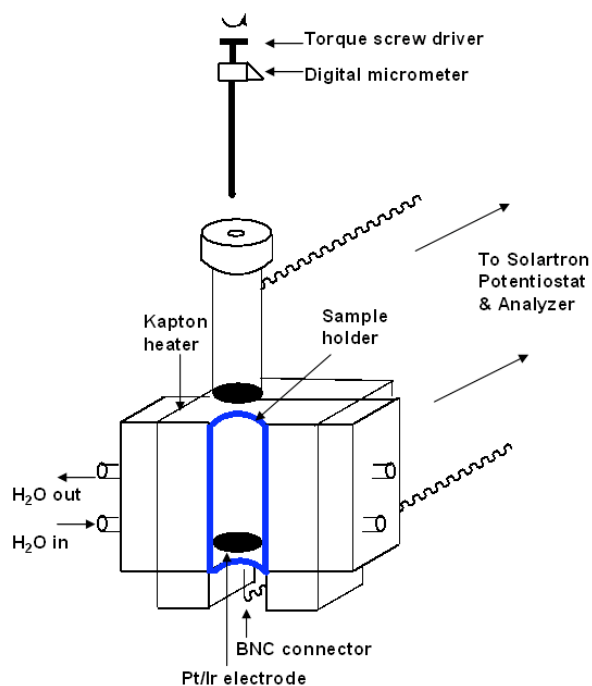


Figure S-3.1 Hydrated conductivity setup

3.6 References:

1. Roziere, J.; Jones, D. J., *Annual Review of Materials Research* **2003**, 33, 503-555.
2. Ren, X. M.; Springer, T. E.; Zawodzinski, T. A.; Gottesfeld, S., *Journal of the Electrochemical Society* **2000**, 147, (2), 466-474.
3. Verbrugge, M. W., *Journal of the Electrochemical Society* **1989**, 136, (2), 417-423.
4. Costamagna, P.; Yang, C.; Bocarsly, A. B.; Srinivasan, S., *Electrochimica Acta* **2002**, 47, (7), 1023-1033.
5. Alberti, G.; Casciola, M., *Annual Review of Materials Research* **2003**, 33, 129-154.
6. Yin, Y.; Fang, J. H.; Cui, Y. F.; Tanaka, K.; Kita, H.; Okamoto, K., *Polymer* **2003**, 44, (16), 4509-4518.
7. Kreuer, K. D., *Journal of Membrane Science* **2001**, 185, (1), 29-39.
8. Chang, H. Y.; Lin, C. W., *Journal of Membrane Science* **2003**, 218, (1-2), 295-306.
9. Shao, Z. G.; Joghee, P.; Hsing, I. M., *Journal of Membrane Science* **2004**, 229, (1-2), 43-51.
10. Alabi, C. A.; Davis, M. E., *Chemistry of Materials* **2006**, 18, (24), 5634-5636.
11. Chen, S. L.; Xu, K. Q.; Dong, P., *Chemistry of Materials* **2005**, 17, (24), 5880-5883.
12. Hamoudi, S.; Kaliaguine, S., *Microporous and Mesoporous Materials* **2003**, 59, (2-3), 195-204.
13. Holmberg, B. A.; Hwang, S. J.; Davis, M. E.; Yan, Y. S., *Microporous and Mesoporous Materials* **2005**, 80, (1-3), 347-356.
14. Karthikeyan, C. S.; Nunes, S. P.; Prado, L. A. S. A.; Ponce, M. L.; Silva, H.; Ruffmann, B.; Schulte, K., *Journal of Membrane Science* **2005**, 254, (1-2), 139-146.

15. Choi, P.; Jalani, N. H.; Datta, R., *Journal of the Electrochemical Society* **2005**, 152, (3), E123-E130.
16. Park, J. W.; Kim, Y. C.; Jeong, Y. J.; Kim, S. D.; Ha, H. Y.; Kim, W. J., *Microporous and Mesoporous Materials* **2008**, 114, (1-3), 238-249.
17. Colomban P, N. A., *Proton Conductors: Solids, Membranes, and Gels--materials and Devices*. Illustrated ed.; Cambridge University Press: Cambridge, 1992; p 38-55, 384-387.

Chapter IV

**Insights into the Nature of Synergistic Effects in Proton Conducting 4,4-
1*H*,1*H*-Bitriazole-Poly(ethylene oxide) Composites**

4.1 Abstract

We have designed a new nitrogen containing heterocycle (NCH), 4,4-*1H-1H*-bi-1,2,3-triazole (bitriazole) capable of mimicking water in the solid state and investigated its ability to conduct protons in the presence of poly(ethylene oxides) under anhydrous conditions. Bitriazole is shown to have sufficient thermal and electrochemical stability for fuel cell applications. The composites formed between bitriazole and poly(ethylene oxides) show a Vogel-Tamman-Fulcher (VTF) behavior suggestive of coupling between polymer segmental motion and ion transport. Our results confirm the bitriazole N-*H* proton to be the source of conductivity and reveals that both bitriazole and poly(ethylene oxides) work synergistically, through specific intermolecular interactions and polymer-induced segmental motion, to create a pathway proton transport via structural diffusion.

4.2 Introduction

Proton conductors are a special class of solid electrolytes that conduct hydrogen ions via several transport mechanisms, such as structural diffusion, vehicular transport, and tunneling. These solid electrolytes are an essential part of several devices such as sensors, batteries, and fuel cells. The operation and full-scale commercialization of the latter, in particular, the hydrogen fuel cell, hinges on the development of low-cost proton conductors that can operate at both low and intermediate temperatures (up to 150 °C) under dry (non-humidified) conditions with high conductivities. The current solid electrolyte membranes such as Nafion™ and other acidic polymers are based on incorporation of strong hydrophilic Brønsted acids onto different hydrophobic polymer backbones. In spite of their excellent conductivities below the dew point of water, their dependence on acidic water through which they attain fast proton mobility cripples their performance under preferred fuel cell working conditions of intermediate temperatures and low humidity. Fuel cells operated at intermediate temperatures have faster kinetics and lower overall fuel-cells costs. The latter is due to a reduction in the required platinum loading as a result of reduced carbon monoxide poisoning at the anode.

As an alternative approach, the use of amphoteric nitrogen containing heterocycles (NCHs) as the proton conducting species has been proposed by Kreuer.^{1,2} These compounds mimic water with respect to their hydrogen bonding capabilities and amphoteric nature. In this category, several monomeric NCH (Table 4.1) and polymeric NCH blends with acids³⁻⁹ have been prepared. Studies carried out with imidazole,^{10,11} triazole,^{9,12} benzimidazole¹³ and pyrazoles² as the proton conducting groups have revealed that proton conductivity in these NCHs depends on two factors. The first is local mobility, which can be achieved by heating

the NCHs close to their melting points where high mobility is realized, or by tethering the NCHs to flexible polymer backbones whereby conductivity is governed by the flexibility of the polymer matrix. The latter is preferred because of the potential for leaching or vaporization of the small monomeric components from the blended mixture especially at high temperatures ($> 120^{\circ}\text{C}$) where most NCHs liquefy. The second factor involves the effective concentrations of mobile protons in the membranes, i.e., charge carrier density, which plays a large role at higher temperatures where mobility of the NCHs is no longer an issue. The effective charge carrier density is a function of the acidity of the NCH group. Li and co-workers have evaluated the effect of reducing the pKa of the NCH group and found that decreasing the basicity of the NCH results in an appreciable increase in proton conductivity.^{4,9}

Through careful design and adoption of these two basic principles, i.e. mobility and charge density, anhydrous proton conductivity has been realized in several polymeric-NCHs, where the NCHs have been tethered either by alkyl chains or by short poly(ethylene oxide) (PEO) spacers. Schuster et al. studied proton transport in imidazole-terminated ethylene oxide (EO) oligomers as model immobilized materials and found structural diffusion to be the dominant conduction process by comparing conductivity values to ^1H NMR diffusion coefficients.^{10,11} Subsequently, Hertz et al. investigated two polymeric systems; polystyrene-tethered imidazoles and benzimidazole tethered to a polysiloxane network.¹⁴ Higher conductivities were observed in the former due to improved polymer mobility. Persson and Jannasch studied the proton conductivity in benzimidazole-tethered ABA-PEO triblock copolymers and found conductivity to be promoted by high benzimidazole concentrations and high segmental mobilities.^{15,16} These two factors were at odds with each other as higher

benzimidazole concentrations led to more rigid (lower T_g) polymers. This result was further highlighted by benzimidazole containing poly(ethylene glycol) (PEG)-acrylates synthesized by Coughlin et al.¹⁷ Here, it was found that decreasing T_g by increasing the PEG content in the polymer led to enhanced conductivities at low temperatures and converging conductivities at higher temperatures (where the T_g of the parent polymer was surpassed). The conductivities converged at higher temperatures due to a decrease in charge carrier density (as seen in the normalized T- T_g plots) as the volume fraction of the PEG increased. However, when the heterocycle is switched to a triazole,¹⁸ an increase in PEG composition led to an increase in conductivity at all temperatures, which implies an improvement in conductivity despite a reduction in proton carrier density. The authors mentioned the possibility of a synergistic effect and suggested that the dielectric constant of the PEG could have a positive influence on the conductivity as seen in lithium conducting polymer systems.

Table 4.1 Chemical properties of NCH

NCH/Water	b.p.	m.p.	Acidic pKa	Basic pKa	H-bond donor	H-bond acceptor
Water	100	0	15.7	-1.7	2	2
Imidazole	257	90	14.1	7.2	1	1
Benzoimidazole	360	178	12.6	5.7	1	1
1,2,3-triazole	203	23	8.7	1.5	1	2
1,2,4-triazole	256	120	9.9	2.4	1	2
Bitriazole	-	210 ^a	6.4 ^b	-1 ^b	2	2

^a Decomposition temperature ^b Calculated according to Advanced Chemistry Development (ACD/Labs) Software V8.19 for Solaris

The objective of this work is to investigate and gain a fundamental understanding of the origin and mechanism of proton conductivity in a NCH-polymer composite towards aiding the design of future anhydrous organic-based proton electrolyte membranes. We chose

to decouple the polymer from the NCH so as to clearly study intermolecular polymer-NCH interactions, as well as the effect of polymer type, length, and concentration on the conductivity of the NCH with high accuracy. The success of this strategy relied on the synthesis of a NCH that remains a stable solid throughout the temperature range of interest, i.e., room temperature to 150°C. This is required because our conductivity setup (as described in the experimental section) calls for a free-standing membrane. Benzimidazole was the only proton conductive NCH from Table 4.1 that met this criterion, but over time was found to sublime at 150°C. Thus, for this work, we chose to synthesize a new amphoteric NCH with desirable proton conductive properties. Through careful design, 4,4-*1H*-*1H*-1,2,3-triazole (bitriazole), a stable NCH capable of mimicking water in the solid state was synthesized.

As shown in Table 4.1, bitriazole remains a stable solid up until its decomposition temperature at 210°C, has a similar basic pKa to the hydronium species, is much less basic than the widely used NCHs, and similar to water, can form four hydrogen bonds per molecule, a feature unattainable by other NCHs. Unfortunately, this last feature appears to be responsible for the highly rigid nature of bitriazole, and as reported below, its very poor anhydrous proton conductivity. However, its rigidity and stable crystalline structure allows for the incorporation of up to 0.05 mol% low molecular weight PEGs with good free-standing structural features at temperatures up to 150°C. Since PEG polymers have been used to increase lithium ion conductivities in lithium salts,¹⁹ we postulated that proton conductivity in bitriazole could be augmented by a similar mechanism.

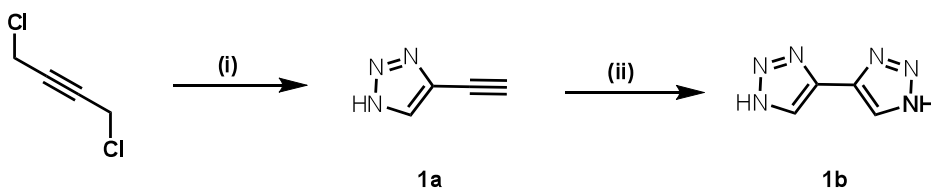
In this study, the source of proton conductivity in bitriazole-poly(ethylene oxide) composites is revealed and a Grotthus (structural diffusion) mechanism of proton transport is

proposed based on supporting experimental findings. In addition, evidence of synergistic effects between bitriazole and poly(ethylene oxide) as they relate to anhydrous proton conductivity enhancement is discussed.

4.3 Results

4.3.1 General properties of bitriazole and its poly(ethylene oxide) composite

Bitriazole is synthesized in two steps from 1,4-dichlorobutyne via 4-ethynyl-1*H*-1,2,3-triazole (**1a**) as an intermediate as shown in Scheme 4.1. The intermediate, **1a** is formed via an aza-butatriene rearrangement after addition of sodium azide to 1,4-dichlorobutyne. Compound **1b** is obtained from **1a** via click chemistry with a trimethylsilyl protected azide which undergoes deprotection *in situ*. Compound **1b**, i.e., the bitriazole, is obtained after sublimation as a crystalline white solid.



Scheme 4.1 Synthesis of bitriazole (i) NaN₃, NaOH, water, MeOH (ii) TMS-N₃, CuI, DMF, MeOH

Since strong adsorption of some NCHs, such as imidazole, to the surface of platinum due to their basicity leads to poisoning of the fuel cell electrode,²⁰ it is important to assess the electrochemical stability of any new NCH under redox conditions in the presence of platinum. Cyclic voltammograms (CVs) for bitriazole and imidazole in acetonitrile solutions purged with O₂ are shown in Figure 4.1. Unlike imidazole where a large irreversible oxidation peak appears after the first cycle near +1.3 V, the bitriazole shows no observable redox peaks in the 0 to +1.8 V (vs Ag/Ag⁺) potential range, implying that

bitriazole has sufficient electrochemical stability under fuel-cell operating conditions. The hysteresis observed in the CV of bitriazole is due to electrode overpotential.

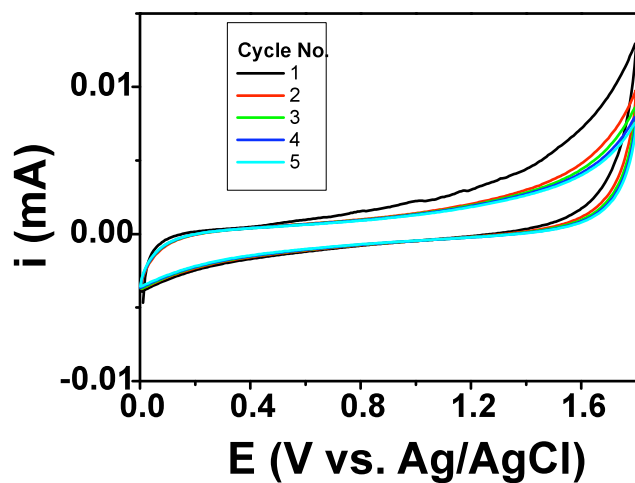
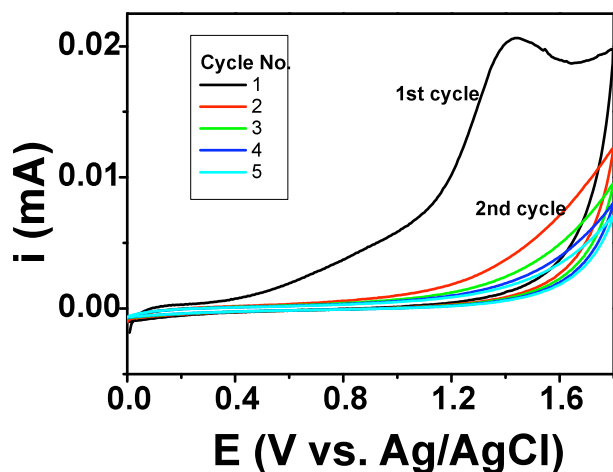


Figure 4.1 Cyclic voltammograms of imidazole (top) and triazole (bottom). Working electrode: Pt foil, counter electrode: Pt wire, reference electrode: Ag/AgCl, electrolyte: $5 \times 10^{-3} \text{ mol/dm}^3$ of azole purged with O_2 in 0.1 mol/dm^3 CH_3CN solution of TBABF_4

Thermal analysis was conducted to assess the stability of bitriazole at intermediate temperatures. As seen in Figure 4.2, both bitriazole and bitriazole-poly(ethylene oxide) in a 20:1 ratio appear stable up to 200°C .

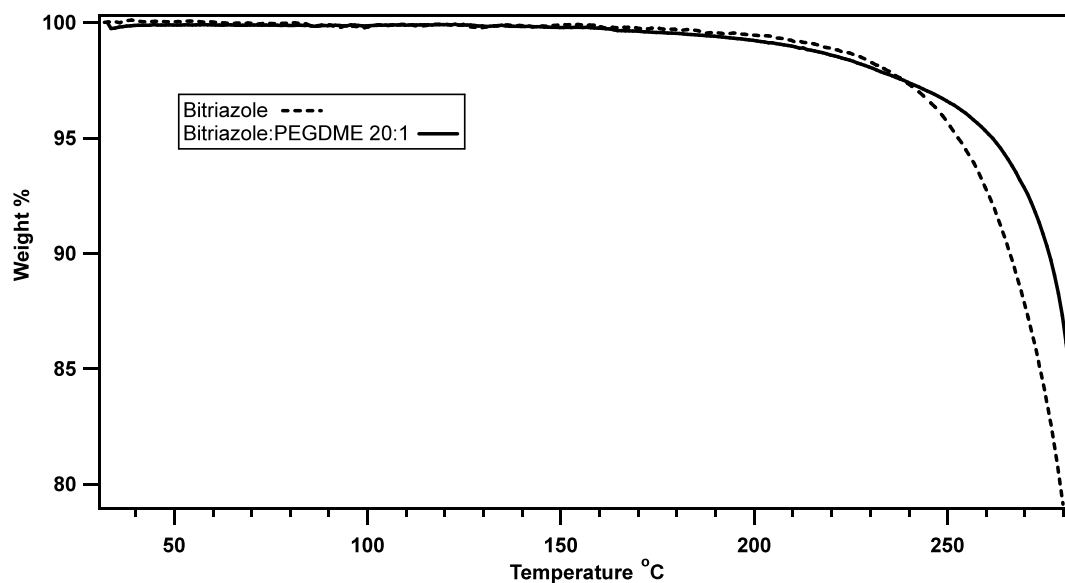


Figure 4.2 TGA of bitriazole and bitriazole-poly(ethylene glycol)dimethyl ether ($M_n \sim 1000$) 20:1

During our early investigations into the proton conductivity of pristine bitriazoles, it became apparent that these compounds, though not visually hygroscopic, hold on tightly to water molecules (slight mass loss between 50 and 200 °C) and these bound water molecules, assumed to reside between the grain boundaries of the bitriazole particles (as bitriazole has negligible water solubility below 70°C), were responsible for the preliminary conductivities observed. Results to this effect can be seen in Figure 4.3.

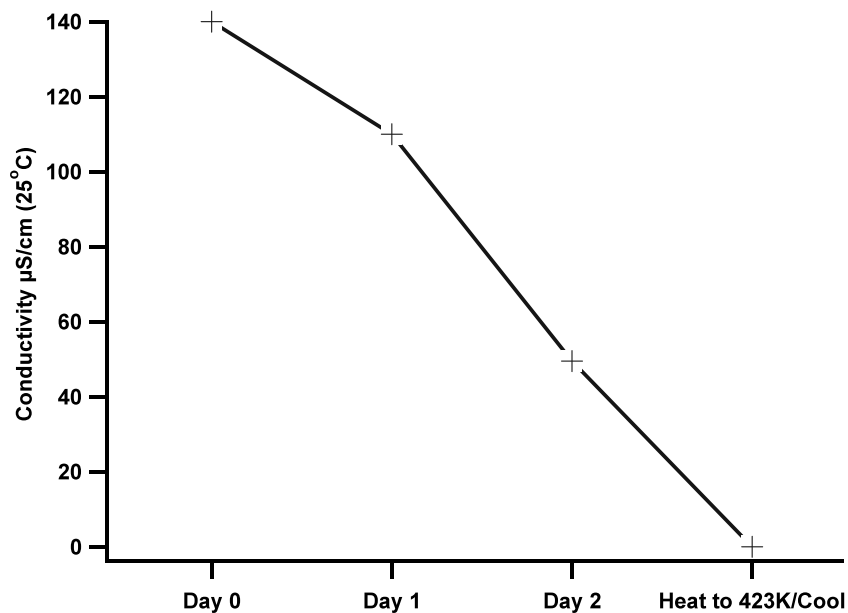


Figure 4.3 Proton conductivity of bitriazole at room temperature as a function of time and temperature

When fully dried under anhydrous conditions, bitriazole gives negligible conductivity both at room temperature and at 150°C. This lack of proton motion in pristine bitriazole can be attributed to its densely packed hydrogen-bonded structure, as evidenced by the retention of its crystallinity after heat treatment from room temperature to 150°C (Figure 4.4).

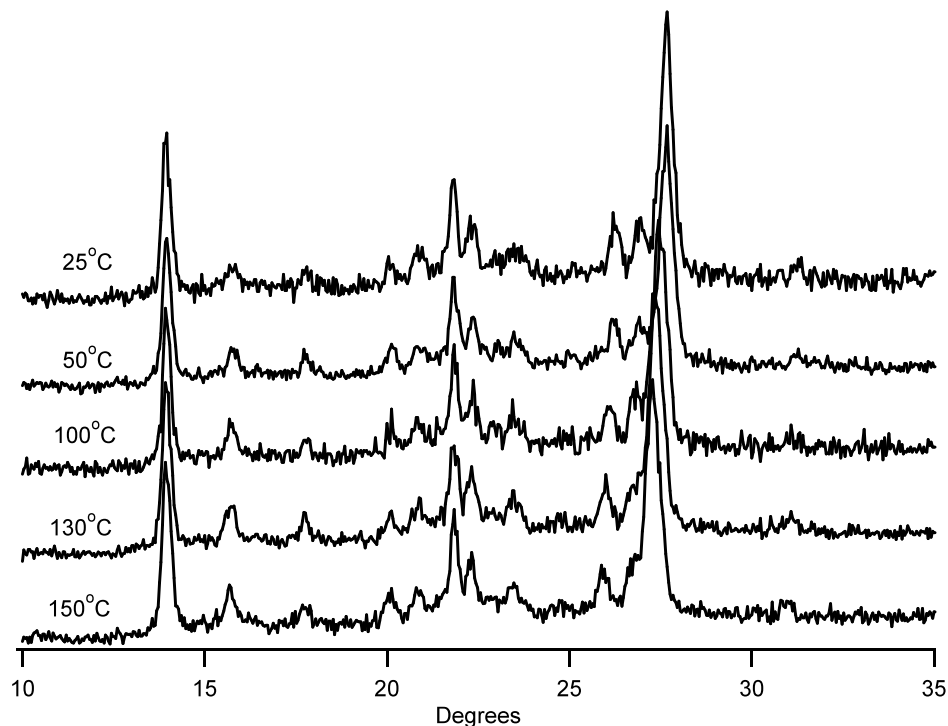


Figure 4.4 VT-Powder XRD of bitriazole under dry purging argon

Since ethylene oxide based polymers are known to dramatically increase the conductivity of lithium ion salts via segmental motions of the ethylene oxide units and high dielectric constants,²¹ we hypothesized that the conductivity in pristine bitriazoles could also be augmented in a similar fashion by mixing a poly(ethylene glycol) dimethyl ether (PEGDME) with bitriazole. These composites, as shown by the representative TGA data of the 20:1 mixture (Figure 4.2), display similar stabilities (up to 180°C) as pristine bitriazole. The bitriazole-PEGDME composites were fully dehydrated *in situ* before each experiment. The length and temperature required for dehydration was predetermined by running an isothermal desorption experiment on the composite samples under flowing argon in the TGA.

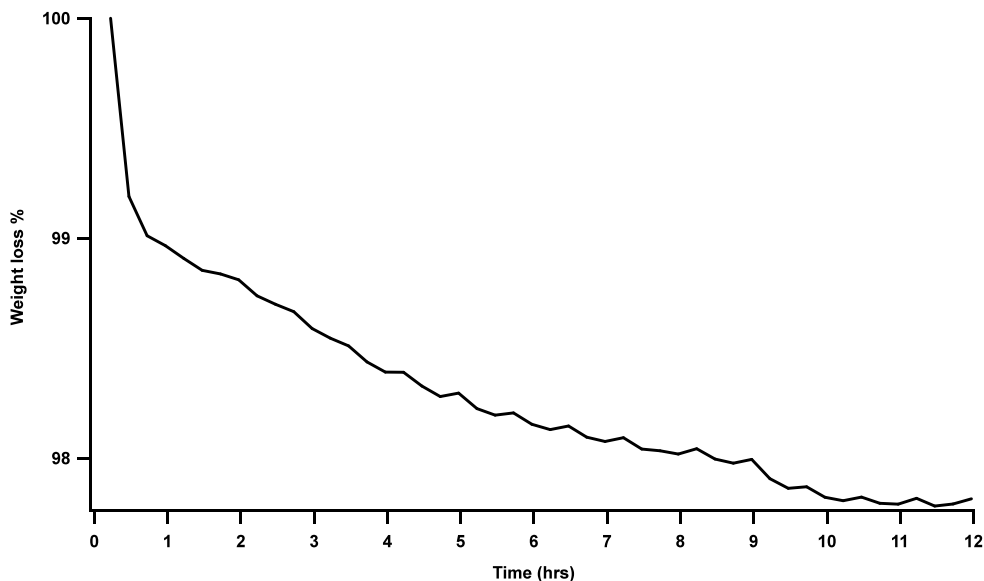


Figure 4.5 Isothermal dehydration of bitriazole:PEGDME-1K (i.e., $M_n \sim 1000$) 20:1 at 407 K under flowing argon

As shown in Figure 4.5, it takes about 10 hours for complete dehydration of the bitriazole-PEGDME samples to take place at 407 K, after which no weight loss is observed.

The DSC of bitriazole (not shown) has no thermal transitions between -40°C and 160°C .

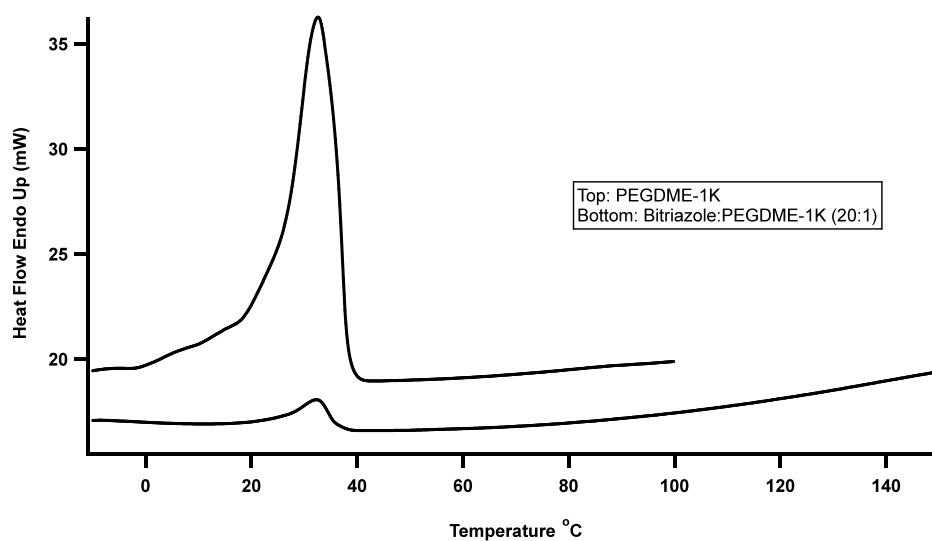
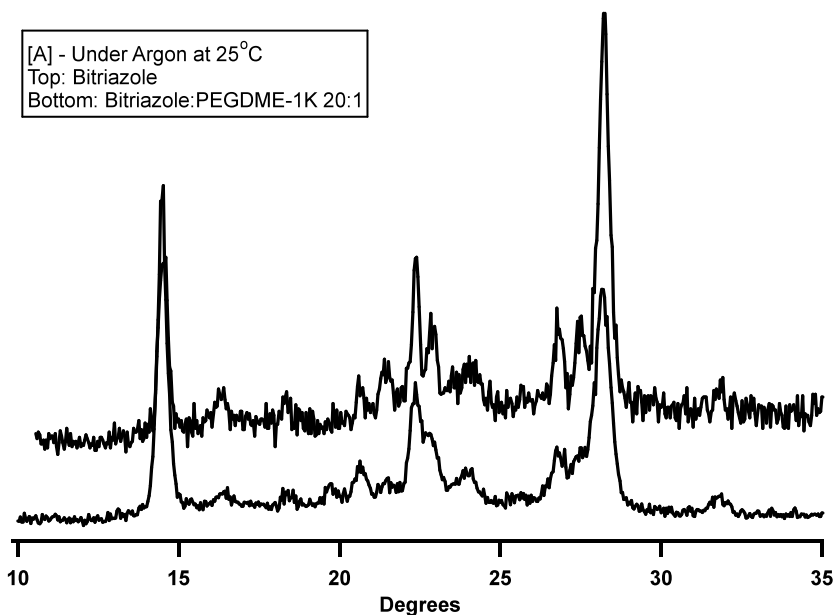


Figure 4.6 DSC curves of PEGDME-1K and bitriazole-PEGDME-1K (20:1) recorded under N_2 atmosphere with a heating rate of 10 K/min

Figure 4.6 shows the DSC plot of pure PEGDME-1K and bitriazole-PEGDME-1K. The melt transition of PEGDME-1K at 32.5°C is also seen in the bitriazole-PEGDME-1K composite material, implying that a few crystalline regions of PEGDME are still present in the composite sample at room temperature. However, the degree of crystallinity is greatly reduced due to the presence of bitriazole, as seen by the large reduction in the melting peak area. A large reduction in PEGDME-1K crystallinity due to the bitriazole should also concomitantly lead to a decrease in the degree of bitriazole crystallinity as shown in Figure 4.7.



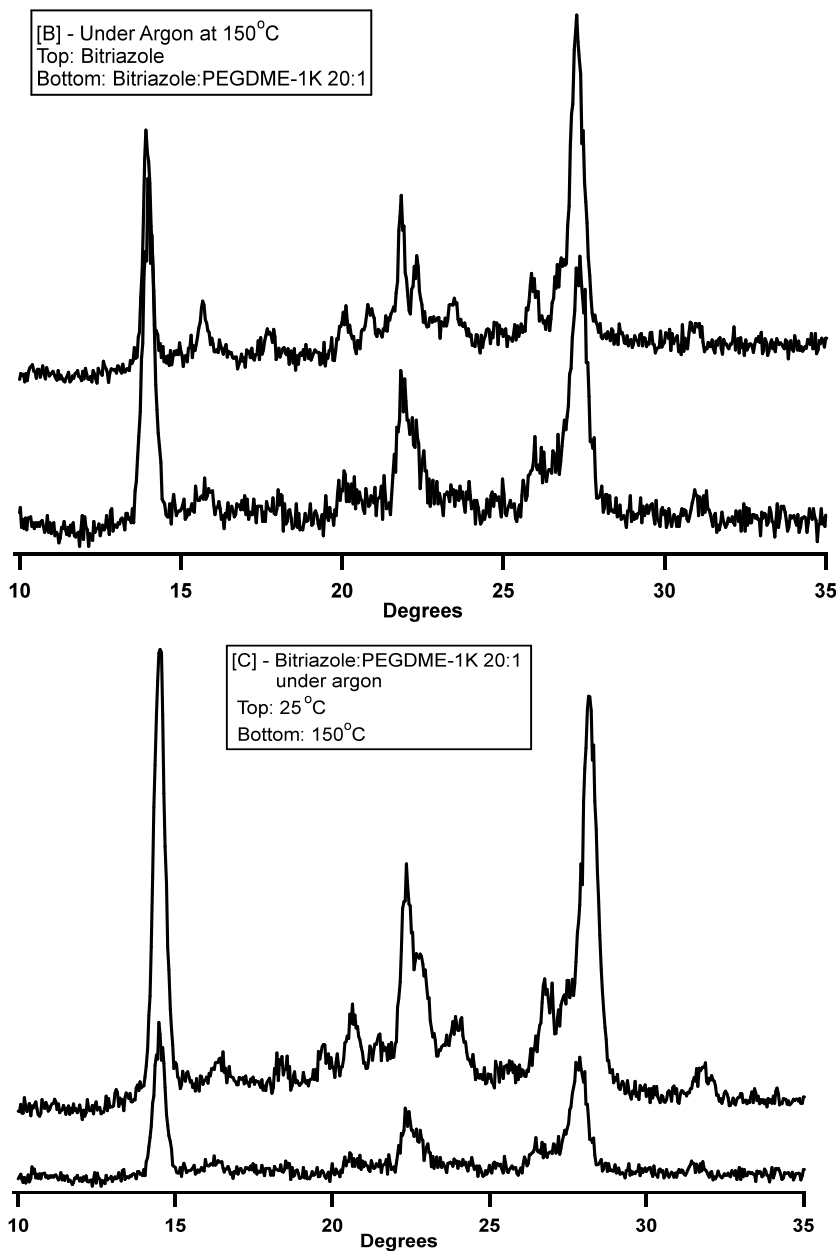


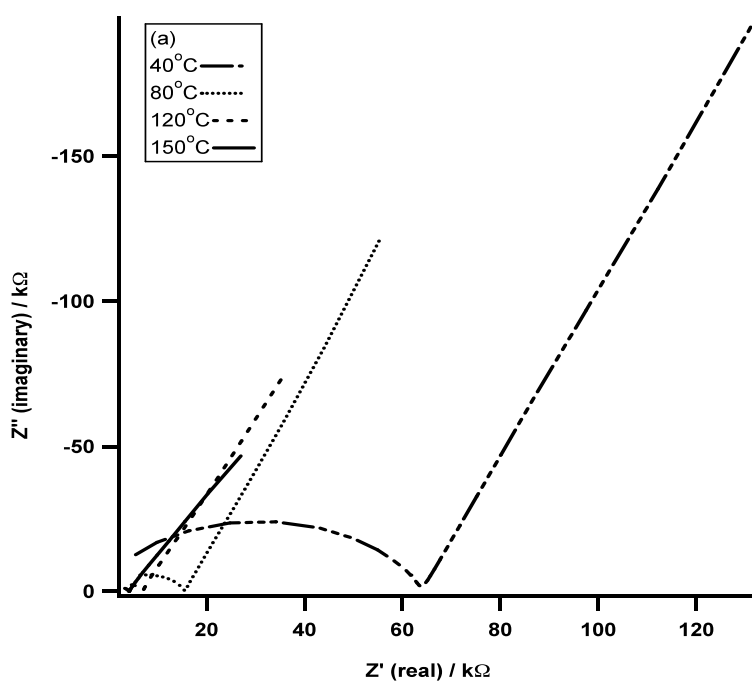
Figure 4.7 XRD spectra of bitriazole and bitriazole-PEGDME-1K under argon at 25°C and at 150°C

The XRD spectra of bitriazole-PEGDME-1K in contrast to pristine bitriazole (Figure 4.7A and 4.7B) at room temperature and especially at 150°C shows a significant decrease in the reflections at 15.7°, 20.1°, and 20.9° while those at 17.9° and 23.6° are completely lost. This decline in the degree of bitriazole crystallinity signifies the generation of more

amorphous regions in the composite. Based on the large reduction in the semi-crystalline nature of PEGDME, the amorphous phase should be rich in polymer and thus be at a ratio less than the starting 20:1. In Figure 4.7C, we see that as the temperature of bitriazole-PEGDME-1K composite is increased, the bitriazole crystallinity decreases, and thus the composition of bitriazole in the amorphous phase with the polymer increases. Increasing the composition of bitriazole in the amorphous phase with the polymer increases. Increasing the composition of bitriazole in the PEGDME-1K amorphous phase should facilitate proton mobility by way of high segmental motion.

4.3.2 Source of Anhydrous Proton conductivity in bitriazole-PEGDME composites

Anhydrous proton conductivity of the bitriazole-PEGDME-1K composite was obtained from impedance response (Cole-Cole or Z' vs. Z'' plots). Representative Cole-Cole plots and the frequency dependence of AC conductivity at different temperatures is shown in Figure 4.8.



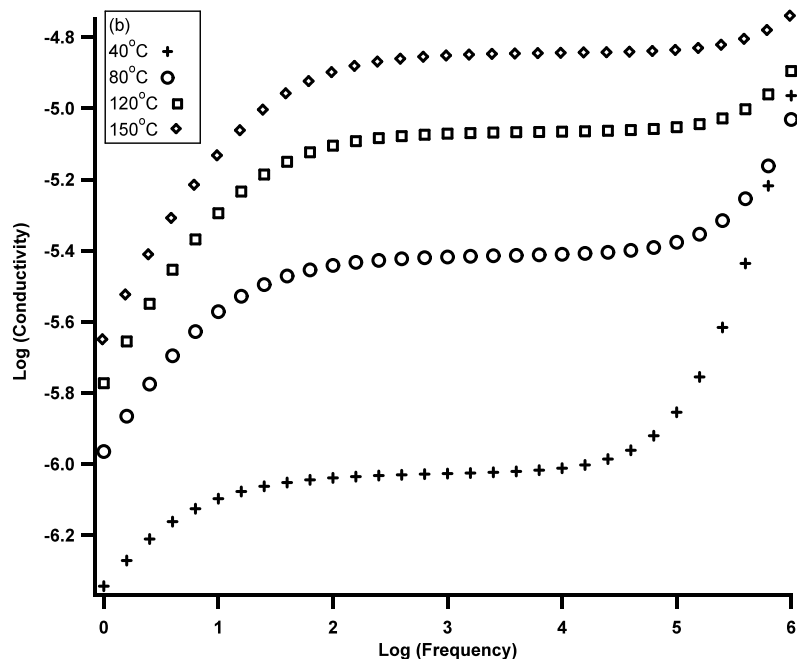


Figure 4.8 (a) Representative Cole-Cole plots of bitriazole:PEGDME-1K composite in a 20:1 ratio at various temperatures. (b) Log AC conductivity, σ_{AC} vs. Log frequency at various temperatures

DC Conductivities, σ_{DC} were calculated from resistance values by applying $\sigma_{DC} = l / RS$ where l represents the thickness of the pellet, S is the cross-sectional area of the pellet (i.e., the electrode area) and R is the resistance of the composite membrane. The resistance was obtained by extrapolating the Cole-Cole plots to the real axis. This point represents the frequency independent plateau, which corresponds to DC conductivity in the samples. Frequency independence occurs when the rate of change of electric field is in resonance with ion motion through the sample. As seen from Figure 4.8B, the position of the frequency independent region, i.e., σ_{DC} , shifts towards higher frequencies as the temperature increases due to the increase in the rate of proton motion. This corresponds to a left shift in the Cole-Cole plots towards lower resistance values, i.e., higher conductivities. The conductivity

dependence in the low-frequency regime is caused by electrode polarization (i.e., piling up of protons) due to blocking effect of the platinum electrodes.

The conductivity plot illustrating the temperature-dependence of proton conductivity of bitriazole-PEGDME-1K is shown in Figure 4.9. The 20:1 bitriazole-to-PEGDME-1K ratio was chosen because it corresponds to a 1:1 ratio of bitriazole to ethylene oxide groups in the polymer.

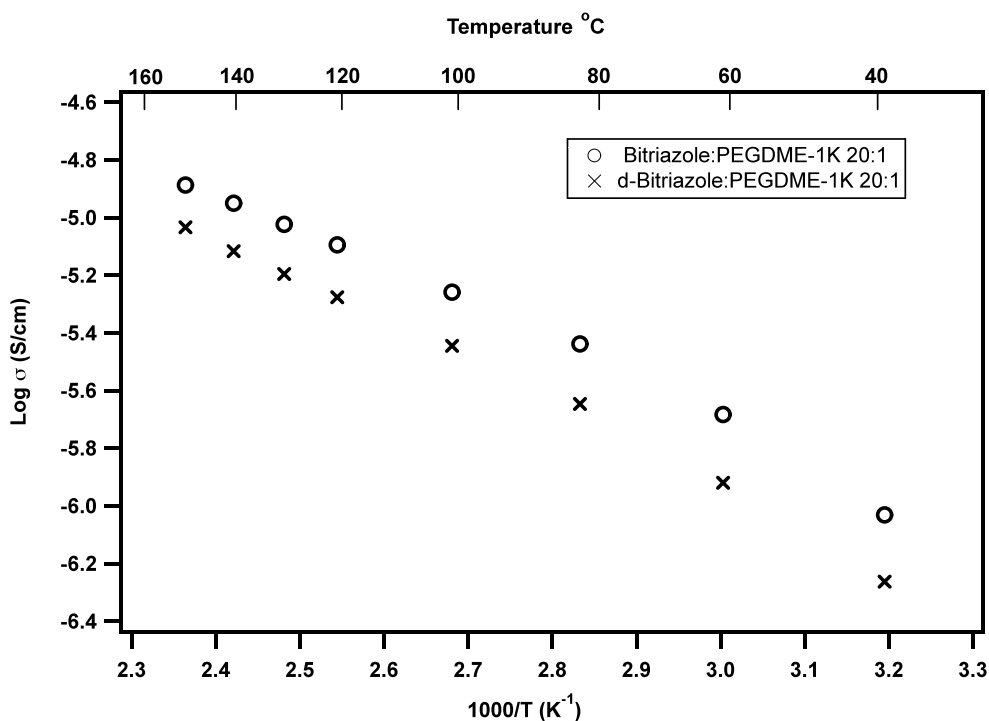


Figure 4.9 Conductivity plots for bitriazole-PEGDME-1K and d-bitriazole-PEGDME-1K samples, both at a 20:1 ratio. Conductivity measurements were taken after heating samples at 150°C overnight (> 12hrs) during cooling. Each point is an average of three measurements.

The conductivity of the bitriazole-PEGDME-1K composite reached a maximum value of 13 $\mu\text{S}/\text{cm}$ at 150 °C. To determine the source of proton conductivity, we carried out a kinetic isotope effect experiment. This was done by substituting the N-*H* protons on bitriazole with N-*D*. The substitution was confirmed via ^1H NMR by the complete

disappearance of the broad bitriazole N-H peak centered at 15.2 ppm without a change in the C-H peak at 8.21 ppm (see experimental section).

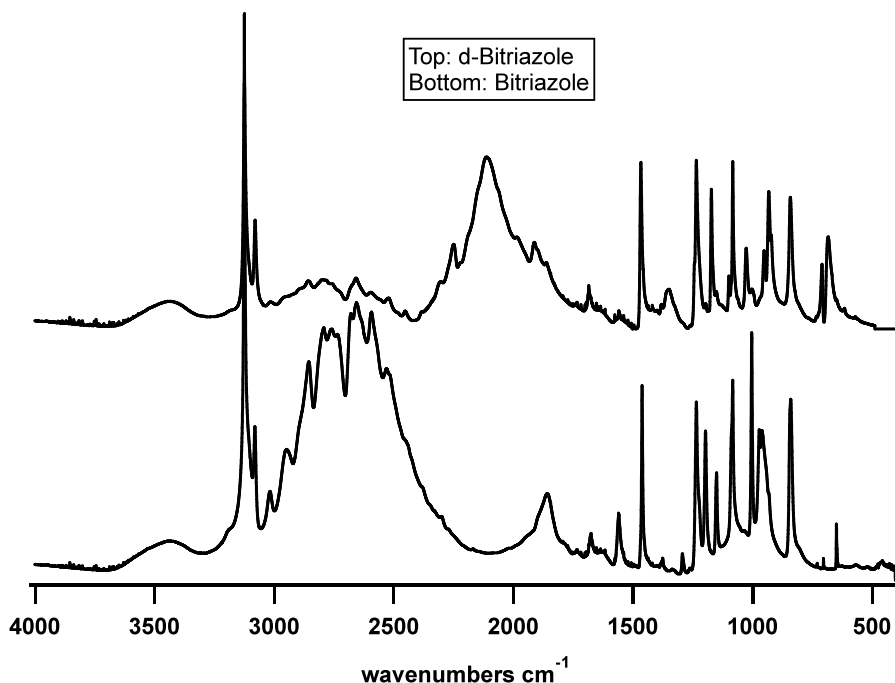


Figure 4.10 FT-IR spectra at room temperature of bitriazole before and after N-H deuterium exchange

Further support of deuterium substitution was obtained from the FT-IR spectrum in Figure 4.10 of bitriazole-H and bitriazole-D. An almost complete red shift of the hydrogen-bonded N-H stretch between 2300 and 3000 cm^{-1} to 1800 and 2400 cm^{-1} (N-D) is observed due to the heavier deuterium atom. The C-H stretch at $\sim 3200 \text{ cm}^{-1}$ remained constant in both samples, again confirming selective deuteration only at the bitriazole N-H site.

The isotopic substitution of N-H with N-D gives rise to a primary isotope effect shown in Figure 4.9. This indicates that the N-H bond is involved in the rate-determining step and is thus responsible for proton conductivity in the bitriazole PEGDME composite.

The ratio of the rate constants k_H/k_D increases as the temperature decreases (Figure 4.11) as expected, due to the larger effect of mass on ion motion at lower temperatures.

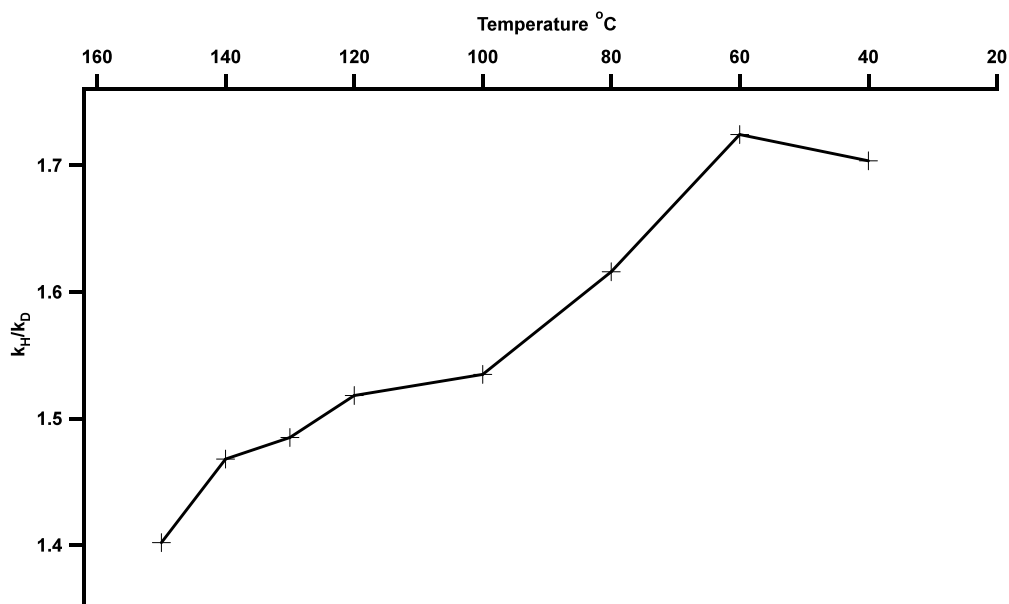


Figure 4.11 Variation of k_H/k_D in plain and deuterated bitriazole-PEGDME-1K 20:1 as a function of temperature

The theoretical maximum of k_H/k_D is 4.2 at room temperature, based on the full dissociation of the N-H bond in the transition state (ν_H and ν_D were obtained from FT-IR data). However, k_H/k_D from our experimental data gives a value of ~ 1.7 . The difference between the theoretical and experimental values suggests that proton transfer in the transition state does not involve the complete dissociation of N-H bonds. At lower temperatures, i.e., below 60°C, k_H/k_D appears to level off. This could be due to the PEG crystallization around this temperature thus leading to a different mechanism of proton transport.

4.3.3 Anhydrous proton conductivity as a function of polymer composition

4.3.3.1 Effect of polymer concentration:

The 20:1 bitriazole-to-PEGDME-1K ratio was the maximum amount of PEGDME-1K that could be blended with bitriazole to give a stable free-standing pellet. Above this ratio, the mechanical integrity of the composite pellet was compromised. In order to investigate the effect of PEGDME content on the conductivity of bitriazole, the bitriazole-to-PEGDME ratio was increased.

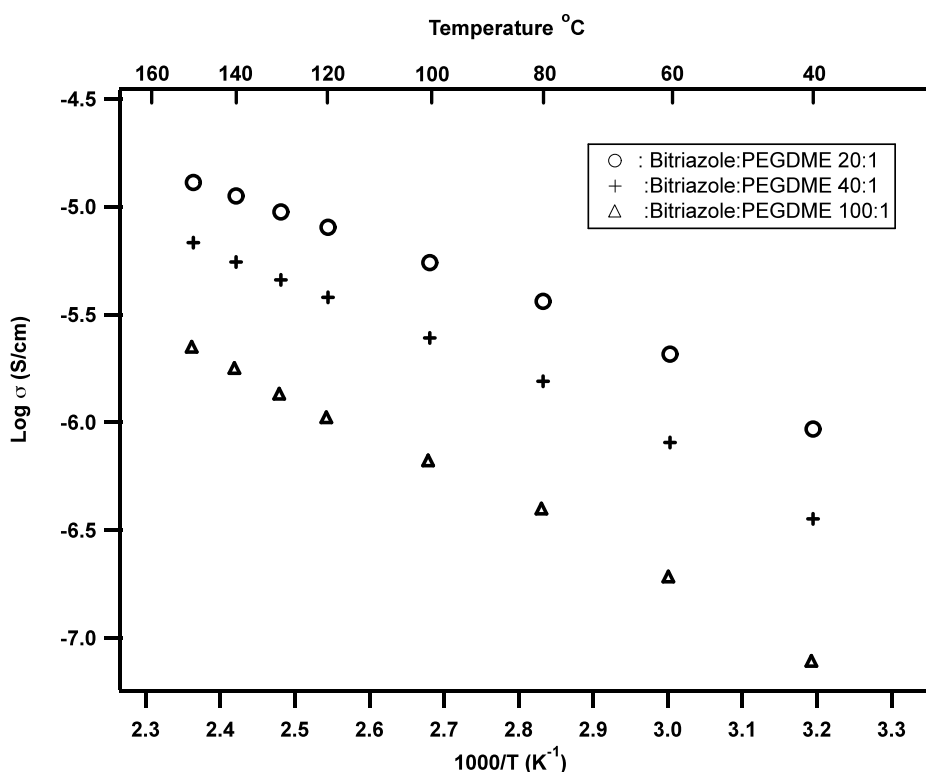


Figure 4.12 Conductivity plots for bitriazole-PEGDME-1K composites with increasing bitriazole content

Composites with higher bitriazole fractions (40:1 and 100:1) had lower conductivities and appeared to be more temperature dependent. The lower conductivities can be attributed

to a decrease in the polymer-rich phase in the composite as the fraction of bitriazole-to-PEGDME increases. The increase in temperature dependence implies a higher activation energy and stronger dependence on segmental motion. The slight curvature of the data points in Figure 4.12 suggests non-Arrhenius behavior suggestive of coupling between polymer segmental motion and ion transport. In proton conductive systems where polymers are involved with the charge carriers, conductivity depends not only on the number of charge carriers, their type and mobility, but also on the conformational changes in free volume. The temperature dependence on conductivity incorporating the latter has been described by the Vogel-Tamman-Fulcher (VTF) equation.²²

$$\sigma = \sigma_0 e^{(-B/R(T-T_0))} \quad [4.1]$$

where σ_0 is the pre-exponential factor and correlates to the maximum number of mobile charge carriers in the system, B is an empirical parameter known as the Vogel activation energy, and T_0 is widely described as the temperature at which all the free volume vanishes. T_0 is usually 50-70 K below the glass transition temperature. The experimental data in Figure 4.12 were fit to the VTF model (Equation 4.1) and the fitting parameters are summarized in Table 4.2.

Table 4.2 Fitting parameters obtained from conductivity data in Figure 4.12 fitted with the VTF equation [4.1]

Bitriazole:PEGDME ratio	T_0 (K)	σ_0 [S cm^{-1}] x 10^{-3}	B (kJ/mol)	R^2
20:1	115.42	1.09	11.35	0.9999
40:1	122.82	1.02	12.55	0.9996
100:1	127.95	0.86	14.69	0.9988

The experimental data points were perfectly fitted by the VTF equation, as shown by the high R^2 values in Table 4.2. As the fraction of bitriazole in the composite increases, the pre-factor σ_0 decreases. This suggests that although there are more charge carriers in the composite, the number of those charges actually available for proton conduction decreases. This observation can be explained by the increase in the vanishing mobility T_0 with increasing bitriazole ratio. Since vanishing mobility has been shown to track with the T_g , its increase suggests a higher degree of rigidity in the composite as the bitriazole content increases. Thus, increasing bitriazole content decreases the fraction of polymer-rich regions, which leads to a decrease in segmental motion resulting in a lower concentration of mobile bitriazole protons, hence lower conductivities. Along the same line, the Vogel activation energy also increases, as expected, with increasing bitriazole fraction. Complimentary to these results, Goward et al. performed a comprehensive solid-state ^1H NMR study and found that proton transport in imidazole-terminated oligomers occurs almost exclusively in the amorphous disordered phase.²³

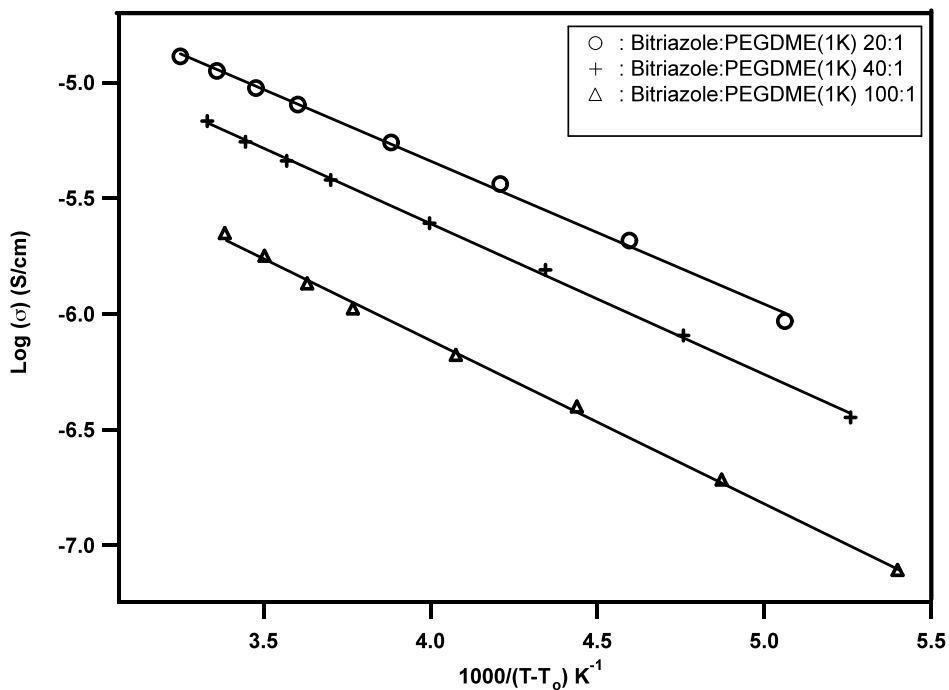


Figure 4.13 Linear fits to VTF equation after applying the vanishing mobility, T_0 to the data points from Figure 4.12

To verify the VTF behavior, the plot of $\text{Log}(\sigma)$ should vary in a linear fashion with $(T-T_0)^{-1}$. This linear relationship is observed in Figure 4.13 for all three different bitriazole:PEGDME-1K ratios. The right shift of the linear conductivity plots in Figure 4.13 towards higher temperatures as bitriazole content increases is the result of the increase in vanishing mobility as previously discussed. Since conductivity is dominated by free volume conformational changes,¹¹ the downward trend and constant slopes in the normalized plot of $\text{Log}(\sigma)$ vs. $T-T_0$ even at high temperatures reflects a decrease in protonic charge carrier density both on an absolute and normalized scale. This further confirms that only the bitriazole protons associated with PEGDME participate in conductivity.

4.3.3.2 Effect of PEGDME length

We have also investigated the effect of PEGDME length on conductivity. As an extension of the previous study, where increasing the bitriazole content decreased segmental mobility and thus conductivity, we expect the incorporation of higher molecular weight PEGDMEs to lead to a decrease in segmental mobility and proton conductivity.

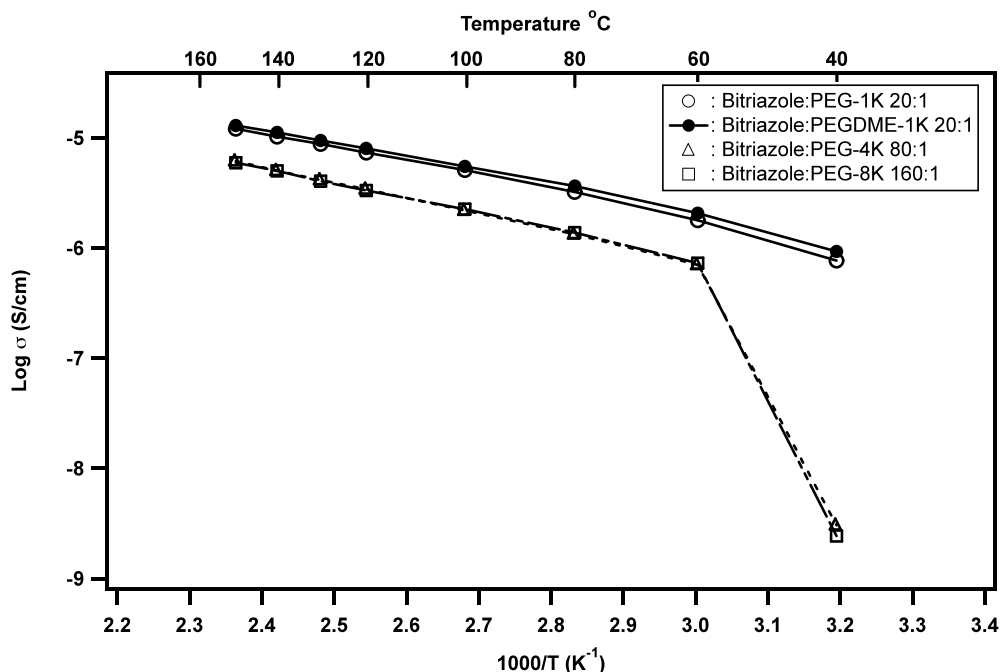


Figure 4.14 Conductivity plots of bitriazole with different poly(ethylene glycol) PEG sizes as a function of temperature

Since higher molecular weight PEGDMEs were not available, we chose to use PEGs, i.e., without the dimethoxy terminal cap. To investigate the effect of the terminal hydroxyl end groups, we compared bitriazole:PEG-1K to the bitriazole:PEGDME-1K composites, both at 20:1. As shown in Figure 4.14, the terminal hydroxyl groups do not have much of an effect on conductivity. The bitriazole:PEG-4K and PEG-8K ratios were adjusted to 80:1 and 160:1 in order to maintain the same 1:1 ratio of bitriazole to ethylene glycol unit within each composite. In contrast to the bitriazole-PEG-1K composite, the conductivities of bitriazole

composites with PEG-4K and PEG-8K undergo a sudden drop below 60°C. The drop in conductivity was similar for both compounds because all high molecular weight PEGs (above $M_n \sim 4000$) have similar melt temperatures between 59-61°C. Below this temperature, these high molecular weight PEGs form crystalline regions, which lack mobility and thus lead to a sharp decline in conductivity. Above their melt temperature, the conductivities of bitriazole-PEG-4K and PEG-8K composites are lower than that of the bitriazole-PEG-1K composite due to their lower mobility. However, the bitriazole-PEG-4K and PEG-8K composites appear to have no appreciable difference in their conductivity curves. This data seems to suggest that above a certain PEG molecular weight (~ 4000), the differences in mobility with respect to their influence on proton conductivity is diminished.

4.3.3.3 Effect of PEG-terminated acidic groups

Proton conductivity in NCHs has been shown to increase with the addition of strong acid dopants, such as trifluoroacetic acid (TFA), methane sulfonic acid (MSA), or para-toluenesulfonic acid (pTSA). These small-molecule acids have pKa values lower than the basic pKa of most NCHs and are thus able to protonate the basic sites leading to an increase in the concentration of charge carriers. However, direct addition of these small molecules introduces the possibility of proton vehicular transport along these small strong acids. Besides, addition of these agents to the bitriazole:PEGDME mixture lead to significant reduction in the mechanical integrity of the composite structure. In order to circumvent this issue, the acidic dopants of different acid strength were tethered to the terminal ends of the PEGs. This allowed us to specifically study the influence of the strength of acid dopants on protonic structural diffusion in our bitriazole-poly(ethylene oxide) composites.

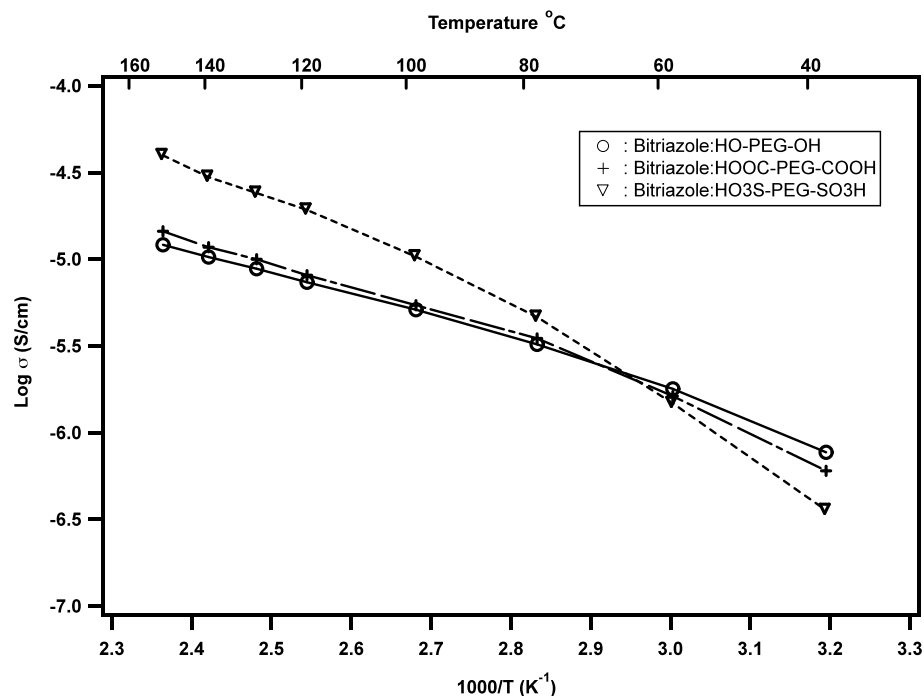


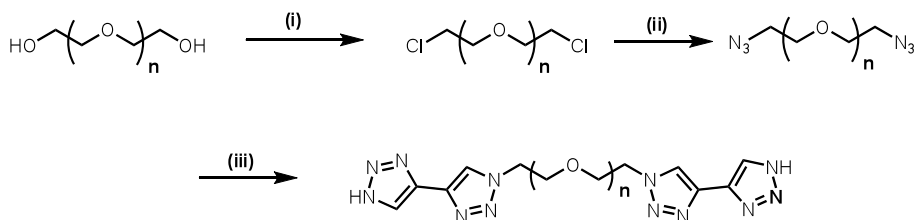
Figure 4.15 Conductivity plots of bitriazole with different PEG-diacids (20:1 ratio) as a function of temperature. The 20:1 bitriazole:PEG(1K)-Acid corresponds to 9.1mol% acid groups.

The terminal hydroxyl groups in PEG-1K were shown in Figure 4.14 to have negligible effects on the proton conductivity. In order for an acidic group to protonate the bitriazole, its pKa must be at or lower than the basic pKa of bitriazole (basic pKa \sim -1). As shown in Figure 4.15, both terminal alcohols and carboxylic acids aren't able to effect much change in the composites because their pKa's (\sim 15.2 and \sim 4.8, respectively) are higher than the basic pKa of bitriazole. The lack of an appreciable increase in proton conductivity of the bitriazole-PEG-dicarboxylic acid composite (COO-*H* pKa 4.8 vs. bitriazole-*H* pKa 6.4) implies that the proposed structural diffusion pathway of proton conduction occurs via the bitriazole molecules. The PEG-disulfonic acid with a pKa of \sim -2 gives a three-fold increase in proton conductivity at higher temperatures. This increase is on par with literature values which report about an order of magnitude increase in conductivity with small-molecule

dopant concentrations of 5-15%. The additional three fold increase in literature values may be due to contributions from vehicular transport of the small molecule acid groups used. The conductivity curve of the PEG-disulfonic acid shows higher temperature dependence and its conductivity falls below that of the PEG at low temperatures. The lower conductivity at low temperatures could be due to a higher T_g in the polymer due to the introduction of the terminal sulfonic acids that are able to electrostatically interact with the bitriazole. A lower T_g will lead to a stiffer polymeric system thus leading to the higher temperature dependence observed.

4.3.3.4 Effect of bitriazole spacing with ethylene oxides:

Since segmental motion plays a major role in the conductivity, we hypothesized that weakening the interactions between the bitriazole units should lead to more mobile systems and higher conductivities. To do this, we covalently linked two bitriazole molecules via ethylene oxide spacers of different lengths.



Scheme 4.2 Synthesis of di-bitriazoles with ethylene oxide spacers (BtzEO- n) where $n = 1-4$. $n = 0$ corresponds to plain bitriazole. (i) SOCl_2 , DMF, PhMe, 95°C , 2 h (ii) NaN_3 , KI, DMF, 75°C , 15 h (iii) Alkynyltriazole, Cu(I)Br , DMF, 60°C , 15 h.

The di-bitriazolyl ethylene oxides (Scheme 4.2) were synthesized from their respective ethylene glycols. After converting the glycols to diazides, di-bitriazoles were

obtained via click chemistry with an alkynyltriazole in the presence of a copper (I) catalyst which ensures 1, 4-regioselectivity.²⁴ The 1,5-regioisomer was not observed.

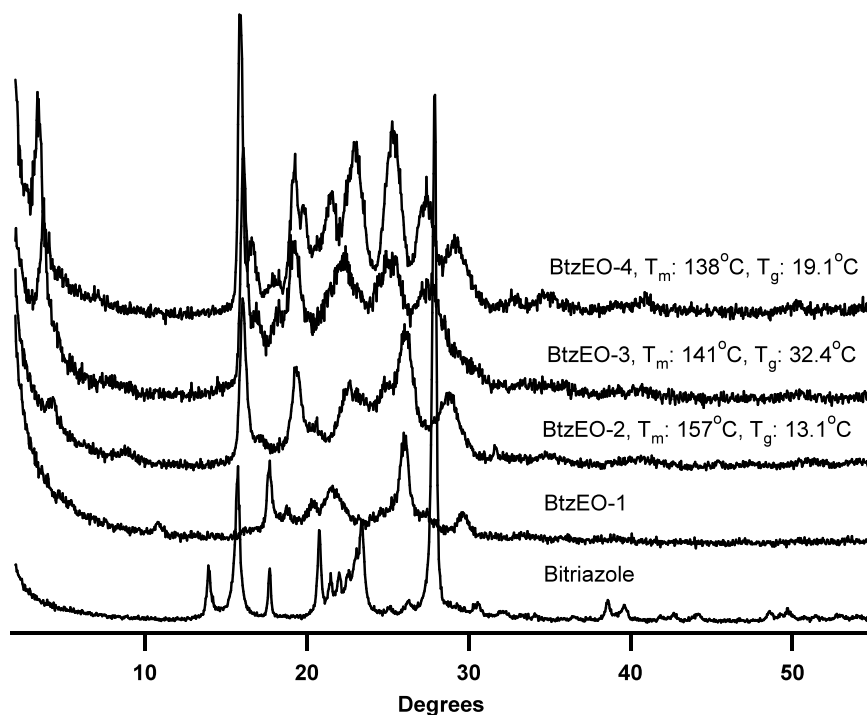


Figure 4.16 XRD spectra of BtzEO-n (0-4) along with T_m and T_g determined via DSC

All bitriazole-ethylene oxides (BtzEO-n) synthesized were semi-crystalline (melt transitions given in Figure 4.16). The melting points of these BtzEO-n (n = 2, 3, 4) compounds decreased with increasing ethylene oxide content. The first 2θ reflections in the powder XRD spectra for these BtzEO-n compounds were 26.5, 23.5, 20.6 Å for n = 2, 3, and 4, respectively (the first peak in n = 1 could not be observed). The 3Å difference in these reflections correlates with the length of an ethylene oxide unit (~ 3.5Å). The intensity of these reflections also increases with increasing ethylene oxide groups. Since some of these

compounds had low melt transitions, their conductivities could only be measured up to 120°C.

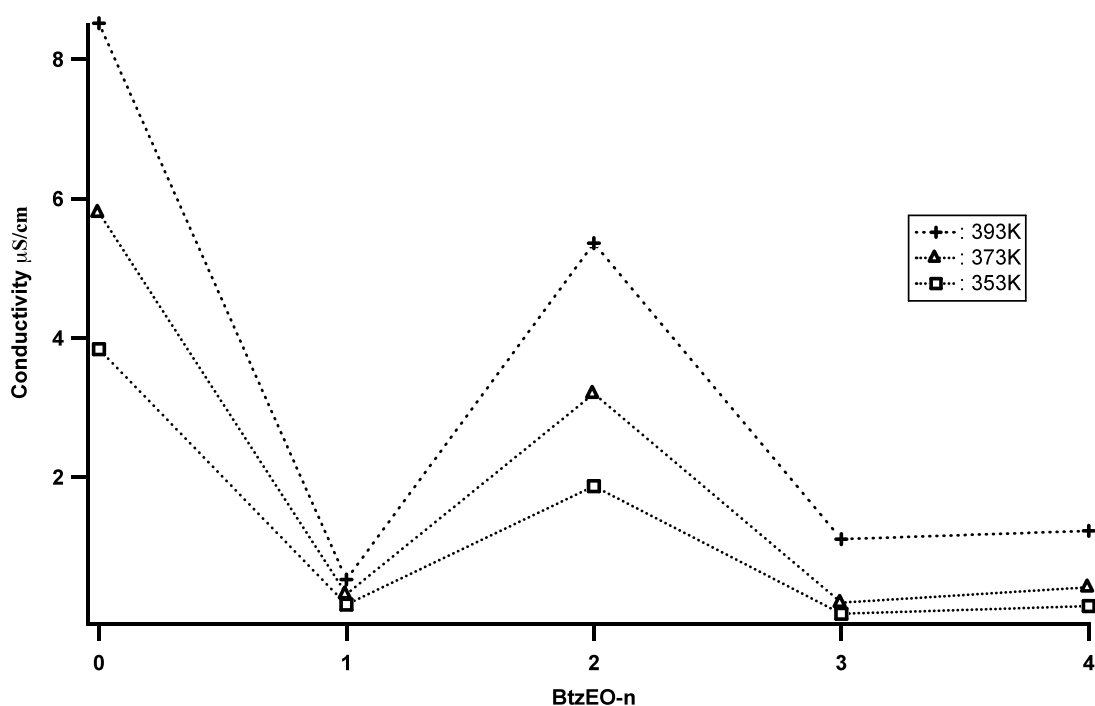


Figure 4.17 Conductivity of BtzEO-n (0-4):PEGDME-1K composites (20:1) at 353, 373, and 393K

Pristine BtzEO-n compounds, similar to bitriazole, do not show any appreciable conductivity at temperatures up to 120°C. Contrary to our initial thought, the conductivity plots in Figure 4.17 show that the BtzEO-0 (i.e., plain bitriazole) gives higher conductivities than all the other BtzEO-n compounds sampled at temperatures up to 120°C. In addition, the conductivity does not appear to follow a dependence on the T_m or the T_g of new compounds. Since proton conductivity is believed in bitriazole to occur via structural diffusion, the spacing between the bitriazole molecules must come into play and appears critical to the proton conductivity process. Plain bitriazole associated with PEGDME in the amorphous state can undergo free rotation and conformational changes to a much easier extent than

BtzEO-n compounds due to its size. The conformational changes needed by the BtzEO-n compounds with PEGDME will be dictated by a combination of their size, flexibility, and bitriazole arrangement. Figure 4.17 shows that among BtzEO-n compounds, BtzEO-2 with two ethylene oxide units between the bitriazoles gives the highest conductivities up to 120°C. The conductivity experiments of these BtzEO-n composites further supports the notion of structural diffusion along the bitriazole protons and suggests that the hopping distance and molecular conformation in the amorphous phase are critical to creating a clear pathway for the protons to move through.

4.3.3.5 Effect of polymer type

We attempted to probe the synergistic effects between bitriazole and the PEGs by investigating the effect of other flexible polymers on proton conductivity. If conductivity were governed only by the free volume of conformational changes in the polymer, then we would expect that the use of a different polymer with similar molecular weight and flexibility (i.e. similar T_g) should give comparable results. Towards this end, we chose polypropylene glycol (PPG) with a similar $M_n \sim 1000$ as our probe polymer. This polymer unlike PEG is completely amorphous (no melt transition) and shows a similar T_g to PEG and PEGDME (lit. values $\sim -70^\circ\text{C}$). In theory, PPG should be just as flexible (if not more) as PEG and should give comparable conductivity values as the bitriazole-PEG-1K composites.

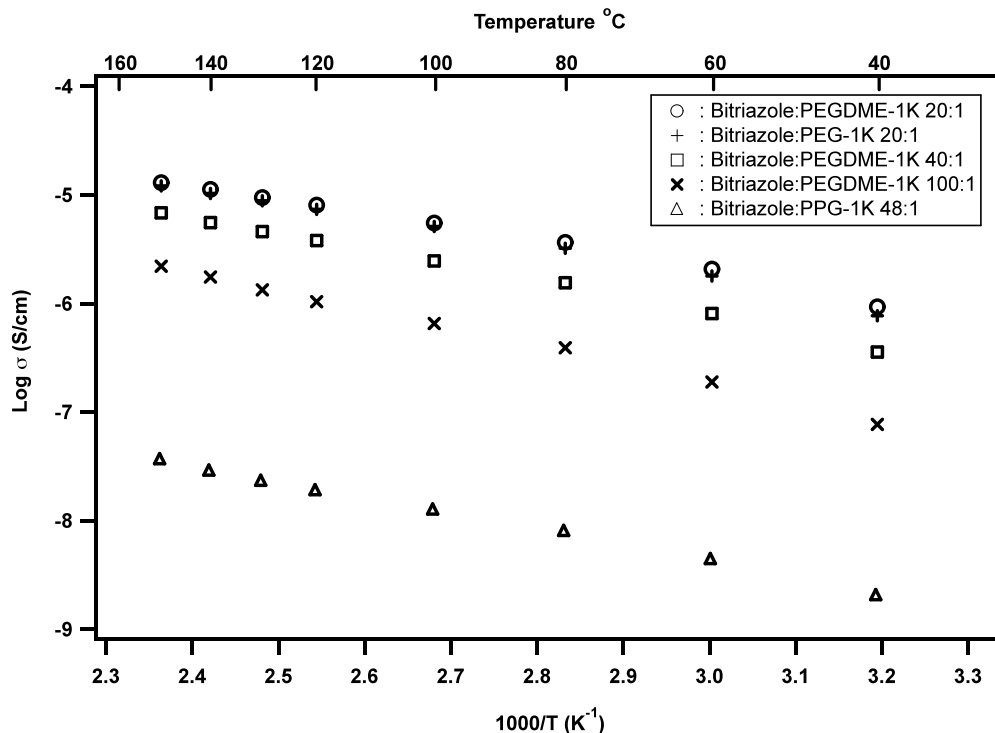


Figure 4.18 Conductivity plots of bitriazole with PEG, PEGDME, and PPG polymers. All polymers have a $M_n \sim 1000$.

PPG-1K was mixed with bitriazole at a 16:1 ratio. This was done to maintain a 1:1 bitriazole-to-propylene oxide ratio. The bitriazole to PEG and PEGDME ratios in all the composites were confirmed by ^1H NMR, after conductivity experiments, to be the same as the initial loading. However, with PPG, leaching was observed during composite preparation suggestive of poor incorporation of the PPG polymer. ^1H NMR after the conductivity experiment gave a bitriazole to PPG ratio of 48:1 as reported in Figure 4.18. The conductivity vs. temperature plot of the bitriazole:PPG composite gives much lower values when compared to the 40:1 or even the 100:1 bitriazole:PEGDME composites. This significant difference in conductivity between the two polymers indicates that the conductivity enhancement observed in the bitriazole:PEGDME composites is not a sole function of segmental motion. In addition, the difference highlights the importance of the

ethylene oxide group and suggests a cooperative interaction between the ethylene oxides and the bitriazole proton. Since ethylene oxides are known as excellent cationic chelators due to their electron donating properties, these groups may promote proton conduction by interrupting the strong hydrogen bonds between the bitriazole molecules. This specific chelating interaction is absent in the PPG composite, possibly due to the presence of the extra methyl group, which deters association with the bitriazole proton either via hydrophobicity or steric hindrance.

4.3.4 Probing the synergistic effect between bitriazole and PEGDME via solid and liquid state ^1H NMR

In an effort to further probe and understand the synergistic effect between bitriazoles and the ethylene oxides in bitriazole:PEGDME composites, we looked to solid- and liquid-state ^1H NMR techniques to provide some information about the structural properties of these composites.

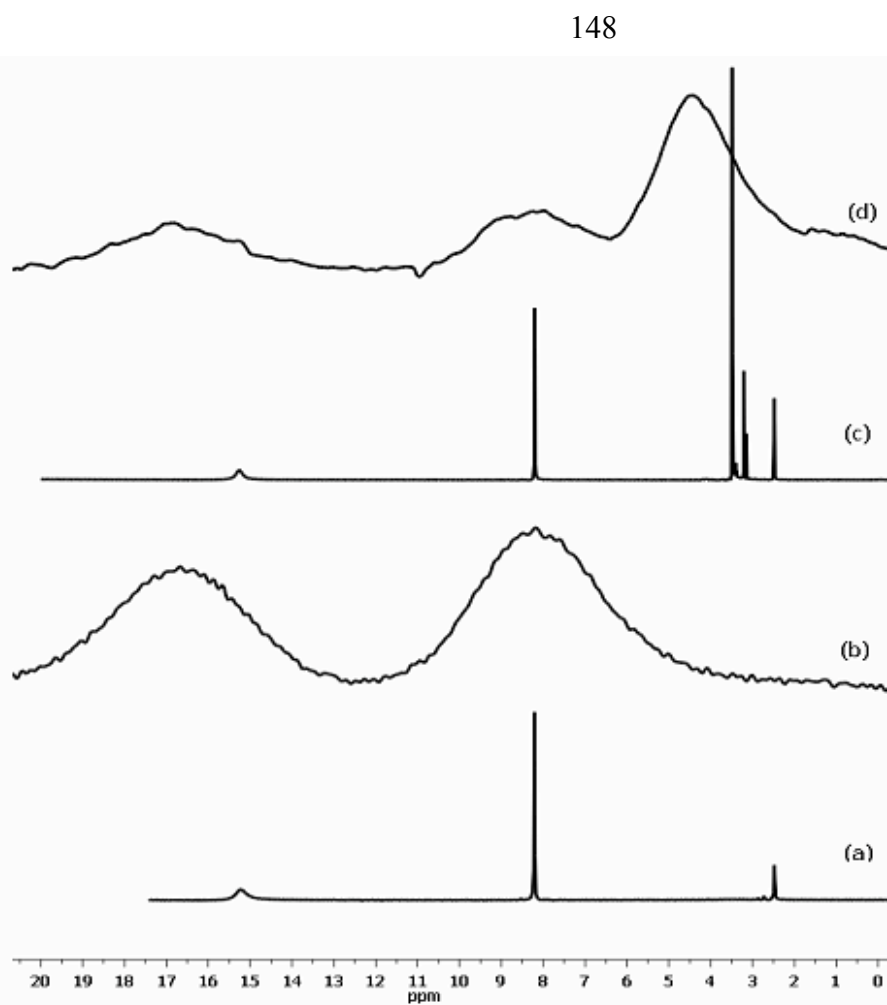
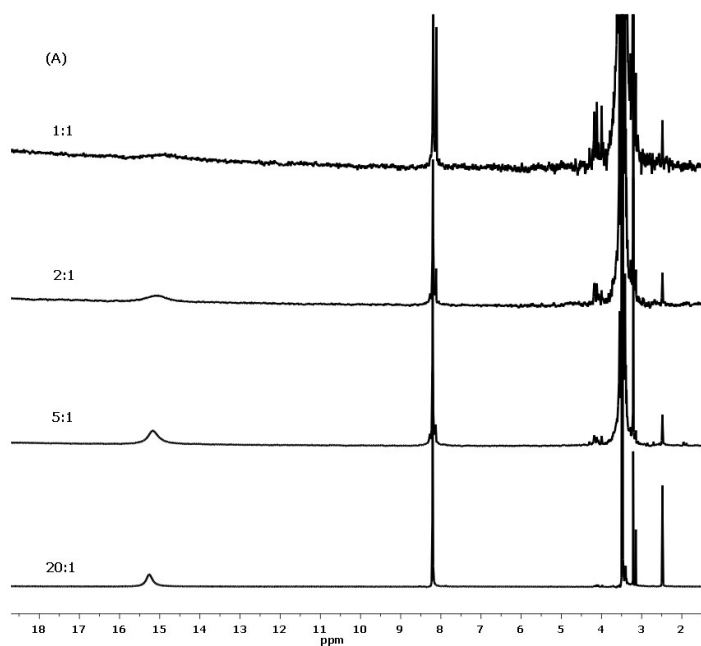


Figure 4.19 Room temperature solid-state ^1H MAS NMR at spin speed of 13 kHz of (b) bitriazole and (d) bitriazole:PEGDME-1K (20:1), and liquid ^1H NMR in DMSO-d_6 of (a) bitriazole and (c) bitriazole:PEGDME-1K (20:1). Residual proton peak for DMSO appears at 2.35 ppm

Both the solid- and liquid-state ^1H NMRs of bitriazole and its PEGDME composite were almost identical, as expected. In the liquid ^1H NMR, the C-*H* proton appeared at 8.21 ppm as a sharp singlet while the N-*H* proton appeared further downfield at 15.26 ppm as a broad averaged singlet. However, due to residual strong dipolar coupling in the solid-state MAS NMR, the C-*H* and N-*H* protons appeared as broad averaged resonances (full width at half max of 3.7 ppm) with peak centers at 8.2 ppm and 16.7 ppm, respectively. The large downfield shift of the N-*H* proton, which typically occurs around 8-10 ppm in the liquid state

of other NCHs, such as imidazole and benzimidazole, is due to extensive intra- and intermolecular hydrogen bonding between bitriazole molecules. The ^1H NMR of the bitriazole:PEGDME-1K (20:1) composite, both in the liquid and solid state (Figure 4.19), looks like a superimposition of bitriazole and PEGDME (not shown) ^1H NMR spectra, i.e., no new peaks or shifts was observed. However, in the liquid-state NMR, when the ratio of bitriazole to PEGDME is decreased from a 20:1 to 1:1 ratio, two new peaks at 8.11 and 8.20 ppm arise, as shown in Figure 4.20.



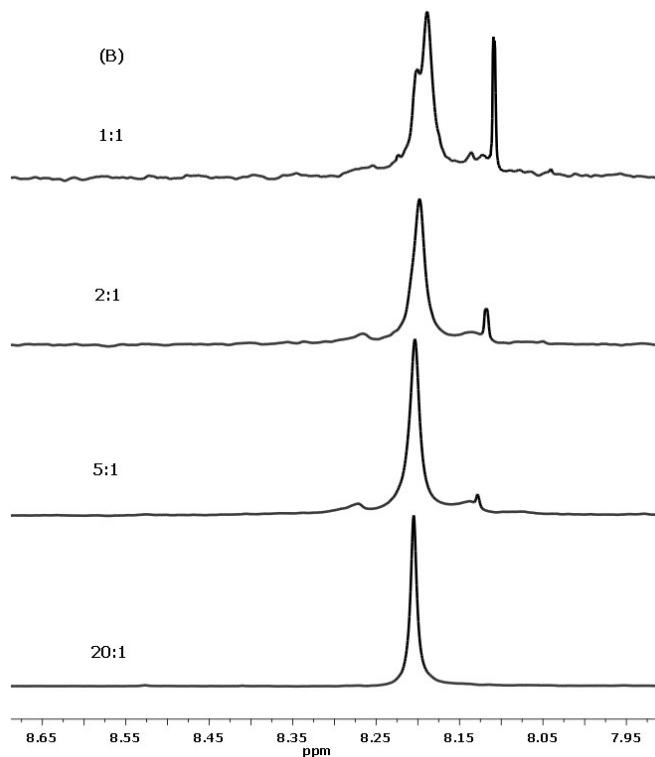


Figure 4.20 (A) ^1H NMR (liquid) in $\text{DMSO-}d_6$ of bitriazole:PEGDME-1K with increasing PEGDME fraction from 20:1 to 1:1., (B) expanded region from (A)

As the fraction of PEGDME increases, the intensity of the 8.11 and 8.21 ppm peaks increase and the intensity of the N-*H* peak at 15.3 ppm decreases. This proton is associated with the nitrogen atom on the bitriazole as confirmed by a D_2O shake test. The upfield N-*H* shift is suspected to be due to interruption of the strong intermolecular hydrogen bonds between the bitriazoles by the ethylene oxides in PEGDME, which are known to form complexes with metal cations in solution. The hydrogen bonds formed between the ethylene oxides of PEGDME and the N-*H* of the bitriazole, i.e., N-*H*...O, are weaker (~ 1.9 kcal/mol) than those between two bitriazoles, i.e. N-*H*...N (~ 3.1 kcal/mol).²⁵ These weaker hydrogen bonded bitriazole protons will appear upfield from their strongly bound counterparts. It is interesting to note that these new peaks only appear at high PEGDME concentrations. Thus,

it appears that multiple ethylene oxides are needed to break apart the strong hydrogen bonds between the bitriazoles.

The 8.11 and 8.20 ppm N-*H* protons were not seen in the solid-state NMR due to the broad signals (Figure 4.19). To investigate the possible role of these N-*H* protons in the conductivity, we carried out the liquid-state NMR of bitriazole-PPG-1K at a 1:1 ratio for comparison.

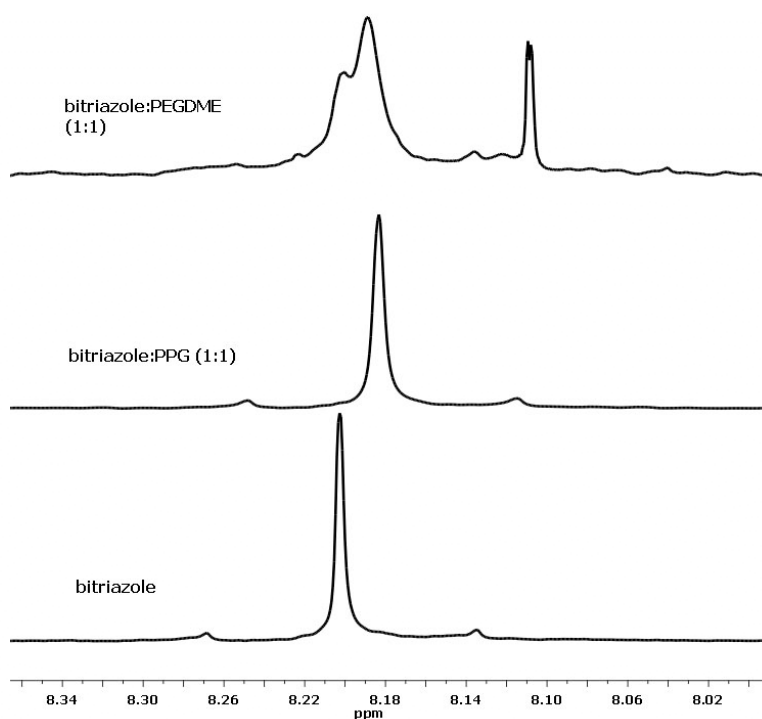


Figure 4.21 ¹H NMR of bitriazole, bitriazole:PPG (1:1) and bitriazole:PEGDME (1:1) in DMSO-*d*₆ (expanded region)

The 8.11 and 8.21 ppm protons were absent in the bitriazole:PPG-1K 1:1 complexes (Figure 4.21). This is most likely due to steric destabilization as a result of the extra methyl group in propylene oxide, which may also be the reason for the poor observed proton conductivity (Figure 4.18). We believe that the 8.11 and 8.20 ppm protons seen in Figure 4.20 are present in the solid state, albeit at very low concentrations, and these protons are

responsible for the observed proton conductivity. This can be rationalized by examining the way the composite materials were created. The composite is prepared via evaporation of a methanol solution containing both dissolved bitriazole and PEGDME in a 20:1 ratio. As the methanol slowly evaporates, small precipitates begin to form from the saturated solution. Since the solubility of the PEGDME in methanol is much higher than bitriazole and bitriazole is present in excess, the fraction of bitriazoles in the primary precipitates must be much higher than 20:1. Further along during evaporation, this ratio decreases and a polymer rich phase is obtained. Thus, although mixed at a 20:1 ratio, the composite material contains bitriazole-rich regions, as well as PEGDME-rich regions with bitriazole:PEGDME ratios approaching or exceeding 1:1. We believe the latter, though present in small amounts is responsible for the proton conductivity seen via the observed upfield 8.11 and 8.20 ppm peaks.

4.4 Further discussion and conclusion

The unique conductivity of acids in water has been explained by structural diffusion, whereby a proton hops within hydrogen bonds, following the center of symmetry of the evolving hydrogen bond coordination from one cluster to the next.²⁶⁻²⁹ This transfer is mediated by significant local dynamics with respect to the formation and cleavage of hydrogen bonds within protonated bulk ionic water clusters. Reconstruction of the protonic environment by expansion of the static water cluster via the construction of new hydrogen bonds ultimately leads to the formation of a clear path for fast proton movement. By adapting some of these key principles that allow for fast proton motion in water, such as extensive hydrogen bonds and significant local dynamics as it pertains to hydrogen bond cleavage and reconstruction, we have designed a new amphoteric water-like NCH, 4,4-1*H*-1*H*-bi-1,2,3-triazole and investigated its ability to conduct protons via cooperative interactions with PEGDME.

Our goal in this work was to explore the origin and mechanism of proton conductivity in the bitriazole-PEGDME composites. This was accomplished by systematically varying different aspects of the individual components in order to understand their contributions and thus the requirements for conductivity. We began by taking a look at the properties of bitriazole, as those for PEGDME were already well known from literature. Bitriazole was chosen for its extensive hydrogen bonding network capabilities, as it is able to potentially form four hydrogen bonds per molecule, similar to water. With regards to conductivity, the strong, extensive, hydrogen-bonded network in bitriazole (as evidenced by the stability of its crystal structure up to 150°C) precludes the possibility of the significant local dynamics needed for efficient proton transport. Thus, water-free pristine bitriazole shows no appreciable

conductivity between room temperature and 150°C. In order to introduce significant mobility and thus dynamics into the bitriazole network, PEGDME was incorporated at a 20:1 bitriazole-to-PEGDME ratio, so as to achieve a 1:1 bitriazole-to-ethylene oxide ratio. The introduction of PEGDME (Figure 4.7) led to a significant reduction in the bitriazole crystallinity at room temperature and to a higher extent at 150°C. The decrease in bitriazole crystallinity, i.e., the creation of more amorphous regions, resulted in proton conductivity, which increased with increasing temperature (Figure 4.9). In order to probe the source of this conductivity, we carried out a kinetic isotope effect (KIE) measurement.

KIE experiments are used gain information on certain aspects of the mechanism of a reaction such as the role, if any, of the isotopically substituted nuclei (in our case the N-*H* proton) in the rate-determining step (R.D.S). Upon isotopic substitution of the bitriazole N-*H* proton to N-*D* (Figure 4.10), an Arrhenius conductivity plot was generated for the *d*-bitriazole-PEGDME-1K composite, and the ratio of k_H/k_D was obtained over a range of temperatures (Figure 4.11). The magnitude of the KIE (> 1.7 at room temperature) implies a primary kinetic isotope effect. This means that the bitriazole N-*H* proton is involved in the R.D.S, and confirms our assumption that the bitriazole proton is responsible for proton conductivity. The calculated value is on the lower end of primary KIEs and falls below the theoretical value of 4.2 (calculated from the N-*H* and N-*D* vibrational frequencies) for full N-*H* dissociation. This implies that the N-*H* bond is only partially broken in the transition state. In order to apply this information towards a mechanism of proton transfer, we need to identify the nature of the rate-determining step. To do this, we systematically modified the polymer concentration, length, and type so as to gain some information on the polymer properties required for conductivity.

The PEGDME concentration was varied by increasing the bitriazole fraction in the composite from 20:1 to 100:1. Increasing the bitriazole fraction led to lower conductivities at all temperatures. In addition, each of the Arrhenius plots in Figure 4.12 presented a slight curvature, which typically is a sign of a VTF-type behavior indicating the influence of polymer segmental motion on ion transport. This behavior was verified by fitting the curves perfectly to the VTF relationship (Equation 4.1) and obtaining fit parameters given in Table 4.2. This data illustrated that although the source of protons is increasing, i.e., increasing bitriazole content, the actual maximum number of protons that can partake in the conductive process decreases, as represented by the decrease in σ_0 . The reason for this is explained by the vanishing mobility, T_0 , which increases with increasing bitriazole fraction indicating that the mobility in the composite decreases as the bitriazole content increases. Thus, segmental motion via the fluid regions of PEGDME plays a large role in constructing a pathway for proton motion.

To investigate the possibility of proton hopping along the PEGDME chain, we examined the effect of longer PEG chains as well as PEGs bearing terminal acidic groups with different pKa values on conductivity. Proton conductivity with longer PEG chain composites (Figure 4.14) decreased with respect to the shorter PEG-1K composite due to the decrease in mobility of the longer PEGs. However, above a M_n of 4000 there seemed to be no appreciable change in conductivity with increasing PEG length. Incorporating acidic groups that are unable to protonate the bitriazole, such as terminal hydroxyl and carboxylic acid groups (Figure 4.15), did not lead to any increase in conductivity. If proton hopping were simply occurring via the PEG ether groups, then the terminal carboxylic acid groups would increase the conductivity, since the acidic pKa of this group is lower than that of the

acidic pKa of bitriazole. However, when terminal sulfonic acid groups capable of protonating the basic bitriazole nitrogen were incorporated, the conductivity increased by threefold at high temperatures. This implies that although proton conductivity necessitates PEGDME, the hopping process occurs via movement of the bitriazole protons along bitriazole molecules (i.e., via structural diffusion). This point was further strengthened by the results from the di-bitriazolyl ethylene oxides which showed that the hopping distance between bitriazoles along with molecular conformation were critical parameters to ensure proton motion through the composites.

With the picture almost complete, we turned to address the nonconvergence of the normalized $\text{Log } \sigma_0$ vs. $1/T-T_0$ plots in Figure 4.13 also observed by Coughlin et al. in some of their triazole-based heterocyclic polymers. This nonconvergence could indicate that the dilution effect on proton carrier density is being masked by some other cooperative effect between the PEG and the bitriazole. Another possibility could be that we simply didn't go high enough in temperature to observe the convergence with the different amounts of PEGDME. Since the T_g of all the polymers are quite low ($\sim -70^\circ\text{C}$), and the T_m is surpassed by over 100°C , the latter scenario doesn't seem likely. To address the former point, we probed the specific effect of the PEGDME by creating a bitriazole composite with a PPG amorphous polymer with the same molecular weight and similar flexibility (i.e., similar T_g). The Arrhenius plots based on this polymer showed much lower conductivities when compared to the PEGDME composites (Figure 4.18). This indicated that flexibility and segmental motion in the PEGDME bitriazole composites are not the only factors responsible for proton conductivity.

Probing the system further via solid-state NMR did not yield any results due to the broad nature of the peaks arising from residual strong dipolar coupling. However, probing the liquid ^1H NMR revealed new peaks at 8.11 and 8.20 ppm in the NMR as the PEGDME concentration in the composite increased (Figure 4.20). These peaks were absent in pure bitriazole and bitriazole-PPG composites at the same ratios. The two new peaks were N-*H* peaks, as confirmed by a D_2O shake test. The upfield shift of the N-*H* proton is likely due to the interruption of the strong hydrogen bonds in bitriazole by the ethylene oxides of the PEGs. The multiple ethylene glycols required to affect this change attests to the strength of the intermolecular hydrogen bonds between the bitriazole molecules even in solution, where the bitriazoles are suspected to be present as oligomeric clusters. The ability to break apart these clusters in solution decreases the amount of crystalline bitriazole network formed after solvent evaporation in the solid state, thus increasing the proton conductivity.

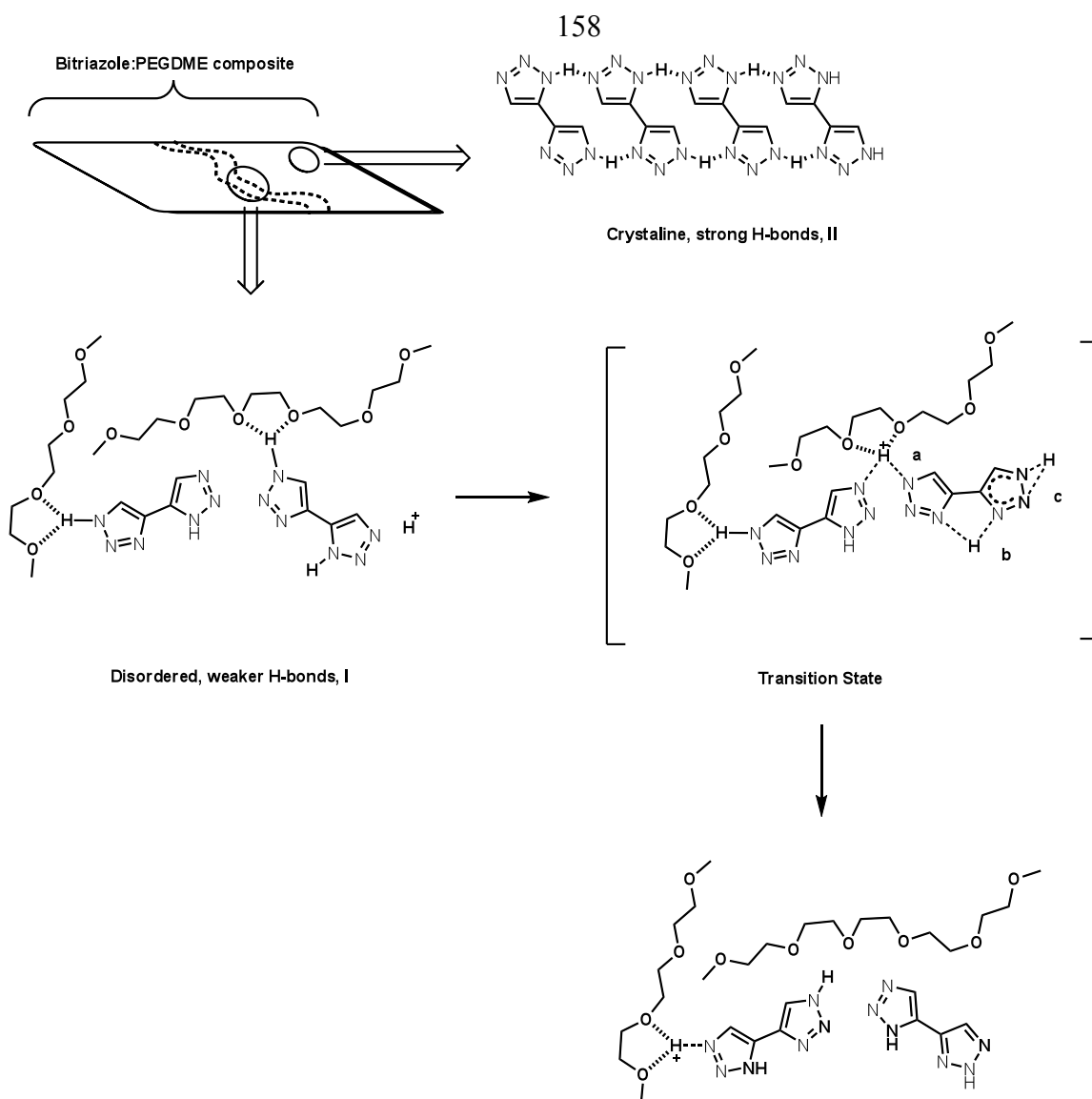


Figure 4.22 Proposed proton conduction mechanism. One of several possible pathways for proton conduction

Based on the data collected, the proton conductive pathway in the bitriazole-PEGDME system involves three key steps. The first is the formation of an amorphous polymer-rich bitriazole phase (I, Figure 4.22) from the liquid phase due to positive interactions between the ethylene glycols in PEGDME and the bitriazole proton. This is created within a within a crystalline bitriazole network (II, Figure 4.22), which provides the structural mechanical integrity for the composite. Second, the mobility of the polymer

increases with temperature and infuses segmental motion into the polymer-rich bitriazole phase, which contains bitriazole molecules associated possibly via weak hydrogen bonds to the ethylene oxides in PEGDME. The proton being transferred most likely arises from intra- or intermolecular autoprotolysis of bitriazole (defect sites), similar to that in water. Third, segmental motion as a result of PEGDME leads to significant local dynamics, which fosters proton transfer via structural diffusion from one mobile bitriazole molecule to the next due to their amphoteric nature. Triazoles unlike imidazoles are tautomeric and can thus undergo intramolecular 1,2 prototropic shifts from the N3 (C_s) to the N2 (C_v) position.³⁰ With bitriazoles, there is also the possibility of intramolecular proton transfer between the two triazole rings. Thus, the transition state could involve a combination of any one of the three states illustrated in Figure 4.22 (a, b, c). What we do know is that, based on the data from the KIE experiment, the proton is not fully dissociated in the transition state but bridges between two nitrogen atoms, which is consistent with three proposed modes of transfer.

This work presents several results confirming the concept of anhydrous proton conductivity via structural diffusion of the bitriazole proton in a polymer-rich region within a crystalline nonconductive bitriazole framework. A rich amorphous phase with high segmental mobility is essential, along with ethylene oxide groups, which increase the amount of available protons via positive interactions with the NCH. In addition, acidic groups with pKa values lower than the basic pKa of the NCH are crucial to obtaining higher conductivities at elevated temperatures. Thus, these results provide valuable information for the design and further development of future polymeric NCHs as polymer electrolyte membranes for fuel-cell and other electrolyte applications.

4.5 Experimental

Materials

Sodium azide, copper iodide, trimethylsilyl azide, polyethylene glycol dimethyl ether ($M_n \sim 1000$, 4000, and 8000 g/mol), polyethylene glycol dimethyl ether ($M_n \sim 1000$), polypropylene glycol ($M_n \sim 1000$), and polyethylene glycol dithiol were purchased from Sigma-Aldrich and used as received. Polyethylene dicarboxylic acid was purchased from Quanta Bio-design. 1,4-dichlorobut-2-yne was purchased and used as received from Alfa Aesar. All solvents were purified by fractional distillation from the appropriate drying agents or dried by filtration through the appropriate drying agents prior to use.

Instrumentation

^1H and ^{13}C liquid NMR (300 MHz) spectra were obtained on a Varian Mercury-300 NMR Spectrometer with samples dissolved in either d-chloroform or d-dimethylsulfoxide (DMOS-d_6). ^1H and ^{13}C solid-state CP MAS NMR spectra were recorded at 10-13 kHz using a Bruker Avance 500 MHz spectrometer with a 4 mm rotor. Thermogravimetric analyses (TGA) were performed on a Netzsch STA 449 C with Pt/Rh crucibles. The samples were heated under argon or air at a heating rate of $10^\circ\text{C}/\text{min}$ for all data collections. Mid-infrared spectra were recorded on a Nicolet 800 FTIR spectrometer. Powder X-ray diffraction patterns were collected using a Scintag XDS 2000 diffractometer using Cu $k\text{-}\alpha$ radiation. The temperature-programmed X-ray diffraction sample measurements were performed on the same diffractometer using a Scintag high-temperature chamber equipped with a Pt-Rh alloy sample

holder/strip heater. The chamber was connected to a dry argon flow. Glass transition and melting temperatures were obtained by differential scanning calorimetry (DSC) using a Perkin-Elmer DSC-7 with a heating rate of 10°C/min under nitrogen flow. Electrochemical impedance data was obtained using a Solatron 1287 potentiostat/1260 frequency response analyzer. The composites were sandwiched between two platinum blocking electrodes and dried *in situ* in a Buchi oven under purging argon for at least 12 hrs prior to measurement. Sample measurements were obtained during cooling by applying a 100 mV excitation voltage with a logarithmic frequency sweep from 1×10^{-1} Hz to 1×10^6 Hz. Resistance values were taken at the minimum imaginary response in a Z' vs. Z'' plot to determine the conductivity in the low-frequency limit.

Synthesis of 4-Ethynyl-1*H*-1,2,3-triazole

To an aqueous solution of sodium azide (6.58 g, 0.101 moles in 30 g H₂O) was added 1,4-dichlorobut-2-yne (25 g, 0.203 moles) in methanol (120 mL). The resulting solution was protected from light with aluminum foil and stirred at 30 °C for 24 hours. After 24 hours, a sodium chloride precipitate was visible and a solution of sodium hydroxide (20 mL of a 50% NaOH solution) in methanol (600 mL) was added, and mixing was continued at 30°C for another 24 hours. The mixture was worked up by diluting with 250 mL of distilled water followed by titration with hydrochloric acid until a pH of 5-6 was attained. The aqueous methanol solution was then extracted with ether (500 mL, 4X), dried over magnesium sulfate and concentrated under vacuo. The solid obtained was purified via recrystallization from dichloromethane to give 2.9g of the desired product. ¹H NMR (DMSO-d₆), δ (ppm) 4.40 (s, 1H), 8.19 (s, 1H), 15.4 (bs, 1H). FAB+ (M+H) 94.02

Synthesis of 4,4'-1*H*,1'*H*-1,2,3-bitriazole

Trimethylsilylazide (4.63 g, 40.2 mmol) was added to a stirring mixture of 4-ethynyl-1*H*-1,2,3-triazole (2.49 g, 26.8 mmol) and copper iodide (255 mg, 5 mol%) in purged DMF/MeOH (40 mL, 8:1). The resulting mixture was stirred under argon for 16 hours at 100°C. The mixture was cooled to room temperature, filtered over celite and washed lightly with methanol. The solvents were removed under vacuo and the resulting brown solid was re-suspended in methanol and heated to reflux. The insolubles were filtered out and discarded and the remaining solution was again dried under vacuo. The deep yellow solid obtained was washed with methanol at room temperature to remove the yellow coloration and the resulting light brown solid was dried under vacuo for 1 hour and subsequently sublimed at 195°C/< 0.1 mtorr to give the 1.1 g of the desired product as a white solid (yield 30%). ¹H NMR (DMSO-d₆), δ (ppm) 8.21 (s, 2H), 15.26 (bs, 2H). ¹³C NMR (DMSO-d₆), δ (ppm) 128.5, 138.3. FAB+ (M+H) 137.05

Synthesis of polyoxoethylene bis(azides)

Polyoxoethylene bis(azides) were synthesized from their halide precursors following a literature preparation³¹ via a reaction with NaN₃ and KI in DMF at 75°C overnight. When a bromide precursor was used, the addition of potassium iodide was not necessary. The halide precursors were either purchased or synthesized via a standard halogenation reaction of their glycol precursors with SOCl₂ and DMF.³¹

General procedure for the synthesis of polyoxoethylene di(4,4'-1*H*,1'*H*-1,2,3-bitriazole)

4-Ethynyl-1*H*-1,2,3-triazole and Cu(I)Br were placed in a flask and purged with argon. Degassed DMF was added and the mixture was stirred for a few minutes. Polyoxoethylene bis(azide) dissolved in 1 mL of degassed DMF was added to the mixture. The reaction was stirred at 60°C for 15 hours. After cooling, DMF was removed on the rotovap and the waxy residue was mixed with methanol and sonicated at 40°C for 1 hour. The grey suspension formed was removed via centrifugation (3000 x g) and the methanol solution was concentrated.

1,5-di(4,4'-1*H*,1'*H*-1,2,3-bitriazol)-1-yl-3-oxa-pentane (BtzEO-1): 4-Ethynyl-1*H*-1,2,3-triazole (267 mg, 2.87 mmol), CuBr (95 mg, 50 mol%), degassed DMF (5 mL), 1-azido-2-(2-azidoethoxy)ethane (200 mg, 1.31 mmol). The desired product was recrystallized from MeOH in 17% yield. ¹H NMR (DMSO-*d*₆), δ (ppm) 3.87 (t, 4H), 4.58 (t, 4H), 8.12 (s, 2H), 8.37 (s, 2H), 15.03 (bs, 2H). FAB+ (M+H) 343.15

1,8-di(4,4'-1*H*,1'*H*-1,2,3-bitriazol)-1-yl-3,6-dioxa-octane (BtzEO-2): 4-Ethynyl-1*H*-1,2,3-triazole (257 mg, 2.76 mmol), CuBr (91 mg, 50 mol%), degassed DMF (5 mL), 1,2-bis(2-azidoethoxy)ethane (250 mg, 1.26 mmol). The desired product was purified via flash chromatography (CH₂Cl₂:MeOH 10:1) to give a yield of 21%. ¹H NMR (DMSO-*d*₆), δ (ppm) 3.87 (t, 4H), 4.58 (t, 4H), 8.12 (s, 2H), 8.37 (s, 2H), 15.03 (bs, 2H). ¹³C NMR (DMSO-*d*₆), δ (ppm) 123.06, 70.05, 69.25, 50.18. FAB+ (M+H) 387.18

1,11-di(4,4'-1*H*,1'*H*-1,2,3-bitriazol)-1-yl-3,6,9-trioxa-undecane (BtzEO-3): 4-Ethynyl-1*H*-1,2,3-triazole (209.3 mg, 2.25 mmol), CuBr (74.3 mg, 50 mol%), degassed DMF (5 mL), 1,11-diazido-3,6,9-trioxaundecane (250 mg, 1.02 mmol). The desired product was purified via flash chromatography (CH₂Cl₂:MeOH 10:1). ¹H NMR (DMSO-*d*₆), δ (ppm) 3.43 (d, 4H), 3.48 (d, 4H), 3.81 (t, 4H), 4.55 (t, 4H), 8.09 (s, 2H), 8.41 (s, 2H), 15.05 (s, 0.64H), 15.42 (s, 0.28H), 15.89 (s, 0.04H). ¹³C NMR (DMSO-*d*₆), δ (ppm) 139.8, 131.64, 123.1, 70.25, 70.17, 69.23, 50.19. FAB+ (M+H) 431.20

1,14-di(4,4'-1*H*,1'*H*-1,2,3-bitriazol)-1-yl-3,6,9,12-tetraoxa-tetradecane (BtzEO-4): 4-Ethynyl-1*H*-1,2,3-triazole (177.4 mg, 1.91 mmol), CuBr (62.9 mg, 50 mol%), degassed DMF (4 mL) and 1,14-diazido-3,6,9,12-tetraoxatetradecane (250 mg, 0.867 mmol). The desired product was purified via flash chromatography (CH₂Cl₂:MeOH 10:1) to give a yield of 60%. ¹H NMR (DMSO-*d*₆), δ (ppm) 3.43 (m, 4H), 3.49 (m, 2H), 3.82 (t, 4H), 4.57 (t, 4H), 8.17 (s, 2H), 8.43 (d, 2H), 15.20 (bs, 2H). ¹³C NMR (DMSO-*d*₆), δ (ppm) 123.02, 70.35, 70.22, 70.19, 69.25, 50.20. FAB+ (M+H) 475.23

Synthesis of 4,4'-1*D*,1'*D*-1,2,3-bitriazole

4,4-1*H*,1*H*-1,2,3-bitriazole was dissolved in d-H₂O and heated to 85°C for 4 hours. The aqueous mixture was then cooled and lyophilized overnight. The resulting solid was re-dissolved in d-MeOH and heated at 50°C for 1 hour. The methanol solution was cooled, and dried under vacuo at 60°C to give the desired compound in 100% yield. ¹H NMR (DMSO-*d*₆), δ (ppm) 8.22 (s, 1H). ²H Solid-state MAS NMR δ (ppm) 12.9 (broad)

Synthesis of PEG-bis-SO₃H

To a 4 mL vial containing PEG dithiol ($M_n \sim 1500$, 0.5 g) dissolved in acetic acid (0.5 mL) was added cooled peracetic acid (1 mL, 0°C). The reaction was stirred for 2 hours and the solvents were removed via lyophilization. The residual acetic acid was removed via heating to 50°C under vacuum. Oxidation was confirmed by titration.

Preparation of 4,4-1*H*,1*H*-1,2,3-bitriazole:PEG composites

The desired ratio of 4,4-1*H*,1*H*-1,2,3-bitriazole to poly(ethylene oxide) was dissolved in anhydrous methanol. The mixture was heated for a few minutes to ensure complete dissolution and stirred at room temperature for another 15 minutes. The methanol was then removed and the resulting solid was dried for 3 hours under vacuum (500 mtorr). 20 mg of the dried solid was weighed out, placed in a 6.1 mm die set sandwiched between two platinum blocking electrodes (6 mm circular plates) and pressed at 2000 lbs for 1-2 minutes. Average pellet thickness fell between 100-300 μm .

4.6 References

1. Kreuer, K. D., *Solid State Ionics* **1997**, 94, (1-4), 55-62.
2. Kreuer, K. D.; Fuchs, A.; Ise, M.; Spaeth, M.; Maier, J., *Electrochimica Acta* **1998**, 43, (10-11), 1281-1288.
3. Bozkurt, A.; Meyer, W. H.; Wegner, G., *Journal of Power Sources* **2003**, 123, (2), 126-131.
4. Li, S. W.; Zhou, Z.; Zhang, Y. L.; Liu, M. L.; Li, W., *Chemistry of Materials* **2005**, 17, (24), 5884-5886.
5. Liu, Y. F.; Yu, Q. C.; Yuan, J.; Ma, L. L.; Wu, Y. H., *European Polymer Journal* **2006**, 42, (9), 2199-2203.
6. Pu, H. T.; Liu, G. H., *Polymers for Advanced Technologies* **2004**, 15, (12), 726-730.
7. Yamada, M.; Honma, I., *Polymer* **2004**, 45, (25), 8349-8354.
8. Yamada, M.; Honma, I., *Polymer* **2005**, 46, (9), 2986-2992.
9. Zhou, Z.; Li, S. W.; Zhang, Y. L.; Liu, M. L.; Li, W., *Journal of the American Chemical Society* **2005**, 127, (31), 10824-10825.
10. Schuster, M.; Meyer, W. H.; Wegner, G.; Herz, H. G.; Ise, M.; Schuster, M.; Kreuer, K. D.; Maier, J., *Solid State Ionics* **2001**, 145, (1-4), 85-92.
11. Schuster, M. F. H.; Meyer, W. H.; Schuster, M.; Kreuer, K. D., *Chemistry of Materials* **2004**, 16, (2), 329-337.
12. Subbaraman, R.; Ghassemi, H.; Zawodzinski, T. A., *Journal of the American Chemical Society* **2007**, 129, (8), 2238-+.
13. Persson, J. C.; Jannasch, P., *Chemistry of Materials* **2003**, 15, (16), 3044-3045.

14. Herz, H. G.; Kreuer, K. D.; Maier, J.; Scharfenberger, G.; Schuster, M. F. H.; Meyer, W. H., *Electrochimica Acta* **2003**, 48, (14-16), 2165-2171.
15. Persson, J. C.; Jannasch, P., *Solid State Ionics* **2006**, 177, (7-8), 653-658.
16. Persson, J. C.; Jannasch, P., *Chemistry of Materials* **2006**, 18, (13), 3096-3102.
17. Woudenberg, R. C.; Yavuzetin, O.; Tuominen, M. T.; Coughlin, E. B., *Solid State Ionics* **2007**, 178, (15-18), 1135-1141.
18. Surangkana Martwiset, R. C. W., Sergio Granados-Focil, Ozgur Yavuzcetin, Mark T. Tuominen, E. Bryan Coughlin, *Solid State Ionics* **2007**, *In press*.
19. Cowie, J. M. G.; Cree, S. H., *Annual Review of Physical Chemistry* **1989**, 40, 85-113.
20. Deng, W. Q.; Molinero, V.; Goddard, W. A., *Journal of the American Chemical Society* **2004**, 126, (48), 15644-15645.
21. Ratner, M. A.; Shriver, D. F., *Chemical Reviews* **1988**, 88, (1), 109-124.
22. Ratner, M. A., In *Polymer Electrolyte Reviews*, Elsevier Applied Science: New York, 1987; p 173.
23. Goward, G. R.; Schuster, M. F. H.; Sebastiani, D.; Schnell, I.; Spiess, H. W., *Journal of Physical Chemistry B* **2002**, 106, (36), 9322-9334.
24. Rostovtsev, V. V.; Green, L. G.; Fokin, V. V.; Sharpless, K. B., *Angewandte Chemie-International Edition* **2002**, 41, (14), 2596-+.
25. Emsley, J., *Chemical Society Reviews* **1980**, 9, (1), 91-124.
26. Kreuer, K. D., *Chem. Mater.* **1996**, 8, (3), 610-641.
27. Kreuer, K. D., *Solid State Ionics* **2000**, 136, 149-160.
28. Agmon, N.; Goldberg, S. Y.; Huppert, D., *Journal of Molecular Liquids* **1995**, 64, (1-2), 161-195.

29. Agmon, N., *Chem. Phys. Lett.* **1995**, 244, (5-6), 456-462.
30. Lunazzi, L.; Parisi, F.; Macciantelli, D., *Journal of the Chemical Society-Perkin Transactions 2* **1984**, (6), 1025-1028.
31. Toth, E.; van Uffelen, I.; Helm, L.; Merbach, A. E.; Ladd, D.; Briley-Saebo, K.; Kellar, K. E., *Magnetic Resonance in Chemistry* **1998**, 36, S125-S134.

Chapter V

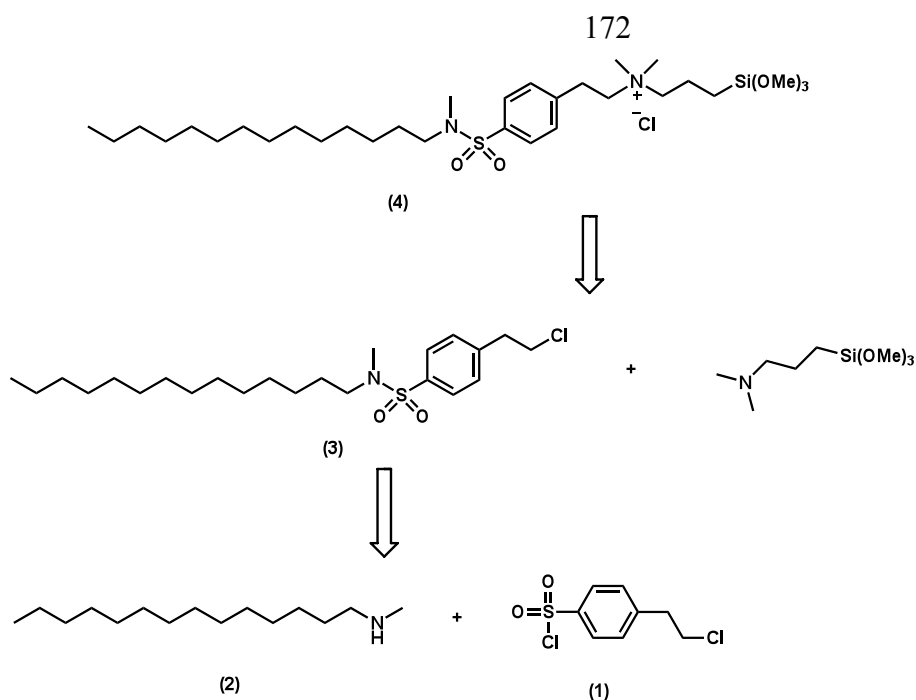
Future Directions and Recommendations

5.1 Abstract

The results in Chapters II and III demonstrate a new approach to high organic incorporation onto the interior pore walls of mesostructured silicates and the advantages of using such a technique towards increasing proton conductivity. Although we were able to demonstrate a positive correlation between acid density and proton conductivity as a proof of concept in these organosilicates, their actual conductivities are too low to be used as actual PEMs in DMFCs. In this chapter, a few recommendations are offered both at the molecular and material level towards increasing the proton conductivity of these acid functionalized organosilicates. In addition, techniques to augment the conductivities of bitriazole-PEG composites under anhydrous conditions without sacrificing membrane integrity are also discussed.

5.2 Increasing the acid strength of densely packed organosilicates

Although we were able to show enhanced conductivities resulting from an increased organic acid density, the absolute values of the proton conductivities obtained were only moderate at best, especially when compared to the proton conductivity of Nafion ($\sim 10^{-2}$ S/cm at room temperature). The low conductivities are the result of the low acid dissociation constant of the carboxylic acid group, which was used only for a proof of concept. For practical device purposes, such as use as PEMs, the conductivities of these silicates under fully humidified conditions will have to be up in the 10^{-2} - 10^{-1} S/cm range. To do this, we need to incorporate stronger acids such as sulfonic acids into the pores of these silicates. However, data from Chapter II indicate that post functionalization does not go to completion due to tight organic packing, which results in steric hindrance during post modification. In order to achieve a homogeneous acid density over the entire interior surface, the desired sulfonic acid functional group will have to be incorporated into the surfactant structure and cleaved thereafter. This can be achieved by masking the sulfonic acid within the surfactant as a sulfonamide functional group. Sulfonamides are prepared from the reaction of an amine with a sulfonyl chloride in the presence of a base. Aryl sulfonamides are stable to alkaline hydrolysis and thus will be stable to the alkaline hydrothermal silicate synthesis. The schematic for the preparation of a surfactant bearing an aryl sulfonamide group is shown in Scheme 5.1 below.



Scheme 5.1 Retrosynthesis for the preparation of aryl sulfonamide surfactant

After sol-gel synthesis of the organosilicate, the resulting aryl sulfonamide bonds can be cleaved via acid hydrolysis to generate densely packed aryl sulfonic acid groups within the pore space of the organosilicates. Varying the position of the sulfonamide bond within the surfactant by using different methylene chain lengths in compounds (1) and (2) will lead to the preparation of sulfonic acid modified silicates with different degrees of interior hydrophobicity.

5.3 Conductivity enhancement via thin films

The mesostructured organosilicates prepared in Chapters II and III were all in the powder form with a wide distribution of particle sizes (2-50 μm), as determined by SEM. The performance of these silicates as stand-alone proton conductive membranes, especially under nonhumidified conditions, will be highly dependent on the silicate particle size due to

grain boundary effects. Grain boundaries in the absence of water as a medium act as electrical shorts to proton conduction. Thus, in order to realize the full potential of these organosilicates, proton conductivity through their channels will have to be maximized. This can be achieved for silicates with a 3-D interconnected pore structure, such as MCM-48, via the preparation of continuous thin films. Inorganic thin films have several desirable properties such as high strength, thermal stability, and uniformity. Thin films of mesoporous solids have been prepared as free-standing films at air-water and oil-water interfaces¹⁻³ and on various supports by solvent evaporation,⁴ flow field induction,⁵ dip coating,⁶ and spin coating.⁷

However, with regards to 2-D noninterconnected silicates such as MCM-41, the orientation of the channels in the thin films have to be aligned perpendicularly to the plane of the thin film in order to reap the benefits of direct proton conduction down the pore channels. Orientation of the pore channels in MCM-41 silicates has been achieved in supported thin films by techniques such as flow-field induction,⁵ magnetic field alignment,⁸ and pulsed laser deposition.⁹ Pore channel alignment has also been achieved within the pores of anodic alumina membranes by evaporation-induced self assembly.¹⁰ Our synthetic approach to the incorporation of organic groups at a high density within the pore channels is compatible with all the aforementioned techniques for thin film preparation, and should thus yield thin-film acidic organosilicates that can be used as PEMs in fuel cells. In addition, preparation of these organosilicates as thin films will confine methanol permeation strictly through the pore channels, which, as shown in Chapter III can be tailored with different organic tail lengths to deter methanol permeation without sacrificing conductivity.

5.4 Incorporation of bitriazole/PEG composites into pore space of acid modified organosilicates

In Chapter IV, we presented results confirming structural diffusion of protons in the polymer-rich region of bitriazole-PEG composites encapsulated within a crystalline non-conductive bitriazole network. The latter provides the membrane with its structural integrity. As part of our investigation, we observed increasing conductivities with decreasing PEG molecular weights due to higher mobilities. Unfortunately, PEGs with molecular weights under 1000 could not be used due to their low melting point. For example, the use of a 500 molecular weight PEG polymer led to the complete collapse of the bitriazole-PEG composite membrane. Another factor that led to an increase in conductivity, albeit only at higher temperatures, was incorporation of sulfonic acid groups at the distal ends of the PEG. However at low temperatures, the presumed higher T_g of the polymer resulted in lower conductivities. These barriers to further conductivity enhancement can be overcome by impregnating the pores of mesoporous organosilicates, prepared as thin films, with the bitriazole-PEG composites. The pore channels of the organosilicates should serve as a container or host to the bitriazole-PEG, mixture ensuring its structural stability irrespective of the length and amount of PEG used (so long as the pores are large enough to accommodate the PEG). Incorporation of organic acid groups on the surface of the silicate, such as the sulfonic acids suggested in Section 5.2, should serve as an additional proton source and thus increase the conductivity without sacrificing mobility. The overall mobility of the bitriazole-PEG mixture within the silicate pore space will hinge on the pore size of the silicate, which can be tailored via the introduction of organic additives as swelling agents during sol-gel synthesis.¹¹

5.5 References

1. Brown, A. S.; Holt, S. A.; Dam, T.; Trau, M.; White, J. W., *Langmuir* **1997**, 13, (24), 6363-6365.
2. Ryoo, R.; Ko, C. H.; Cho, S. J.; Kim, J. M., *Journal of Physical Chemistry B* **1997**, 101, (50), 10610-10613.
3. Yang, H.; Coombs, N.; Sokolov, I.; Ozin, G. A., *Nature* **1996**, 381, (6583), 589-592.
4. Ogawa, M., *Journal of the American Chemical Society* **1994**, 116, (17), 7941-7942.
5. Hillhouse, H. W.; Okubo, T.; vanEgmond, J. W.; Tsapatsis, M., *Chemistry of Materials* **1997**, 9, (7), 1505-&.
6. Lu, Y. F.; Ganguli, R.; Drewien, C. A.; Anderson, M. T.; Brinker, C. J.; Gong, W. L.; Guo, Y. X.; Soyez, H.; Dunn, B.; Huang, M. H.; Zink, J. I., *Nature* **1997**, 389, (6649), 364-368.
7. Huang, L.; Kawi, S.; Hidajat, K.; Ng, S. C., *Microporous and Mesoporous Materials* **2005**, 82, (1-2), 87-97.
8. Tolbert, S. H.; Firouzi, A.; Stucky, G. D.; Chmelka, B. F., *Science* **1997**, 278, (5336), 264-268.
9. Gimon-Kinsel, M. E.; Balkus, K. J., *Microporous and Mesoporous Materials* **1999**, 28, (1), 113-123.
10. Platschek, B.; Petkov, N.; Bein, T., *Angewandte Chemie-International Edition* **2006**, 45, (7), 1134-1138.
11. Beck, J. S.; Vartuli, J. C.; Roth, W. J.; Leonowicz, M. E.; Kresge, C. T.; Schmitt, K. D.; Chu, C. T. W.; Olson, D. H.; Sheppard, E. W.; Mccullen, S. B.; Higgins, J. B.; Schlenker, J. L., *Journal of the American Chemical Society* **1992**, 114, (27), 10834-10843.

PART II

Targeted Nanoparticles for siRNA Delivery

Chapter VI

Introduction

6.1 Nanoparticle-based nucleic acid delivery

The use of therapeutic nucleic acids such as short interfering RNAs (siRNA) to silence disease-causing genes has enjoyed limited success due to numerous biological barriers. Those specifically inherent to siRNAs are their instability in plasma due to degradation by ubiquitous nucleases and the potential for off-target effects.¹ Other biological barriers inherent to the systemic administration of any therapeutic drug include macrophage and other non-specific uptake pathways, arrival at the desired organ location, recognition by the desired target tissues within the organ space, immune response, cellular entry and lysosome degradation within the cell.² With regards to siRNAs, most of these barriers can be circumvented by using nanoparticle-based delivery vehicles that protect the encapsulated nucleic acids and ensure their delivery and release only at the desired site. Navigation of nanoparticle-based therapeutic agents through these biological barriers is accomplished via passive and active targeting to desired disease sites by tuning their unique size and surface properties.

6.2 Targeting nanoparticles: passive and active delivery

6.2.1 Passive targeting

The small size of therapeutic nanoparticles (i.e., sub-100 nm) enables them to extravasate through blood vessels and tissue, especially tumor tissue, which are often dilated and fenestrated with an average pore size less than a micron compared to normal tissue.³⁻⁵ Passive targeting of nanoparticle-based delivery vehicles occurs as a result of the enhanced permeability and retention (EPR) effect,⁶ a process by which submicron-size particles

selectively accumulate in tumor tissue due to the leaky vasculature and poor lymphatic drainage that result from rapidly dividing tumor cells. Normal tissues contain capillaries with tight junctions that are less permeable to nanoparticles. Other modes of passive targeting include the use of surface charge to facilitate nanoparticle adhesion to negatively charged cell walls or targeting lymphoid organs such as lymphatic vessels and spleen that function as filtration devices. Upon arrival at the disease site, cellular internalization of the nanoparticle is required for biological activity.

Nanoparticles with diameters under 200 nm are typically internalized via clathrin-coated pits, while larger particles are internalized via caveole membrane invaginations.^{7, 8} Other internalization mechanisms exist, such as nonspecific fluid pinocytosis and phagocytosis and receptor-mediated endocytosis. All uptake mechanisms listed above allow the nanoparticles to evade certain kinds of drug resistance due to transmembrane protein transporters, such as P-glycoprotein (Pgp) and multidrug resistance protein (MDRP) family,^{9, 10} that pump out anticancer drugs that diffuse into the plasma membrane. Because these transporters recognize drug in the plasma membrane, internalized particles bypass this mechanism and are able to release their cargo within the cytoplasm or endosomal vesicles, thus increasing the efficacy of the therapeutic.

6.2.2 Active targeting

Active targeting is achieved by modifying the nanoparticle surface with proteins or antibodies that specifically bind to receptors present only on certain cell types. The high specificity of the protein or antibody to the receptor displayed on the cell surface allows surface modified nanoparticles to “target” these cells. This is especially true for targets that

are readily accessible from the vasculature, such as B cell lymphoma and multiple myeloma.^{11, 12}

The primary role of active targeting is to enhance cellular uptake into target cells and to minimize the accumulation in normal tissue. This has been shown to be the case for both lipid-based¹³ and polymer-based¹⁴ nanoparticles. This implies that passive targeting of nanoparticles dictates their biodistribution and nonspecific uptake, whereas active targeting via cell-specific targeting ligands enhances intracellular uptake at the targeted disease site. As a result, the targeting ligand affinity and surface density on the nanoparticle will have a large influence on cellular uptake. The latter is a useful feature for ligands with weak affinity to their target receptors, as their overall avidity can be increased via multivalent interactions.

6.3 Targeted delivery to B-cells

Our goal in this report is to carry out antibody-mediated targeting with our well established CDP nanoparticles¹⁵⁻¹⁸ containing therapeutic oligonucleotides to epitopes expressed at the surface of cancer cells as a means of increasing site-specific therapeutic delivery. We are particularly interested in the CD20 receptor known to be expressed on pre-, naïve, and mature B cells but not on plasma cells or early pro-B cells. The CD20 receptor is thus a B-cell specific marker and has been used as a target¹⁹ for antibody therapy in patients with B-cell lymphoma. It is a tetraspan membrane protein that binds to many antibodies, including the therapeutic antibody, rituximab (anti-CD20). Although its exact function is unknown, it appears to play a role in lymphocyte activation and evidence suggests that it may also function as a calcium channel.²⁰ Rituximab targeting of the CD20 receptor has been reported as “slowly or noninternalizing” in comparison to its CD19 counterpart and mixed

reports exist with regards to the rate of internalization upon conjugation of rituximab to small molecules or nanoparticles. Thus, in this study, we wish to investigate, in a B-cell lymphoma model, the characteristics of rituximab antibody fragment targeting ligands as well as their effect on the binding, internalization, and efficacy of targeted CDP-nucleic acid therapeutic nanoparticles.

6.4 References

1. Aagaard, L.; Rossi, J. J., *Advanced Drug Delivery Reviews* **2007**, 59, (2-3), 75-86.
2. White, P. J., *Clin. Exp. Pharmacol. Physiol.* **2008**, 35, (11), 1371-1376.
3. Kondo, S.; Barna, B. P.; Morimura, T.; Takeuchi, J.; Yuan, J. Y.; Akbasak, A.; Barnett, G. H., *Cancer Research* **1995**, 55, (24), 6166-6171.
4. Monsky, W. L.; Fukumura, D.; Gohongi, T.; Ancukiewicz, M.; Weich, H. A.; Torchilin, V. P.; Yuan, F.; Jain, R. K., *Cancer Research* **1999**, 59, (16), 4129-4135.
5. Yuan, F.; Dellian, M.; Fukumura, D.; Leunig, M.; Berk, D. A.; Torchilin, V. P.; Jain, R. K., *Cancer Research* **1995**, 55, (17), 3752-3756.
6. Matsumura, Y.; Maeda, H., *Cancer Research* **1986**, 46, (12), 6387-6392.
7. Koval, M.; Preiter, K.; Adles, C.; Stahl, P. D.; Steinberg, T. H., *Experimental Cell Research* **1998**, 242, (1), 265-273.
8. Rejman, J.; Oberle, V.; Zuhorn, I. S.; Hoekstra, D., *Biochemical Journal* **2004**, 377, 159-169.
9. Chang, G., *Febs Letters* **2003**, 555, (1), 102-105.
10. Schinkel, A. H.; Jonker, J. W., *Advanced Drug Delivery Reviews* **2003**, 55, (1), 3-29.
11. de Menezes, D. E. L.; Pilarski, L. M.; Allen, T. M., *Cancer Research* **1998**, 58, (15), 3320-3330.
12. de Menezes, D. E. L.; Pilarski, L. M.; Belch, A. R.; Allen, T. M., *Biochimica Et Biophysica Acta-Biomembranes* **2000**, 1466, (1-2), 205-220.
13. Kirpotin, D. B.; Drummond, D. C.; Shao, Y.; Shalaby, M. R.; Hong, K. L.; Nielsen, U. B.; Marks, J. D.; Benz, C. C.; Park, J. W., *Cancer Research* **2006**, 66, (13), 6732-6740.

14. Bartlett, D. W.; Su, H.; Hildebrandt, I. J.; Weber, W. A.; Davis, M. E., *Proceedings of the National Academy of Sciences of the United States of America* **2007**, 104, (39), 15549-15554.
15. Belloq, N. C.; Pun, S. H.; Jensen, G. S.; Davis, M. E., *Bioconjugate Chemistry* **2003**, 14, (6), 1122-1132.
16. Davis, M. E.; Pun, S. H.; Belloq, N. C.; Reineke, T. M.; Popielarski, S. R.; Mishra, S.; Heidel, J. D., *Current Medicinal Chemistry* **2004**, 11, (2), 179-197.
17. Heidel, J. D.; Liu, J. Y. C.; Yen, Y.; Zhou, B. S.; Heale, B. S. E.; Rossi, J. J.; Bartlett, D. W.; Davis, M. E., *Clinical Cancer Research* **2007**, 13, (7), 2207-2215.
18. Pun, S. H.; Davis, M. E., *Bioconjugate Chemistry* **2002**, 13, (3), 630-639.
19. Ong, G. L.; Elsamra, S. E.; Goldenberg, D. M.; Mattes, M. J., *Clinical Cancer Research* **2001**, 7, (1), 192-201.
20. Bubien, J. K.; Zhou, L. J.; Bell, P. D.; Frizzell, R. A.; Tedder, T. F., *Journal of Cell Biology* **1993**, 121, (5), 1121-1132.

Chapter VII

Antibody Modification for Nanoparticle Targeting

7.1 Abstract

We report on the preparation rituximab antibody fragments and their conjugation to PEG adamantane linkers towards their use in the assembly of an anti-CD20 targeted CDP delivery vehicle. Rituximab IgG along with its Fab and F(ab')₂ fragments bind to the CD20 receptors on Daudi cells, albeit with different affinities. The affinity of the Fab fragment to CD20 was observed to be an order of magnitude lower than both rituximab IgG and F(ab')₂, suggestive of cooperative effects between two Fab fragments. Mono-PEGylated Fab and F(ab')₂ were successfully synthesized and the PEGylated Fab adamantane is shown to have similar binding properties with the unmodified Fab.

7.2 Introduction

Targeting ligands provide specific interactions between a therapeutic nanoparticle and the cell surface. These interactions determine the fate of the nanoparticle upon arrival at the inter-tumoral space, which is known to occur via the EPR effect. The strength of the binding interaction between the nanoparticle and its target on a cell surface is dependent on two factors. The first is the affinity of the ligand-target interaction, while the second is the targeting ligand density present on the surface of the nanoparticle; a feature particularly useful for ligands that have a weak affinity to their target receptors. Since nanoparticles have a high surface-area-to-volume ratio, multiple low-affinity targeting ligands can be affixed to their surface to allow for multivalent binding to cell-surface receptors.¹ Upon binding to the cell surface, these ligands enable the nanoparticle to enter the cells via receptor-mediated endocytosis. Recent work done in our group² and confirmed by others³ have revealed that the main role of targeting ligands is to promote cellular internalization of the nanoparticles into the cancer-bearing cells, as opposed to increasing overall tumor accumulation.

Targeting ligands include any molecule or substance that can recognize and bind to target antigens or receptors. For use *in vivo*, the target antigens or receptors must be either overexpressed or selectively expressed by particular cells or tissue components. Examples of some targeting ligands include antibodies or their fragments, peptides, other glycoproteins, carbohydrates, re-engineered proteins, hormonotoxins, growth factors, and synthetic polymers. Among this list, antibodies and their fragments are by far the most used, due to the well-known ability to raise monospecific antibodies that discretely target the numerous cell surface markers known to proliferate in human solid tumors.

The incorporation of ligands onto the surface of nanoparticles is achieved by attaching a coupling group or linker to the ligand. The most widely used coupling group is polyethylene glycol (PEG), because this polymer creates a hydrophilic surface that improves the circulation half life of the particles by shielding their cationic surface charge, thus minimizing their interactions with plasma. With regards to antibodies and proteins, attachment of the coupling agent is typically carried out by conjugating PEG polymers, with one end modified with electrophilic groups, directly or indirectly to nucleophilic functional groups present in proteins. Some of these groups include the ϵ -amino lysine groups, the α -amino N-terminal group, and the carboxylic acid C-terminal group. The latter two functional groups are typically avoided for the following reasons: The α -amino group of the N-terminal is typically situated near the complimentary determining regions (CDR) so that conjugation at this site may lead to an erosion of antibody affinity. Coupling at the C-terminal involves EDC/NHS chemistry that may lead to cross coupling between proteins. In addition to the three functional groups mentioned, other masked functional groups such as cystine disulfides and 1,2-dihydroxyl groups are also available for PEG conjugation. However, cleavage of these groups may lead to damage of the 3-D protein structure and loss of affinity.⁴ As a result, the most common and widely used functional group on proteins and antibodies for PEG modification is the ϵ -amine group on lysine residues.

The other end of the PEG polymer typically contains a molecule that can be used to incorporate the ligand-coupling agent conjugate to the nanoparticle surface. The identity of this molecule is dependent on the composition of the nanoparticle therapeutic. Over the past decade, our lab has developed a cyclodextrin-based polymer delivery system consisting of two components. The first component is a cyclodextrin-containing polycation (CDP) that is

used for nucleic acid condensation into nanoparticles,⁵⁻⁷ and the second component is an adamantane-terminated PEG polymer used for charge stabilization. The adamantane molecule interacts with the cyclodextrins on the surface of the particle via the formation of an inclusion complex. This second component can be made with a targeting ligand on the distal end. In the past, our lab has successfully investigated the use of the transferrin protein as a targeting ligand in the formulation of a targeted CDP nanoparticle system for the delivery of therapeutic oligonucleotides and plasmids to subcutaneous tumors expressing transferrin receptors in nude mice.^{4, 8, 9}

In this chapter, we report on the preparation of PEGylated antibody fragment conjugates of rituximab with adamantane groups on their distal end towards their use in the assembly of an anti-CD20 targeted CDP delivery vehicle for siRNA delivery towards the treatment of B cell lymphoma.

7.3 Results and discussion

7.3.1 Antibody specificity for CD20 on Daudi cells

Daudi (Human Burkitt's Lymphoma) cells, which are suspension cells of the B-cell lineage, were chosen as our model since they have been reported to over-express CD20 on their surface.¹⁰ To confirm the presence of CD20 on these cells in our hands, we carried out a cell binding assay with rituximab conjugated to a fluorescent dye, Alexafluro488 (AF488). We also carried out a binding study with AF488-conjugated transferrin in order to compare its relative density to CD20, being that transferrin receptors are expressed on most cells. The amount of bound protein was followed via FACS measurements.

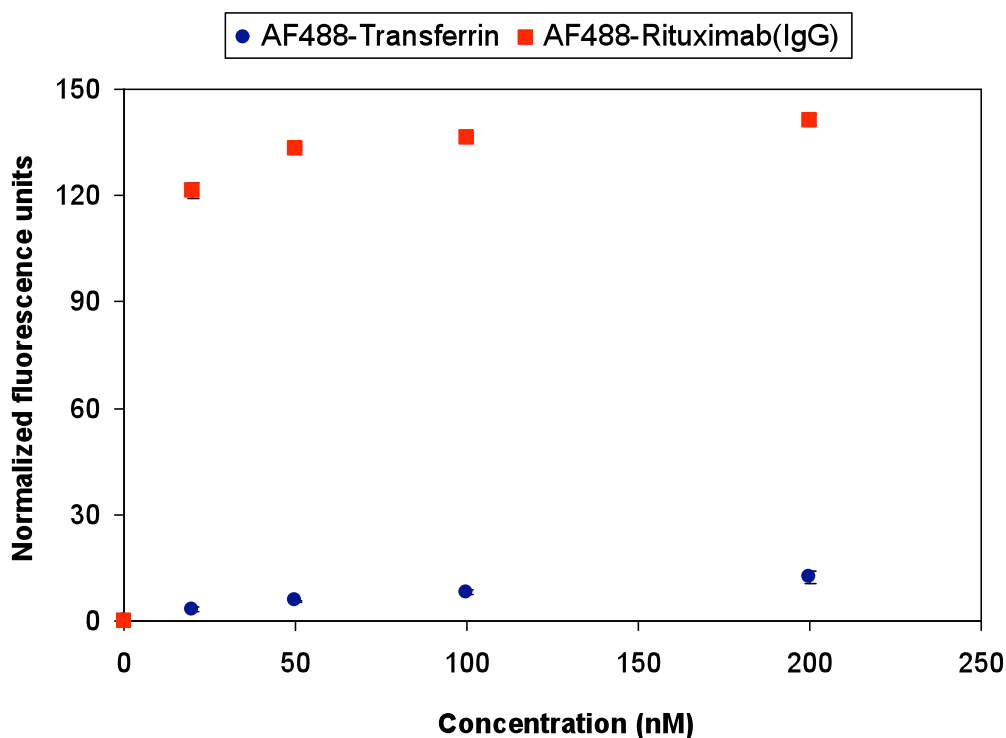


Figure 7.1 FACS of IgG-AF488 and holo-transferrin-AF488 binding to Daudi cells known to have a high density of CD20 and low density of transferrin receptors

The binding of rituximab antibody to Daudi cells at saturation is an order of magnitude higher than transferrin (Figure 7.1). This data highlights the large difference in the relative rate of CD20 and transferrin receptor expression on the Daudi cell surface. The presence of both receptors and their large relative difference in expression levels can be exploited to study the effect of receptor type and density (avidity) on the protein targeting. With regards to their use as internalization agents for nanoparticle therapeutic cellular delivery, their relative rates of internalization once bound to the surface of the nanoparticles will have to be investigated. In addition to FACS measurements, we also probed the rituximab-CD20 interaction by confocal microscopy as shown in Figure 7.2.

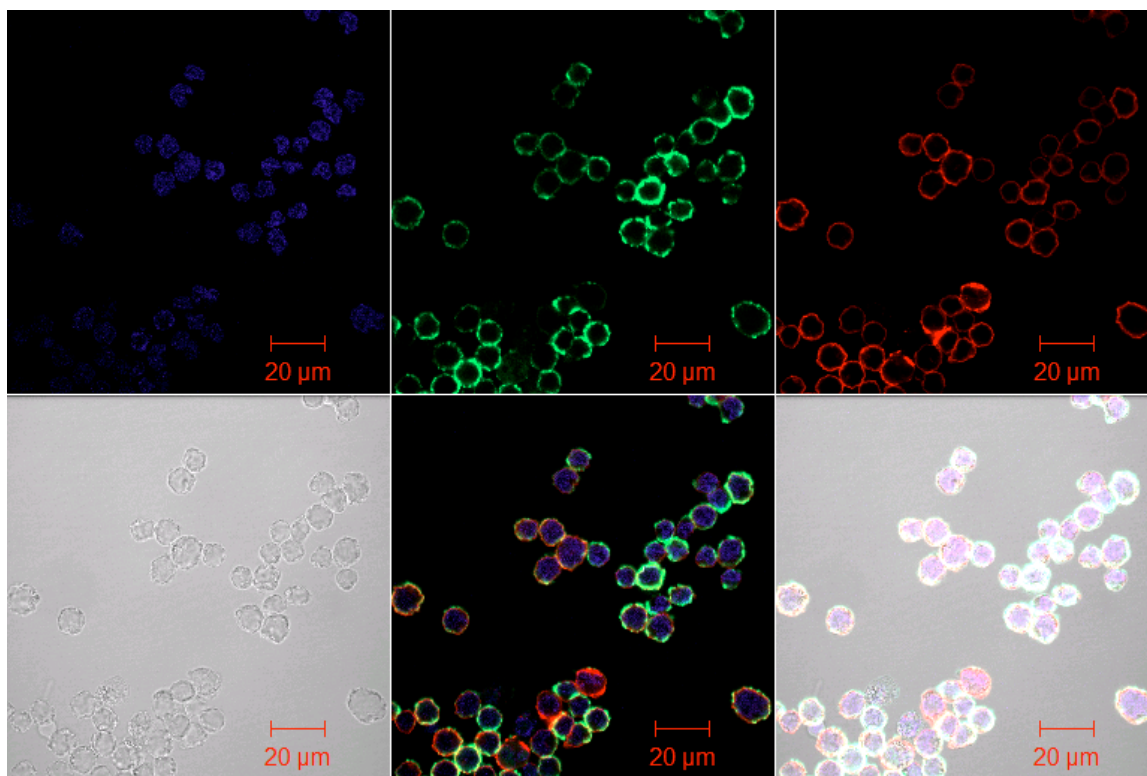


Figure 7.2 Dark and bright field fluorescence images of IgG binding to the external surface of Daudi cells that over-express CD20 receptors. IgG-Alexa (green), F-actin-phalloidin label (red), dsDNA nucleus stain (blue)

The confocal images were taken on fixed but not permeabilized cells. Both the nucleus and cytoplasm stains (DAPI and rhodamin-phalloidin) are small molecules that are able to diffuse across the cellular membrane after fixing. The images shown in Figure 7.2 were taken after 5 minutes at 4°C and are almost identical to those taken after an hour at 37°C (not shown). The images were taken at 4°C to suppress internalization or membrane recycling of the antibody. The Daudi cell nucleus occupies a large portion of the cell volume thus leaving the cytoplasm as a very thin region. Rituximab-AF488 (green) can be seen to localize on the circumference of these cells and partially overlap with the cytoplasm. However, the lack of an appreciable cytoplasmic volume and limiting resolution of the microscope prevented us from accurately determining whether the antibody is simply bound externally to the cell surface or internalized into the cytoplasm. Since rituximab is known to slowly internalize,¹¹ we believe that some rituximab antibody ends up internalized in the cytoplasm.

7.3.2 Preparation of Fab and F(ab')₂ fragments of rituximab

Although monoclonal antibodies can be highly selective for their target receptors, their properties are not ideal for continuous administration in patients, since immune responses can occur, particularly to antibodies derived from different species containing foreign regions. Antibody fragments such as Fab, F(ab')₂, diabodies, and scFv fragments lack the F_c antibody fragment, and thus the main immunogenic determinants that promote elimination via macrophage uptake or antibody-dependent cell-mediated cytotoxicity (ADCC). Elimination of the F_c region also reduces the size of the conjugate, which may or may not be detrimental, depending on its final use. For use in antibody drug conjugates

(ADCs), the smaller size of the fragments will be detrimental due to faster renal clearance rates. Alternatively, researchers have found ways around this issue by exploiting PEGylation strategies. For use as targeting agents, the smaller antibody fragment size is beneficial because a small targeting ligand will reduce the overall nanoparticle size, which may aid inter-tumor diffusion.

Cleavage of the F_c region of IgG can be done via enzymes that selectively cleave either beneath the hinge region (PEPSIN) to give $F(ab')_2$ fragments or above the hinge region (PAPAIN) to give two Fab fragments. A schematic of these two processes is given in Figure 7.3.

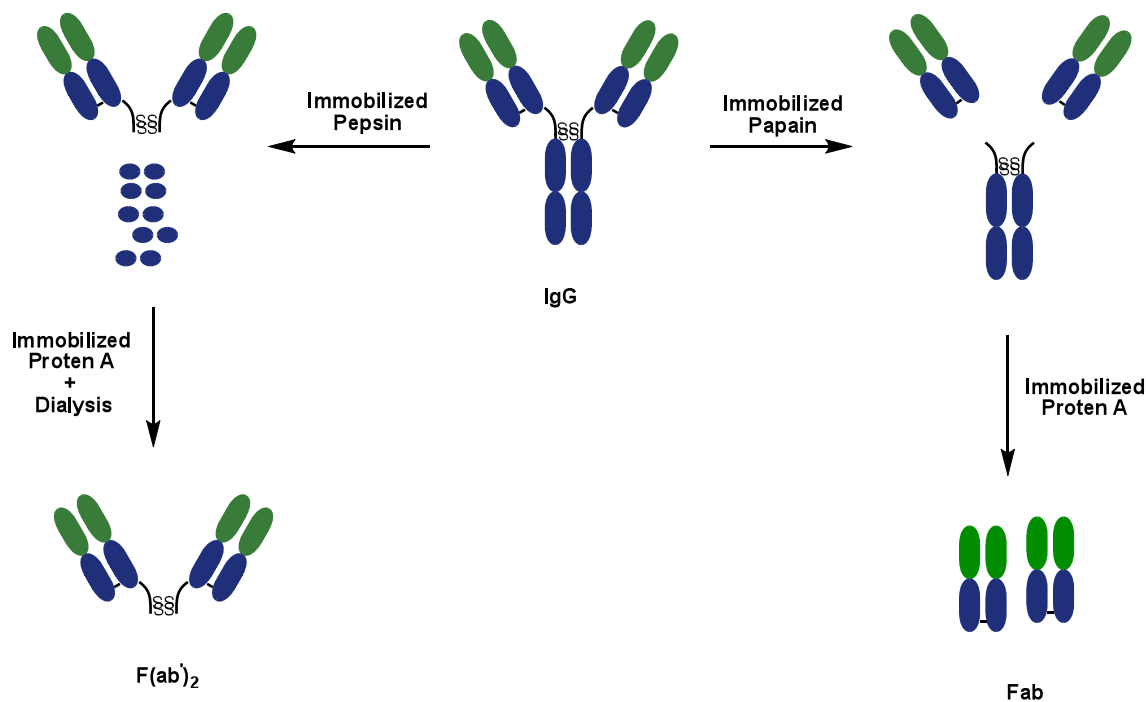


Figure 7.3 Cleavage of IgG to give Fab or $F(ab')_2$ via PEPSIN and PAPAN

The Fab fragment is generated via a nonspecific thiol-endopeptidase, papain, which enzymatically cleaves the whole IgG just above the hinge region to create two Fab fragments and one F_c fragment per antibody molecule (Figure 7.3).

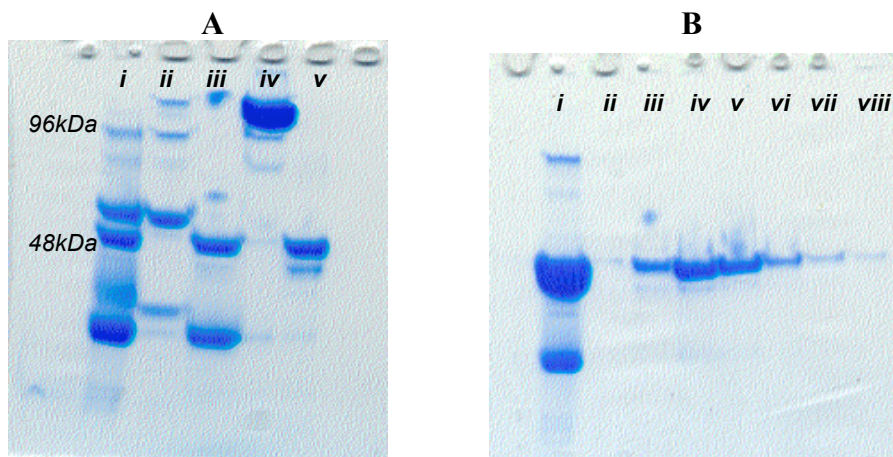


Figure 7.4 SDS PAGE Gel of PAPAINE digest; A. Lane *i*-digest, *ii*-F_c bound to protein A, *iii*-protein A flow through, *iv*-IgG-standard, *v*-Fab-standard; B. Lane *i*-crude, HPLC fractions: *ii*-34 *iii*-35 *iv*-36 *v*-37 *vi*-38 *vii*-39 *viii*-40 (minutes, see Figure S1)

The resulting mixture is purified over a protein A column that binds specifically to the F_c region of immunoglobulins, especially IgG. The polyacrylamide gel of the digest, protein A, and column flow-through in Figure 7.4A illustrates the effectiveness of the protein A column towards removing the F_c fragment that appears at 50-60 kDa. A 25 kDa fragment also appears in the protein A flow-through indicative of the heavy and light chain pieces of the Fab fragment. This is due to the reduction of the disulfide bond that holds these two fragments together. However, purification of the flow through via SEC gives the pure Fab fragment as the major peak (Figure 7.4B) and no other peaks of smaller fragments appearing after the Fab peak (Figure S.1). This suggests that the 25 kDa fragments recombine during purification to give the Fab fragment. Recombination of the disulfide bonds has been reported for Fab fragments and is suggested to be due to the strong intermolecular non-

covalent attraction between both heavy and light chains.¹² The pure Fab peak collected from the HPLC fractions (Figure 7.4B) was confirmed via MALDI with a molecular weight of ~48 kDa (Figure S.2).

The F(ab')₂ fragment is generated via a different nonspecific endopeptidase, pepsin, which enzymatically digests the F_c portion of the entire IgG right below the disulfide bonds in the hinge region. This fragment is structurally composed of two Fab fragments connected via a pair of disulfide bonds. The pepsin digest is purified over protein A column to remove undigested IgG and the flow-through is diazlyed with a 50 kDa to remove the F_c digest. The polyacrylamide gel of the pepsin digest in Figure 7.5A shows two prominent fragments. The first corresponds to F(ab')₂ and the other is an unknown fragment.

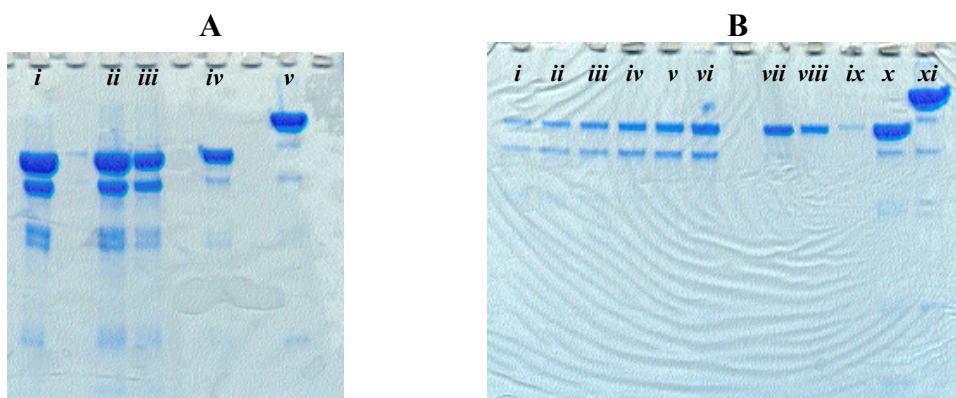


Figure 7.5 SDS PAGE Gel of PEPSIN digest; A. Gel after cleavage of IgG to F(ab')₂, *i-iii*: pepsin digest *iv*: F(ab')₂ standard, *v*: IgG standard; B. Gel after SEC purification, *i-ix*: 30 second fractions from 30.5-35 mins on HPLC (Figure S3), *x*: F(ab')₂ standard, *xi*: IgG standard

The dialyzed digest was further purified via SEC to give the pure F(ab')₂ fragment (Figure 7.5B, lanes *vii-ix*) confirmed by MALDI analysis at 96.5 kDa (Figure S4). The binding activity of the F(ab')₂ and Fab rituximab fragments relative to rituximab-IgG were analyzed via a FACS competitive binding assay (Figure 7.6).

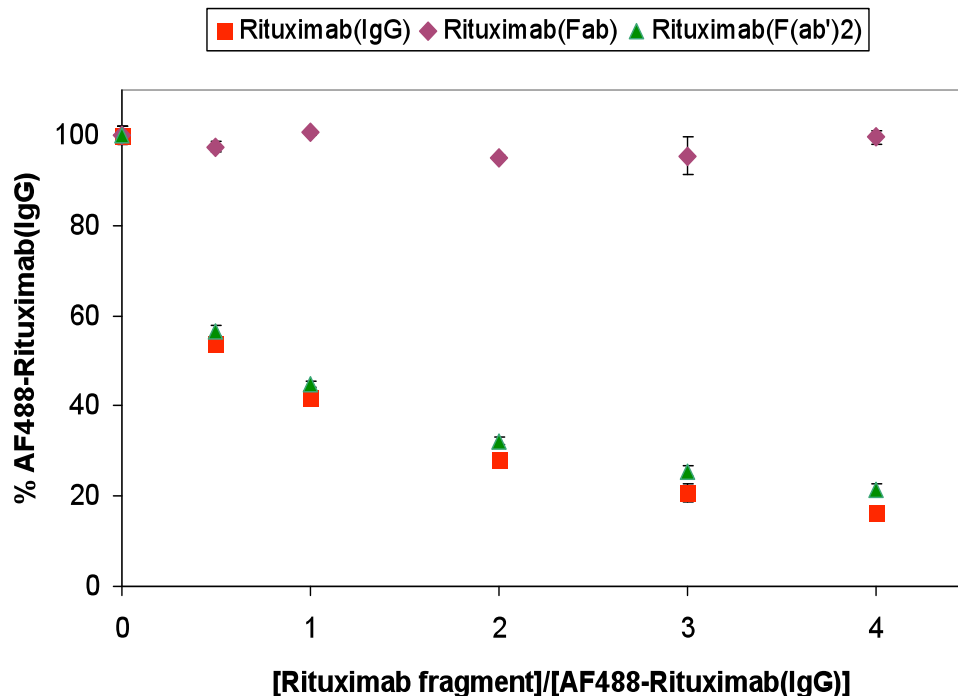


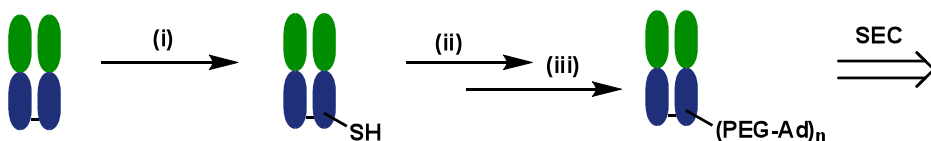
Figure 7.6 Competitive binding assay of rituximab IgG-AF488 with F(ab')₂ and Fab

A competitive binding assay involves carrying out a cell binding experiment using different ratios of a competing antibody or fragment to a fluorescently tagged competitor. The competitor in this case is rituximab IgG-AF488. The fluorescence readout, based on the amount of IgG-AF488 bound to the cell surface, should decrease as the amount of competing fragment increases as long as their affinities are similar. Figure 7.6 shows the competitive curves for rituximab IgG, F(ab')₂, and Fab fragments. The curves for the full antibody IgG and F(ab')₂ are identical, and the amount of bound IgG-AF488 decreases with increasing IgG and F(ab')₂. This indicates that the affinity of the F(ab')₂ is identical to that of the full IgG. This result is expected, because the epitope of human CD20 is bound at the large pocket formed by the CDR L3, H1, H2, and H3 of rituximab Fab.¹³ Thus, cleavage of the F_c region should in no way affect the binding of the F(ab')₂ to the CD20 receptor. In contrast, the affinity of the Fab fragment is much weaker than both IgG and F(ab')₂, as it is barely able to

compete with the rituximab IgG-AF488. Independent results from Ernst et al. report the K_d for rituximab Fab as being two orders of magnitude higher than that of rituximab IgG (63 nM vs 0.32 nM). This large difference in affinity suggests that avidity effects may play a role in the binding of rituximab to B-cells. The large relative difference in affinity between the $F(ab')_2$ and Fab fragments will be used to study the effects of affinity vs. avidity on the protein targeting of therapeutic nanoparticles. The presence of avidity effects can be probed with the Fab fragment by varying the amount of Fab ligand present on the nanoparticle surface.

7.3.3 Preparation of Fab and $F(ab')_2$ PEGylated conjugates

The Fab and $F(ab')_2$ fragments were modified with 5 kDa polyethylene glycol (PEG) polymers bearing adamantane molecules on their distal end. A schematic for the conjugation of the antibodies to the polymers is given below.



Scheme 7.1 Procedure for PEGylation of Fab (and $F(ab')_2$) fragment. (i) Trauts (10 eq.), 1 h, pH 7.5; (ii) Mal-PEG-Ad, pH 6.5, 2 h; (iii) iodoacetic acid, 1 h. $n = 0 - 4$

The ϵ -amines on the lysines of the antibody fragment are activated to thiols via a reaction with Trauts reagent. After removal of excess free thiols (hydrolyzed Trauts), the activated antibody fragment is conjugated to PEG-adamantane bearing a proximal maleimide functional group. The reaction of the thiol to the maleimide is selective at pH 6.5. The excess amine groups on the protein are protonated at this pH and thus do not react with the maleimide groups. After conjugation, excess unreacted thiols are capped with iodoacetic

acid. The entire mixture is then dialyzed and further purified via SEC. Since this synthetic procedure is carried out in a batch format, a complex mixture of products is obtained. This includes unreacted protein, PEGylated proteins with varying degrees of PEGylation, and unreacted PEG. Some of these reaction products are seen in the MALDI of the unpurified product mix shown for the reaction of Fab with Mal-PEG-Ad in Figure 7.7.

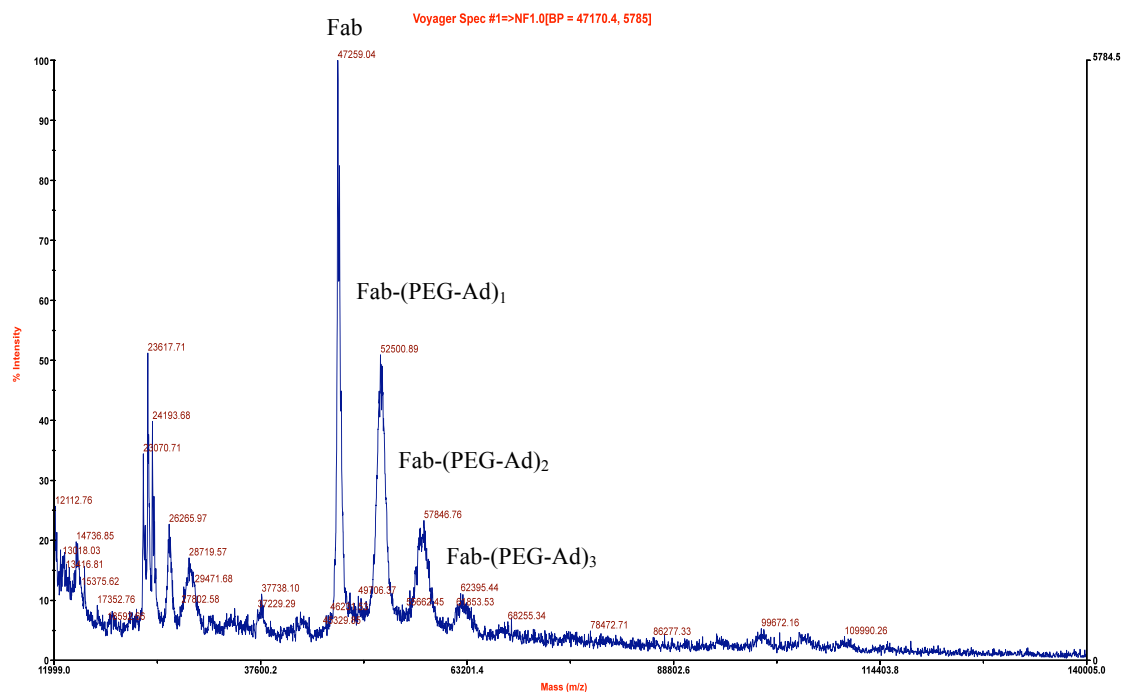


Figure 7.7 MALDI of PEGylated Fab reaction mixture

The relative intensities of the Fab proteins in Figure 7.7 are not indicative of the relative amounts of proteins present in the sample. This is because the MALDI analysis tends to ionize smaller fragments with greater ease than larger ones. In addition, the presence of PEG groups on the proteins effectively screens some of the charges present on the protein conjugates. This decreases the total available number of ionization sites, thus leading to lower intensities as the number of PEGs conjugated to the protein increases. The product mixture containing randomly PEGylated Fab proteins is purified via SEC to isolate the

mono-PEGylated fraction. Mono-PEGylated proteins are generally desirable because they give a more homogeneous product with better bioactivities than their multi-PEGylated counterparts. The improvement in bioactivity arises because a single PEG polymer has a lower probability of obstructing the binding site on a protein when compared to multiple PEG polymers. With regards to their use in nanoparticle targeting, multi-PEGylation may lead to bridging between particles causing unwanted aggregation.

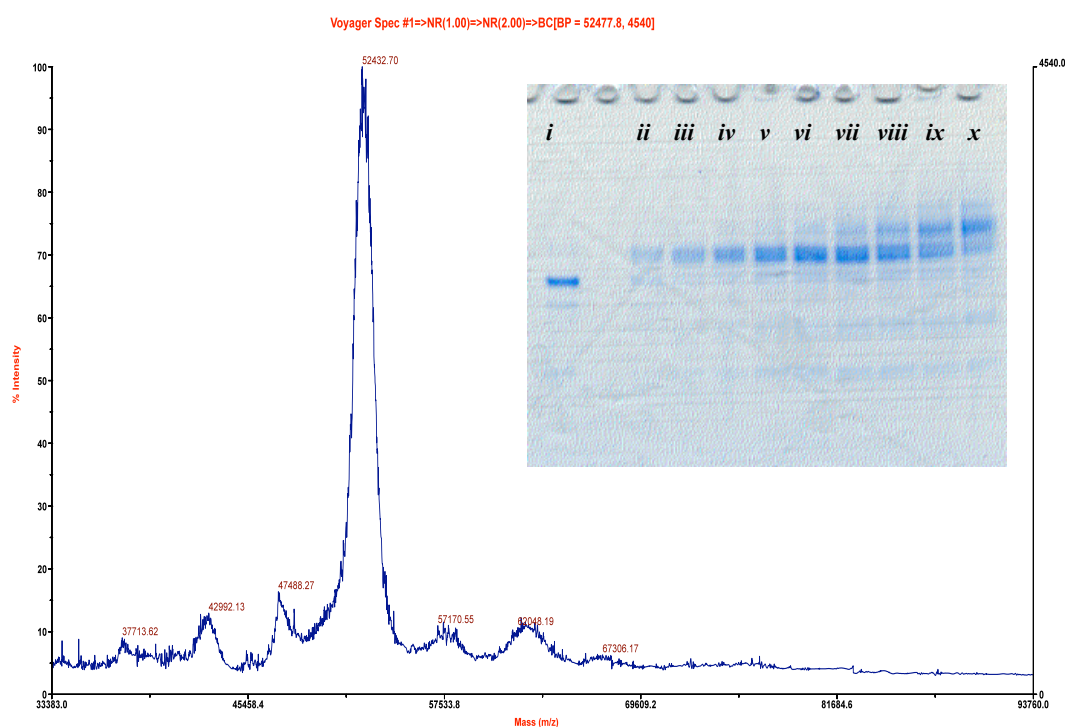


Figure 7.8 MALDI trace of purified mono-PEGylated Fab fragment. Inset shows PAGE gel of purified mono-PEGylated Fab fractions; *i*: Fab control *ii-x*: fractions 36.5 - 32.5, fractions collected every 30 seconds (Figure S5)

The mono-PEGylated fraction was isolated as the second peak in the HPLC trace (Figure S.5) and identified as a 52.5 kDa conjugate via MALDI (Figure 7.8). Since PEGs are known to behave like proteins 4 times their molecular weight (i.e., a 5 kDa PEG behaves as though it were a 20 kDa protein), the purified Fab-PEG-Ad conjugate can be discerned from

the unconjugated Fab fragment via electrophoresis on a PAGE gel (Figure 7.8 inset). The same set of reactions for the Fab conjugation shown in Scheme 7.1 was applied to the preparation of $F(ab')_2$ PEG conjugates. The MALDI for this batch reaction is shown in Figure 7.9.

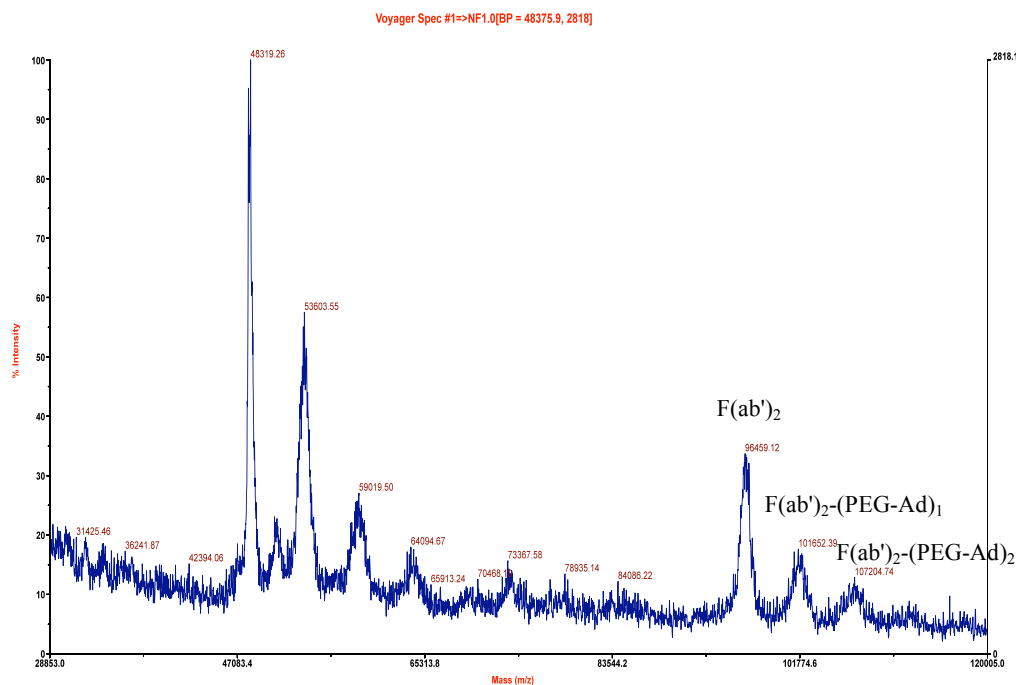


Figure 7.9 MALDI of PEGylated $F(ab')_2$ reaction mixture

Again, the MALDI bias towards smaller fragments and against PEGylated proteins is seen in the relative intensities of the $F(ab')_2$ PEGylated peaks. The peaks between 48 and 59 kDa are simply the M/Z^{2+} fragments. The SEC purified mono-PEGylated $F(ab')_2$ protein was confirmed by its MALDI peak at 101.4 kDa (Figure 7.10). PAGE gel electrophoresis also shows separation between PEGylated and unmodified $F(ab')_2$ fractions (Figure 7.10, inset) although the relative difference isn't as pronounced as that of Fab and mono-PEGylated Fab,

due to the lower resolving power of the 4-20% gradient gel for separating higher molecular weight proteins.

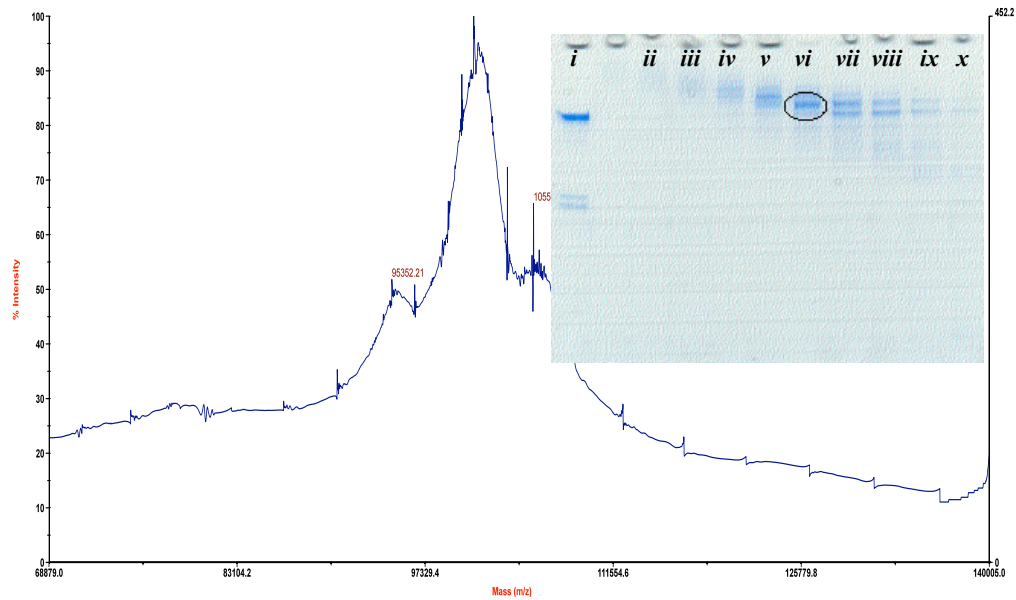


Figure 7.10 MALDI trace of purified mono-PEGylated F(ab')₂ fragment. Inset shows PAGE gel of purified mono-PEGylated F(ab')₂ fraction (circled); *i*: F(ab')₂ control *ii-x*: fractions 26 - 36, fractions collected every 30 seconds (Figure S.6)

7.3.4 Effect of mono-PEGylation on Fab-PEG-Ad affinity

The effect of mono-PEGylation on the ability of the Fab-PEG-Ad to bind CD20 was assessed via a competitive binding assay with Fab-AF488. The competitive binding curves in Figure 7.11 show that the affinity of the Fab-PEG-Ad decreases slightly relative to the unmodified protein. This is most likely a result of the random PEGylation strategy employed, which might lead to a fraction of Fab fragments with polymer groups obstructing the Fab CDR binding regions. Nonetheless, the conjugate still appears active as confirmed by the competitive binding in Figure 7.11 and confocal imaging (not shown).

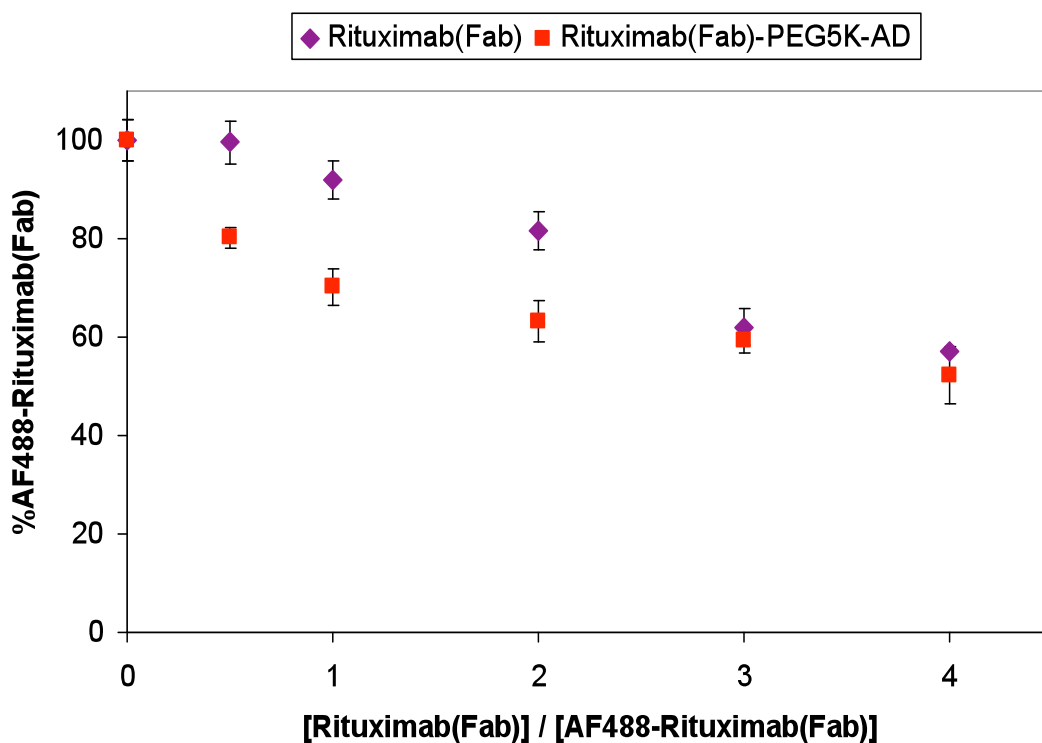


Figure 7.11 Competitive binding assay of rituximab Fab-AF488 with unmodified Fab and Fab-PEG-Ad

7.4 Further discussion and conclusion

We have investigated the binding properties of rituximab (anti-CD20) and its fragments to Daudi cells via the CD20 receptor for the purpose of studying the effect of the targeting ligand on uptake of nanoparticles localized at the tumor site. Cellular binding experiments of rituximab IgG and transferrin with Daudi cells indicate that the CD20 receptor is over-expressed on the Daudi cell surface relative to the transferrin receptor. The presence of both receptors and their large relative difference in expression levels provides a model to study the effect of cell surface receptor density on protein targeting. Although confocal studies give a visual confirmation of the binding results, information with regards to antibody internalization could not be obtained due to the inability to resolve the cell boundary and cytoplasmic space.

The Fab and F(ab')₂ fragments were generated via papain and pepsin, two nonspecific proteases. Papain cleaves the whole IgG just above the hinge region to create two Fab fragments, while pepsin digests the F_c portion of the IgG below the hinge region leaving behind the Fab fragments connected by a pair of disulfide bonds, F(ab')₂. Competitive binding assays of the two fragments show that the affinity of F(ab')₂ is identical to rituximab IgG, while that of the Fab fragment is much weaker than both IgG and F(ab')₂. The large difference in affinity suggests that avidity effects may play a role in the binding of rituximab to the CD20 receptor. This large relative difference in affinity can also be used to study the effects of affinity vs. avidity on the protein targeting of therapeutic nanoparticles. Avidity effects can be probed by varying the density of the Fab fragment ligand on the nanoparticle surface.

The Fab and F(ab')₂ fragments were subjected to PEGylation in a batch format to give a complex mixture of products which was purified via SEC. The mono-PEGylated Fab and F(ab')₂ fragments were isolated and confirmed MALDI with molecular weights at 52.5 kDa and 101.4 kDa, respectively. Mono-PEGylated fragments were desired because multi-PEGylation may lead to bridging between particles that may lead to aggregation. In addition, the affinities of mono-PEGylated proteins are higher than multi-PEGylated proteins. The competitive binding assay of Fab-PEG-Ad relative to Fab shows that the affinity of the PEGylated conjugate only decreases slightly, due to the random PEGylation strategy, compared to the unmodified protein. With these Fab and F(ab')₂ functional conjugates in hand, the next step will be the assembly of the CDP therapeutic nanoparticle with these new targeting agents and an *in vitro* study on the effects of targeting ligand properties such as affinity and density on intracellular uptake.

7.5 Methods and Experimental

NMR and Mass spectrometry

^1H NMR (300 MHz) spectra were recorded on a Varian Mercury-300 NMR Spectrometer with samples dissolved in either d-chloroform or d-dimethylsulfoxide (DMOS-d_6). Mass spectrometry was recorded on a DE-PRO time-of-flight mass spectrometer equipped with a matrix-assisted laser desorption ionization (MALDI) ion source. Data was acquired with a 20 Hz nitrogen laser operating in a linear ion mode. Samples were vigorously desalted via dialysis or the use of a C_4 zip tip before analysis. All samples employed a sinnapinic acid or α -cyano matrix.

Size Exclusion Chromatography

Size exclusion chromatography was carried out using an Agilent 1100 HPLC system, comprising a vacuum degasser, quaternary pump, an autosampler with 100 μL injection, a column oven with column switching valve, a diode array detector, and an evaporative light scattering detector. The mobile phase for all experiments was 50 mM sodium phosphate buffer with 100 mM NaCl, pH 7.2 at a flowrate of 0.3 or 0.5 mL/min. The columns used as the stationary phase were a Superdex-75 (10 by 300 mm, GE Healthcare) for the Fab fragments and a G3000SW_{XL} (7.8 by 300 mm, TOSOH biosciences) for the $\text{F(ab}')_2$.

PAGE gel electrophoresis

All gels were run under nonreducing conditions. The desired samples to be run were mixed in a 2 to 1 ratio with a loading buffer (SDS, bromophenol blue, glycerol). The mixture was heated at 100°C for 5 minutes then cooled to room temperature. After cooling, 30 μL or less of the sample was added to the wells of a polyacrylamide gel (PIERCE, 4-20% gradient).

The gels were electrophoresed in a TRIS-SDS-HEPES buffer (PIERCE) at 120 V for about an hour and stained with comassie overnight for visualization.

Flow cytometry

Daudi (Burkitt's Lymphoma) cells were cultured in complete DMEM media and supplemented with 10% fetal bovine serum (Invitrogen), 100 units/mL penicillin, and 100 units/mL streptomycin. 2×10^4 cells were plated in a 24 well plate two days prior to transfection. On the day of transfection, 20 nM AF488-conjugate and different molar ratios of the antibody fragments in 300 μ L were incubated with the cells. After transfections, the cells were rinsed with 1X PBS to remove any unbound conjugates, passed through a 40 μ m thick filter, and detected for average fluorescence with a Becton Dickinson FACSCalibur flow cytometer using a blue (488 nm) laser as the excitation wavelength.

Confocal microscopy

Daudi (Burkitt's Lymphoma) cells were cultured in RPMI-1640 media (ATCC formulation) and supplemented with 10% fetal bovine serum (Invitrogen). 1×10^6 cells were washed and resuspended in Opti-MEM I containing 20 nM of the Rituxan IgG-Alexafluor488 dye conjugate. The cells were incubated at 4°C for 5 mins after which the dye solution was removed and cells washed with 1X PBS containing 5% FBS to remove excess dye. The cells were then fixed with 100 μ L of fixing media (3-7% formaldehyde in PBS), labeled with rhodamine phalloidin (stains F-actin), and mounted on a glass slide with prolong gold containing DAPI (nucleus stain). The glass slide was allowed to cure overnight in the dark before imaging. Confocal microscopy was carried out using a Zeiss 410 laser scanning confocal microscope.

Trauts reagent was removed via diafiltration with buffer B over a 30 kDa membrane. After exchange into buffer B (10 $\mu\text{g}/\mu\text{L}$), Mal-PEG-Ad (20 eq.) was added directly to the mixture and the solution was vortexed to dissolve and stirred for an additional 2 hours at room temperature. The excess unreacted thiols in solution were quenched by incubating the mixture iodoacetic acid (40 eq.) for another hour. The mixture was finally dialyzed with a 30 kDa membrane to remove excess Mal-PEG-Ad and iodoacetic acid.

7.6 Supporting Information – HPLC and MALDI traces

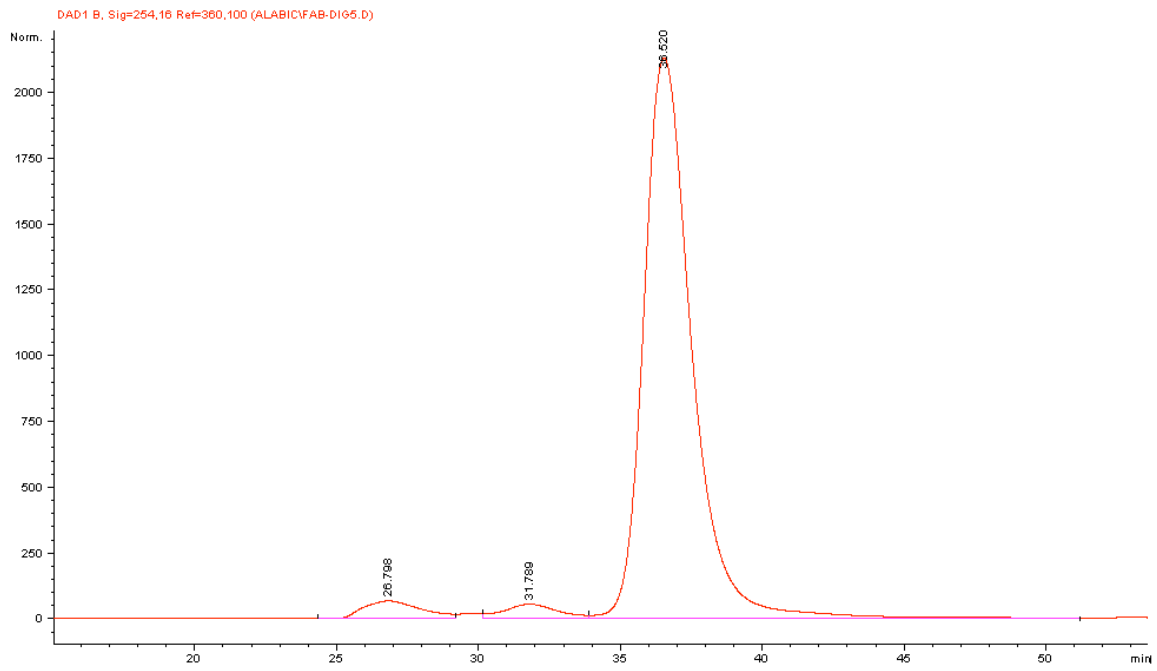


Figure S7.1 HPLC trace from PAPAINE digest

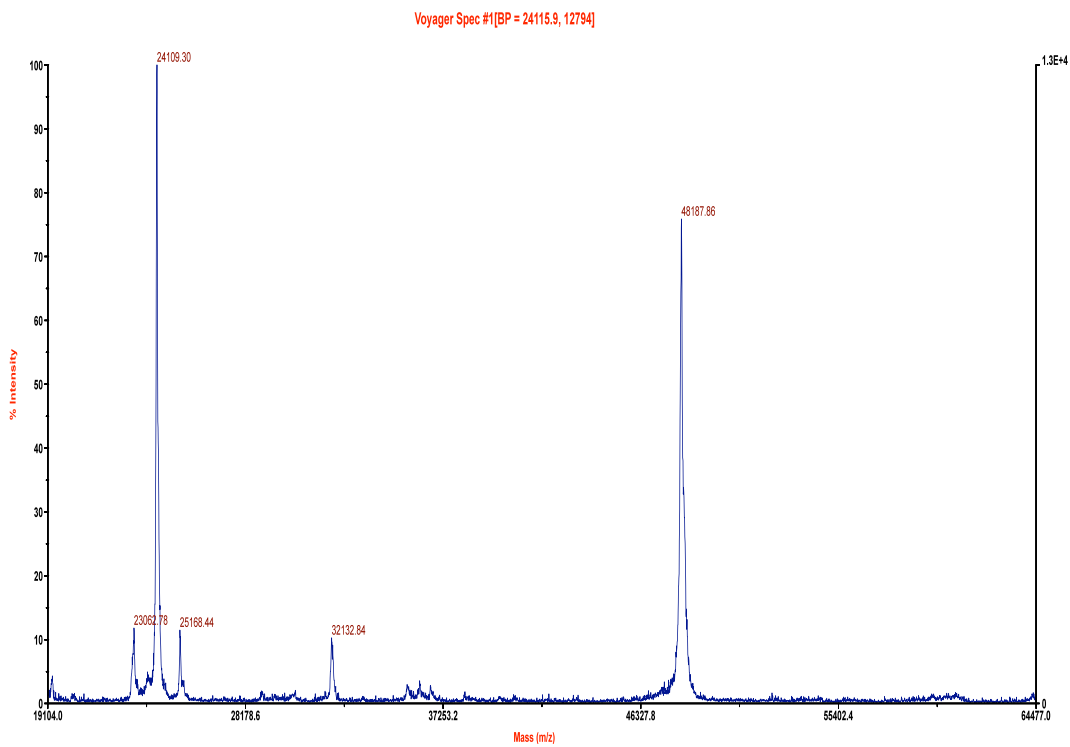


Figure S7.2 MALDI of Fab fragment

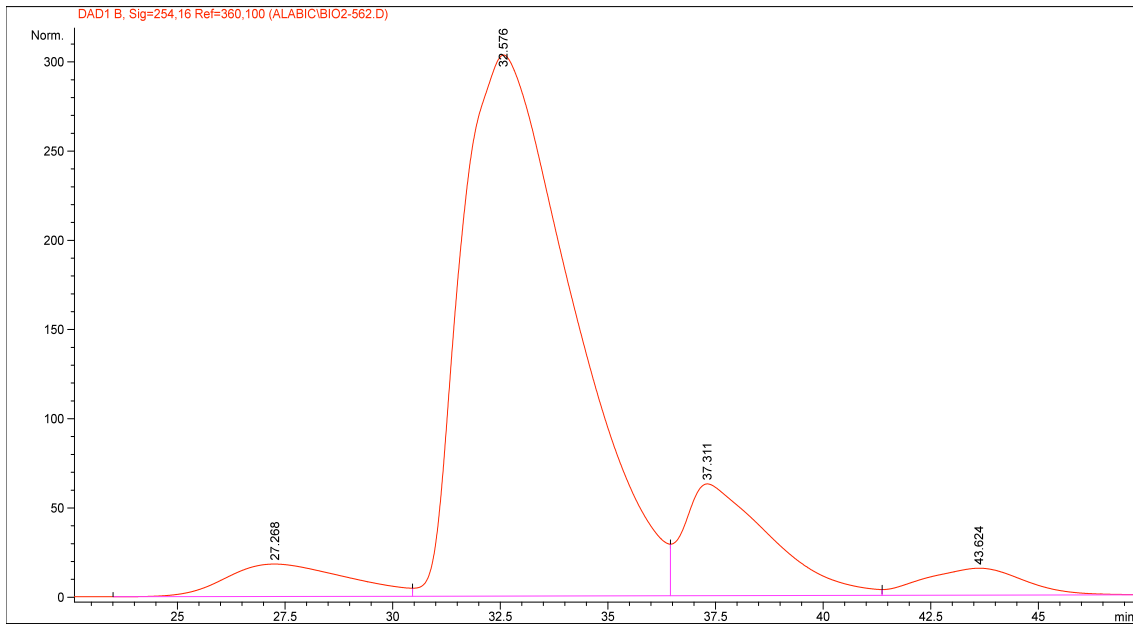


Figure S7.3 HPLC trace from PEPSIN digest

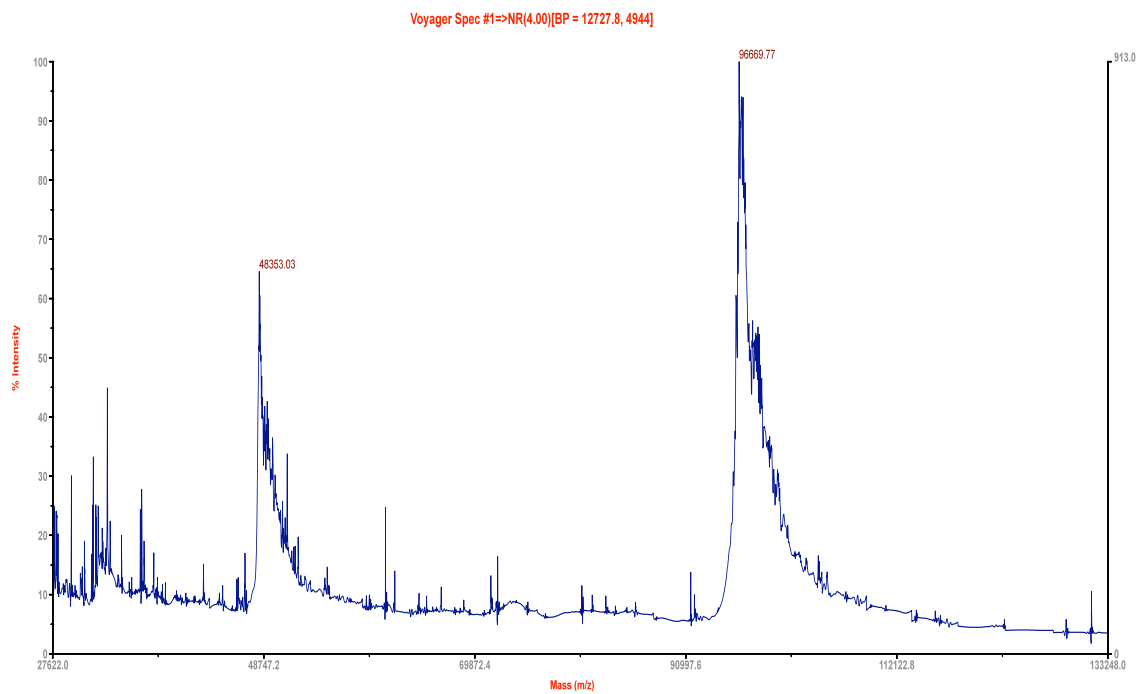


Figure S7.4 MALDI of F(ab')₂ fragment

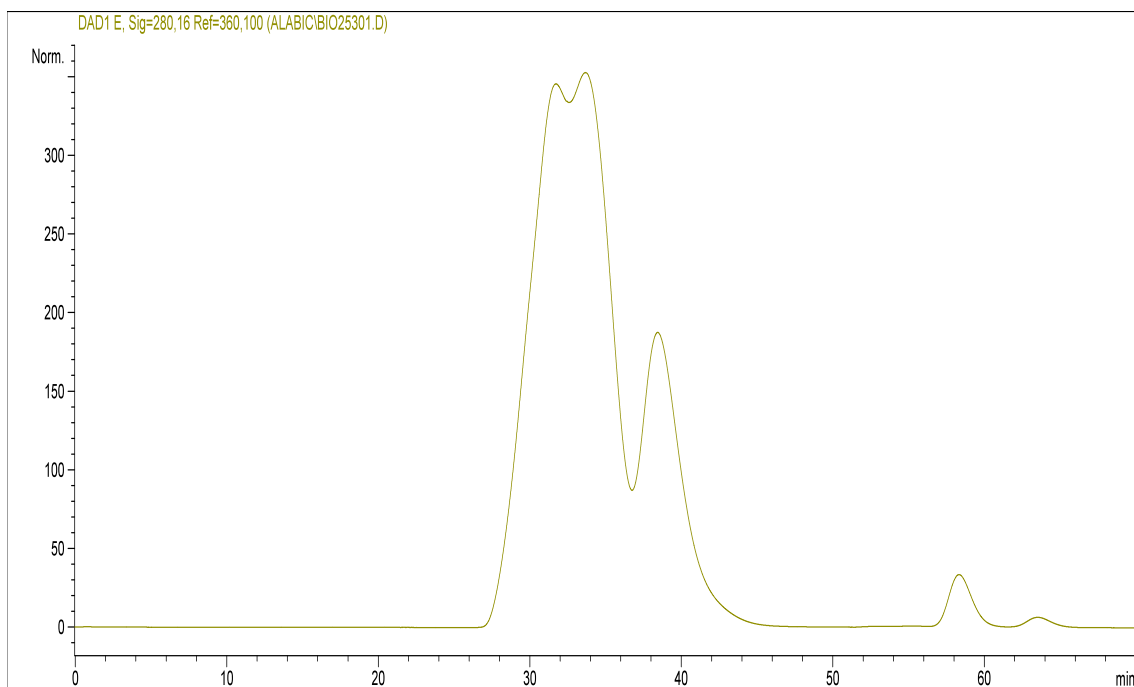


Figure S7.5 HPLC trace of crude Fab-PEG-AD reaction mixture

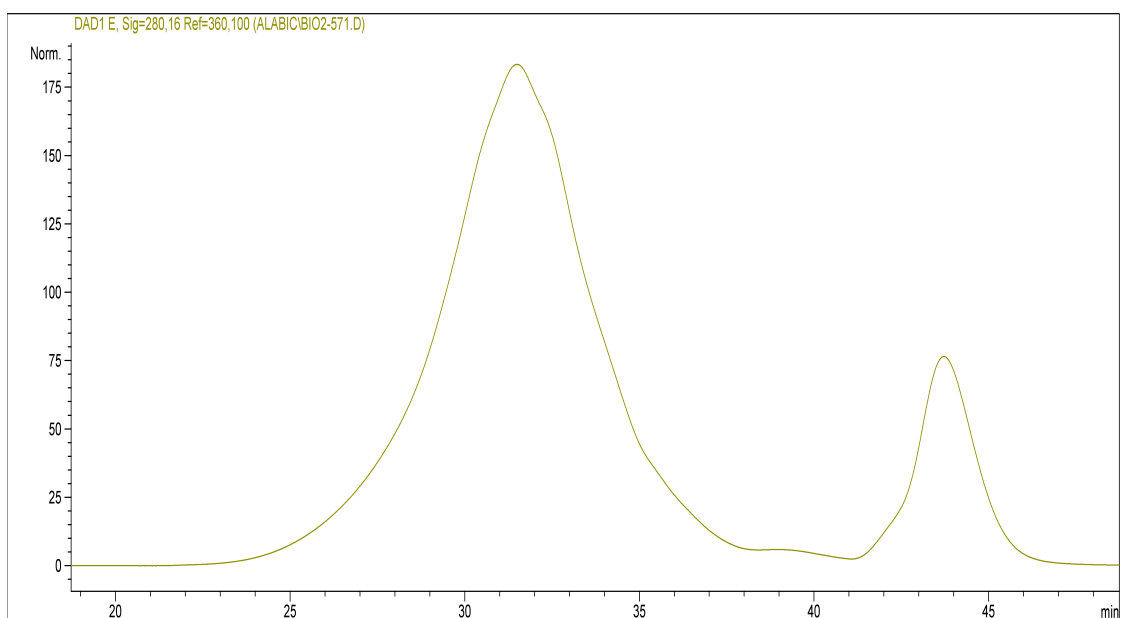


Figure S7.6 HPLC trace of crude F(ab')₂-PEG-AD reaction mixture

7.7 References

1. Hong, S.; Leroueil, P. R.; Majoros, I. J.; Orr, B. G.; Baker, J. R.; Holl, M. M. B., *Chemistry & Biology* **2007**, 14, (1), 107-115.
2. Bartlett, D. W.; Su, H.; Hildebrandt, I. J.; Weber, W. A.; Davis, M. E., *Proceedings of the National Academy of Sciences of the United States of America* **2007**, 104, (39), 15549-15554.
3. Kirpotin, D. B.; Drummond, D. C.; Shao, Y.; Shalaby, M. R.; Hong, K. L.; Nielsen, U. B.; Marks, J. D.; Benz, C. C.; Park, J. W., *Cancer Research* **2006**, 66, (13), 6732-6740.
4. Bellocq, N. C.; Pun, S. H.; Jensen, G. S.; Davis, M. E., *Bioconjugate Chemistry* **2003**, 14, (6), 1122-1132.
5. Gonzalez, H.; Hwang, S. J.; Davis, M. E., *Bioconjugate Chemistry* **1999**, 10, (6), 1068-1074.
6. Hwang, S. J.; Bellocq, N. C.; Davis, M. E., *Bioconjugate Chemistry* **2001**, 12, (2), 280-290.
7. Pun, S. H.; Davis, M. E., *Bioconjugate Chemistry* **2002**, 13, (3), 630-639.
8. Bellocq, N. C.; Davis, M. E.; Engler, H.; Jensen, G. S.; Liu, A. J.; Machemer, T.; Maneval, D. C.; Quijano, E.; Pun, S. Z. H.; Schluep, T.; Wen, S. F., *Molecular Therapy* **2003**, 7, (5), S290-S290.
9. Pun, S. H.; Tack, F.; Bellocq, N. C.; Cheng, J. J.; Grubbs, B. H.; Jensen, G. S.; Davis, M. E.; Brewster, M.; Janicot, M.; Janssens, B.; Floren, W.; Bakker, A., *Cancer Biology & Therapy* **2004**, 3, (7), 641-650.
10. Nadler, L. M.; Ritz, J.; Hardy, R.; Pesando, J. M.; Schlossman, S. F.; Stashenko, P., *Journal of Clinical Investigation* **1981**, 67, (1), 134-140.

11. Law, C. L.; Cervený, C. G.; Gordon, K. A.; Klussman, K.; Mixan, B. J.; Chace, D. F.; Meyer, D. L.; Doronina, S. O.; Siegall, C. B.; Francisco, J. A.; Senter, P. D.; Wahl, A. F., *Clinical Cancer Research* **2004**, 10, (23), 7842-7851.
12. Humphreys, D. P.; Heywood, S. P.; Henry, A.; Ait-Lhadj, L.; Antoniów, P.; Palframan, R.; Greenslade, K. J.; Carrington, B.; Reeks, D. G.; Bowering, L. C.; West, S.; Brandt, H. A., *Protein Engineering Design & Selection* **2007**, 20, (5), 227-234.
13. Du, J. M.; Wang, H.; Zhong, C.; Peng, B. Z.; Zhang, M. L.; Li, B. H.; Huo, S.; Guo, Y. J.; Ding, J. P., *Journal of Biological Chemistry* **2007**, 282, (20), 15073-15080.

Chapter VIII

Characterization of Targeted Nanoparticles for siRNA delivery

8.1 Abstract

We investigate the effects of AD-PEG conjugates of rituximab fragments as targeting ligands on CDP-siRNA nanoparticle formation, binding, and functional siRNA delivery to lymphoma B-cells. Nanoparticles of rituximab Fab- and F(ab')₂-PEG-AD conjugates formulated at a 3± charge ratio resulted in particle sizes between 60-90 nm and surface charges under +10 mV. Rituxan Fab-targeted nanoparticles were able to prevent salt-induced aggregation for 20 minutes while F(ab')₂-targeted nanoparticles got slightly bigger due to modest aggregation upon salt addition. *In vitro* binding of Fab-targeted nanoparticles with Daudi cells was shown to be specific and increased with increasing targeting ligand density. Daudi cells were transfected with targeted and nontargeted nanoparticles with and without free rituximab in solution to highlight binding and uptake pathways. Knockdown of the luciferase gene was only observed with Fab- and F(ab')₂- targeted nanoparticles, demonstrating their ability to bind and deliver functional siRNAs to target cells, unlike nontargeted particles. Transfection in the presence of free rituximab suggests a receptor-mediated process and confirms our FACS results showing weaker binding of the Fab relative to F(ab')₂ fragment. Incomplete recovery of luciferase expression after transfection in the presence of excess rituximab-IgG suggests the presence of avidity effects.

8.2 Introduction

Over the past decade, our group has developed a synthetic delivery system based on a cyclodextrin-containing polycation. This delivery system is completely formulated by self-assembly and has shown great promise for use in systemic nucleic acid delivery.¹ As previously mentioned, the delivery vehicle consists of two components. The first component is an imidazole-capped cyclodextrin-containing polycation (CDP) possessing cationic amidine groups separated by six methylene units, as shown in Figure 8.1.

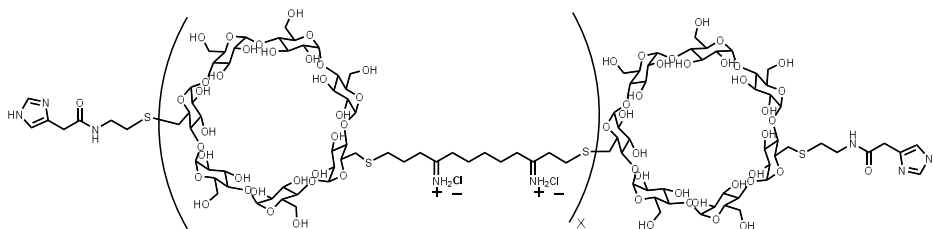


Figure 8.1 Structure of imidazole-terminated β -cyclodextrin-containing polycation

The terminal imidazole modification promotes particle release from the endosome via buffering the pH of the endosomal vesicles.^{2, 3} The CDP component is used for nucleic acid condensation into nanoparticles (or polyplexes).⁴ However, polyplexes formed via this route aggregate under physiological salt solution due to their exposed positively charged surface. This problem was overcome by introducing an adamantane-poly(ethylene glycol) (AD-PEG) conjugate as the second component. The AD-PEG conjugate interacts with the β -CD on the CDP chains via the formation of a strong noncovalent inclusion complex.⁵ This permits the introduction of PEG stabilizing groups at sites allosteric to those involved in nucleic acid binding. Polyplex stabilization is conferred by sterically minimizing nanoparticle-nanoparticle interactions and charge shielding. These two components, i.e., CDP and AD-PEG, self assemble with nucleic acids to give stable sub-100 nm particles.

The ligand in the second component (AD-PEG) allows for incorporation of targeting agents towards cell-specific targeting. Previous work in our group concentrated on the preparation of transferrin-targeted nanoparticles to target a broad spectrum of cancer cells. CDP nanoparticles carrying siRNA against ribonucleotide reductase subunit 2 (R2)⁶ are currently being investigated in humans (Phase I clinical trial). In this report, we investigate the use of the anti-CD20 (rituximab) Fab- and F(ab')₂-PEG-AD conjugates synthesized in the previous chapter towards the formulation of a complete delivery vehicle for systemic applications. These fragments have been shown in the previous chapter to target the CD20 receptor on lymphoma B-cells. Although anti-CD20 targeting of the CD20 receptor has been reported as “slowly or noninternalizing” in comparison to its CD19 counterpart, mixed reports exist with regards to the rate of internalization upon conjugation of anti-CD20 to small molecules. We will show preliminary data indicating that these delivery vehicles can successfully target and deliver oligonucleotides to lymphoma B-cells (we use a Daudi cell line that expresses luciferase as a model) *in vitro*.

8.3 Results and discussion

8.3.1 Formulation of targeted nucleic acid particles

Targeted nucleic acid nanoparticles were formulated with 0.5 mol% (i.e., percentage of the total AD-PEG in the mixture) of each target. The ratio of positive charges on CDP (2 mol of positive charge per CDP or β -CD) to negative charges on the nucleic acid (1 mol of negative charge per nucleotide) is defined as the formulation charge ratio. The charge on the protein targeting agent is not factored into the formulation charge ratio, but its influence on surface properties is discussed later.

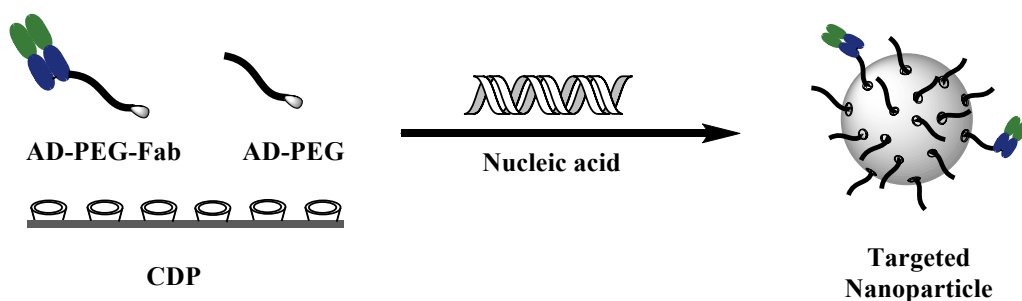


Figure 8.2 Schematic of CDP nucleic acid particle assembly

A schematic for nanoparticle assembly with nucleic acids is shown in Figure 8.2. All particles were formulated at a charge ratio of 3 \pm so as to ensure complete nucleic acid encapsulation. The particles were prepared by mixing the following components (in water) in equal volumes: (1) CDP, for nucleic acid condensation, (2) adamantane-PEG (AD-PEG) for stabilization against nonspecific interactions such as self aggregation, (3) AD-PEG-Fab (or F(ab')₂ or Tf) for targeting CD20 receptors over-expressed on Daudi cells, and (4) siRNA. The first three components were pre-mixed and then added to the fourth solution.

Transferrin-targeted nanoparticles were included in the characterization studies for comparison.

8.3.2 DLS, zeta potential and salt stability studies

The particle size was measured by dynamic light scattering in pure water. The particles were dialyzed with 100 kDa membranes prior to measurements so as to remove unbound components that may form micelles, such as PEGs, and interrupt with particle size measurements. The effective diameter of the targeted nanoparticles fell between 70-90 nm, whereas, nontargeted nanoparticles gave sizes in the 50-60 nm range. The general size increase upon targeting can be attributed to the hydrodynamic size of the targeting agents.

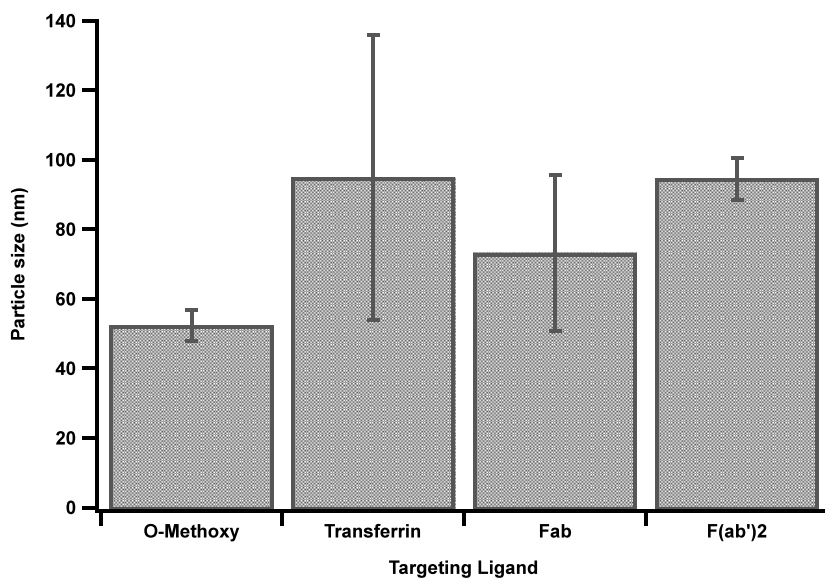


Figure 8.3 Effect of targeting ligand on particle size (effective diameter)

The surface charge on the nanoparticles upon the addition of 0.5 mol% targeting agent was investigated by measuring the zeta potential of the particles in a 1 mM KCl

solution. Non-PEGylated CDP-nucleic acid nanoparticles typically give zeta potentials of +20 mV.³

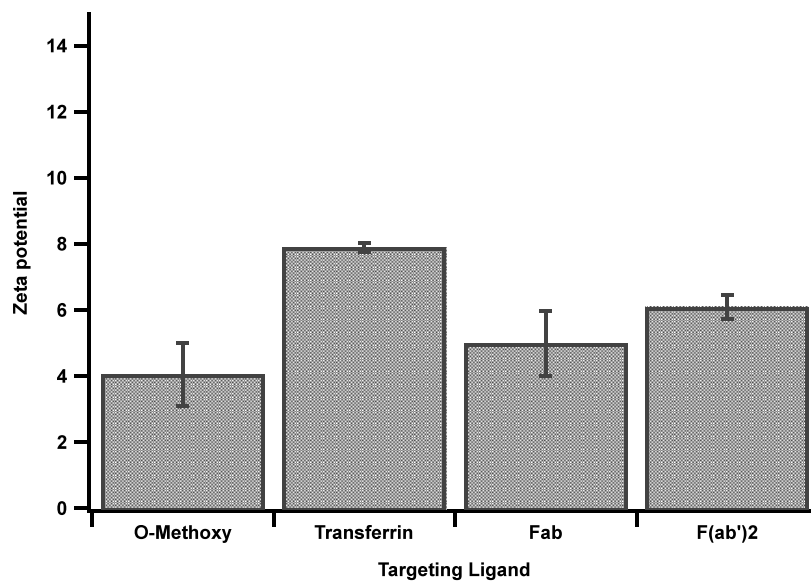


Figure 8.4 Effect of targeting ligand on zeta potential

The low positive value for the zeta potentials for all the analyzed samples suggest that the surface charge of the particles is well shielded by the AD-PEG stabilizing agent (zeta potential for unPEGylated particles ~ 20 mV). Upon addition of the targeting ligands, the zeta potential increases only slightly, however, all values stay below 10 mV. Zeta potential values between +/- 10 are typically considered neutral.

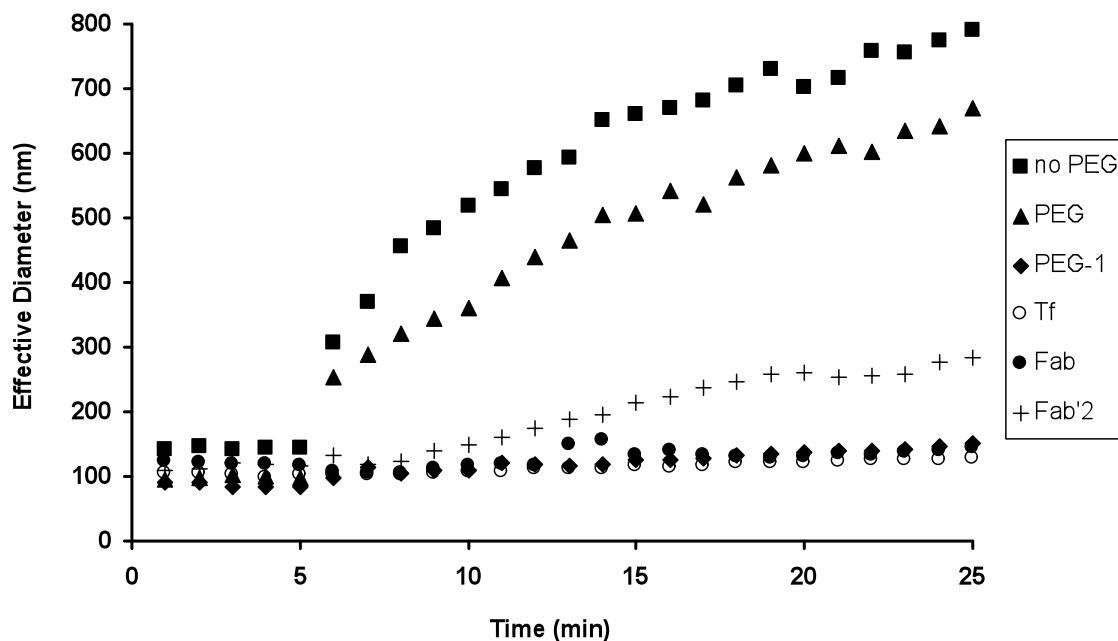


Figure 8.5 Aggregation of siRNA particles in physiological salt ($1\times$ PBS). Particles were formulated at a $3\pm$ charge ratio. No PEG (filled squares); non-PEGylated particles, PEG (filled triangles); PEGylated particles after dialysis, PEG-1 (filled diamonds); 25% of stoichiometric PEG needed for $1\pm$ added to PEGylated particles after dialysis, Tf (open circles); PEGylated particles with 0.5 mo% Tf-PEG-AD, Fab (filled circles); PEGylated particles with 0.5 mo% Fab-PEG-AD, $F(ab')_2$ (cross); PEGylated particles with 0.5 mo% $F(ab')_2$ -PEG-AD

Nanoparticle aggregation was monitored by DLS-based kinetic studies. The effective diameter of the particles was measured every minute in water for 5 minutes, after which the appropriate volume of $10\times$ PBS was added to give a $1\times$ PBS nanoparticle solution. Non-PEGylated particles quickly aggregate in $1\times$ PBS as previously observed by Bartlett et al.⁷ Particles formulated with PEG followed by dialysis with a 100 kDa membrane to remove excess CDP and PEG experienced aggregation upon salt addition. However, aggregation was abated via the addition of extra PEG (25% of stoichiometric PEG needed for $1\pm$). Since the particles do not aggregate in $1\times$ PBS before dialysis,⁷ the observed aggregation is likely due to the removal of a higher fraction of PEG relative to CDP during dialysis. The transferrin,

Fab- and F(ab')₂-targeted nanoparticles were prepared similarly to the PEGylated sample. Transferrin and Fab-targeted nanoparticles were able to prevent detectable aggregation for 20 minutes. Modification with the F(ab')₂ target, on the other hand, leads to modest aggregation upon salt addition. This could be due to inefficient charge screening due to the larger size of the targeting agent.

8.3.3 In vitro binding and internalization studies

Previous binding experiments carried out with transferrin-targeted nanoparticles by Bartlett et al. showed that the percentage of polyplexes bound to HeLa cells increased with increasing surface transferrin ligand density. We carried out a similar experiment with Fab-targeted CDP polyplexes at 4°C to measure the amount of binding in the absence of internalization.

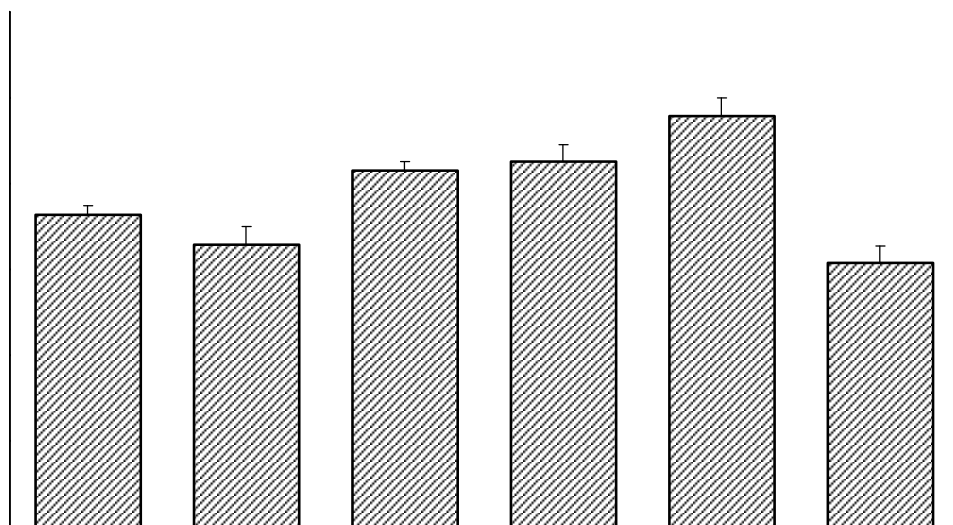


Figure 8.6 Live cell binding of nanoparticles at 4°C. All polyplexes were PEGylated and formulated at a 3+/- charge ratio. A - no targeting ligand, B - no targeting ligand + 25×Fab, C - Fab-PEG-AD (0.1 mol%), D - Fab-PEG-AD (0.5 mol%), E - Fab-PEG-AD (2.5 mol%), F - Fab-PEG-AD (2.5 mol%) + 25×Fab

The results in Figure 8.6 show that Fab targeting increases the amount of cell-associated particles under noninternalization conditions. Nonspecific association of the nanoparticles to the cell surface is due to weak electrostatic interactions between the slightly charged nanoparticle and cell surface. The uptake of particles seems to be slightly reduced upon introduction of a large excess of free rituxan-Fab. We attribute this to a possible cell surface charge screening upon specific binding of Fab fragments. We also see from Figure 8.6 that the amount of binding increases with targeting ligand density. Addition of free rituximab Fab fragments to Fab-PEG-AD targeted polyplexes lead to a significant reduction in the amount of bound polyplexes as a result of competition with the free Fab fragments.

To assess in vitro delivery and efficacy of the targeted nucleic acid nanoparticles, we developed a luciferase-targeting siRNA sequence against the pMOD-LucSh gene in Daudi cells stably. The synthetic target was the LucSh fusion gene (LucSh- Δ CpG). The top three sequences obtained from the Dharmacon blast analysis were purchased and transfected using RNAiMAX into the Daudi cells to examine the potency of each sequence. Each sequence was tested at three different concentrations and compared to a control scrambled sequence.

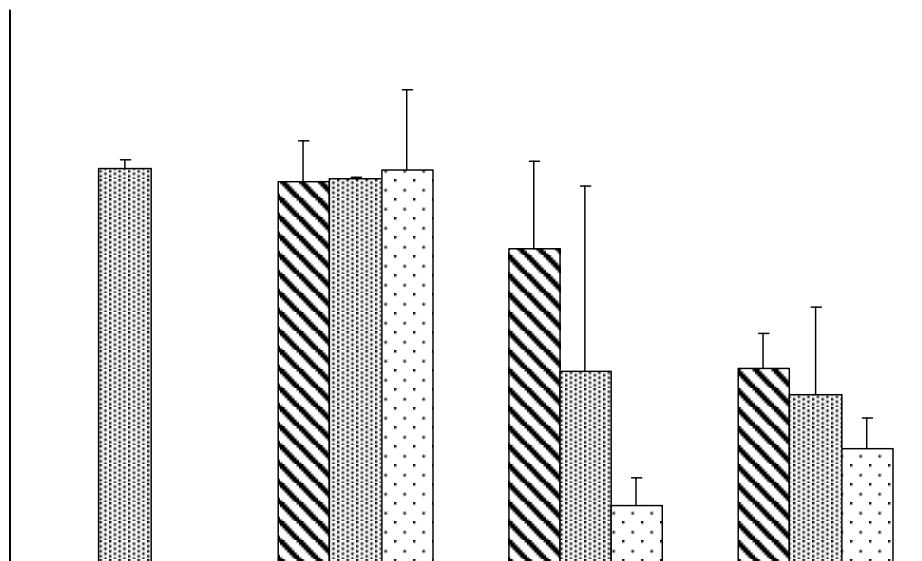


Figure 8.7 Luciferase expression 48 hours after transfection of Daudi-Luc cells with siCON, siMOD1, siMOD2, and siMOD3. The average of three replicate treatments is presented as the ratio of luciferase level (RLU; relative light units) to total protein level for each sample. Data are normalized to the luciferase level in untransfected cells.

As shown in Figure 8.7, down-regulation of luciferase expression in Daudi-Luc cells is observed 2 days post transfection with siMOD-2 and siMOD-3 and appears to be sequence specific and concentration dependent. The siMOD-2 sequence gives the largest knockdown at 20 nM while siMOD-3 shows better potency at lower siRNA concentrations. Higher potency at lower concentration is desired due to the potential for off-target effects at higher siRNA concentrations (typically above 50 nM). Based on the results in Figure 8.7, we proceeded with siMOD-3 for the investigation into the ability of targeted polyplexes to deliver functional siRNA to cells.

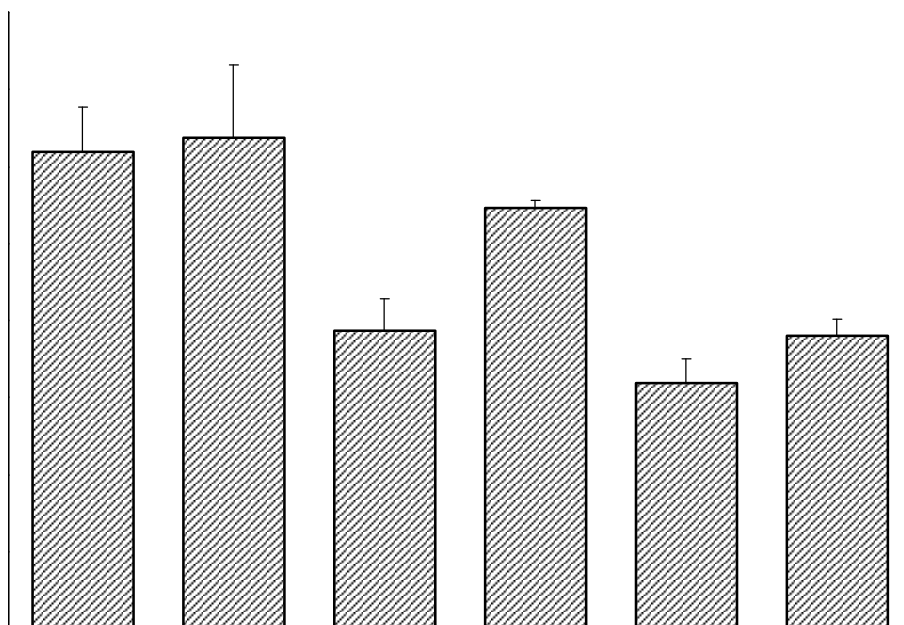


Figure 8.8 Luciferase expression after 48 hours transfection of Daudi-Luc cells with particles containing siMOD-3. Particles were formulated with CDP, PEG, and siMOD-3 at a 3+/- charge ratio. Contents of the transfection listed from the left are – Opti-MEM, PEGylated particles, 0.5 mol% Fab-PEG-AD targeted particles, 0.5 mol% Fab-PEG-AD targeted particles + free IgG (30×), 0.5 mol% F(ab')₂-PEG-AD targeted particles, and 0.5 mol% F(ab')₂-PEG-AD targeted particles + free IgG (30×).

The results in Figure 8.8 show down regulation of the luciferase signal upon transfection with the Fab-targeted particles in contrast to the nontargeted PEGylated particles. This result in combination with the results from the binding experiment suggests that the targeting ligands are required for specific uptake of PEGylated polyplexes in Daudi cells *in vitro*. This specific uptake is further highlighted by the reduction in the extent of knockdown upon introduction of rituxan-IgG, which competes with the particles for the CD20 binding sites. The lack of complete recovery of luciferase expression with rituxan-IgG suggests the presence of avidity effects. This will have to be probed further with the use of varying amounts of targeting ligand densities. A similar relative extent of knockdown is

observed with the $F(ab')_2$ targeted nanoparticles, however, competition with rituxan-IgG is lower than with the Fab-targeted particles. Such a low degree of competition with $30\times$ rituxan-IgG also points towards the presence of avidity effects in the $F(ab')_2$ -targeted nanoparticles. The combined results indicate that the targeting ligands mediate nanoparticle internalization, which leads to the delivery and activity of functional siRNAs.

8.4 Further discussion and conclusion

Subcellular localization and delivery of nanoparticles is dependent on their size and surface properties. We have investigated the ability of nanoparticle conjugates of anti-CD20 (Rituximab) fragments to target and deliver their payload via the CD-20 receptor on lymphoma B-cells. Although anti-CD-20 targeting of the CD-20 receptor has been reported as “slowly or noninternalizing” in comparison to its CD-19 counterpart, mixed reports exist with regards to the rate of internalization upon conjugation of anti-CD-20 to small molecules or nanoparticles.

We have conjugated Fab and $F(ab')_2$ fragments of Rituximab via a PEG linker to the surface of our cyclodextrin polycation (CDP) nanoparticles complexed with an siRNA targeted against the luciferase-expressing gene in Daudi cells (lymphoma B-cells). All formulations were made at a $3\pm$ charge ratio and resulted in particle sizes between 60 and 90 nm. Targeted polyplexes gave slightly larger particle size distributions than the untargeted polyplexes, possibly due to the added hydrodynamic diameter of the targeting agents. Zeta potential values of targeted and untargeted particles were positive but under 10 mV indicating steric stabilization. Steric stabilization was further confirmed via salt-induced aggregation studies with $1\times$ PBS. Fab targeted nanoparticles were able to prevent detectable

aggregation for 20 minutes while $F(ab')_2$ targeted nanoparticles lead to modest aggregation upon salt addition. In vitro binding of Fab-targeted nanoparticles with Daudi cells was shown to be specific and dependent on targeting ligand density.

Daudi cells were transfected with targeted and nontargeted nanoparticles with and without free Rituximab in solution to highlight binding and uptake pathways. The results in Figure 8.7 show knockdown of the luciferase gene only with Fab- and $F(ab')_2$ -targeted nanoparticles, which demonstrates their ability to bind and deliver functional siRNAs to target cells (unlike nontargeted particles). Transfections in the presence of free Rituximab show that the uptake process is receptor mediated and confirms our FACS results that indicate that binding of the Fab fragment is much weaker than that of $F(ab')_2$. Evidence of avidity effects were seen for both Fab- targeted and $F(ab')_2$ -targeted polyplexes but were more pronounced with the $F(ab')_2$ -targeted polyplexes. The two scenarios expected with these targeting ligands are illustrated in Figure 8.9 below.

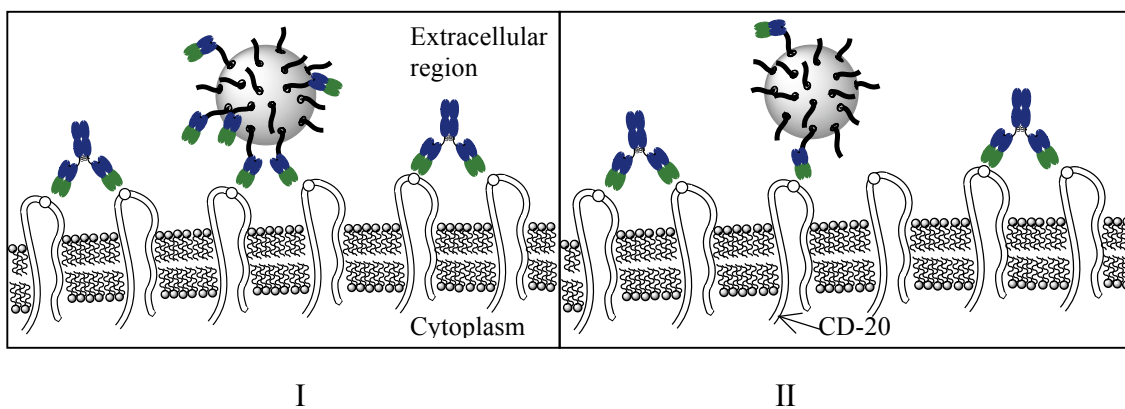


Figure 8.9 Representation of Fab targeted nanoparticle and IgG binding to daudi cell surface expressing CD20 receptors (extracellular loops). I – high Fab density, II – low Fab density

At high Fab-targeting ligand densities, the particle surface is expected to simulate the $F(ab')_2$ targeting ligand where multiple CD20 receptors on the surface are engaged by a single particle (Figure 8.9I). At this limit, competition with free IgG will be diminished due to this multi-binding avidity effect. However, at a low Fab-targeting ligand density, the particle surface will behave like a single Fab fragment (Figure 8.9II) and thus competition with free IgG will be pronounced. These two scenarios' can be studied by investigating the effects of targeting ligand density on apparent binding affinities and transfection efficiencies. The slowly internalizing CD20 surface receptor⁸ is a great model for studying avidity effects because these effects are expected to be more pronounced for slowly internalizing uptake mechanisms.

8.5 Methods and Experimental

Polymers

An imidazole-terminated, cyclodextrin-containing polycation (CDP) was used for all the studies in this chapter and was obtained as a generous gift from Calando pharmaceuticals. Adamantane-poly(ethylene glycol) (AD-PEG) and transferrin-PEG-AD were also obtained as a generous gift from Calando pharmaceuticals. Targeting ligands and their AD-PEG conjugates were synthesized as described in the previous chapter.

Nucleic acids

Dharmacon-predicted siRNAs were tested to obtain a potent siRNA sequence against the luciferase gene of pMOD-LucSh in Daudi cells stably expressing the pMOD-LucSh plasmid gene (obtained from City of Hope). The target is the synthetic LucSh fusion gene (LucSh- Δ CpG). The sequences designed from Dharmacon were purchased from IDT.

Sense sequence:

siMOD-1 AGAAGGAGAUUGUGGACUA-UU

siMOD-2 GGAAAGACCAUGACUGAGA-UU

siMOD-3 GGAUGAGGAUGAGCACUU-UU

Nanoparticle formulation

A 3/1 (+/-) charge ratio was used for all studies in this chapter. All formulations were pre-PEGylated as follows: CDP was mixed with AD-PEG at a 1:1 AD-PEG/ β -CD (mol/mol) ratio in water. Targeted particles were added at 0.5 mol% (unless otherwise stated) of the total AD-PEG in the mixture where indicated. After incubation for 30 minutes, this mixture

was added to an equal volume of nucleic acid in water such that the ratio of positive to negative charges came out to 3/1 (+/-). The resulting mixture was incubated for 30 minutes before use.

Dynamic Light Scattering (DLS)

Particle size measurements were carried out in a 70 μL sample volume using micro-cuvettes with a ZetaPALS (Brookhaven Instruments Corporation) instrument. The reported particle sizes are effective hydrodynamic diameters which represent an average of 5-10 one-minute runs. The zeta potentials were taken on the same instrument by diluting the 70 μL sample to 1.4 mL with a 1 mM KCl solution. The zeta potential measurements represent an average of 10 individual runs.

Live cell binding of nanoparticles

Daudi (Burkitt's Lymphoma) cells (suspension) were cultured in complete DMEM media and supplemented with 10% fetal bovine serum (Invitrogen), 100 units/mL penicillin, and 100 units/mL streptomycin. 1×10^5 daudi cells in complete growth media were washed twice with $1 \times$ PBS and plated in 100 μL of PBS in a 96 well plate and kept at 4°C . Polyplexes were formulated with a Cy3-labelled control siRNA (Cy3 attached to the 5' end of the sense strand) in 100 μL of water such that the final siRNA concentration after addition of the polyplexes to each well was 50 nM. The 200 μL mixture was then incubated at 4°C for 30 mins, after which the 96 well plate was centrifuged at $200 \times g$ to pellet the cells. 100 μL of supernatant was collected from each well and placed into black plates for fluorescence readings using a Tecan Safire plate reader. The percent bound (fraction associated with cell

pellet) was determined by subtracting the fluorescence remaining in the supernatant from the initial amount added.

Daudi cell transfections, luciferase assay

Reverse transfection of siMOD1, siMOD2, and siMOD3 with RNAiMAX:

The appropriate amount of RNAiMAX reagent (following manufacturer's instructions, Invitrogen) was formulated with the siRNAs in Opti-MEM1 and added to the empty wells. 5×10^4 cells in full growth media were added to the 24 well plate in the appropriate volume to give the indicated siRNA concentration. Transfection was allowed to proceed for 48 hours, after which the growth medium was removed and replaced with cell culture lysis reagent. After completion of cell lysis, the luminescence of the lysates was determined using a promega luciferase assay system. Monolight 3010, 2.0 sec. inject/measure, 5.0 sec. measuring time.

Forward transfection of siMOD3 using CDP:

Cells were seeded in 24 well plates at 5×10^4 cells per well. The formulated polyplexes at a charge ratio of 3/1(+/-) were incubated with the cells in serum-free medium (Opti-MEM) for 4 h, after which complete growth media was added to the wells to give 80% serum. The cells were then harvested as previously described 48 hours post transfection and assayed for luciferase expression.

8.6 References

1. Davis, M. E.; Pun, S. H.; Bellocq, N. C.; Reineke, T. M.; Popielarski, S. R.; Mishra, S.; Heidel, J. D., *Current Medicinal Chemistry* **2004**, 11, (2), 179-197.
2. Mishra, S.; Heidel, J. D.; Webster, P.; Davis, M. E., *Journal of Controlled Release* **2006**, 116, (2), 179-191.
3. Mishra, S.; Webster, P.; Davis, M. E., *European Journal of Cell Biology* **2004**, 83, (3), 97-111.
4. Gonzalez, H.; Hwang, S. J.; Davis, M. E., *Bioconjugate Chemistry* **1999**, 10, (6), 1068-1074.
5. Pun, S. H.; Davis, M. E., *Bioconjugate Chemistry* **2002**, 13, (3), 630-639.
6. Heidel, J. D.; Liu, J. Y. C.; Yen, Y.; Zhou, B. S.; Heale, B. S. E.; Rossi, J. J.; Bartlett, D. W.; Davis, M. E., *Clinical Cancer Research* **2007**, 13, (7), 2207-2215.
7. Bartlett, D. W.; Davis, M. E., *Bioconjugate Chemistry* **2007**, 18, (2), 456-468.
8. Vangeepuram, N.; Ong, G. L.; Mattes, M. J., *Cancer* **1997**, 80, (12), 2425-2430.

Chapter IX

Future Directions and Recommendations

9.1 Abstract

The results shown in chapters 7 and 8 illustrate the successful formulation of rituximab Fab- and F(ab')₂-targeted CDP-nucleic acid nanoparticles and their use towards gene knock down in B-cells. However, this work only demonstrates the feasibility of targeting and delivery. Further work is required in order to understand the parameters needed to maximize the targeting efficiency and thus therapeutic potency. Towards this end, this chapter outlines some suggested experiments and ideas that may provide a better understanding of how these targeted nanoparticles internalize as a function of targeting ligand type, density, affinity, and rate of internalization. In order to carry out these investigations effectively, the nanoparticle composition will have to be accurately determined. Suggested ideas towards obtaining a compositional analysis and nanoparticle purification from possible fragments will be discussed.

9.2 Quantitative binding studies of targeting ligands and particles

Our initial efforts in Chapter 7 were focused on determining the effect of PEG-AD conjugation on the relative binding affinities of our Fab and F(ab')₂ conjugates via competitive binding experiments. However, in order to compare CD-20 specificity of our conjugated rituximab fragments to other targeting ligands receptor interactions in literature, we need to quantify their binding affinities. This can be achieved via two methods. The first involves carrying out a surface plasmon resonance (SPR) direct binding analysis with the CD20 receptor. Since the purified recombinant or native CD20 protein is unavailable, it will have to be synthesized via expression of the CD20 gene in bacterial cells followed by purification. The second method involves carrying out a cell binding experiment with increasing concentrations of radiolabeled or fluorescently labeled anti-CD20 conjugate and measuring the amount bound at each concentration until saturation is reached. The maximum bound ligand (B_{\max}) and binding affinity (K_d) can be calculated by via a nonlinear regression on the data or by plotting the data as a Scatchard plot. This study can also be carried out on targeted nanoparticles at different ligand densities after removal of unbound targeting ligands that may interfere with the binding assay. The apparent K_d for the nanoparticles can be obtained as a function of targeting ligand density so that multivalent interactions can be accurately determined. A method for the determination of bound ligand density on the nanoparticles surface is discussed below.

9.3 Nanoparticle composition: quantification of ligand density

The amount of Fab- or F(ab')₂-PEG-AD bound to the surface of the nanoparticle can be obtained by separating the nanoparticle from its free components via size exclusion chromatography. This can be achieved with a HPLC modified with large capillaries to reduce back pressure or with a fast protein liquid chromatography (FPLC) instrument equipped with a U.V/Vis, fluorescent and evaporative light scattering detector (ELSD) to monitor the nanoparticle components. Sephacryl S-400HR or S-500HR gels (GE Healthcare) can be packed into an empty column and used as the stationary phase. These polymer-based gels are made of 47 μm dextran-acrylamide particles with an exclusion limit between 60-100 nm. Thus particles that fall within or above this limit elute in the void volume. Other smaller components should interact with the column and elute at later retention times. As a result, free components of the CDP-nucleic acid nanoparticle such as free polymer, siRNA, PEG-AD and Fab- or F(ab')₂-PEG-AD targeting ligands should elute at much later time points due to their smaller sizes (all < 5 nm) relative to the size of the nanoparticles (60-90 nm). The nanoparticle's protein ligand density can be determined by quantifying the amount of free protein via its A280 signal obtained on the U.V/vis detector after purification and subtracting this amount from the total amount of protein added. This is contingent on the ability to separate free protein (53.5 kDa for Fab and 101.5 kDa for F(ab')₂) from free siRNA (13.5kDa), polymer (10 kDa), and PEG-AD (5 kDa). Separations of proteins with similar size ranges have been successfully carried out with these columns by Sperling et al.¹ The other free components can be detected by the ELSD or fluorimeter if a Cy3 conjugated siRNA is used.

9.4 Rate of targeted nanoparticle internalization

The in vitro gene down-regulation studies carried out in Chapter 8 provided proof that the CD20 receptors on the Daudi cells must be internalizing. However, the rate of internalization and extent to which the rituximab Fab and F(ab')₂ targeting ligands affect this rate is not known. This information can be obtained by modifying the live cell nanoparticle binding experiments carried out in Figure 8.5. In Figure 8.5, the cells were treated with saturating concentrations of rituximab Fab targeted nanoparticles containing Cy3 labelled siRNA and the siRNA concentration in the supernatant after centrifugation was subtracted from the initial concentration to get the cell-bound percentage. In order to track internalization, the cells can be further incubated at 37°C, after the initial incubation at 4°C for 30 minutes, to promote internalization. The concentration of the supernatant can be obtained as a function of time in order to determine the percent bound over time at 37°C. This data will provide a relative rate of internalization for each targeted nanoparticle and can be used to compare the effect of targeting ligand on the rate of internalization. Repeating the aforementioned experiments with different targeting ligand densities will provide data regarding the effect of targeting ligand density on the rate of nanoparticle internalization. A comparison of the internalization data to gene inhibition data after transfection can be used to derive some information about the role of internalization rates on therapeutic potency.

9.5 Multivalent interactions of Fab and F(ab')₂ targeted nanoparticles

The effect of simultaneous binding events of multiple Fab and F(ab')₂ ligands to multiple receptors, otherwise known as multivalent interactions, may be crucial to the

internalization of our Fab- and F(ab')₂-targeted nanoparticles. These multiple interactions have been shown in several cases to give rise to 10-10000-fold enhancements in the K_d of the multivalent conjugate.²⁻⁴ The presence and relative degree of multivalency can be investigated by carrying out competitive binding assays with the nanoparticles. The rituximab-AF488 competitive binding curves of purified Fab- and F(ab')₂-targeted particles should give rise to a greater displacement of rituximab-AF488 at higher targeting ligand concentrations than the free monomeric conjugates at similar concentrations if multivalent interactions are indeed present. If found to be present, then real binding curves with targeted nanoparticles containing encapsulated labeled siRNA can be conducted over Daudi cells at 4°C in order to obtain apparent binding affinities, K_d, for the particles. The valency on the particle needed to give rise to the multivalent or avidity effect can also be calculated.

9.6 References

1. Sperling, R. A.; Liedl, T.; Duhr, S.; Kudera, S.; Zanella, M.; Lin, C. A. J.; Chang, W. H.; Braun, D.; Parak, W. J., *Journal of Physical Chemistry C* **2007**, 111, (31), 11552-11559.
2. Hong, S.; Leroueil, P. R.; Majoros, I. J.; Orr, B. G.; Baker, J. R.; Holl, M. M. B., *Chemistry & Biology* **2007**, 14, (1), 107-115.
3. Rossi, E. A.; Goldenberg, D. M.; Cardillo, T. M.; Stein, R.; Wang, Y.; Chang, C. H., *Cancer Research* **2008**, 68, (20), 8384-8392.
4. Stella, B.; Arpicco, S.; Peracchia, M. T.; Desmaele, D.; Hoebeke, J.; Renoir, M.; D'Angelo, J.; Cattel, L.; Couvreur, P., *Journal of Pharmaceutical Sciences* **2000**, 89, (11), 1452-1464.